

UNCLASSIFIED

AD NUMBER

AD922382

LIMITATION CHANGES

TO:

Approved for public release; distribution is unlimited.

FROM:

Distribution authorized to U.S. Gov't. agencies only; Test and Evaluation; SEP 1974. Other requests shall be referred to Air Force Flight Dynamics Laboratory, FEC, Wright-Patterson AFB, OH 45433.

AUTHORITY

affdl ltr, 2 dec 1978

THIS PAGE IS UNCLASSIFIED

**L**  
**AFFDL-TR-74-93**

**DESIGN AND DEVELOPMENT  
OF CRYOGENIC TURBO REFRIGERATOR SYSTEMS**

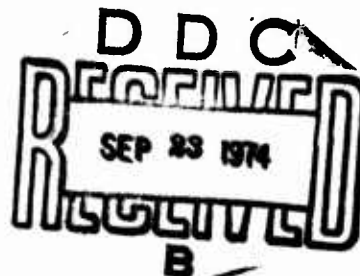
**D. B. Colyer, et al.  
Power Generation and Propulsion Laboratory  
Corporate Research and Development  
General Electric Company  
Schenectady, New York 12301**

**AD 922382**

**TECHNICAL REPORT AFFDL-TR-74-93**

**April 1974**

**Distribution limited to U. S. Government  
agencies only; test and evaluation; state-  
ment applied September 1974. Other re-  
quests for the document must be referred  
to: Air Force Flight Dynamics Laboratory  
(FEC), Wright-Patterson Air Force Base,  
Ohio 45433.**



**AIR FORCE FLIGHT DYNAMICS LABORATORY  
AIR FORCE SYSTEMS COMMAND  
WRIGHT-PATTERSON AIR FORCE BASE, OHIO 45433**

**SRD-74-094**

## NOTICE

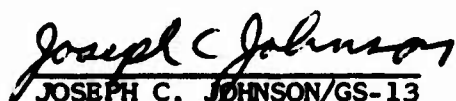
When Government drawings, specifications, or other data are used for any purpose other than in connection with a definitely related Government procurement operation, the United States Government thereby incurs no responsibility nor any obligation whatsoever; and the fact that the government may have formulated, furnished, or in any way supplied the said drawings, specifications, or other data, is not to be regarded by implication or otherwise as in any manner licensing the holder or any other person or corporation, or conveying any rights or permission to manufacture, use, or sell any patented invention that may in any way be related thereto.

This final report was submitted by the Research and Development Center of the General Electric Company under Contract F33615-71-C-1003, job order 641A0002. The technical effort was directed by the Air Force Flight Dynamics Laboratory, Wright-Patterson Air Force Base, Ohio 45433. Forrest R. Stidham, FEE, was the engineer in charge.

This technical report has been reviewed and is approved for publication.

  
FORREST R. STIDHAM/GS-13  
Project Engineer

FOR THE COMMANDER

  
JOSEPH C. JOHNSON/GS-13  
Tech Mgr., Adv. Cryo Cooler Sys.  
Environmental Control Branch  
Vehicle Equipment Division

Copies of this report should not be returned unless return is required by security considerations, contractual obligations, or notice on a specific document.

The pages of this report are printed on 100 percent recycled paper in the General Electric Company's continuing interest in resource conservation and pollution abatement.

Unclassified

SECURITY CLASSIFICATION OF THIS PAGE (When Data Entered)

REPORT DOCUMENTATION PAGE		READ INSTRUCTIONS BEFORE COMPLETING FORM
1. REPORT NUMBER AFFDL-TR-74-93.	2. GOVT ACCESSION NO.	3. RECIPIENT'S CATALOG NUMBER
4. TITLE (and Subtitle)  DESIGN AND DEVELOPMENT OF CRYOGENIC TURBO REFRIGERATOR SYSTEMS		5. TYPE OF REPORT & PERIOD COVERED Final Report 10-17-72 - 3-30-74
		6. PERFORMING ORG. REPORT NUMBER SRD-74-094
7. AUTHOR(s)  D.B. Colyer, et al.		8. CONTRACT OR GRANT NUMBER(s)  F33615-71-C-1003
9. PERFORMING ORGANIZATION NAME AND ADDRESS Corporate Research and Development General Electric Company Schenectady, New York		10. PROGRAM ELEMENT, PROJECT, TASK AREA & WORK UNIT NUMBERS  Project 641A
11. CONTROLLING OFFICE NAME AND ADDRESS Air Force Flight Dynamics Laboratory Air Force Systems Command Wright-Patterson Air Force Base, Ohio		12. REPORT DATE April 1974
		13. NUMBER OF PAGES 211
14. MONITORING AGENCY NAME & ADDRESS (if different from Controlling Office)		15. SECURITY CLASS. (of this report)  Unclassified
		15a. DECLASSIFICATION/DOWNGRADING SCHEDULE
16. DISTRIBUTION STATEMENT (of this Report) Distribution limited to U.S. Government agencies only; test and evaluation; statement applied September 1974. Other requests for the document must be referred to Air Force Flight Dynamics Laboratory (FEC), Wright-Patterson Air Force Base, Ohio 45433.		
17. DISTRIBUTION STATEMENT (of the abstract entered in Block 20, if different from Report)		
18. SUPPLEMENTARY NOTES		
19. KEY WORDS (Continue on reverse side if necessary and identify by block number) Cryogenics                      Turboalternator Heat exchanger                Turbocompressor Refrigerator		
20. ABSTRACT (Continue on reverse side if necessary and identify by block number) This Phase C final technical report describes the analysis, design, and manufacturing work directed toward the advanced development of a miniature cryogenic turbo refrigerator for cooling infrared sensors, superconducting elements, and electronic devices. An important goal of the program is the demonstration of long life (30,000 hours) and maintenance-free operation, with a 5000-hour endurance test. The refrigeration requirement for the turbo refrigerator is:		

Unclassified



Unclassified

SECURITY CLASSIFICATION OF THIS PAGE(When Data Entered)

**20. Abstract (Continued)**

- 1.5 watts at 12°K
- 40.0 watts at 60°K

During this report period, the design of the components and the complete system has been completed. Manufacture and final testing of the cryogenic heat exchanger was completed, and substantial testing has been conducted with the cryogenic turboalternators. Most of the parts of the centrifugal compressors are near completion. From the analysis, design studies, and tests conducted to date, it is concluded that the long-life, cryogenic turbo refrigerator system can be constructed to satisfy contract goals with respect to input power levels.

Unclassified

SECURITY CLASSIFICATION OF THIS PAGE(When Data Entered)

## **FOREWORD**

This final technical report covers Phase C development work performed under Contract No. F33615-71-C-1003 with the Department of the Air Force, Air Force Systems Command, Air Force Flight Dynamics Laboratory, Wright-Patterson Air Force Base, Ohio. The work was performed by the Mechanical Engineering Laboratory in the Research and Development Center of the General Electric Company in Schenectady, New York. Work described herein covers the period from 17 October 1972 through 30 March 1974. Work was initiated 17 August 1970 under Project 641A.

Development work during Phases A and B are described in the following reports:

- Phase A: AFFDL-TR-71-117, Volumes I and II (for work performed from 17 August 1970 through 12 August 1971)
- Phase B: AFFDL-TR-72-154, Volumes I through III (for work performed from 13 August 1971 through 17 October 1972)

The program was under the direction of F.R. Stidham, of the Air Force Flight Dynamics Laboratory (FEC); this report was submitted in April 1974.

The General Electric Program Manager was D.B. Colyer, and this report was authored by the principal contributors to the program:

D.B. Colyer  
R.B. Fleming  
H.E. Marx  
W.R. Oney  
R.K. Terbush

# TABLE OF CONTENTS

<u>Section</u>		<u>Page</u>
1	INTRODUCTION AND SUMMARY . . . . .	1
	Types of Long-Life Refrigerators . . . . .	3
	Description of Turbo Refrigerators . . . . .	4
	Accomplishments Under Contract. . . . .	6
	Contract Changes . . . . .	6
2	TURBOCOMPRESSORS . . . . .	9
	Introduction and Status . . . . .	9
	Design. . . . .	10
	Requirements . . . . .	10
	Compressor Subsystem Design. . . . .	16
	Mechanical Design . . . . .	17
	Shaft . . . . .	17
	Compressor Gas Bearing System. . . . .	21
	Initial Bearing Clearance Determination. . . . .	23
	Journal Bearing Pad Installation . . . . .	30
	Shimming Spring-Loaded Stem . . . . .	30
	Initial Setting. . . . .	30
	Final Setup . . . . .	31
	Thermal Design . . . . .	33
	Electrical Design. . . . .	36
	Design . . . . .	36
	Breadboard Motor Tests. . . . .	38
	Corona . . . . .	39
	Electrical Balance . . . . .	39
	Excitation Curve . . . . .	40
	Locked Rotor Torque . . . . .	40
	Torque Slip Tests. . . . .	41
	Discussion and Summary of Tests . . . . .	42
	Fabrication . . . . .	43
	Shaft . . . . .	43
	Scrolls . . . . .	44
	Impellers . . . . .	44
	Journal Bearing Pads . . . . .	44
	Journal Bearing Pivots . . . . .	48
	Thrust Bearings . . . . .	49
	Housings. . . . .	51
	Feedthrough Bulkheads . . . . .	52
	Gas Bearing Simulator Hardware . . . . .	52
	Test Results and Evaluation . . . . .	53
	Thrust Bearing Flatness Tests at Elevated Temperatures . . . . .	53

## TABLE OF CONTENTS (Cont'd)

<u>Section</u>		<u>Page</u>
2	TURBOCOMPRESSORS (Cont'd)	
	Thrust Bearing 1-2780 . . . . .	53
	Thrust Bearing 6-2779 . . . . .	58
	Compressor Shaft Stiffness Tests. . . . .	60
	Gas Bearing Simulator . . . . .	63
	Closed Cycle Compressor Test Loop . . . . .	66
	Turbocompressor Hardware Status . . . . .	72
	Module A . . . . .	72
	Module B . . . . .	72
	Gas Bearing Simulator . . . . .	73
3	TURBOALTERNATORS . . . . .	75
	Fabrication . . . . .	75
	Shafts . . . . .	75
	First-Stage Aluminum Turbine Wheel. . . . .	77
	Journal Bearing Pads . . . . .	77
	Journal Bearing Spring Stems (Double-Spring Design). . . . .	81
	Journal Bearing Pivot Stems. . . . .	81
	Thrust Bearing Gimbal Pivots . . . . .	82
	Weldable Lead Feedthroughs. . . . .	82
	Test and Evaluation. . . . .	83
	Test Objectives and Plans . . . . .	83
	Open-Cycle, Single-Stage Turboalternator Test Plans . . . . .	83
	Closed-Cycle, Two-Stage Turboalternator Test Plans . . . . .	86
	Functional Tests . . . . .	92
	Turboalternator Build 6 . . . . .	92
	Turboalternator Build 7 . . . . .	95
	Turboalternator Build 8 . . . . .	103
	Turboalternator Build 9 . . . . .	106
	Turboalternator Build 10 . . . . .	108
	Performance Tests . . . . .	111
	First-Stage Open Cycle Tests . . . . .	111
	First-Stage Performance Test Results . . . . .	111
	Performance Results . . . . .	122
	Cryogenic Temperature Tests . . . . .	130
4	CRYOGENIC HEAT EXCHANGERS . . . . .	157
	Exchanger System Configuration . . . . .	157
	Basic Exchanger . . . . .	159

## TABLE OF CONTENTS (Cont'd)

<u>Section</u>	<u>Page</u>
<b>4</b>	<b>CRYOGENIC HEAT EXCHANGERS (Cont'd)</b>
	Cover and Manifolding. . . . . 164
	Performance Analysis. . . . . 166
	Basic Approach . . . . . 166
	Design Performance Calculations. . . . . 167
	Testing . . . . . 168
	Test Procedure. . . . . 168
	External Leakage . . . . . 168
	Stream-to-Stream Leakage . . . . . 169
	Thermal Effectiveness Test . . . . . 169
	Pressure Drop . . . . . 172
	Test Results . . . . . 173
	External Leakage . . . . . 173
	Stream-to-Stream Leakage . . . . . 173
	Thermal Efficiency . . . . . 173
	Pressure Drop . . . . . 175
	Summary and Conclusions . . . . . 175
<b>5</b>	<b>HEAT REJECTION SYSTEM . . . . . 179</b>
<b>6</b>	<b>REFERENCES . . . . . 181</b>
<b><u>Appendix</u></b>	
<b>I</b>	<b>HEAT EXCHANGER DESIGN PERFORMANCE</b>
	<b>CALCULATIONS . . . . . 183</b>
<b>II</b>	<b>HEAT EXCHANGER TEST PROCEDURE . . . . . 187</b>
	Leakage Test . . . . . 187
	External Leak Test . . . . . 187
	Stream-to-Stream Leak Test . . . . . 188
	Thermal Effectiveness . . . . . 188
	Preliminary Leak Test . . . . . 188
	Thermal Effectiveness Test . . . . . 189
	Pressure Drop . . . . . 191
<b>III</b>	<b>HEAT EXCHANGER TEST DATA AND DATA</b>
	<b>REDUCTION . . . . . 193</b>
	Effectiveness Data Reduction (Typical) . . . . . 193
	Pressure Drop Data Reduction . . . . . 195
	Nitrogen Flow, Test 2 . . . . . 195
	Helium Flow, Test 3 . . . . . 195
	Pressure Drop Calculation at Test Conditions
	(Typical) -- Nitrogen at Design Flow . . . . . 196

## TABLE OF CONTENTS (Cont'd)

<u>Appendix</u>		<u>Page</u>
IV	COMPRESSOR AFTERCOOLER DESIGN. . . . .	201
	Performance . . . . .	202
	Cleanliness . . . . .	202
	Contamination . . . . .	202
	Oxygen Service . . . . .	204
	Structural Considerations . . . . .	204
V	HEAT REJECTION SYSTEM DESIGN . . . . .	205
	Thermal Performance and Pressure Drop	
	Requirements . . . . .	205
	Design and Construction . . . . .	205
	Controls and Instrumentation. . . . .	207
	System Operation . . . . .	209
	System Components . . . . .	210
	Instrumentation. . . . .	210
	Testing . . . . .	211

### DISTRIBUTION LIST

## LIST OF ILLUSTRATIONS

<u>Figure</u>		
1	Refrigerator Cryosection . . . . .	2
2	Refrigerator Compressor System . . . . .	3
3	Cycles Suitable for Turbomachinery . . . . .	4
4	Final Layout Showing Compressor Subsection with Two-Stage Modules A and B . . . . .	11
5	Requirements for Complete Compressor System . . . . .	12
6	Refrigerator B Compressor Design. . . . .	13
7	Module A, Stages 1 and 2 . . . . .	18
8	Schematic Diagram of Test Setup. . . . .	19
9	Rotor for Modules A and B . . . . .	20
10	Gas Bearing Simulator Arrangement . . . . .	21
11	Gas Bearing Simulator with Dewar . . . . .	22
12	Gas Bearing Simulator Pad Analysis Results . . . . .	24

## LIST OF ILLUSTRATIONS (Cont'd)

<u>Figure</u>		<u>Page</u>
13	Gas-Lubricated Journal Bearings . . . . .	25
14	Schematic Diagram of Pivoted Pad Journal Bearing . . .	28
15	Pivoted Pad Journal Bearing . . . . .	29
16	Triangle Legs Formed on Oscilloscope as Shaft Drops Between Pads . . . . .	31
17	Relative Shaft Motion with Spring-Loaded Pad . . . . .	32
18	Compressor Shaft Thrust Bearing Heat Transfer Model .	33
19	Radial Displacement of Shaft in Journal Bearing Area . .	35
20	Displacements of Thrust Runner Surface A-A . . . . .	35
21	Compressor Centrifugal and Thermal Deflection . . . . .	36
22	Thrust Bearing Warping at 400°F . . . . .	37
23	Cross Section of Magnetically Segmented Shell Around Magnet . . . . .	38
24	Breadboard Motor Excitation at 200 Hertz . . . . .	40
25	Breadboard Motor Locked Rotor Torque . . . . .	41
26	Breadboard Motor Speed-Torque Characteristics . . . . .	41
27	First Completed Shaft . . . . .	43
28	First-Stage Scroll . . . . .	45
29	Second-Stage Scroll . . . . .	46
30	Impellers . . . . .	47
31	Completed Journal Bearing Pads . . . . .	48
32	Spring and Solid Stem . . . . .	49
33	Face of Completed Bearing . . . . .	51
34	Four-Piece Structural Housings . . . . .	51
35	Outer Housing . . . . .	52
36	Feedthrough Bulkheads . . . . .	52
37	Original Condition of Thrust Bearing . . . . .	54
38	Thrust Bearing at Equilibrium (105°C) . . . . .	55
39	Thrust Bearing at Nonequilibrium (60°C) . . . . .	56
40	Thrust Bearing Cooling at Equilibrium (45°C) . . . . .	57

## LIST OF ILLUSTRATIONS (Cont'd)

<u>Figure</u>		<u>Page</u>
41	Thrust Bearing Final Shape . . . . .	58
42	Thrust Bearing Original Shape . . . . .	59
43	Thrust Bearing (100°C) . . . . .	59
44	First Compressor Shaft Deflection Versus Load . . . . .	60
45	Results of Turbocompressor Tests for Natural Frequency Rotor . . . . .	62
46	Results of Turbocompressor Tests for Natural Frequency of Rotor, with Suspended Rotor Excited by Striking . . . .	63
47	Closed Cycle Test Loop Assembly . . . . .	66
48	Mockup of Compressor Module in Place in Loop . . . . .	67
49	Motor-Compressor Test Station . . . . .	68
50	Performance Map . . . . .	69
51	Modified Tilting Pad Journal Bearing . . . . .	78
52	Principal Turboalternator Instrumentation . . . . .	84
53	Closed Cycle Turboalternator Test Station for Module A .	87
54	Closed Cycle Turboalternator Test Station for Module B .	91
55	Turboalternator Shaft and First-Stage Journal Bearings from Build 6 . . . . .	93
56	Closeup of Journal Bearing Pads from First-Stage End of Turboalternator Assembly, Build 6 . . . . .	94
57	Open Cycle Sealed Housing Leak Rate with Feedthroughs Assembled . . . . .	96
58	Turboalternator Heating Effects Noted During Run 110 with Nitrogen Gas at Pressure Ratio of 1.2 . . . . .	98
59	Two-Stage Turboalternator Inner Thrust Bearing Assembly . . . . .	100
60	Kentanium-Grade K-165 Journal Bearing Pads . . . . .	103
61	Shaft Orbits of Second-Stage Turboalternator Assembly, Build 8, Operating at 100,000 Rpm . . . . .	105
62	Shaft Axial Motion Between Thrust Bearings of Turboalternator Assembly, Build 8, Operating at 100,000 Rpm . . . . .	105



## LIST OF ILLUSTRATIONS (Cont'd)

<u>Figure</u>		<u>Page</u>
63	Shaft Orbits of First-Stage Turboalternator Assembly, Build 10, Operating at 100,000 Rpm . . . . .	109
64	Shaft Axial Motion Between Thrust Bearings of Turboalternator Assembly, Build 10, Operating at 100,000 Rpm . . . . .	109
65	Turboalternator Performance -- Overall Efficiency Versus Velocity Ratio for Helium Gas at Room Temperature. . . . .	112
66	Turboalternator Performance -- Overall Efficiency Versus Velocity Ratio for Nitrogen Gas at Room Temperature. . . . .	113
67	Turboalternator Performance -- Wheel Efficiency Versus Velocity Ratio for Helium Gas at Room Temperature. . . . .	114
68	Turboalternator Performance -- Wheel Efficiency Versus Velocity Ratio for Nitrogen Gas at Room Temperature. . . . .	115
69	Turboalternator Performance -- Flow Factor Versus Velocity Ratio for Helium Gas at Room Temperature. . . . .	116
70	Turboalternator Performance -- Flow Factor Versus Velocity Ratio for Nitrogen Gas at Room Temperature. . . . .	117
71	Turboalternator Performance -- Pressure Ratio Versus Velocity Ratio for Helium Gas at Room Temperature. . . . .	118
72	Turboalternator Performance -- Pressure Ratio Versus Velocity Ratio for Nitrogen Gas at Room Temperature. . . . .	119
73	Turboalternator Performance -- Corrected Torque Versus Velocity Ratio for Helium Gas at Room Temperature. . . . .	120
74	Turboalternator Performance -- Corrected Torque Versus Velocity Ratio for Nitrogen Gas at Room Temperature. . . . .	121
75	Flow Factor Versus Overall Pressure Ratio for Helium . . . . .	122

## LIST OF ILLUSTRATIONS (Cont'd)

<u>Figure</u>		<u>Page</u>
76	Flow Factor Versus Overall Pressure Ratio for Nitrogen .	123
77	Flow Factor and Efficiency Versus Velocity Ratio . . . .	125
78	Leakage Ratio and Torque Versus Velocity Ratio . . . . .	126
79	Efficiency Versus Velocity Ratio . . . . .	127
80	Single-Stage Turboalternator Open Cycle Performance with Helium Gas at Room Temperature . . . . .	128
81	Single-Stage Turboalternator Open Cycle Performance with Nitrogen Gas at Room Temperature . . . . .	129
82	Turboalternator Performance -- Overall Efficiency Versus Velocity Ratio for Helium Gas at 318°R, 177°K . .	132
83	Turboalternator Performance -- Wheel Efficiency Versus Velocity Ratio for Helium Gas at 318°R, 177°K . .	133
84	Turboalternator Performance -- Flow Factor Versus Velocity Ratio for Helium Gas at 318°R, 177°K . .	134
85	Turboalternator Performance -- Flow Factor Versus Corrected Speed for Helium Gas at 318°R, 177°K .	135
86	Turboalternator Performance -- Corrected Torque Versus Velocity Ratio for Helium Gas at 318°R, 177°K . .	136
87	Turboalternator Performance -- Electrical Output Power Versus Speed for Helium Gas at 318°R, 177°K . . . . .	137
88	Turboalternator Performance -- Flow Factor Versus Pressure Ratio for Helium Gas at 318°R . . . . .	138
89	Turboalternator Performance -- Pressure Ratio Versus Velocity Ratio for Helium Gas at 318°R. . . . .	139
90	Turboalternator Performance -- Flow Factor Versus Corrected Speed for Helium Gas at Room Temperature . . . . .	140
91	Turboalternator Performance -- Flow Factor Versus Corrected Speed for Nitrogen Gas at Room Temperature . . . . .	141
92	Turboalternator Performance -- Pressure Ratio Versus Velocity Ratio for Helium Gas at Room Temperature . . . . .	142

## LIST OF ILLUSTRATIONS (Cont'd)

<u>Figure</u>		<u>Page</u>
93	Turboalternator Performance -- Corrected Torque Versus Velocity Ratio for Nitrogen Gas at Room Temperature . . . . .	143
94	Turboalternator Performance -- Flow Factor Versus Velocity Ratio for Helium Gas at Room Temperature . . . . .	144
95	Turboalternator Performance -- Flow Factor Versus Velocity Ratio for Nitrogen Gas at Room Temperature . . . . .	145
96	Turboalternator Performance -- Pressure Ratio Versus Velocity Ratio for Nitrogen Gas at Room Temperature . . . . .	146
97	Turboalternator Performance -- Wheel Efficiency Versus Velocity Ratio for Helium Gas at Room Temperature . . . . .	147
98	Turboalternator Performance -- Corrected Torque Versus Velocity Ratio for Helium Gas at Room Temperature . . . . .	148
99	Turboalternator Performance -- Wheel Efficiency Versus Velocity Ratio for Nitrogen Gas at Room Temperature . . . . .	149
100	Turboalternator Performance -- Overall Efficiency Versus Velocity Ratio for Helium Gas at Room Temperature . . . . .	150
101	Turboalternator Performance -- Overall Efficiency Versus Velocity Ratio for Nitrogen Gas at Room Temperature . . . . .	151
102	Turboalternator Performance -- Flow Factor Versus Pressure Ratio for Helium Gas at Room Temperature . . . . .	152
103	Turboalternator Performance -- Flow Factor Versus Pressure Ratio for Nitrogen Gas at Room Temperature . . . . .	153
104	Turboalternator Performance -- Electrical Output Power Versus Speed for Helium Gas at Room Temperature . . .	154
105	Turboalternator Performance -- Electrical Output Power Versus Speed for Nitrogen Gas at Room Temperature . .	155

## LIST OF ILLUSTRATIONS (Cont'd)

<u>Figure</u>		<u>Page</u>
106	Reinforced Plastic Heat Exchanger Assembly -- As Tested . . . . .	158
107	Basic Heat Exchanger System . . . . .	160
108	Basic Heat Exchanger System -- Layout . . . . .	161
109	Basic Exchanger Construction . . . . .	162
110	Typical Lamina . . . . .	162
111	Typical Screen Parts . . . . .	163
112	Manifold Lamina . . . . .	163
113	Basic Exchanger System . . . . .	164
114	Exchanger and Cover . . . . .	165
115	Test System and Exchanger with Vacuum Chamber Removed . . . . .	169
116	Test System with Vacuum Chamber Installed . . . . .	170
117	Schematic Diagram of Test System . . . . .	171
118	Helium Flow Versus Nitrogen Boiloff . . . . .	173
119	Effectiveness Versus Mass Flow for Section 7 . . . . .	175
120	Pressure Drop Versus Mass Flow (Nitrogen at STP High-Pressure Stream of Section 7) . . . .	176
121	Pressure Drop Versus Mass Flow (Helium at 70°F and 20 Psig, High-Pressure Stream of Section 7) . . . . .	176
122	Heat Transfer Data for Mesh and Sphere Packing . . . . .	184
123	Friction Factors for Mesh and Sphere Packing . . . . .	184
124	Effective Thermal Conductivity of Packed Bed . . . . .	185
125	Schematic Diagram of Test System . . . . .	187
126	Test Setup for Stream-to-Stream Leakage . . . . .	188
127	Test Setup for External Leakage Check . . . . .	189
128	Port Locations (RPX 04). . . . .	191
129	Meriam Flowmeter Curve . . . . .	193
130	Schematic Diagram of Aftercoolers with Heat Rejection System . . . . .	201

## LIST OF ILLUSTRATIONS (Cont'd)

<u>Figure</u>		<u>Page</u>
131	Aftercooler Heat Exchanger . . . . .	203
132	Heat Rejection System . . . . .	208
133	Schematic Diagram of System Operation . . . . .	209

## LIST OF TABLES

<u>Table</u>		
1	Design Conditions . . . . .	34
2	Compressor Gas Bearing Losses . . . . .	34
3	Module A Design Point Performance Conditions . . . . .	89
4	Summary of Turboalternator Performance Results (Room Temperature with Helium Gas) . . . . .	97
5	Summary of Turboalternator Performance Results (Room Temperature with Nitrogen Gas) . . . . .	97
6	Comparison of Turboalternator Design and Test Results .	130
7	Summary of Turboalternator Performance Results (Helium Gas at 318°R) . . . . .	131
8	RPX-04 Stacking Order . . . . .	157
9	Performance Calculation Parameters for Heat Exchanger Section 7. . . . .	167
10	Hose and Thermocouple Connections . . . . .	189
11	Test Mass Flows . . . . .	190
12	Pressure Drop . . . . .	191
13	Effectiveness Test Data . . . . .	197
14	Pressure Drop Test Data . . . . .	198
15	Effectiveness Versus Mass Flow . . . . .	199
16	Performance Requirements . . . . .	202
17	Coolanol 20 Specifications . . . . .	206

## Section I

### INTRODUCTION AND SUMMARY

Phase A of this program covered the first year of the contract, beginning 17 August 1970 (Ref. 1). Phase B then covered the period from 13 August 1971 through 17 October 1972 (Ref. 2). This Phase C final report describes work carried out from 17 October 1972 to the time of the partial contract terminations and the subsequent completion of this final report on 30 March 1974. The work has been conducted under Contract No. F33615-71-C-1003, Project 641A, by Corporate Research and Development of the General Electric Company in Schenectady, New York.

Substantial progress has been made in the development of superconducting devices, infrared sensors, and other electronic devices dependent upon cooling at cryogenic temperatures. Applications of these devices require long-life, very reliable, cryogenic refrigerators that are compact and lightweight. It is therefore appropriate at this time to develop reliable cryogenic turbo refrigeration systems suitable for space, airborne, and ground applications.

The elements of the refrigeration systems program are:

- Optimization analysis: reliability, power input, weight, size, and cost
- Design life: 30,000 hours
- Fabrication and development of components
- System tests: performance, environmental, and 5000-hour endurance tests
- Delivery of system: installation, operation, and instruction

Performance goals, as specified in the contract, are:

<u>Characteristic</u>	<u>Refrigerator A</u>	<u>Refrigerator B</u>
Load at temperature	3.5 watts at $5 \pm 0.05^\circ\text{K}$	1.5 watts at $12^{+0.5}_{-12.0}^\circ\text{K}$
	40 watts at $50 \pm 0.5^\circ\text{K}$	40 watts at $60^{+0}_{-10}^\circ\text{K}$
	200 watts at $150 \pm 2.0^\circ\text{K}$	--
Maximum input power goal	16.0 kilowatts	4.0 kilowatts
Maximum weight goal	250 pounds	100 pounds

During this reporting period, the contract was changed to delete Refrigerator A.

Perspective drawings, approximately to scale, of the complete Refrigerator B cryosection and the complete compressor system are shown in Figures 1 and 2.

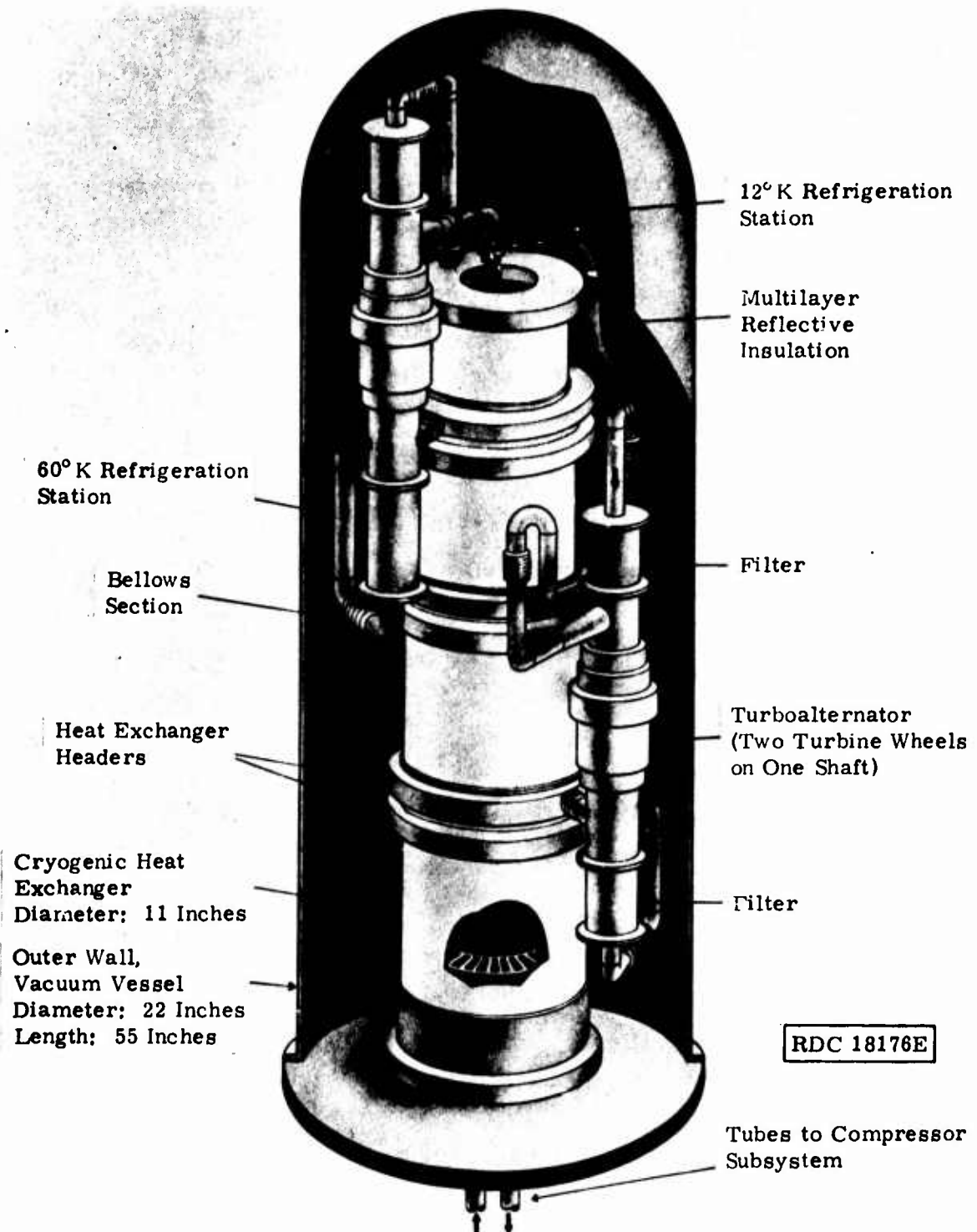


Figure 1. Refrigerator Cryosection

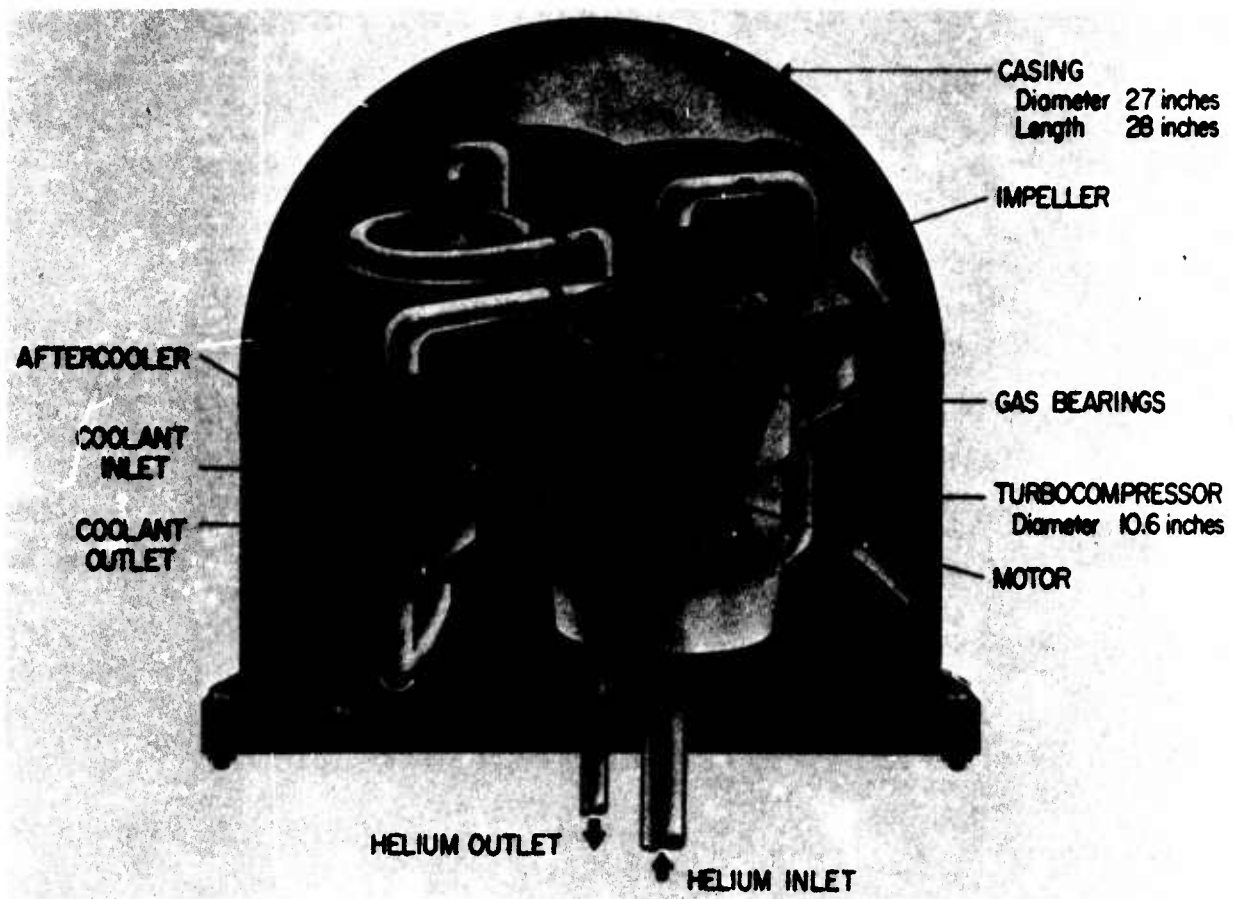


Figure 2. Refrigerator Compressor System

### TYPES OF LONG-LIFE REFRIGERATORS

Three types of refrigeration systems are now being considered by the Air Force, particularly for their performance and maintenance-free, long-life potential. These systems and their principal characteristics are:

- Vuilleumier

- Positive displacement

- Heat power input

- Reciprocating seals

- Thermal regenerators

- Oscillating pressure

- Lack of valving

- Small sealing pressure differences

- Rotary-Free Piston

- Positive displacement



Claude or reversed Brayton cycle

Valving

Gas bearings

No sliding contact

- Turbo Refrigerator

High-speed turbomachinery

Claude or reversed Brayton cycle

Gas bearings

No sliding contact

No valving

Steady pressures

The last of these is the system developed under this contract. This particular type of turbo refrigerator has all rotating components suspended on self-acting, gas-lubricated bearings. The elimination of sliding contact during steady operation avoids the wearout failure mode, providing the potential for maintenance-free, long-life operation.

### DESCRIPTION OF TURBO REFRIGERATORS

Turbomachinery is adaptable to either the reversed Brayton cycle or the Claude cycle (Figure 3). The principal components are:

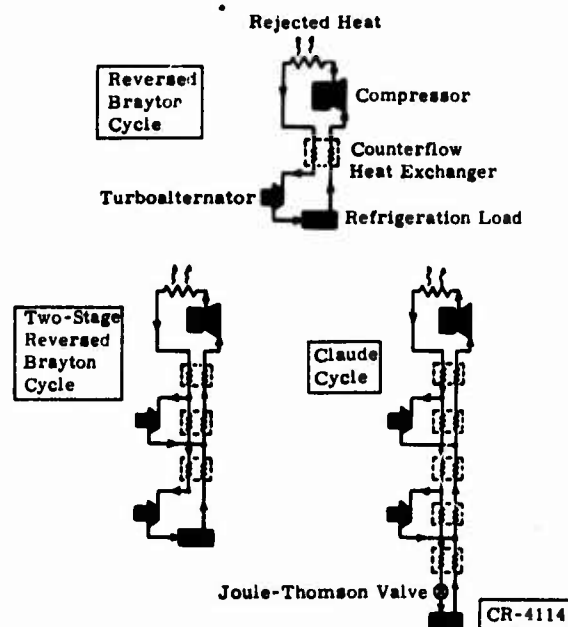


Figure 3. Cycles Suitable for Turbomachinery

- Motor-compressor at ambient temperature
- Cryogenic heat exchangers
- Cryogenic turboalternators

Energy is added to the system by compressing gas at ambient temperature and removing the heat of compression from the refrigerant gas in the after-cooler. The gas is then cooled to cryogenic temperature in the cryogenic counterflow heat exchangers. Energy is removed from the refrigerant by the cryogenic turbines, cooling the gas and dropping its pressure. The turbine mechanical energy is converted to electrical energy by the cryogenic alternator, and this electrical energy is used or dissipated at ambient temperature. The low-pressure, cooled gas is then available for removing heat from the refrigeration load and, finally, for removing heat from the high-pressure incoming gas stream in the cryogenic heat exchangers.

As shown in Figure 3, the Claude cycle differs from the reversed Brayton cycle only in the addition of a Joule-Thomson valve and heat exchanger. Cooling through a Joule-Thomson valve to produce liquid is possible only at temperatures close to the refrigerant critical temperature, where the Joule-Thomson coefficient is above zero.

Characteristics of gas bearing turbo refrigerators are summarized as follows:

- Gas bearings avoid sliding contact, providing potential for long life.
- Components are separable (the compressor or refrigeration station can be remotely located).
- There is essentially no vibration at the position of the refrigeration load.
- Input power is conditioned electrical power or shaft power from a mechanical energy source.
- Refrigeration load cooling is by means of a flowing gas or liquid stream.
- Temperatures of 4°K or lower can be attained.
- Refrigeration can simultaneously be provided at more than one location and at more than one temperature.
- Thermal time constants are large, and cold sections are well isolated, thermally, from warm sections (hence slow cooldown and slow warmup).

The potential for long-life turbo refrigerators is most attractive; hence, the following recent test results are described. A high-speed, partial admission, axial flow, cryogenic turbine-driven alternator, designed and built by the General Electric Company, has been undergoing an endurance test in the

General Electric Cryogenic Refrigeration Laboratory. The turboalternator is being continuously operated with gaseous nitrogen above 100,000 rpm, with a liquid nitrogen gas supply source. It is intended that this turboalternator be operated for thousands of hours at room temperature, to show some measure of the reliability of this type of high-speed, miniature, gas bearing turbo-machinery. To date, over 20,000 hours have been accumulated.

## **ACCOMPLISHMENTS UNDER CONTRACT**

During this reporting period, the design of the refrigerator system was completed. Also during the time period covered by this report, the principal components were further designed and developed. The compressor designs were essentially completed, and bench tests were conducted on many of the critical parts. The cryogenic turboalternator components were functionally tested and performance-tested. The cryogenic heat exchangers were developed, and the residual problems were identified.

## **CONTRACT CHANGES**

The contract was cut back in a series of steps; finally it was partially terminated, leaving only some of the data items to be completed. The first termination notice resulted in reducing the contract to a component development effort.

By a telegram dated 17 January 1973, Mr. W.E. Boger, Termination Contracting Officer, advised General Electric Corporate Research and Development:

Priority termination notice. For your immediate action reference contract F33615-71-C-1003 Docket #RC-248. Subject contract is hereby partially terminated for the convenience of the Government effective immediately upon receipt of this notice. Terminate all work except the fabrication and performance testing of the turbo compressor/turbo expander and cryogenic heat exchanger assembly. Also terminate the following Data Items: Sequence #B006/B009/B011 and B014. Since Sequence B006 (Test Report) is being terminated the data acquired from the component performance testing is to be included in item Sequence #B008 (Technical Report), Final Phase II. Immediately stop all work/terminate subcontracts and place no further orders except to the extent that you or subcontractor wish to retain and continue for own account, any work in processes or other materials. Telegraph similar instructions to all subcontractors and suppliers. Confirming copy with instructions follows.

The above data items are:

B006	Test Reports
B008	Phase B Final Technical Report

B009	Test Plan
B0011	Interim Technical Report
B0014	Phase C Final Technical Report

A slight modification was made by a telegram dated 23 January 1973. The General Electric Corporate Research and Development was advised:

Priority revision to termination notice reference contract F33615-71-C-1003. Docket Number RC-248. Termination notice is hereby amended to reinstate Data Item B014. Also delete the sentence "since Sequence No. B006 (Test Reports) is being terminated the data acquired from the component performance testing is to be included in item Sequence No. B008 (Technical Reports, Final Phase II)."

Finally the turbomachinery component development work was terminated by another notice. By a telegram dated 7 February 1973, Mr. W. E. Boger, Termination Contracting Officer, advised the General Electric Corporate Research and Development:

Termination notice priority action for your immediate action. Reference Contract Number F33615-71-C-1003. Docket Number RC-250. Subject contract is hereby partially terminated for the convenience of the Government, effective immediately upon receipt of this notice. Terminate all performance testing of the turbocompressor and turboexpanders. Immediately stop all work, terminate subcontracts, and place no further orders except to the extent that you or a subcontractor wish to retain and continue for your own account any work in process or other materials. Telegraph similar instructions to all subcontractors and suppliers. Confirming copy with instructions follows.

This notice resulted in a residual order of priorities of:

1. Complete all contract data items.
2. Manufacture turboalternator and turbocompressor parts.
3. Assemble turboalternators and turbocompressors.
4. Test turboalternators and turbocompressors functionally.
5. Complete the cryogenic heat exchanger.

Finally the turbomachinery development work was completely stopped. This action was taken as a result of a telegram dated 30 March 1973 from Mr. W. E. Boger, Termination Contracting Officer:

Priority action termination notice for your immediate action. Reference Contract F33615-71-C-1003. Docket Number RC-257.

Subject contract is hereby partially terminated for the convenience of the Government effective immediately upon receipt of this notice. Terminate all contract work except the heat exchanger and the following Data Items: Sequence Numbers B008/B010/B012/B013/B014/B015 and B016. Immediately stop all work/terminate subcontracts and place no further orders except to the extent that you or a subcontractor wish to retain and continue for own account any work in process or other materials. Telegraph similar instructions to all subcontractors and suppliers. Confirming copy with instructions follows.

The heat exchanger effort was not terminated because it was being developed by a subcontractor under a fixed price, guaranteed performance contract.

## Section 2

### TURBOCOMPRESSORS

#### INTRODUCTION AND STATUS

The design of the warm section of the refrigerator was completed during this phase of the program. A final layout (Figure 4) was made showing the compressor subsection with two-stage Modules A and B and related equipment contained within the leak-tight dewar. Final design of the majority of the individual components was also completed. Vendor proposals on the heat rejection system and the aftercoolers were received, but no action was taken on these proposals because initial component testing did not warrant obligating contract funds during this period.

The majority of the hardware required to build the first two-stage compressor module has been manufactured. Initial assembly had begun before the work stoppage resulting from contract changes. In addition, the majority of the hardware for the closed cycle test loop was finished, and assembly of the test facility piping and valving was done. No instrumentation had been included in the test stand facility when the work was stopped.

A major problem that arose during the period involved the manufacture of the thrust bearings for the compressor modules. Generating pockets in the surface of tungsten-carbide-coated thrust bearings, 1 mil deep to tolerances of  $\pm 0.000075$  inch, required considerable effort. Electrical discharge machining and ion etching were both considered and evaluated on sample pieces. Both methods proved unsuccessful; they both failed to produce a pocket finish or uniformity that was acceptable. The thrust bearing pockets were finally ground on a jig grinder, using special holding fixtures and extremely small diamond wheels. The results of this grinding were satisfactory and proved to be more economical than originally anticipated.

An analytical and experimental study of the effects of temperature on the journal and thrust bearings was conducted. Due to the temperature, nonuniformities along the compressor shaft and thrust bearing runner were predicted. Corrective design steps were taken to minimize these predicted distortions.

As a result of the design analysis and distortion test, the need to conduct closely monitored tests when the gas bearings were first installed became apparent. It was therefore decided to perform gas bearing tests using Module B compressor parts as a gas bearing simulator, prior to initiation of complete compressor assembly testing. A gas bearing simulator test facility was designed and manufactured. Assembly was just beginning when work was stopped due to contract changes.

## **DESIGN**

### **REQUIREMENTS**

The design performance requirements for the compressors and the design and development philosophy were described in detail in the Phase A final report. A summary of that work is presented below. Many computer runs were made to evaluate the suitability of various types of compressors (centrifugal and regenerative) and the effects of such variables on the number of compressor stages.

The established requirements for the complete compressor system are shown in Figure 5. Some of the overall selected or derived parameters, such as the number of stages and various efficiencies, are also listed. By properly proportioning the pressure rise for each stage to fill the projected stage efficiencies, the speed and induction motor power were kept approximately equal for both modules, thus allowing the use of identical shafts, motor parts, and bearing parts.

The use of two modules, of two stages each, was selected for several reasons:

- A single, simple, axial path is provided for each inlet.
- Motors, shafts, and bearings can be of identical design for both modules.
- Impeller thrusts can be largely counterbalanced by the mating impeller.
- Similar impellers and scrolls can be used.
- The number of bearing assemblies is minimized.
- One stage per module would greatly increase the weight, control problem, and costs.
- More than two stages per module greatly increases the complexity of analysis, design, and manufacturing.

Necessary features for the compressors included:

- Capability of operating at any attitude from 0 to 3.0-g loads
- Capability of normal operation after experiencing 15-g loads, not operating
- All material selections capable of 30,000-hour, continuous operation life
- Material selections compatible with low contamination requirements of refrigeration system and nuclear radiation environments

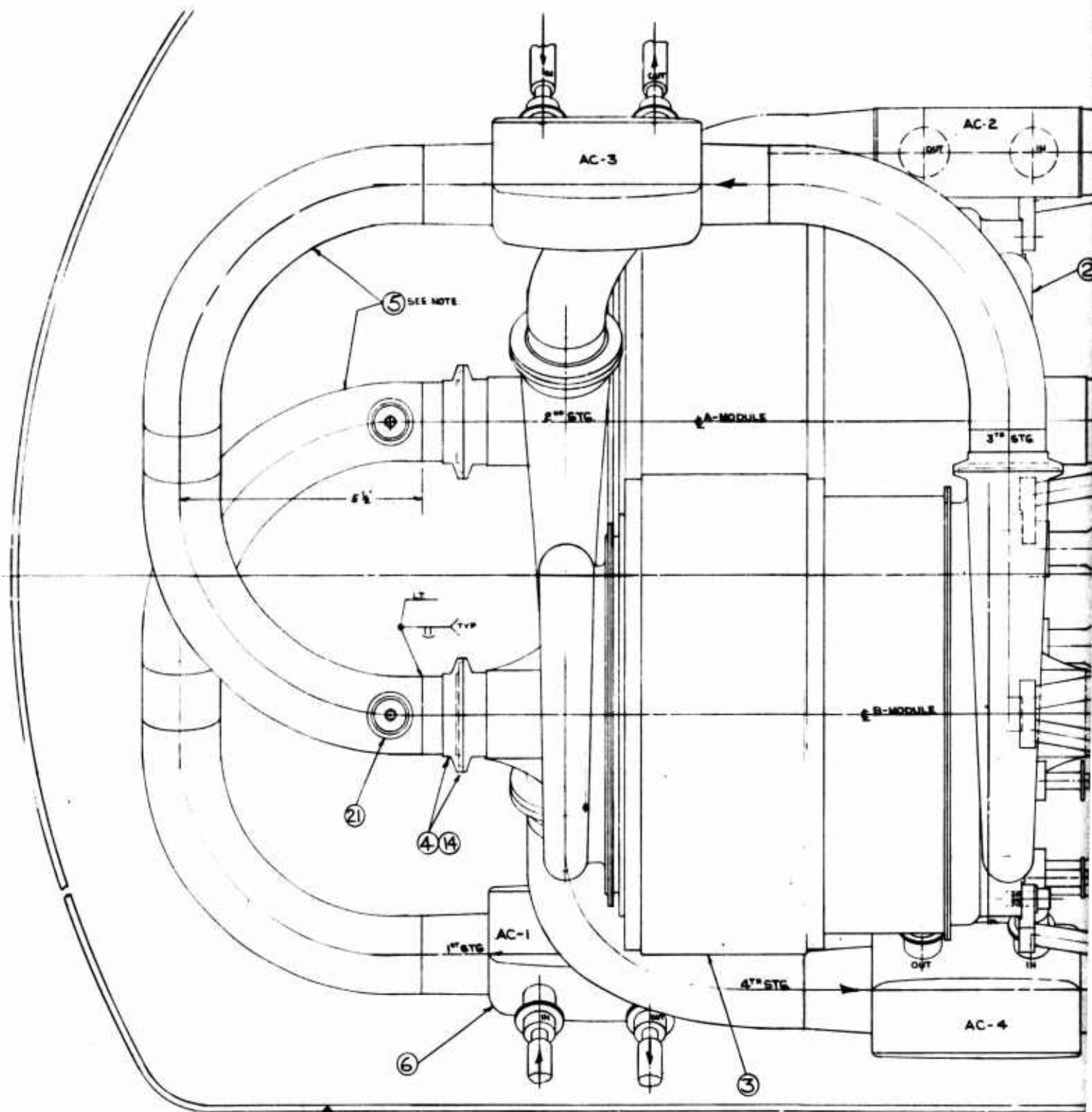
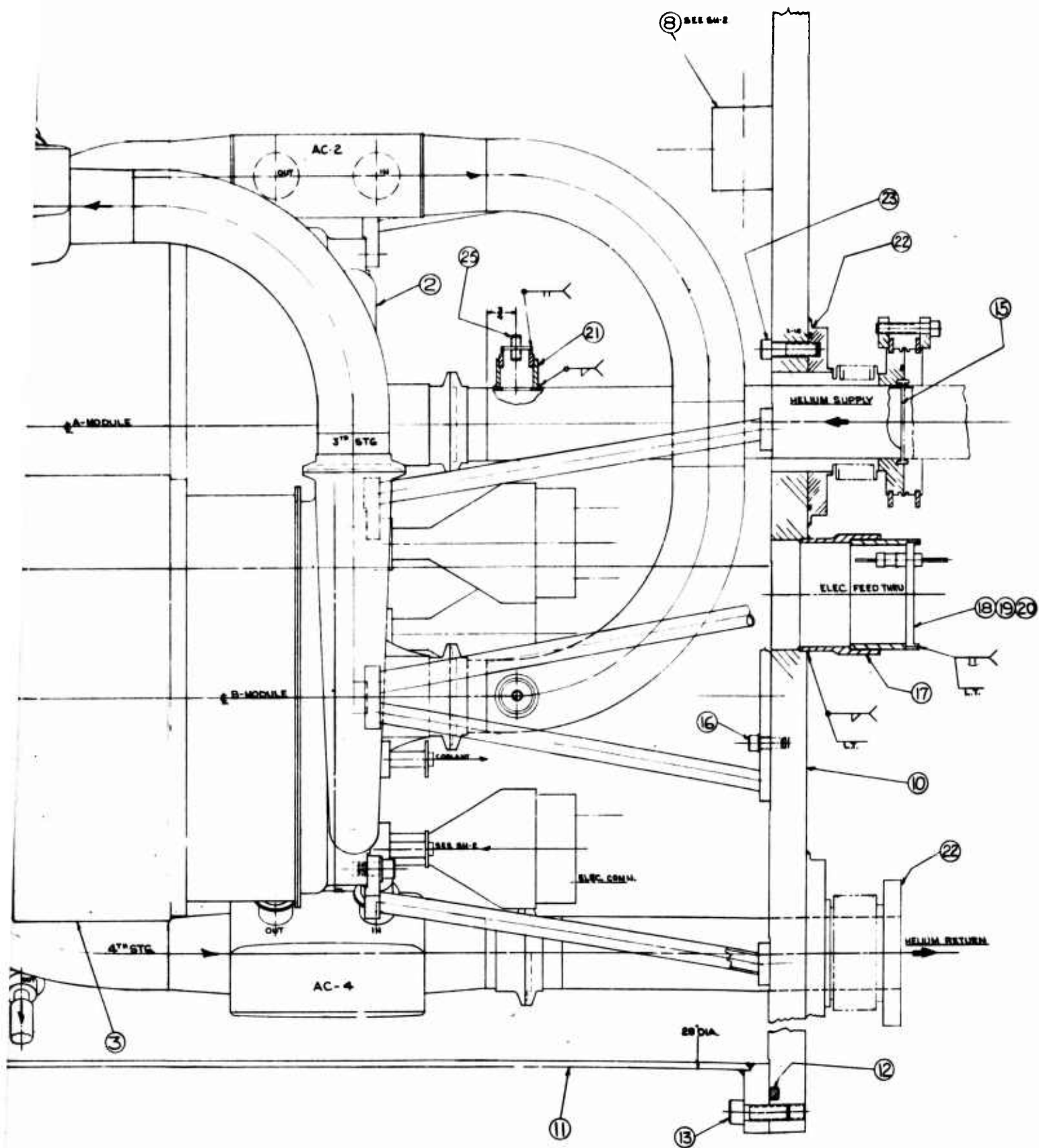


Figure 4. Final Layout Showing Compressor Subsection with





Showing Compressor Subsection with Two-Stage Modules A and B

7

- Gas bearings capable of stable operation within complete ranges of speeds, pressures, and temperatures
- High-speed motor stresses compatible with long design life
- Compact rotor design
- Adequate motor cooling
- Capability of many start-stop cycles
- Low input power to the compressor:
  - High aerodynamic efficiency
  - High motor electromagnetic efficiency
  - Low bearing and windage parasitic losses
- Compressor stage and stages in series operation with comfortable surge margins
- Complete compressor system operation 10 percent on either side of the design point
- Low rotating assembly weight for high critical speed
- Low-weight impellers to reduce the overhung mass for high critical speed
- Compact arrangement to reduce weight and size

CENTRIFUGAL COMPRESSOR DESIGN POINT COMPUTER OUTPUT  
DESIGN CASE 5331021001

OVERALL COMPRESSOR PERFORMANCE

INLET TEMPERATURE (K)	331.1
INLET PRESSURE (ATM)	0.3212
OUTLET TEMPERATURE (K)	335.0
OUTLET PRESSURE (ATM)	0.6650
PRESSURE RATIO	2.070
FLOW (G/SEC)	2.848
SPEED (RPM)	0.9100E+05
AMBIENT TEMPERATURE (K)	322.2
INPUT POWER (KW)	3.978
NUMBER OF MODULES	2.000
CONDIT-CONTROL EFFICIENCY	0.9200
NUMBER OF STAGES	4
OVERALL EFFICIENCY	0.4157

CR-3101

Figure 5. Requirements for Complete Compressor System

**Desirable features include:**

- Minimum development effort
- Low seal leakages
- Reasonable manufacturing costs
- Minimum number of stages for low cost and high reliability
- Low impeller stress levels to use low-strength materials
- Stationary impeller outer shroud, to minimize the impeller stress levels
- Minimum axial thrust for low total bearing losses
- Convenient design arrangement for ease of assembly and disassembly

Using the requirements listed in Figure 5 (inputs relating to bearing and electrical performance and losses) and considering the necessary and desirable features listed above, many component and system analyses and computer runs were completed. The summary program results for both modules (Module 1 and Module 2 for Modules A and B, respectively) are shown in Figure 6.

**MODULE NO. 1**

**PERFORMANCE**

STAGE NO.	1	2
INLET TEMPERATURE (R)	596.0	603.0
INLET PRESSURE (PSIA)	4.719	5.760
OUTLET TEMPERATURE (R)	675.7	682.7
PRESSURE RATIO	1.221	1.210
ACCUM. PRESS. RATIO	1.221	1.477
VOLUME FLOW (CFM)	127.5	105.7
AERO EFFICIENCY	0.6665	0.6459
SPECIFIC SPEED	0.4809E-01	0.4472E-01
AERO POWER (HP)	0.8780	0.8780
ISENTRPIC HEAD (FT)	0.5120E+05	0.4976E+05
TEMPERATURE RISE (R)	79.74	79.74
TIP SPEED (FPS)	1677.	1677.
TIP DIAMETER (IN)	4.224	4.224
EYE DIAMETER (IN)	1.486	1.427
HUB DIAMETER (IN)	0.4973	0.4920
TIP WIDTH (IN)	0.1056	0.9706E-01
COOLER EFFECTIVENESS	0.7598	0.7761
COOLER PRESS. DROP. RATIO	0.1400E-01	0.1400E-01
AFTERCoolER WEIGHT (LBS)	1.097	1.100

**CR-3101**

**Figure 6. Refrigerator B Compressor Design**

## MOTOR DESIGN

ELECTROMAG. EFF. (FR)	0.9300
DIAMETER (IN)	1.681
LENGTH (IN)	1.331
RADIAL GAP (IN)	0.2741E-01
PERIF. SPEED (FPS)	667.2
MOTOR POWER OUTPUT (HP)	2.371
MOTOR POWER LOSS (WATTS)	133.2
CONDIT-CONTROLLER LOSS (W)	165.4
CONDIT-CONTR. IN. POWER(KW)	2.068

## WINDAGE POWER LOSSES (WATTS)

JOURNAL FREE SHAFT LENGTH	25.03
MOTOR ROTOR GAP	5.375
TOTAL WINDAGE LOSS	30.40

## GAS BEARINGS DESIGN

### THRUST BEARING

LOAD(LBS.)	4.963
OUTSIDE DIAMETER(IN)	3.000
DIAMETER RATIO	0.6050
CLEAR. TO DIA. RATIO	0.4410E-03
LOAD COEFFICIENT	0.1923
BEARING NUMBER	21.48
CLEARANCE, LOADSIDE(IN)	0.1323E-02
FRICTION POWER(WATTS)	186.6

### JOURNAL BEARING

LOAD(LBS.)	2.482
LOAD COEFFICIENT	0.3165
BEARING NUMBER	2.000
CLEAR. TO DIA. RATIO	0.2043E-02
MACHINED CLEARANCE	0.3372E-02
PIV. FILM THICK.(IN)	0.1223E-02
FRICTION POWER(WATTS)	121.3

## GAS BEARINGS

ROTATING ASSY. WEIGHT(LBS)	4.963
ACCELERATION OF GRAVITY("G")	1.000
TOT. BEARING FRICTION(WATTS)	429.3
SHAFT LENGTH	8.700

CR-3101

Figure 6. Refrigerator B Compressor Design (Cont'd)

# MODULE NO. 2

## PERFORMANCE

STAGE NO.	1	2
INLET TEMPERATURE (R)	603.0	603.0
INLET PRESSURE (PSIA)	6.971	8.288
OUTLET TEMPERATURE (R)	676.5	670.7
PRESSURE RATIO	1.189	1.171
ACCUM. PRESS. RATIO	1.756	2.056
VOLUME FLOW (CFM)	87.34	73.46
AERO EFFICIENCY	0.6383	0.6326
SPECIFIC SPEED	0.4361E-01	0.4282E-01
AERO POWER (HP)	0.8092	0.7457
ISENTROPIC HEAD (FT)	0.4532E+05	0.4138E+05
TEMPERATURE RISE (R)	73.49	67.73
TIP SPEED (FPS)	1610.	1546.
TIP DIAMETER (IN)	4.055	3.892
EYE DIAMETER (IN)	1.357	1.289
HUB DIAMETER (IN)	0.4943	0.4757
TIP WIDTH (IN)	0.9050E-01	0.8534E-01
CØOLER EFFECTIVENESS	0.7616	0.7465
CØOLER PRESS. DROP. RATIO	0.1400E-01	0.1400E-01
AFTERCØOLER WEIGHT (LBS)	1.104	1.050

## MØTØR DESIGN

ELECTROMAG. EFF. (FR)	0.9300
DIAMETER (IN)	1.681
LENGTH (IN)	1.238
RADIAL GAP (IN)	0.2741E-01
PERIF. SPEED (FPS)	667.2
MØTØR POWER ØUTPUT (HP)	2.191
MØTØR POWER LOSS (WATTS)	123.0
CØNDIT-CØNTØLLER LOSS (W)	152.9
CØNDIT-CØNTR. IN. POWER(KW)	1.911

## WINDAGE POWER LOSSES (WATTS)

JØURNAL FREE SHAFT LENGTH	33.60
MØTØR RØTØR GAP	5.998
TØTAL WINDAGE LOSS	39.60

## GAS BEARINGØ DESIGN

### THRUST BEARING

LOAD(LBS.)	5.021
ØUTSIDE DIAMETER(IN)	3.000
DIAMETER RATIO	0.6050
CLEAR. TØ DIA. RATIO	0.4410E-03
LOAD CØEFFICIENT	0.1352

CR-3101

Figure 6. Refrigerator B Compressor Design (Cont'd)

BEARING NUMBER	14.94	
CLEARANCE, LOADSIDE (IN)	0.1323E-02	
FRICTION POWER (WATTS)	186.8	
JOURNAL BEARING		
LOAD (LBS.)	2.510	
LOAD COEFFICIENT	0.2225	
BEARING NUMBER	2.000	
CLEAR. TO DIA. RATIO	0.1703E-02	
MACHINED CLEARANCE	0.2811E-02	
PIV. FILM THICK. (IN)	0.1223E-02	
FRICTION POWER (WATTS)	124.5	
GAS BEARINGS		
ROTATING ASSY. WEIGHT (LBS)	5.021	
ACCELERATION OF GRAVITY ("G")	1.000	
TOT. BEARING FRICTION (WATTS)	435.9	
SHAFT LENGTH	8.700	CR-3101

Figure 6. Refrigerator B Compressor Design (Cont'd)

### COMPRESSOR SUBSYSTEM DESIGN

Figure 4 shows the final design concept for the warm section of the refrigerator. The outside housing and baseplate form a permanent enclosure for the compressor subsystem. This enclosure is vacuum-tight, preventing any helium leakage from the compressor subsystem. In operation, the housing would first be evacuated and then the compressor subsystem would be charged with helium. A port with a fine filter element is provided on the first-stage inlet line for intake of helium from the housing. This housing volume serves as an accumulator for the helium gas when the system warms up and when the helium pressure rises. The filter prevents in-leakage of particles from the surrounding volume. The principal features of the compressor subsystem are:

- Motor-Compressor. Two separate modules, each with two compressor stages, are combined in series to produce the required overall pressure ratio.
- Four Aftercoolers. These aftercoolers are used, following the individual compression stages, to remove the heat of compression and thereby reduce the required work input. Complete information is included in Section 5, "Heat Rejection System," of this report.
- Helium Ducts. Made from 1-1/2-inch-diameter aluminum tubing, the ducts interconnect the compressor stages. Five-inch radius elbows have been designed to minimize flow distortion and eliminate the need for compressor inlet guide vanes.
- Coolant Manifolds. These two manifolds supply the coolant to the aftercoolers and to the compressor modules, for heat removal.

- Dewar. A cylindrical dewar, 28 inches in diameter and 33 inches high (with a hemispherical end), has been designed. This dewar would be made of aluminum, with a 3/16-inch wall thickness, and would be leak-tight to less than  $10^{-8}$  torr-liter/sec with helium.

- Baseplate. This aluminum plate, approximately 1 inch thick, has provisions for all the feedthroughs required by the compressor subsystem, in addition to a leak-tight joint design for coupling with the dewar.

- Seals. All external joints have provisions for Viton A O-rings, for sealing during development testing. All of these joints have also been designed so they may be welded for a final, leak-tight assembly.

## MECHANICAL DESIGN

As discussed in the Phase B final report, the results of the system designs led to the selection of four centrifugal stages of compression and a two-module arrangement. The stages are arranged in series, and the pressure rise is essentially equal for each stage. Each module was therefore arranged with two stages, one on either end of a common shaft, with an identical motor centrally located in each module. Figure 7 shows Module A, Stages 1 and 2. Module B differs from Module A only in the impeller blading and scroll passage details. Thus the motor, shaft, bearings, and housing are interchangeable between the two modules. The major features of the individual compressor module components are described in detail in the Phase B final report.

## SHAFT

Using the first compressor shaft completed, two tests were run to determine the actual shaft stiffness. The initial test consisted of suspending weights from the center of the shaft, which was supported by its journal on V-blocks. The deflection resulting from the weight used was measured with a capacitance-type sensing probe.

On the basis of the data obtained from that test, it was determined that the stiffness of the compressor shaft was  $2.245 \times 10^6$  lb-in.<sup>2</sup>, compared to an  $EI = 7.28 \times 10^6$  lb-in.<sup>2</sup> used in the original design of the shaft and bearings (where  $E$  = Young's modulus [psi] and  $I$  = moment of inertia).

The original design data were reexamined in light of this variation in shaft stiffness to determine the effect on the compressor design. Using  $EI = 2.245 \times 10^6$  lb-in.<sup>2</sup>, combined with the original design data, produced a first bending critical speed of 61,076 rpm. This speed is of particular concern because it falls below the design operating speed. A rule of thumb for gas bearing design is that the first bending critical should be at least 25 percent above the normal operating speed for stable bearing operation.

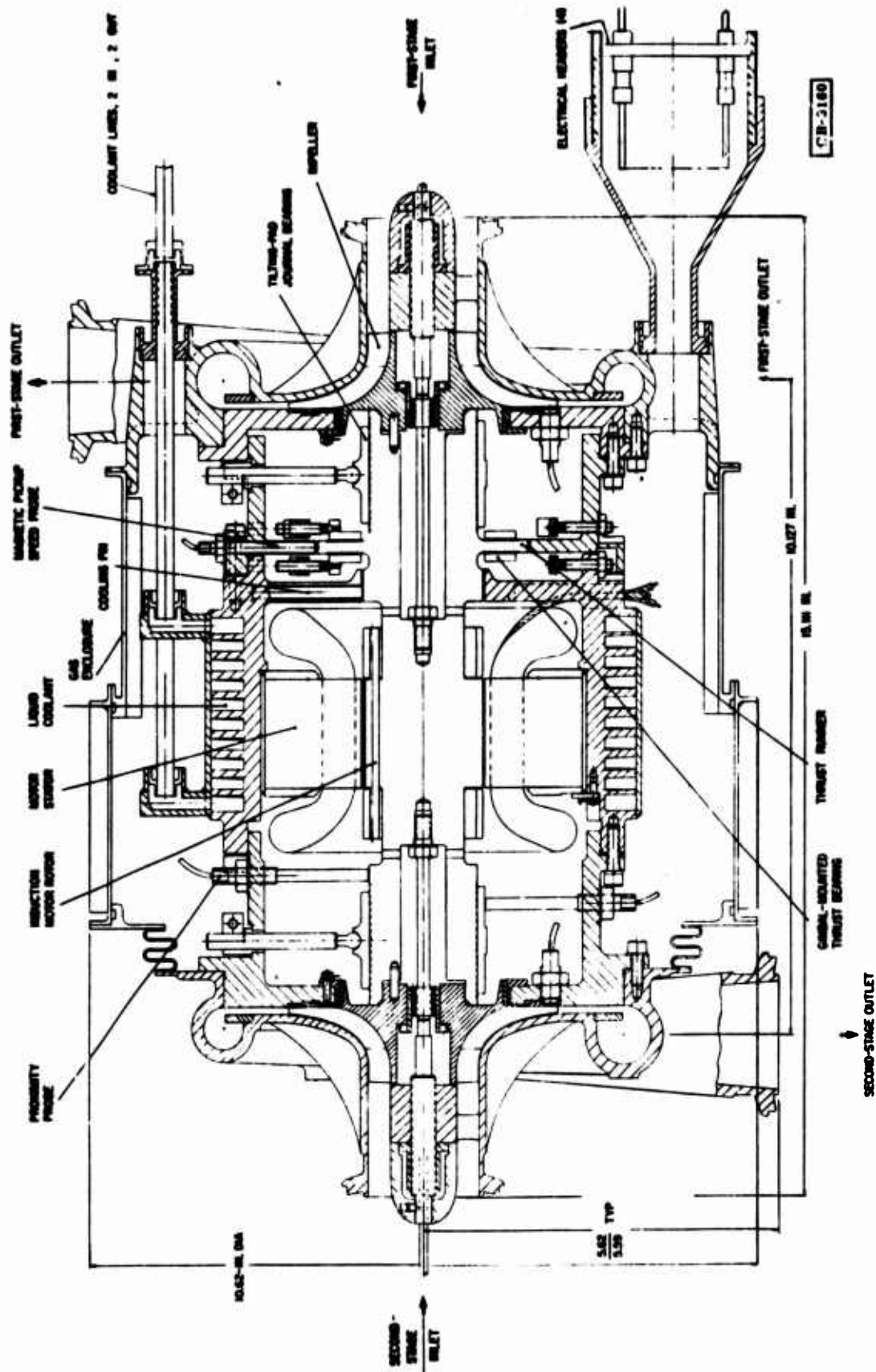


Figure 7. Module A, Stages 1 and 2



To verify that the shaft stiffness calculated from the load-versus-displacement test was valid, a more reliable test was devised. The shaft, with an accelerometer mounted at the midpoint, was hung from two strings so that its axis was in a horizontal plane. An electric coil placed near the shaft was then used to excite the suspended shaft, with the input excitation controlled by a variable-frequency oscillator. The output of the accelerometer was displayed on an oscilloscope. Figure 8 is a schematic diagram of the test setup.

The results of this test indicated that the actual bending critical speed is 156,000 rpm, rather than the 61,076 rpm computed. The shaft stiffness calculated from the results of the initial static load deflection test was invalid, and determination of the actual stiffness value from the dynamic test results became possible.

Using the tilting pad bearing selector program, JSELCT, and the loading shown in Figure 9 to calculate the first bending critical speed, iterations varying the shaft stiffness were made until a first bending critical equal to 156,000 rpm was calculated. This calculation occurred with an  $EI = 1.5 \times 10^7$  lb-in.<sup>2</sup>. This value is approximately double that originally calculated.

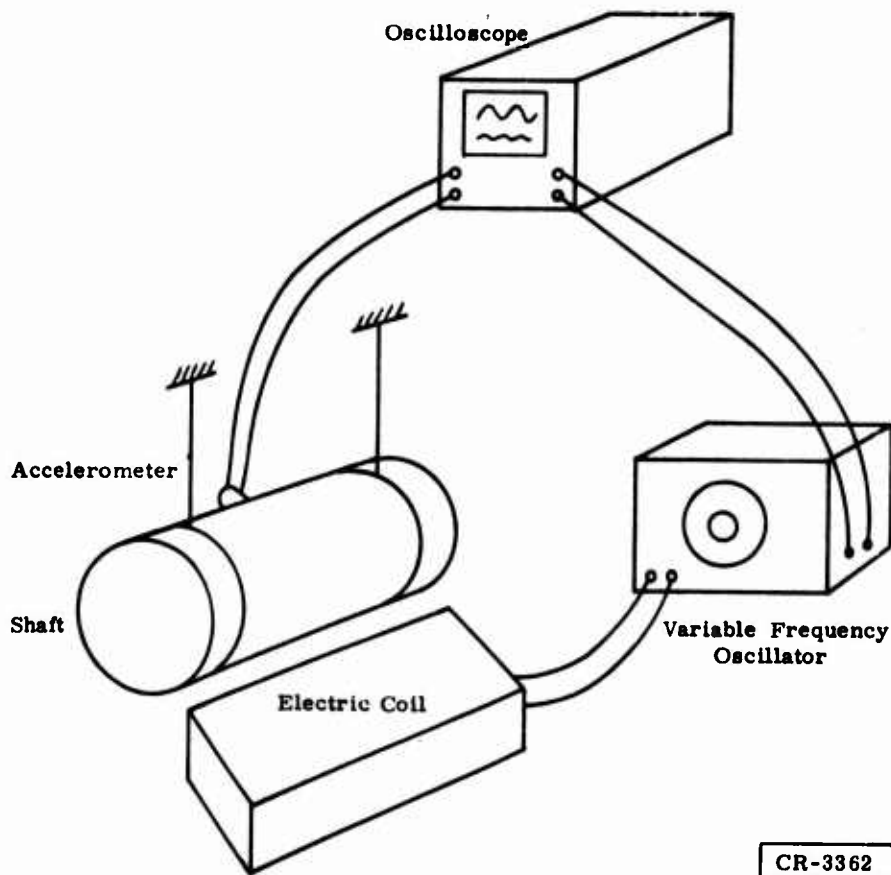


Figure 8. Schematic Diagram of Test Setup

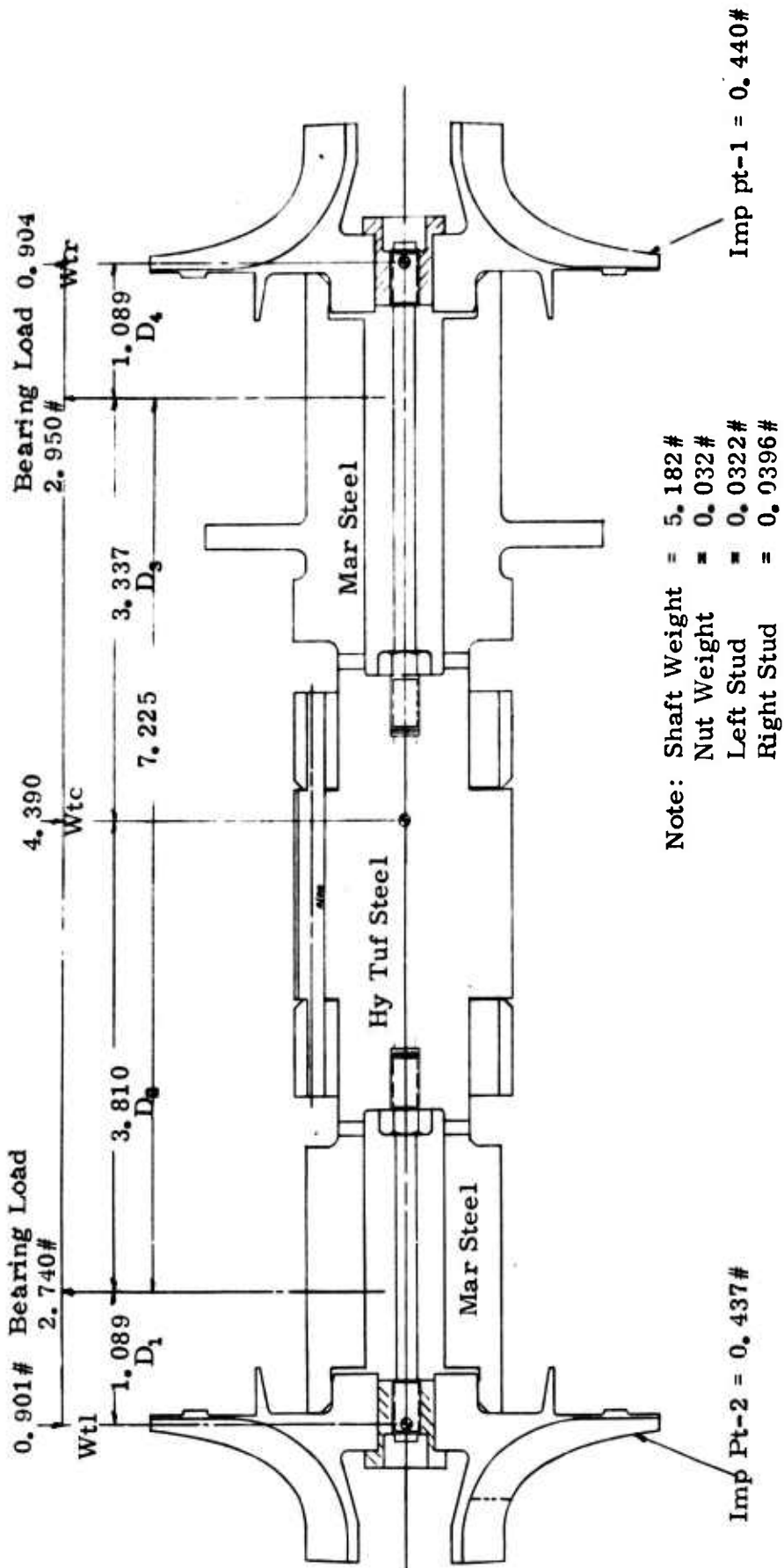


Figure 9. Rotor for Modules A and B

## COMPRESSOR GAS BEARING SYSTEM

The design of the gas bearing simulator to be used for initial testing of the compressor journal and thrust bearings has been completed. The simulator (Figure 10) consists of the rotating assembly, the motor section and support housings, two bell housings, and associated instrumentation, all mounted within a leak-tight, stainless steel dewar on two milling tables.

The rotating assembly consists of the compressor shaft with dummy rotors simulating the mass and center of gravity of the actual impellers mounted on either end. The structural adequacy of these dummy rotors has been analyzed to preclude any failure.

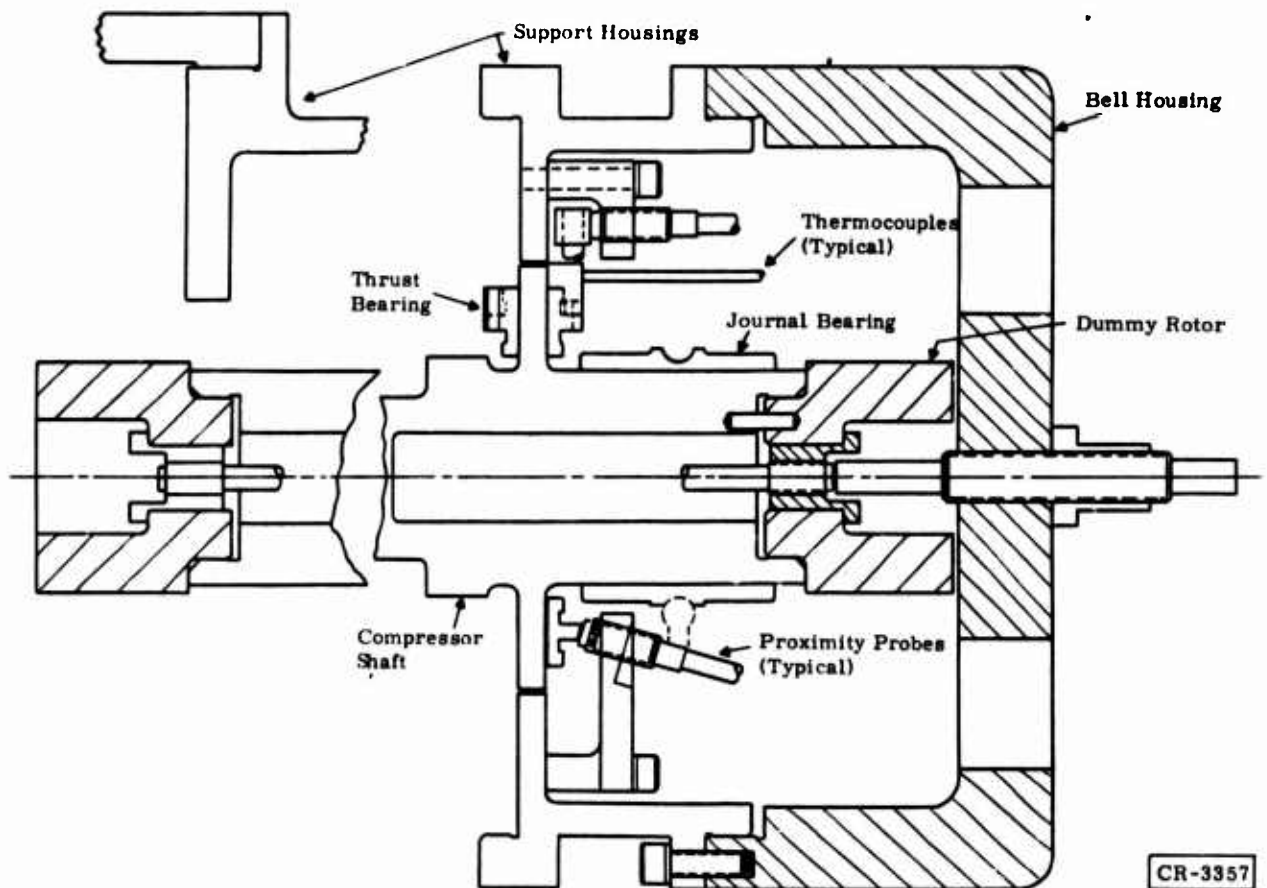


Figure 10. Gas Bearing Simulator Arrangement

The motor section and support housings would be from Module B. Sufficient testing of this motor would have been completed prior to initiation of the bearing tests, to ensure that motor performance will be a known quantity throughout these bearing tests.

Mounted at either end of the actual Module B support housings would be a bell housing made of 6061 aluminum. As shown in Figure 11, these housings provide a mounting surface for the assembly and a support for the shaft capacitance probes. The housings have also been sized to provide the containment capability required in case of any unexpected failure of the dummy rotor or shaft.

Detailed monitoring of the bearing performance parameters would be provided by the instrumentation described below, under "Test Results and Evaluation," in this section. Pertinent shaft and bearing motions would be followed by the use of proximity probes. Thermocouples mounted at strategic points would monitor critical temperatures and temperature gradients during operation.

All of the equipment described above would be mounted within the sheet-metal dewar shown in Figure 11, which would be made leak-tight to less than  $10^{-8}$  torr-liters/sec with helium. This would allow for evacuation of the dewar, by a vacuum pump, for operation at the design ambient pressure of 6 psia. The base of the dewar has been designed for mounting on the milling tables and provides feedthroughs for instrumentation, motor coolant lines, and vacuum lines. Mounting on the milling tables would allow testing in any desired position.

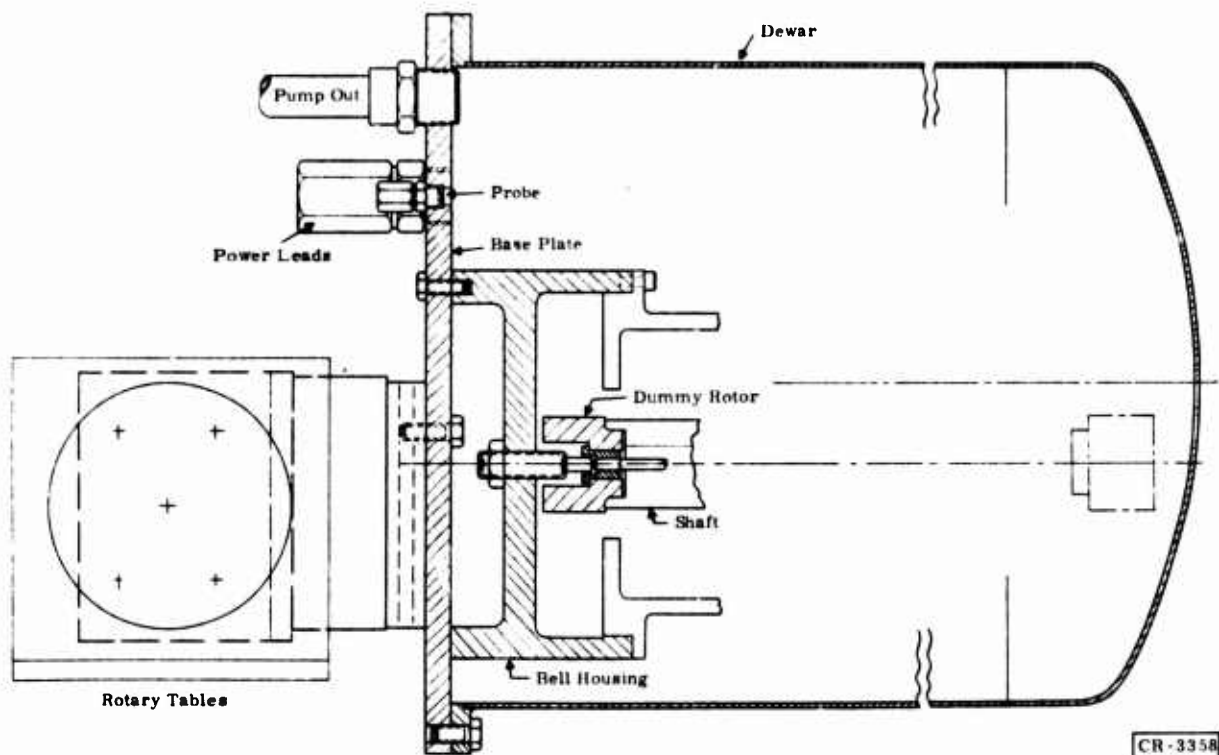


Figure 11. Gas Bearing Simulator with Dewar

## Initial Bearing Clearance Determination

To determine the required journal bearing clearances for operation in the gas bearing simulator and to examine the predicted characteristics of the ambient pressure operation, a series of cases of the JSELCT program were run. In these runs, the film thickness on the spring-loaded pad was varied, while all other input parameters were held constant. In these runs, the machined-in pad clearance ( $C_p$ ) was set at 0.00429 inch in lieu of the actual 0.0045-inch cold machined-in pad clearance, to account for the differential thermal growth of the journal and pad. The ambient temperature in the journal area was set at 750°R, based on the results of the thermal studies performed. The ambient pressure was set at 14.7 psia, to model the testing in the simulator. The most significant results of these computations are plotted in Figure 12.

On the basis of these results, it was decided to initially set up for running with a nondimensional pivot film thickness on the spring-loaded pad ( $H_p$ ) equal to 0.44. As can be seen from the curves plotted, selection of  $H_p = 0.44$ , with an operating speed of 91,000 rpm, places the operating speed sufficiently above the pad pitch and translational critical speeds but well enough below the first bending critical speed of 156,000 rpm, to avoid instability. Operating in this area provides for some pad journal clearance at startup, combined with relatively low film thicknesses at operating conditions, which provide sufficient load carrying capabilities. Operating at values of  $H_p$  much lower than 0.44 would require initial clamping of the pads to the journal at startup, as well as operation closer to the pad pitch and translational critical speeds. Operating at values of  $H_p$  much larger than that chosen increases the operating film thicknesses, thereby reducing the load carrying capability of the bearings.

To ensure that the proper clearances are maintained during assembly, so the operating conditions described above can be achieved, a precision-ground gage shaft must be used for setting the journal bearings. Using the data from Figure 13 (the output of computer program JSELCT with  $H_p = 0.44$  and  $C_p = 0.00429$ ), the size of the gage shaft to be used in the initial setup of the journal bearings was determined as described below.

The calculation for the gage shaft diameter must include the cold journal size combined with centrifugal and thermal growth effects and the desired operating film thicknesses. The spring deflection required to provide the proper load on the spring-loaded pad must also be accounted for. Figures 14 and 15 show a typical pivoted pad journal bearing at operating conditions.  $R_1$  and  $R_2$  (Figure 14) are the radii of the pad operating circle based on the journal growth and fixed-pad film thickness ( $H_{p1}$  and  $H_{p2}$ ).  $R_3$  is the radius of the pad operating circle based on journal growth and the spring-pad film thickness ( $H_{p3}$ ) minus the spring deflection:

$$R_1 = R_2 = 0.826650 \text{ inch}$$

$$R_3 = 0.821870 \text{ inch}$$

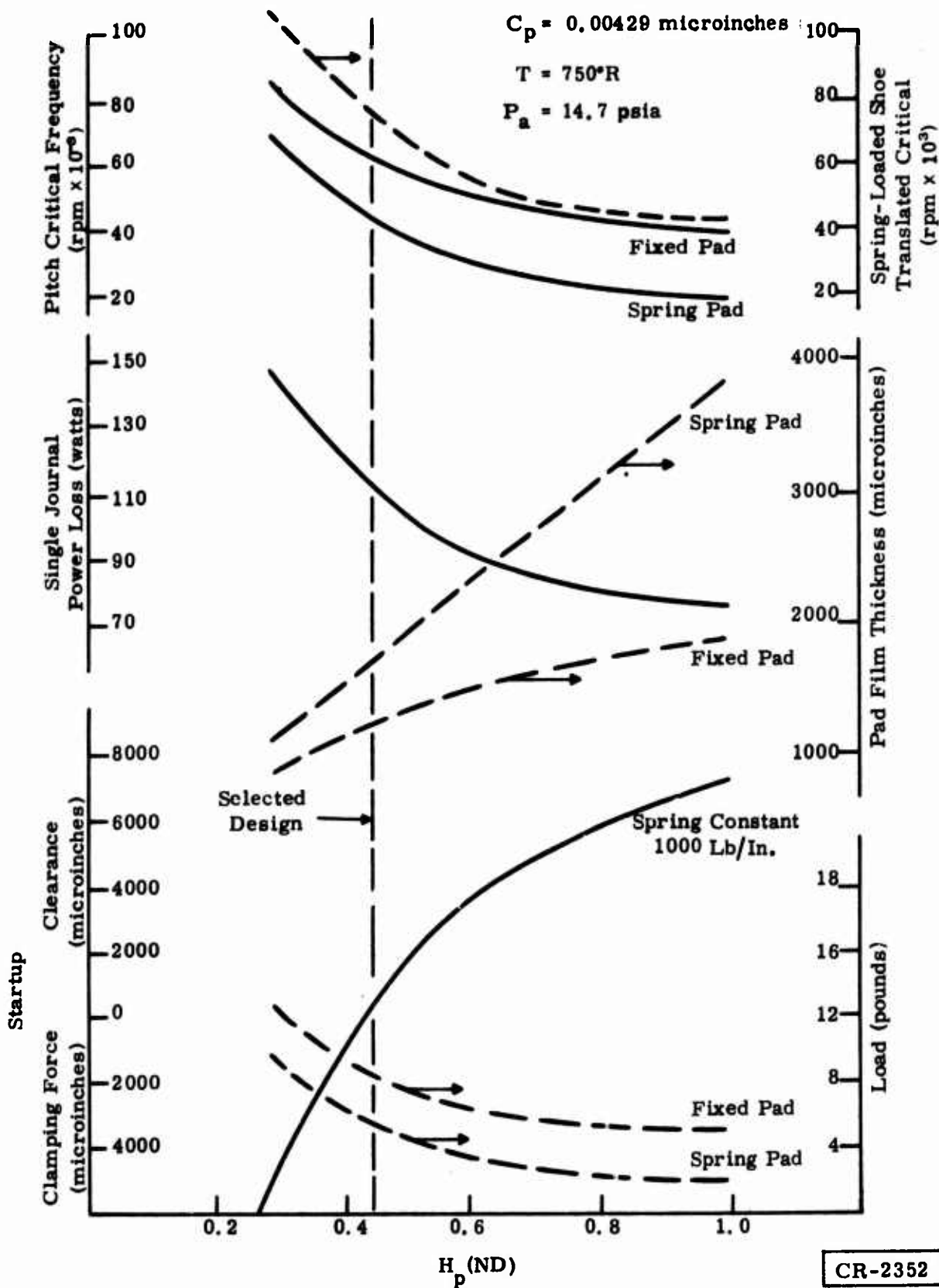


Figure 12. Gas Bearing Simulator Pad Analysis Results

# ★★DESIGN SPECIFICATIONS★★

DESIGN RUN NUMBER 1224

DESIGN SPEED (RPM)	91000.0
TEMP. AT DESIGN SPD (R)	750.00
AMBIENT PRESS, DESIGN SPD (PSIA)	14.70
VISCOSITY, DESIGN (LB*SEC/IN**2)	0.3607E-08
MAX. SPEED (RPM)	95000.0
TEMP. AT MAX SPD (R)	800.00
AMBIENT PRESS, MAX SPD (PSIA)	14.70
VISCOSITY, MAX (LB*SEC/IN**2)	0.3760E-08
JOURNAL DIA. (IN)	1.650
ROTOR WEIGHT (LB)	6.1950
LEFT OVERHUNG WT. (LB)	0.9010
WT. BETWEEN BRGS. (LB)	4.3900
RIGHT OVERHUNG WT. (LB)	0.9040
LEFT WT. TO LEFT BRG. (IN)	1.0890
LEFT BRG. TO CG (IN)	3.8100
CG TO RIGHT BRG. (IN)	3.3370
RT BRG TO RT OVERHUNG WT (IN)	1.0890
G LOADING	1.0000
JOURNAL WALL THICKNESS (IN)	0.4810
YOUNG*INERTIA, (LB*IN**2)	0.1500E+08
PERCENT OF RAD FOR PAD THICK	0.1500
PAD LENGTH (IN)	1.5000
POISSONS RATIO (ND)	0.2600
YOUNGS MODULUS (PSI)	0.2300E+08
WT DEN OF J. MAT. (LB/IN**3)	0.2800
WT DEN OF PAD MAT (LB/IN**3)	0.1600
ANGLE BETWEEN PIVOTS (DEG)	120.0000
MINIMUM PIVOT FILM TK. (IN)	0.001000
SPRING STIFFNESS (LB/IN)	0.1000E+04
MACHINED IN CLEARANCE (IN)	0.004290
STARTING PIVOT FILM THICK. (ND)	0.440000
BALL RADIUS (IN)	0.122000
SOCKET RADIUS (IN)	0.125000

## LAMBDA LOOP

LAMBDA, DES. SPD.	0.634
LAMBDA, MAX. SPD.	0.703
CLEARANCE, DES. SPD. (IN)	0.00388286
CLEARANCE, MAX. SPD. (IN)	0.00384628
WHIRL SPEED (RPM), DESIGN	164252.69
WHIRL SPEED (RPM), MAXIMUM	174692.39

CR-2355

Figure 13. Gas-Lubricated Journal Bearings

**\*\*CONDITIONS AT DESIGN SPEED\*\***

LAMBDA (ND)	0.6339
AMBIENT PRESSURE (PSIA)	14.70
CLEARANCE (IN)	0.003883
JOURNAL DIAMETER (IN)	1.650814
BRG. TRANSVERSE STIFF. (LB/IN)	17038.65
BRG. VERTICAL STIFF. (LB/IN)	6541.95
BRG. POWER LOSS (WATTS)	110.7351

**SHOES WITH FIXED PIVOTS**

LOAD (LB)	8.3440
PIVOT FILM THICKNESS (IN)	0.001244
PITCH STIFFNESS (IN-LB/RAD)	1183.2468
PITCH CRITICAL FREQ. (RPM)	62626.6

**SHOES WITH SPRING MTD. PIVOTS**

LOAD (LB)	5.2465
PIVOT FILM THICKNESS (IN)	0.001708
PITCH STIFFNESS (IN-LB/RAD)	593.5833
PITCH CRITICAL FREQ (RPM)	44357.0
TRANS. CRITICAL FREQ (RPM)	74414.0
STIFF OF PRELOAD SPRING (LB/IN)	1000.0
PIVOT SOCKET RADIUS (IN)	0.1250
PIVOT BALL RADIUS (IN)	0.1220

**\*\*GENERAL CONDITIONS\*\***

WHIRL SPEED LIMIT (RPM)	164252.7
FIRST BENDING CRIT. SPD. (RPM)	157087.9
SHAFT RIGID BODY CRIT SPD (RPM)	19791.1
SHAFT RIGID BODY CRIT SPD (RPM)	13853.6
SHAFT RIGID BODY CRIT SPD (RPM)	12264.8
SHAFT RIGID BODY CRIT SPD (RPM)	8599.6
SHOE PITCH INERTIA (IN-LB-SEC <sup>2</sup> )	0.2751E-04
WEIGHT OF SHOE (LB)	0.046191
THICKNESS OF SHOE (IN)	0.1233
MACHINED-IN CLEARANCE (IN)	0.004290
START-UP CLAMPING FORCE (IN)	0.
START-UP CLEAR ON TOP SHOE (IN)	0.00018

**\*\*CONDITIONS AT MAXIMUM SPEED\*\***

LAMBDA (ND)	0.703
AMBIENT PRESSURE (PSIA)	14.70
CLEARANCE (IN)	0.003846
JOURNAL DIAMETER (IN)	1.650887
BEARING X-STIFFNESS (LB/IN)	17187.532
BEARING Y-STIFFNESS (LB/IN)	6596.245
BEARING POWER LOSS (WATTS)	122.83

**CR-2355**

**Figure 13. Gas-Lubricated Journal Bearings (Cont'd)**



**\*\*CONDITIONS AT DESIGN SPEED\*\***

LAMBDA (ND)	0.6339
AMBIENT PRESSURE (PSIA)	14.70
CLEARANCE (IN)	0.003883
JOURNAL DIAMETER (IN)	1.650814
BRG. TRANSVERSE STIFF. (LB/IN)	17038.65
BRG. VERTICAL STIFF. (LB/IN)	6541.95
BRG. POWER LOSS (WATTS)	110.7351

**SHOES WITH FIXED PIVOTS**

LOAD (LB)	8.3440
PIVOT FILM THICKNESS (IN)	0.001244
PITCH STIFFNESS (IN-LB/RAD)	1183.2468
PITCH CRITICAL FREQ. (RPM)	62626.6

**SHOES WITH SPRING MTD. PIVOTS**

LOAD (LB)	5.2465
PIVOT FILM THICKNESS (IN)	0.001708
PITCH STIFFNESS (IN-LB/RAD)	593.5833
PITCH CRITICAL FREQ (RPM)	44257.0
TRANS. CRITICAL FREQ (RPM)	74414.0
STIFF OF PRELOAD SPRING (LB/IN)	1000.0
PIVOT SOCKET RADIUS (IN)	0.1250
PIVOT BALL RADIUS (IN)	0.1220

**\*\*GENERAL CONDITIONS\*\***

WHIRL SPEED LIMIT (RPM)	164252.7
FIRST BENDING CRIT. SPD. (RPM)	157087.9
SHAFT RIGID BODY CRIT SPD (RPM)	19791.1
SHAFT RIGID BODY CRIT SPD (RPM)	13853.6
SHAFT RIGID BODY CRIT SPD (RPM)	12264.8
SHAFT RIGID BODY CRIT SPD (RPM)	8599.6
SHOE PITCH INERTIA (IN-LB-SEC <sup>2</sup> )	0.2751E-04
WEIGHT OF SHOE (LB)	0.046191
THICKNESS OF SHOE (IN)	0.1233
MACHINED-IN CLEARANCE (IN)	0.004290
START-UP CLAMPING FORCE (IN)	0.
START-UP CLEAR ON TOP SHOE (IN)	0.00018

**\*\*CONDITIONS AT MAXIMUM SPEED\*\***

LAMBDA (ND)	0.703
AMBIENT PRESSURE (PSIA)	14.70
CLEARANCE (IN)	0.003846
JOURNAL DIAMETER (IN)	1.650887
BEARING X-STIFFNESS (LB/IN)	17187.532
BEARING Y-STIFFNESS (LB/IN)	6596.245
BEARING POWER LOSS (WATTS)	122.83

**CR-2355**

**Figure 13. Gas-Lubricated Journal Bearings (Cont'd)**

### SHOES WITH FIXED PIVOTS

LOAD (LR)	8.5475
PIVOT FILM THICKNESS (IN)	0.001279
PITCH STIFFNESS (IN LB/RAD)	1196.9295
PITCH CRITICAL (RPM)	62989.7

### SHOES WITH SPRING MTD. PIVOTS

LOAD (LR)	5.4500
PIVOT FILM THICKNESS (IN)	0.001734
PITCH STIFFNESS (IN LB/RAD)	605.9236
PITCH CRITICAL (RPM)	44817.1
TRANSLATION CRITICAL (RPM)	15707.7

CR-2355

Figure 13. Gas-Lubricated Journal Bearings (Cont'd)

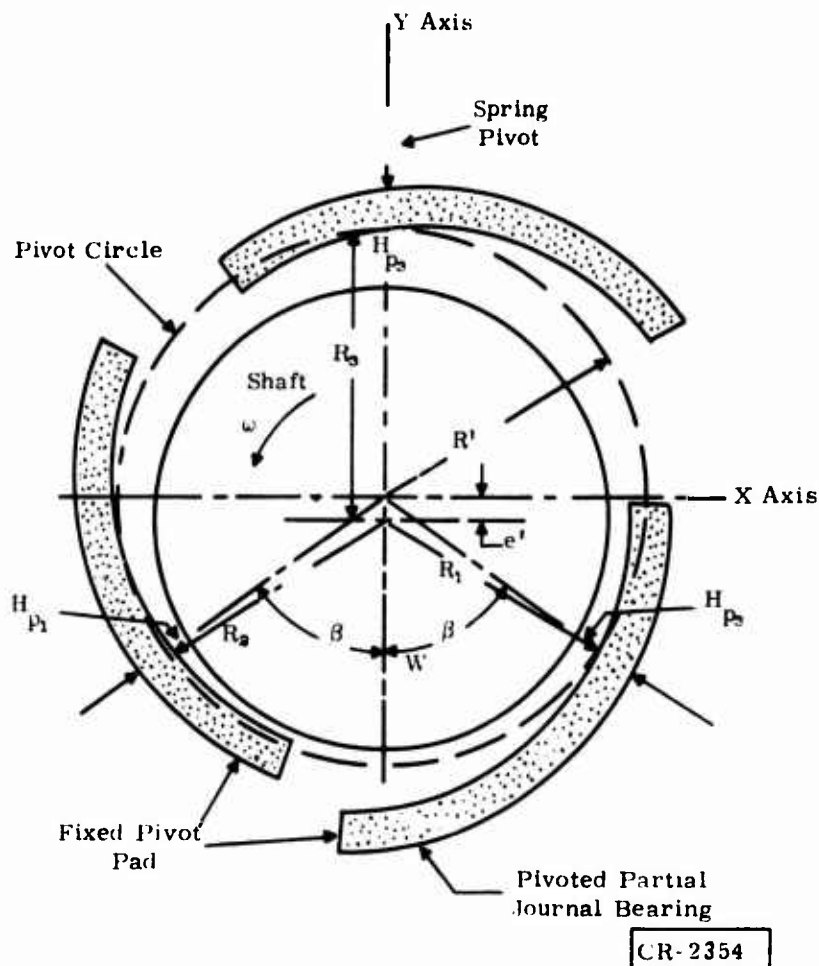


Figure 14. Schematic Diagram of Pivoted Pad Journal Bearing

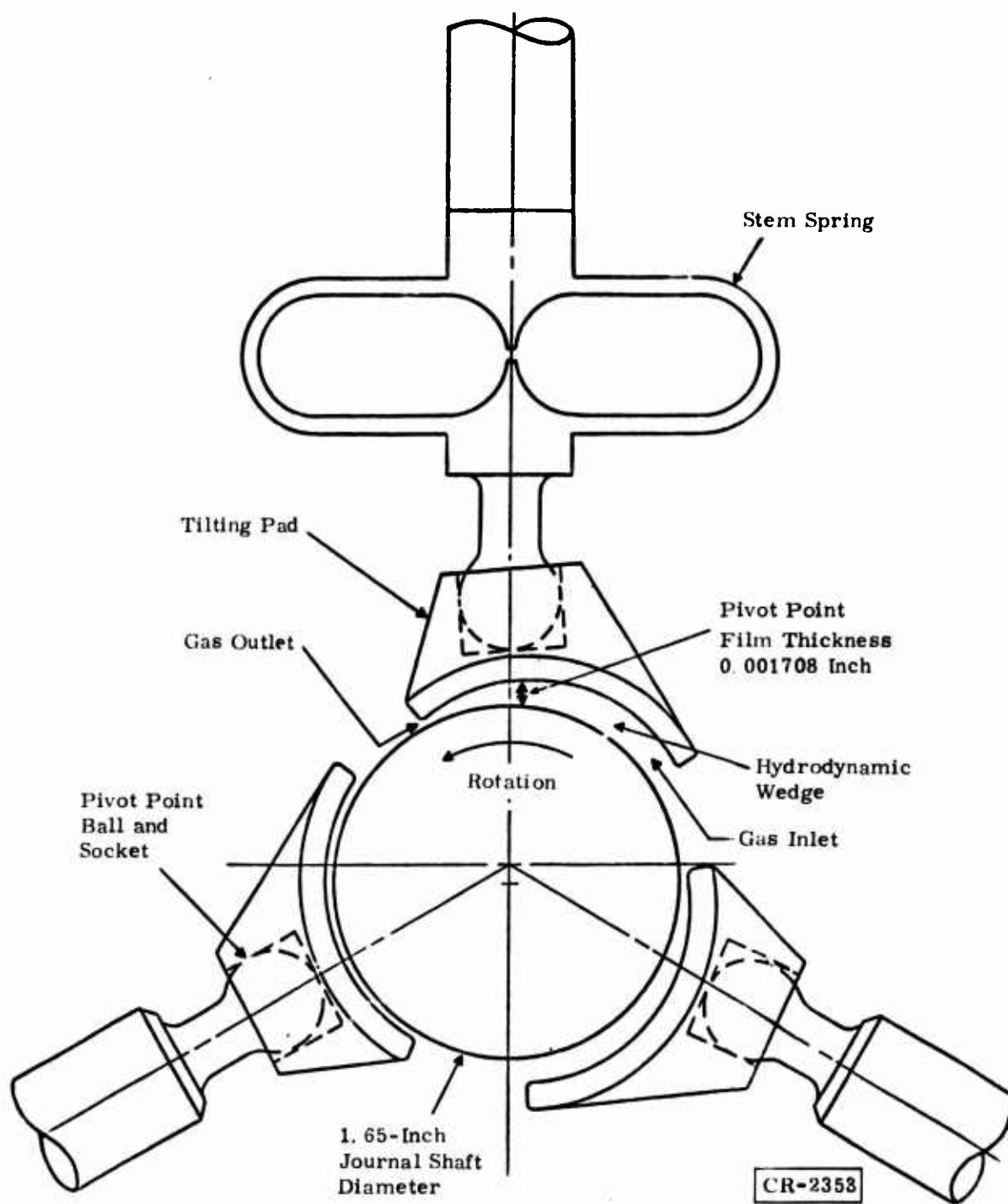


Figure 15. Pivoted Pad Journal Bearing

The radius of the circle which can be drawn through the three points established by these radii is:

$$R_1 = \frac{R_1 + R_2 + 2R_3 \cos \beta}{2 (1 + \cos \beta^\circ)} \quad \text{where } \beta = 60^\circ$$

$$R_1 = \frac{2(0.826650) + 2(0.821870)(0.5)}{2(1.5)}$$

$$R_1 = 0.825057$$

Thus the diameter of the gage shaft is:

$$2R_1 = 1.650114$$

On this basis, the diameter of the gage shaft was held to 1.65012 to 1.65017 inches.

### Journal Bearing Pad Installation

Using the gage shaft ground to the dimensions described above, it was necessary to set the bearing pads relative to this shaft, to attain proper bearing operation.

### Shimming Spring-Loaded Stem

To properly set the journal bearing pads, each pad must have a fixed geometry, so relative motion of the pads does not occur during the initial setting.

To accomplish this fixed-geometry condition on all pads, the spring-loaded pad must be prevented from deflecting during assembly. This would be accomplished by placing shims in the limit stop slot in the springs. This shimming must be done precisely, to prevent incorrect setting of the bearings. Using precision instrumentation, the free length of the individual spring stem must be measured. Shims must then be sized for the slot in the spring, so that when the shims are installed and the stem is lightly loaded axially, the length of the spring stem is unchanged from the initial free length measurement.

### Initial Setting

With the gage shaft held concentric in the support housings by precision fixturing and the spring stems properly shimmed, the individual pad and stem combinations are lowered onto the shaft until the pad is just resting on the shaft. At this point, the stems are clamped in place to maintain this initial setting. Care must be taken during this portion of the assembly to ensure that no undesired clamping forces are imposed on the pads.

## Final Setup

With the journal pads set properly on the gage shaft, the gage shaft is then removed and the motor shaft is installed. This replacement of the gage shaft must be done in a manner that will prevent the pads from falling off; one shaft must be installed as the other is removed, to ensure continuous pad-to-shaft contact. To accomplish this, an intermediate pad centering fixture is required on the second-stage end. This fixture was described in Appendix II, "Assembly Procedures for U.S. Air Force High-Speed, Two-Stage, Centrifugal Turbocompressor," of the Phase B Final Report.

After the motor shaft is in place, resting on the journal bearings, a final check, to ensure that proper pad settings have been attained, will be made by tracking the motion of the journal as the housing is rotated. When this is done, a triangle such as that shown in Figure 16 is generated. The three vertices of this triangle represent the static equilibrium positions of the shaft resting between two pads. The legs of the triangle represent the motion of the shaft as it rides from one equilibrium position to the next.

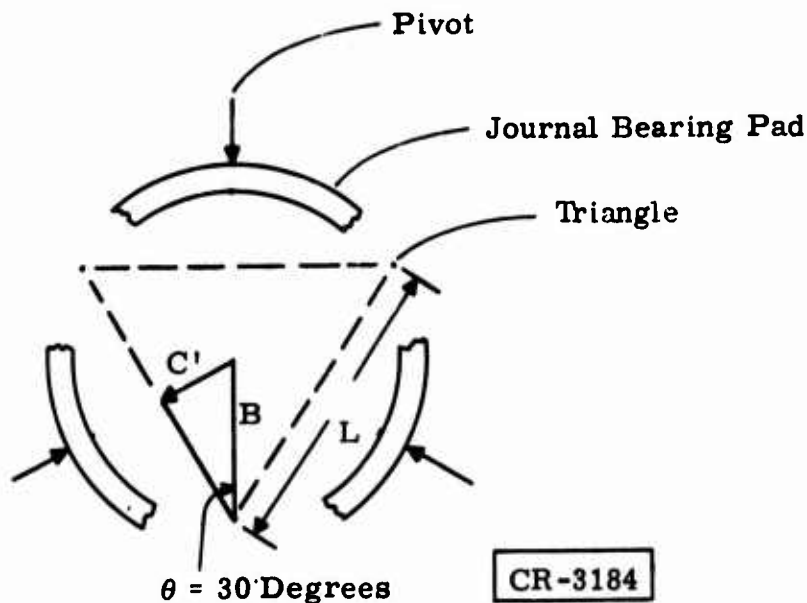


Figure 16. Triangle Legs Formed on Oscilloscope as Shaft Drops Between Pads

To establish this triangle, the relative motion of the shaft is followed with a horizontal and a vertical proximity probe, 90 degrees apart. At each static equilibrium position (the shaft resting between two pads), one point, representing a vertex of the triangle, can be seen on an oscilloscope displaying the output of the proximity probes. By means of a triple exposure of the three positions, the triangle can be established. By cutting a section of the scope grid from a photograph and using this to measure the lengths be-

tween the points, the legs of the triangle formed can be measured. Substituting the average value of the lengths into the following equation, the mean bearing pivot radial clearance, in microinches, can be established:

$$C' = \tan 30^\circ \frac{L}{2} S$$

where:  $C'$  = Average bearing pivot radial clearance (microinches)

$L$  = Average length of the triangle leg (centimeters)

$S$  = Oscilloscope sensitivity ( $\mu\text{in.}/\text{cm}$ )

For the turbocompressor, the average radial clearance,  $C'$ , should equal approximately 100 microinches. The pad stems may then be adjusted until the proper clearance ( $C'$ ) is attained. It should be noted that this procedure is followed for each of the two journal bearings and that adjustments to one bearing can affect the setting of both bearings and must be accounted for.

Figure 16 shows the relationship between the triangle leg ( $L$ ), the maximum bearing pivot radial clearance ( $C'$ ), and the distance the shaft drops from the center as it falls between the journal pads ( $B$ ).

Figure 17 shows the relationship between the motion of the shaft with three fixed pads and the motion of the shaft with two fixed pads and one spring pad. Triangle ACD represents the motion of the shaft on three pads whose pivots are fixed relative to one another; this motion has been described above.

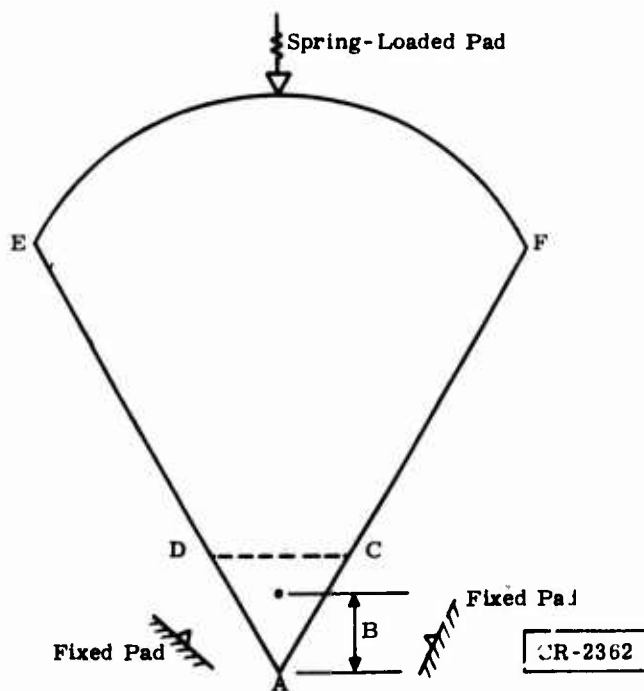


Figure 17. Relative Shaft Motion with Spring-Loaded Pad

Shape AEF shows the motion if the spring-loaded pad is not shimmed and is free to deflect. The drop from center (B) to an equilibrium position between the two fixed pads is the same as previously discussed, but as the housing is rotated, the shaft loads the spring stem, the spring deflects, and shape AEF is generated. Because the deflection of the spring causes motion of the shaft much larger than the radial pivot clearance, this motion must be eliminated by shimming during setup, in order to arrive at the proper clearances.

## THERMAL DESIGN

A review of the design analysis shows that the close clearances between the journal pads and the shaft and between the thrust bearing and the thrust runners requires that distortion of the bearing surfaces be kept to the minimum. The distortion, due to temperature nonuniformities along the compressor shaft and thrust bearing runner, was analyzed, and corrective design steps were taken to minimize distortions. This analysis was described in the Phase B Final Report (Ref. 2).

The design arrangement adopted at the thrust bearing end of the shaft is shown in Figure 18. This arrangement incorporates cooling fins at the shaft and at the thrust runner tip. The thrust runner is also shown extended beyond the thrust bearing, for thrust runner disk cooling.

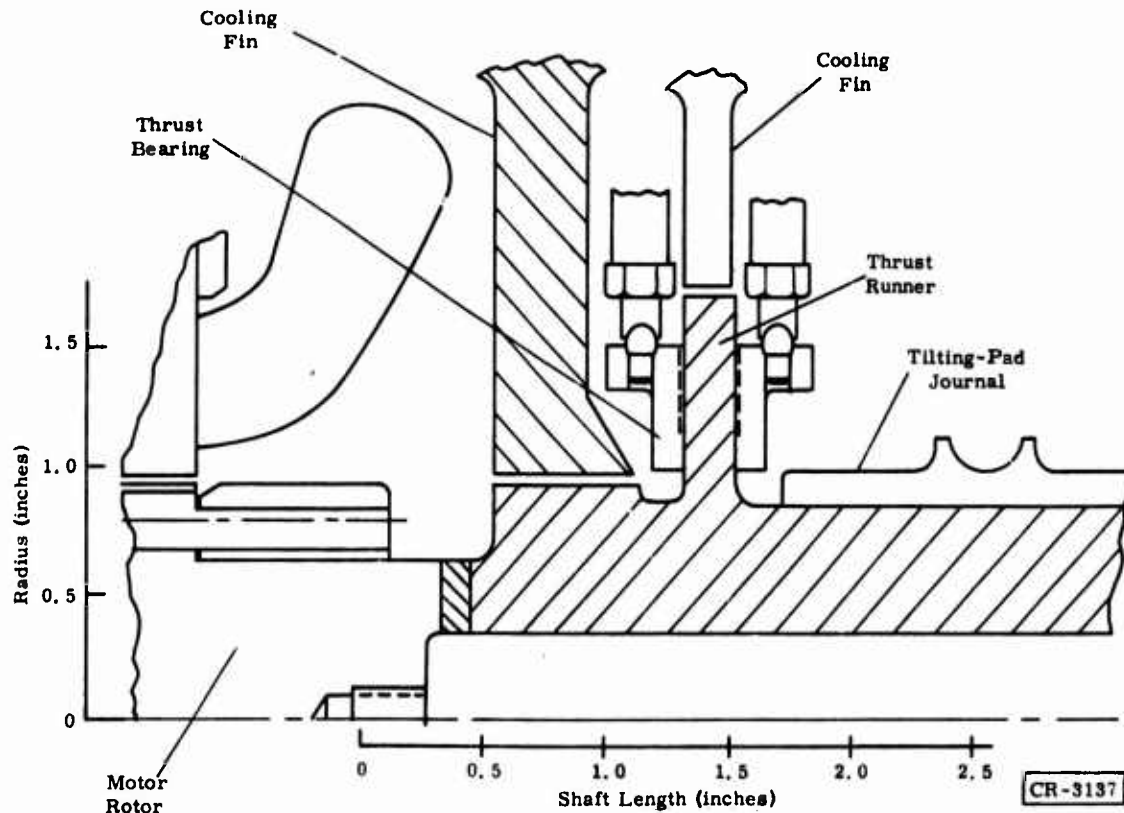


Figure 18. Compressor Shaft Thrust Bearing Heat Transfer Model

The analytically determined shaft distortion under the pad is shown in Figure 19, and the distortion at design conditions of the thrust runner is shown in Figure 20. Figure 21 shows the calculated operating distortions along the shaft, as well as the operating temperatures anticipated.

The above results were obtained, based on the design conditions listed in Table 1. Thus it can be seen that the 91 percent of the heat is generated by the gas bearings.

Table 1  
DESIGN CONDITIONS

Heating, Leakage, and Temperature	Value
Ambient outside temperature	585°R (125°F)
Temperature of gas entering compressor housing	660°R (200°F)
Liquid coolant temperature	588°R (128°F)
Thrust-bearing-end wheel temperature	647°R (187°F)
Heating due to single journal bearing	87.5 watts
Heating due to thrust bearings, both faces	170.0 watts
Heating due to motor end turns	25.0 watts
Interstage leakage rate, from second to first stage	0.19 g/sec

Because the above analysis was completed, the final thrust and journal bearing designs were also completed. Table 2 shows that the bearing powers at the 0-g design conditions are slightly higher than the values used in the analysis. Of course the 1-g and 3-g loads shown in Table 2 result in higher bearing friction losses.

Table 2  
COMPRESSOR GAS BEARING LOSSES

Operation (g)	Thrust Bearing, Both Faces (watts)	Journal Bearing, Each Journal (watts)
0	210.0	105.0
1 horizontal	210.0	123.0
1 vertical	255.0	105.0
3 horizontal	210.0	142.0
3 vertical	300.0	105.0



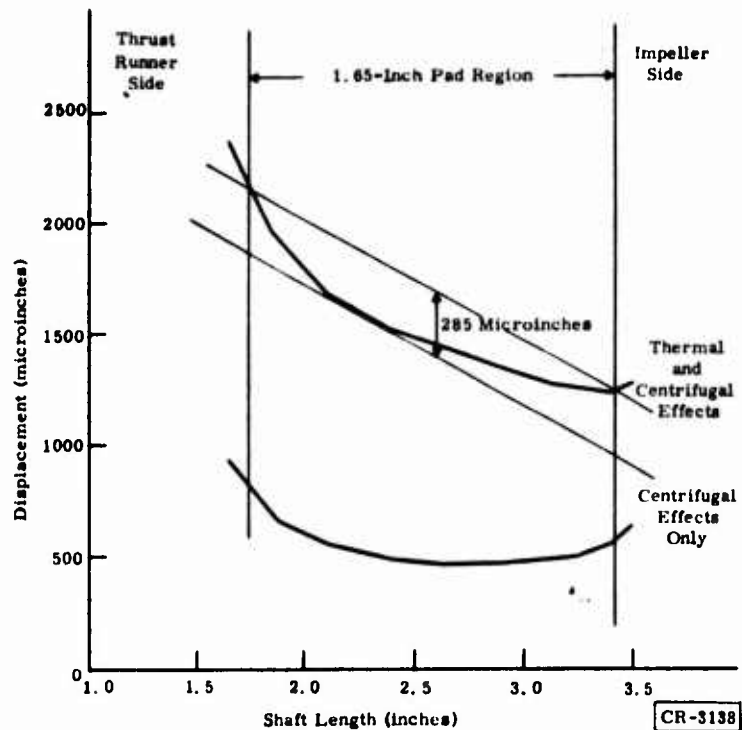


Figure 19. Radial Displacement of Shaft in Journal Bearing Area

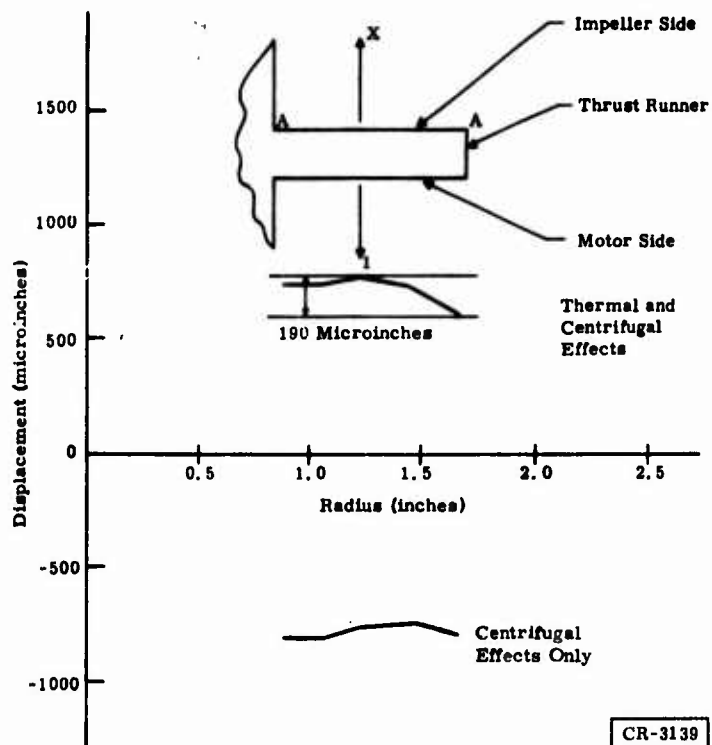


Figure 20. Displacements of Thrust Runner Surface A-A

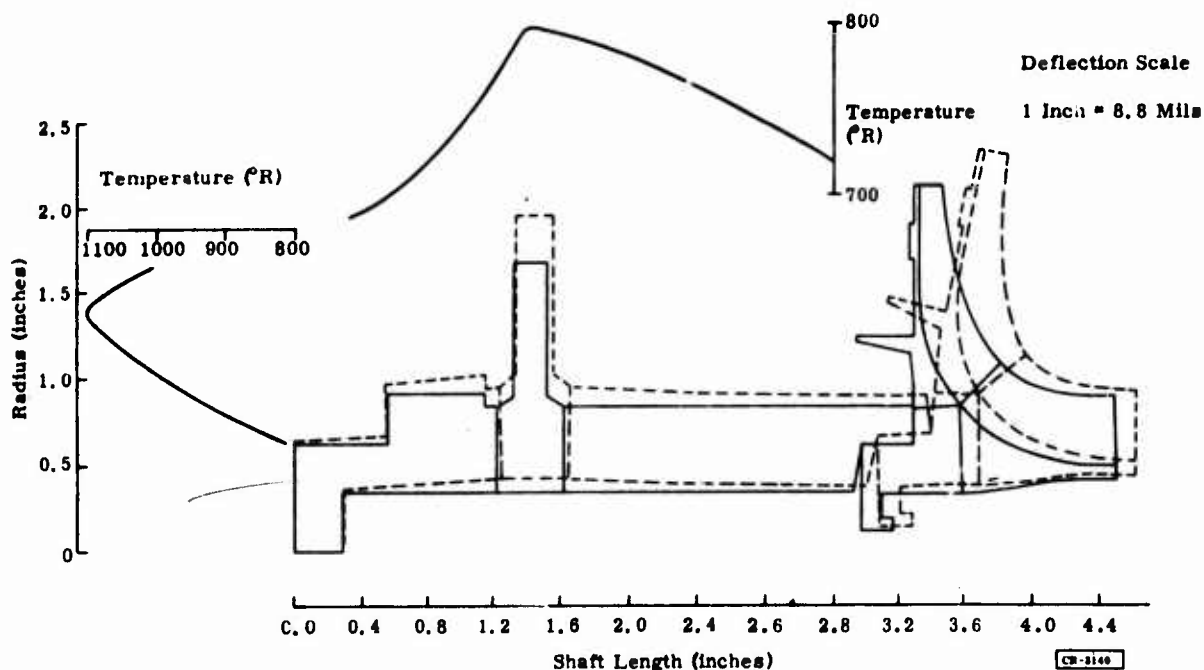


Figure 21. Compressor Centrifugal and Thermal Deflection

Recent measurements have shown that there is a tendency for thrust bearing distortion with temperature change. Thrust bearings with the tungsten carbide flame plate, ground to the final finish but without the pockets etched, were evaluated for flatness at the operating temperature of approximately 400°F. It is significant that two bearings were tested, and each warped symmetrically into a concave surface, with the inside diameter smaller than the outside diameter by 0.000247 and 0.000218 inch. This warping is apparently caused by the slight difference in expansion characteristics of tungsten carbide on the titanium. These special tests are described below under "Test Results and Evaluation."

Figure 21 shows that the temperature actually increases with the thrust bearing radius; therefore, the distortion would probably be more exaggerated than shown in Figure 22. The direction of the distortion is the most favorable direction for the bearing load capacity and angular stiffness, because the least film thickness will be at the outside diameter.

## ELECTRICAL DESIGN

### Design

The breadboard motor stator and rotor are essentially the same design as that for the Module B compressor drive motor. Much has been learned

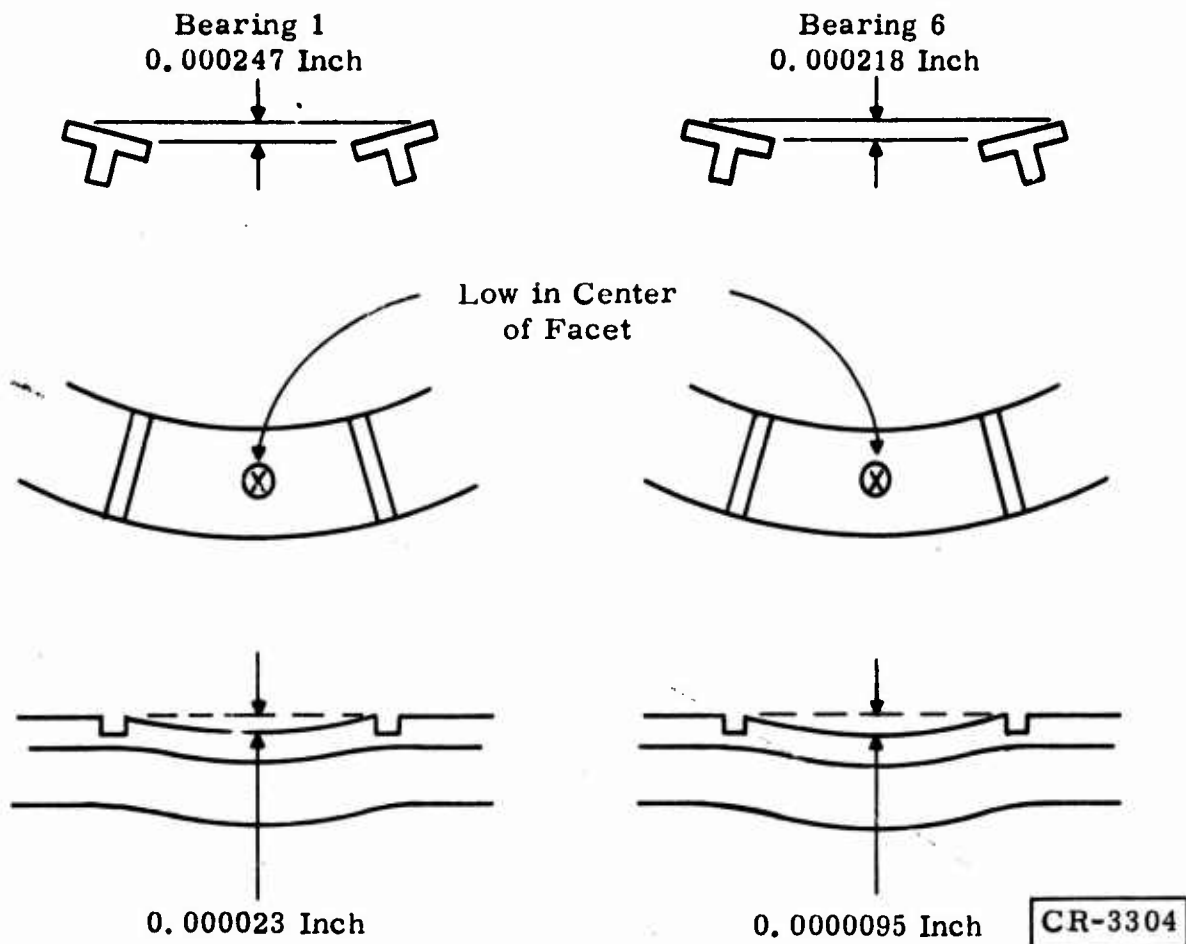


Figure 22. Thrust Bearing Warping at 400°F

from the breadboard motor, in the way of fabrication techniques, that has been applied to the Module B drive motor. This knowledge can be applied beneficially to future motor designs. Figure 23 shows a section of the breadboard motor field. Ball bearings were used to minimize the cost.

Winding a new motor design always involves some learning with regard to end-turn overhang and insulation. This learning has been restricted to the breadboard stator, and the results have been very effectively applied to the high-speed prototype motor.

Although this motor is limited in speed, with antifriction bearings, much useful information has been obtained, and more can be obtained. The maximum operating speed was about 12,000 rpm and the planned tests were:

- Development and Debugging. The original intent of the contract was to build a solid-state power conditioner-controller. Development and debugging of the electrical power subsystem would have

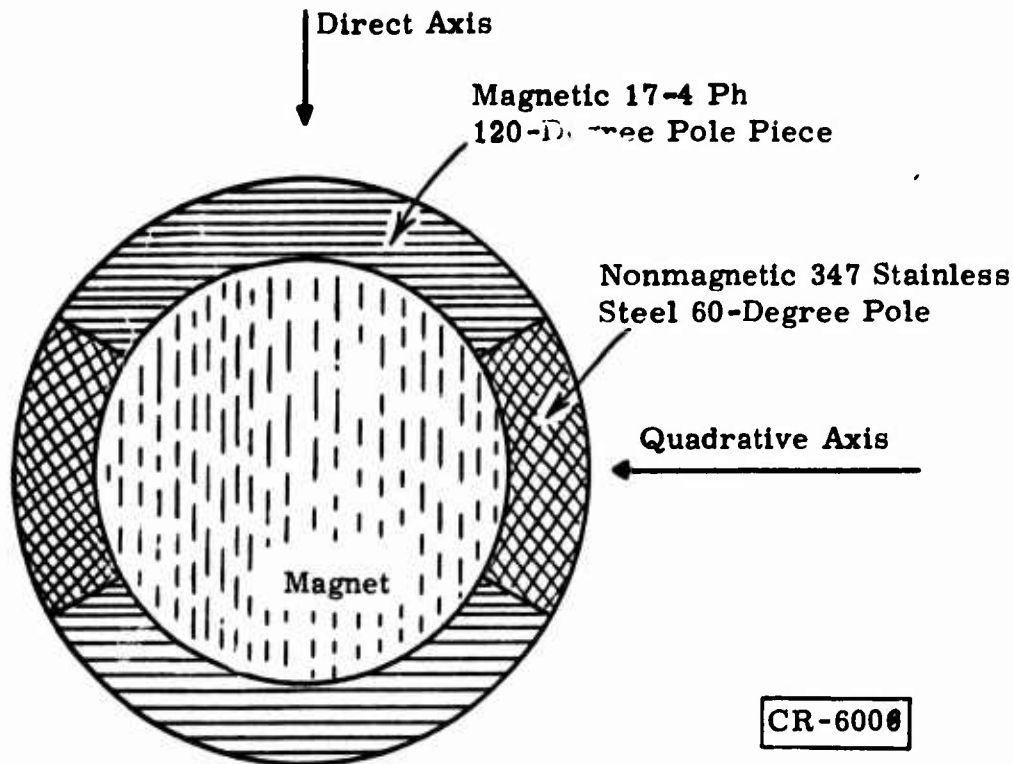


Figure 23. Cross Section of Magnetically Segmented Shell Around Magnet

been greatly facilitated if the power conditioner had been built. A true dynamic load, as provided by the breadboard motor, would have accentuated system deficiencies and aided in their correction, where needed.

- **Locked Rotor Torque.** The compressor drive motor must overcome some static friction in the bearings if it is to break away at the start. The magnitude of the motor torque at a standstill can be determined for inverter voltages and for sine wave voltages for comparison. The information thus obtained can be used to determine the starting mode that puts the least stress on the electrical subsystem.
- **Accelerating Torque.** Optimum volts per cycle can be determined for the minimum surge current and the minimum time to reach the liftoff speed for the gas bearings.

### Breadboard Motor Tests

The planned tests were greatly altered, to conform to timely changes in the contract scope. Both the quality and the quantity of the test data were ultimately compromised as a result of the termination plans. Nevertheless, the following results were obtained before the contract expired. It is anticipated that additional useful data will be obtained in the future.

## Corona

Every effort has been made to ensure a contamination-free system, especially with regard to the motor insulation system. Corona can cause a breakdown of some types of insulation more than other types. However, if no corona is present, then there certainly should be no contamination from this cause.

The safety margin for corona-free operation of the compressor drive motor has been an unknown in previous motor designs. To reduce possible particulate contamination, the varnish treatment has been omitted from the winding. This omission probably reduces the corona start voltage. Air has a corona start voltage gradient of 35.5 kv/cm, while helium has a value of 4.0 kv/cm. While this is deemed only an index, it does indicate a trend that should not be ignored. A minimal investigation was undertaken.

A glass desiccator containing the breadboard motor stator was evacuated to 100 microns and backfilled to 1 psig with helium. This procedure was repeated two more times, to ensure an air-free environment of pure helium. A corona-free voltage source was connected between the stator core and the winding, without disturbing the helium environment.

Corona started to occur at 245 volts rms, which is about three times its rated 83 volts. This margin appears adequate for this application, and no change in the insulation system is anticipated.

## Electrical Balance

Initial tests showed an unexpected unbalance in the magnetizing current. The six line currents were 15.0, 12.3, 15.0, 12.7, 13.6, and 12.8 amperes at 14 volts and 200 hertz. This unbalance prompted a careful analysis of the stator air gap effects and unsymmetrical winding effects. A series of runs was made with the end shield (on the connection end) shifted four ways by about 2 mils from the center. This shift had little or no effect on the magnetizing current unbalance, which remained the same in each motor phase. When the powerlines were shifted, the unbalance remained the same in each motor phase. It was therefore concluded that the unbalance was not in the source.

Subsequently, tests of resistance, reactance, and voltage unbalance very strongly indicated that a single turn was inadvertently left out of one coil in Phase R. The usual procedure in such circumstances would be to strip and rewind the stator; however, in the spirit of phasing out the contract, motor tests were continued to obtain the maximum useful information at the minimum cost.

Testing and development of the breadboard motor have been made to conform to the reduction in the contract scope. While only enough time was al-

lotted to determine the cause for the unbalance in the stator, it was possible to obtain partial test results that have given some insight into this motor and have increased the technology base in the area of leakage reactance.

### Excitation Curve

Full frequency excitation and core loss tests with a dummy laminated rotor were originally planned, but only 200-hertz data with the squirrel cage rotor were obtained. Core loss at 200 hertz is very low, data obtained by extrapolating to 1525 hertz are not accurate, and the excitation current changes little at higher frequencies. Figure 24 shows breadboard motor excitation data at 200 hertz.

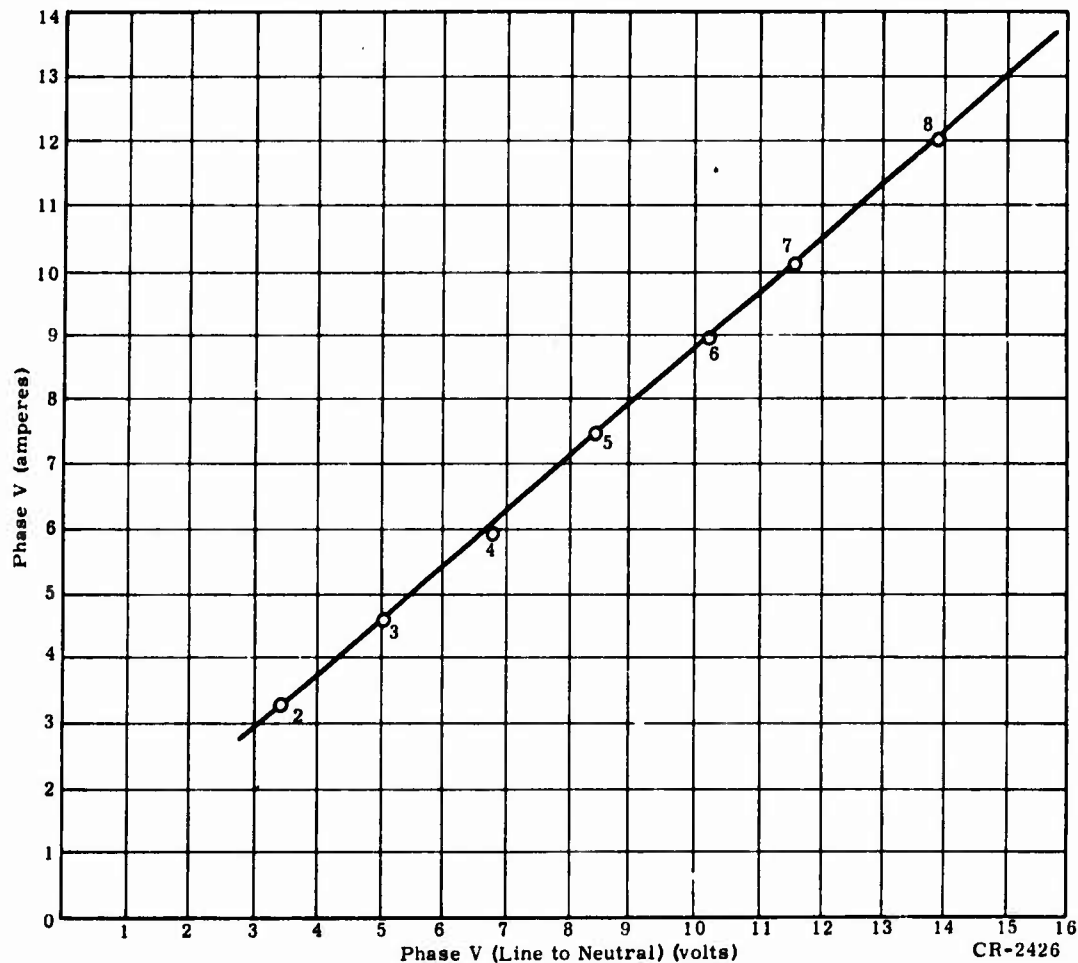


Figure 24. Breadboard Motor Excitation at 200 Hertz

### Locked Rotor Torque

Only two frequencies were used, in testing, to determine the locked rotor torque: 200 and 60 hertz. The torque per ampere is not dramatically different for these two frequencies, as shown in Figure 25. The most favorable frequency should be determined and used at the start, to minimize the stress on the power conditioner.

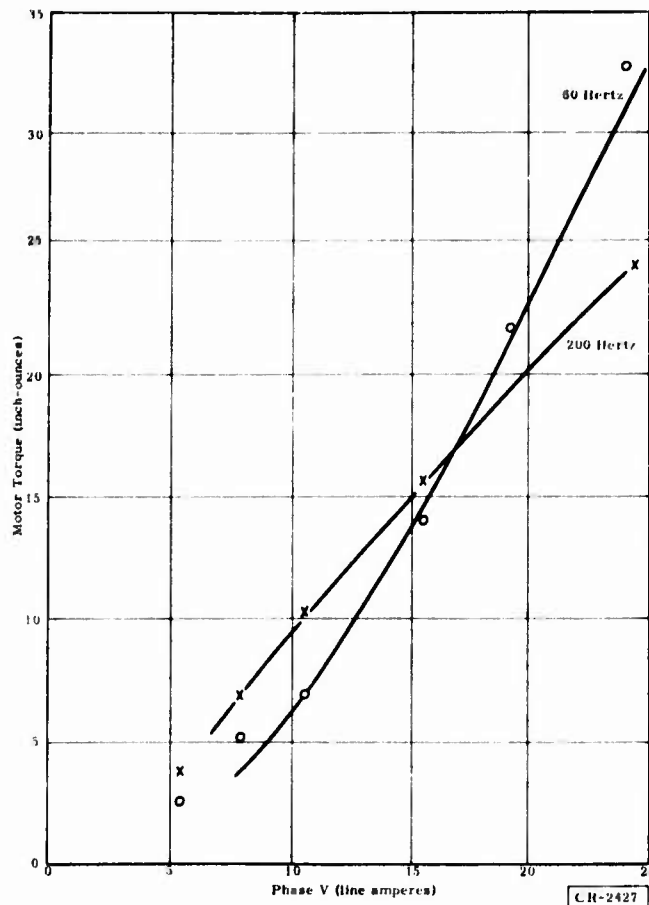


Figure 25. Breadboard Motor Locked Rotor Torque

### Torque Slip Tests

The rated torque for 2.5 hp at 91,000 rpm is 27.7 oz-in. Figure 26 shows the tested shaft torque of 27.7 oz-in. at a frequency of about 205 hertz and a slip of about 315 rpm. A maximum torque of 50 oz-in. occurred at about 6-percent slip, or about 720-rpm slip.

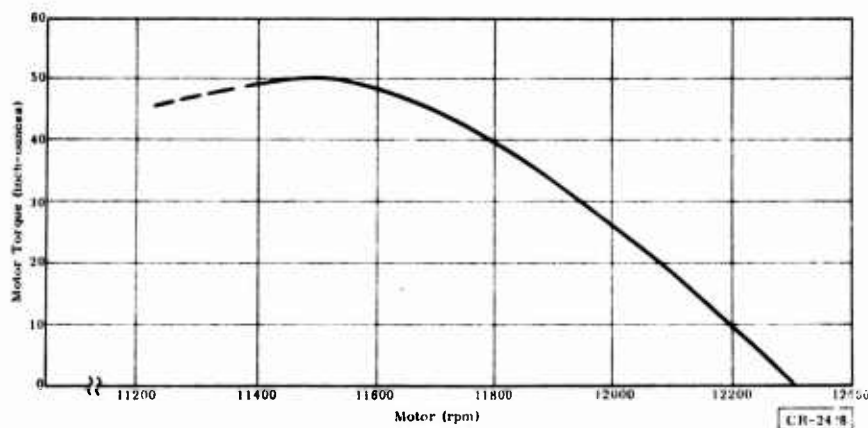


Figure 26. Breadboard Motor Speed-Torque Characteristics (205 Hertz at 10 Volts, Line to Neutral)

## Discussion and Summary of Tests

Testing and development of the breadboard motor have been made to conform to the reduction of the contract scope. The postulated dropped turn in Phase R has been ignored on the basis that some test results are better than none. This approach may be justified, because there are normally 12 turns in each of six phases, and the deficit of one turn will not greatly affect the overall performance of the motor.

Tests were made at 200 hertz and 12,000 rpm, and a few tests were made at 60 hertz.

Running light losses were found to be 40.8 watts at 10.1 volts and 200 hertz. The input power was accurately determined for Phase V and multiplied by six, the number of phases. A Hewlett-Packard digitizer was used and a picture of the volts and amperes was taken on a calibrated oscilloscope. These losses include:

- Stator copper
- Friction and windage
- Negative sequence losses due to unbalance
- Slot harmonic losses
- Core loss

The breadboard rotor was made similar to the prototype rotor. Its retaining ring, which is shrunk on the aluminum end ring, normally has a spacing of 6 to 8 mils from the rotor body. However, these rings were pressed against the rotor body of the breadboard motor rotor, thereby accentuating the reactance problem in the motor. When this was allowed for in the equivalent circuit, the calculated performance more nearly matched the test results.

While these tests were abbreviated to conform to the reduction of the contract scope and little or no analysis is possible, the ability to predict motor performance has been verified at least to a degree. Additional development, tests, and analysis would be desirable. This work would involve:

- Rewinding the breadboard stator
- Reworking the end ring materials and configuration
- Retesting the motor with improved instrumentation
- Data analysis

The objectives of this effort would be to:

- Erase any question concerning the dissymmetry in the stator winding.
- Verify improvement in performance with a new end ring configuration.
- Increase the technology base for this type of motor.



## FABRICATION

All work was stopped on the manufacture of hardware for the turbocompressor. The status of the parts discussed below reflects presently complete hardware and the estimated percent of the hardware remaining to be completed, if further work were directed.

### SHAFT

The manufacture of the first shaft was completed, final inspection was performed, and the shaft was dynamically balanced without the impellers. The inspection showed that the maximum out-of-roundness of one journal was 30 microinches; the other was 40 microinches. The concentricity of the bore (which accepts the impeller hub) relative to the journals was 200 microinches on one end and 140 microinches on the other end. Figure 27 shows the first completed shaft. Three additional shafts were stopped in process, at an estimated 50-percent stage of completion. The shaft center sections have been machined and balanced.

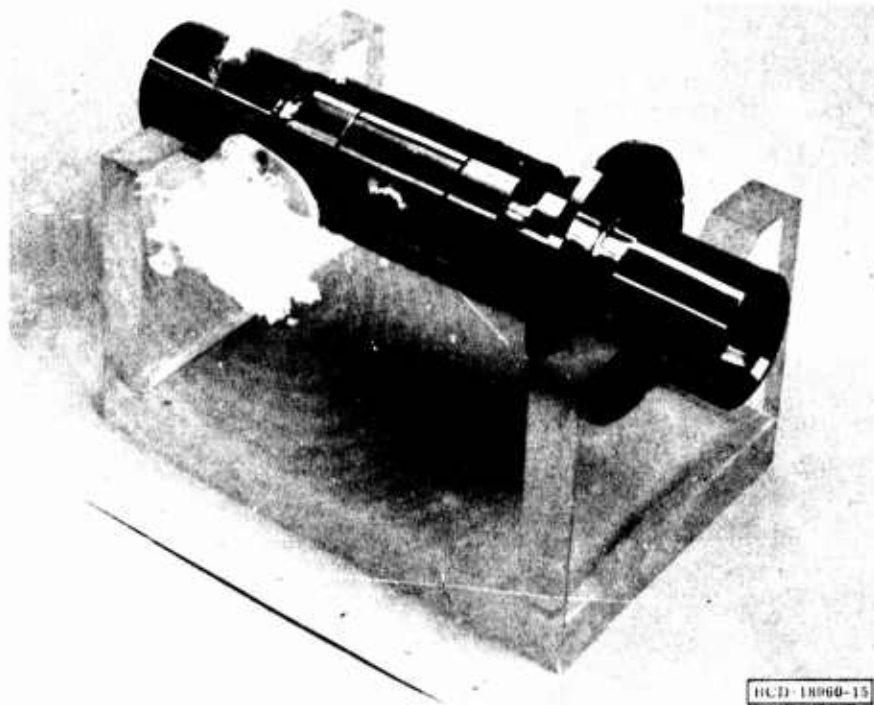


Figure 27. First Completed Shaft

One journal end has been welded to each center section. During the machining of these center sections, prior to the installation of the steel safety rings over the aluminum end rings, the 0.005-inch gap between the aluminum ring and the steel motor section was filled with paraffin, to prevent chips from entering the gap. After the assembly of the aluminum end rings to the steel section, all three shafts were ultrasonically inspected and found to be satis-

factory. Following the inspection, the steel rings were shrunk in place over the aluminum, grinding of the outside diameter and length was finished, and the ends were threaded. The sections were then balanced and welded to one journal section.

Work remaining to complete these shafts includes welding the other journal end to the shaft, nitriding, final machining, grinding, and final balancing.

### SCROLLS

Both the first- and second-stage scrolls have been completed. The first-stage scroll is shown in Figure 28. The second-stage scroll is shown in Figure 29.

The castings for the third- and fourth-stage scrolls have been received from the vendor and have successfully passed receipt inspection. No machining has been performed on these scrolls. Their estimated stage of completion is 25 percent.

### IMPELLERS

As reported in the Phase B final report (Ref. 2), the first- and second-stage impellers have been completed. The third- and fourth-stage impellers have been received and have successfully passed receipt inspection. In addition to the complete machining, a finished spin test to 95,000 rpm has been performed on these rotors by the vendor. These two rotors have not been corrosion-coated. Normally the impeller hubs are corrosion-coated, followed by a coating of Microseal 200-1. These coatings minimize friction problems during assembly of the impellers to the shaft. The four impellers are shown in Figure 30.

### JOURNAL BEARING PADS

As reported in the Phase B final report (Ref. 2), all of the journal bearings had been inadvertently flame sprayed with tungsten carbide, over previously finished hubs. These bearings were returned to the vendor, where they were chemically stripped of the carbide. The pivot sockets were then reworked, and the journal surfaces were replated with tungsten carbide.

When preparing to polish the journal bearing sockets, close inspection disclosed two different defects present in the tungsten carbide coating. Some sockets had radial cracks extending from the rim down toward the bottom. The cause of these cracks is unknown. Other socket surfaces had pits in the carbide coating. It is believed that these pits were the result of a small particle being trapped beneath the electrode during the electrical discharge machining of the sockets.



Figure 28. First-Stage Scroll

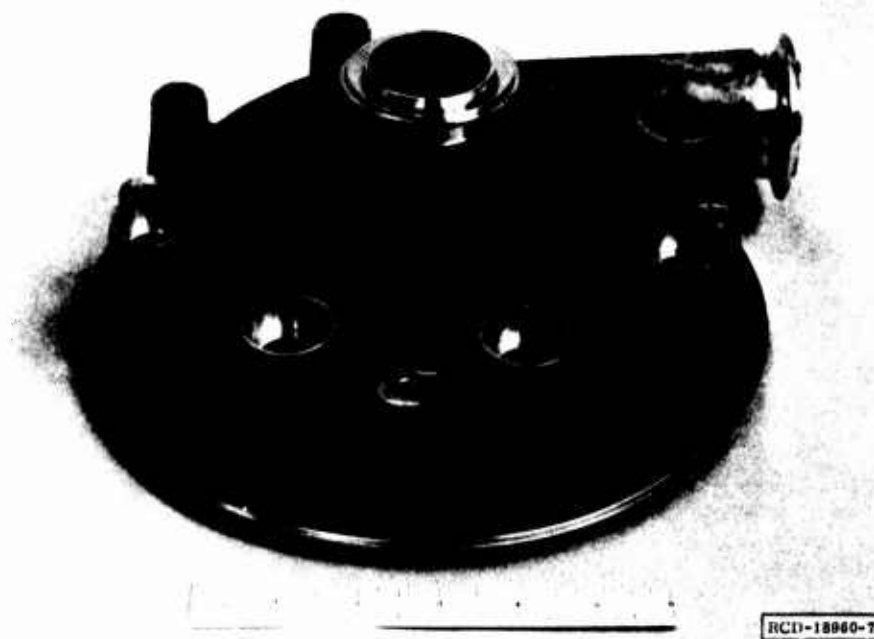


Figure 29. Second-Stage Scroll



Figure 30. Impellers

The 11 defective journal bearing pads were returned to the vendor to have the tungsten carbide flame-spray coat removed from both the journal surface and the pivot sockets. This is a chemical stripping process that does not disturb the base material.

The tungsten carbide flame-spray was then reapplied to the sockets. Machining of the sockets and rough lapping was then performed. The other nine pads that were satisfactory were completed.

The completed pads are shown in Figure 31. During the machining of the remaining 11 journal pads, defects in the tungsten carbide coatings were observed. These defects were in the form of cracks and chips, breaking away along the circumference of the socket at the outer edge. These edges were chamfered by grinding, to remove all of the defective coating.

This is not a critical area, aside from the requirement of a sound surface to prevent any chips from falling into the compressor. The pads were then sent to the Union Carbide Corporation to have the journal surfaces flame-sprayed with tungsten carbide.

Following the coating, the 11 pads were stopped in process. Final grinding and lapping was not begun. Approximately 75 percent of the work had been completed on these pads when the work was halted.

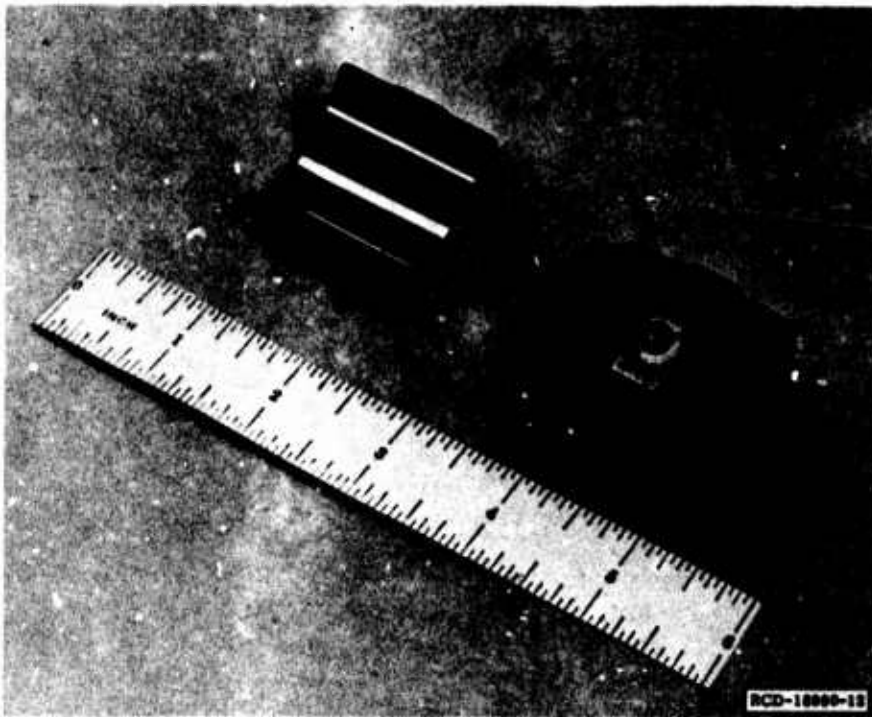


**Figure 31. Completed Journal Bearing Pads**

### **JOURNAL BEARING PIVOTS**

During this period, five spring-loaded pivot stems for the journal bearings were heat-treated, the ball ends were nitrided and polished, and the spring stop slots were machined, completing the manufacture of these parts. The springs were then calibrated to determine the spring rate.

All of the springs were on the high side of this design point, allowing for adjustment, if warranted, by future test results. The spring rates ranged from 980 lb/in. to 1360 lb/in.

Only one more solid stem was required to complete the inventory for both Modules A and B. The first seven solid stems have been completed. Three solid stems were stopped in process, after they were found to have soft tips on the balls, caused by defective nitriding.

For these stems to be usable, the nitriding must be stripped, and the parts must be replated and then reground and polished. All work has stopped on these stems; they are approximately 25 percent complete.

Both the spring and solid stem are shown in Figure 32.



Figure 32. Spring and Solid Stem

### THRUST BEARINGS

Generating the pockets in the surface of tungsten-carbide-coated thrust bearings to tolerances of  $\pm 0.000075$  inch proved to be extremely difficult. Grinding and electrical discharge machining were initially considered, but the decision to use either of these methods was delayed while an alternate method of manufacture, capable of producing the precision required at reduced costs, was sought.

A search for an alternate method was conducted, and a decision was made to try a process called ion etching. Ion etching is a process in which tiny particles are blasted from the surface electrically and are deposited on a target cathode. The environment is low-pressure argon at temperatures up to 600°F. The removal rate is a function of the time at a temperature. All previous applications required the depth of the pockets to be on the order 0.0001-inch maximum, and at this depth, success had been achieved. Unfortunately, the specification for the depth of this bearing was ten times greater.

Several vendors were contacted, and all expressed concern because the specified depth of 1 mil exceeded past experience. The Hohman Plating and Manufacturing Company in Dayton, Ohio returned the lowest quotation and appeared willing to apply itself to further the state-of-the-art. The Hohman Company designed a mask that was manufactured at the General Electric Research and Development Center. A Research and Development Center manufacturing engineer traveled to Dayton with the parts, to discuss this application. It was decided to perform the experiment using the existing tooling.

Monitoring for depth control occurred at increments of 0.0001 inch of stock removal. After 20 hours, the process appeared practical, but as the depth increased, changes in the uniform depth finally proved the process to be unsatisfactory.

After a complete inspection at the Research and Development Center, it was determined that the profile of the etched surface was fairly flat, except small islands protruded above the generally flat surface. The islands represented about 0.1 percent of the surface and were very small in cross section. This condition was invisible to the naked eye, but under microscopic examination they were noticed, and spacing was random.

Unfortunately the depth measurement at the Hohman Plating and Manufacturing Company was performed using a micrometer that measured the height of the islands, because the micrometer anvils bridged several islands. Therefore, the 0.001-inch depth measurement was inaccurate. Also, the average depth of the majority of the surface was much greater than 0.001 inch, as specified. Measured with an electronic indicator, using a very small stylus, the pockets proved to be about 0.002 to 0.0025 inch.

Further communication with Hohman Company personnel about the problems defined above resulted in an assumption that flame-sprayed tungsten carbide was nonuniform in structure and resulted in a much slower etching rate in some areas, which caused the islands. The tapered surface (0.002 to 0.0025 inch) was produced by a type of flux density problem, which may be solved by extensive shielding.

For the immediate future, the ion etch method was set aside. This method is good for etching up to a 0.0001-inch maximum depth. It would be feasible to experiment further if high production of refrigerators justified further experimenting with better quality flame plating and flux shielding-focusing of the ion beam particles. Considerable testing and development would be necessary to make this method successful.

High-precision tools were then made to overcome dimensional control problems associated with electrical discharge machining. The evaluation of the electrical discharge machining of the pockets was made on a sample piece. This method initially appeared successful, with uniformity of the depth of the pockets being held to within 10 microinches.

The early attempts to use electrical discharge machining were promising, but continued test machining on a sample bearing failed to produce a finish, or uniformity, that was satisfactory. As a result, this method also was abandoned. It was then decided to grind the pockets on a jig grinder. Especially small diamond wheels and a holding fixture for the bearings were made.

The grinding of the pockets of two thrust bearings was completed. Figure 33 shows the face of one of the completed bearings. The results are satisfactory and prove to be more economical than first believed, in spite of the special tooling required.

The gimbal pivot screws are now complete. Some cracking of the nitrided hard coat was experienced around the edge of the socket. This area is not



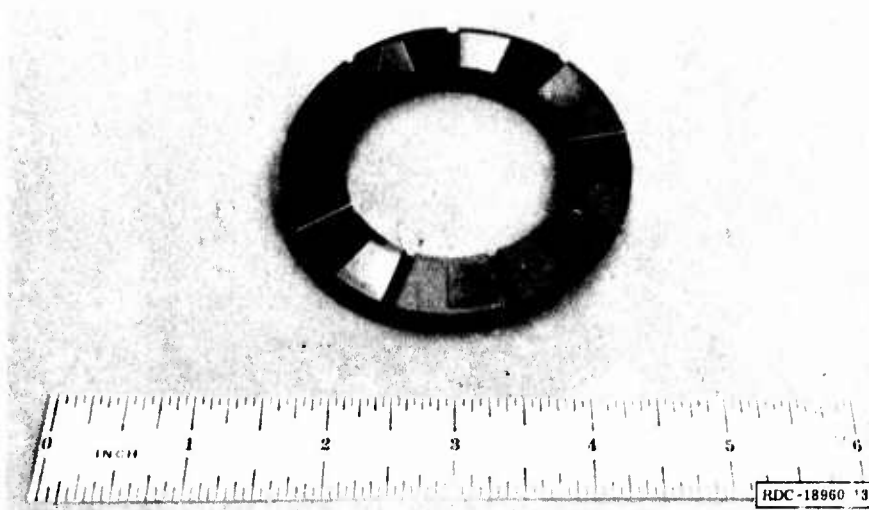


Figure 33. Face of Completed Bearing

critical, but it was feared that further chipping might occur. These areas were ground until a sound surface was established. The pivot screws are satisfactory for use.

Work on three more thrust bearings was stopped in process. These bearings were approximately 50-percent complete. The plating of the bearing surfaces had been completed; lapping and grinding of the pockets was not begun.

#### HOUSINGS

As reported in the Phase B final report (Ref. 2), all work has been completed on the four-piece structural housings shown in Figure 34. In addition, the outer housing, which seals the entire compressor, is finished (Figure 35).

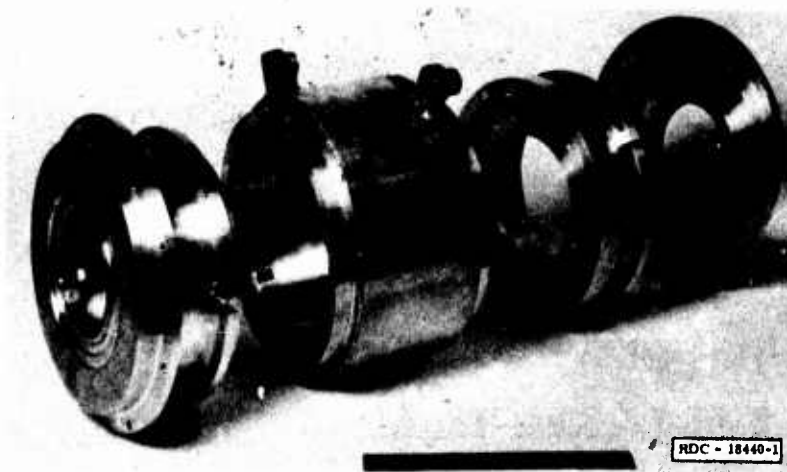
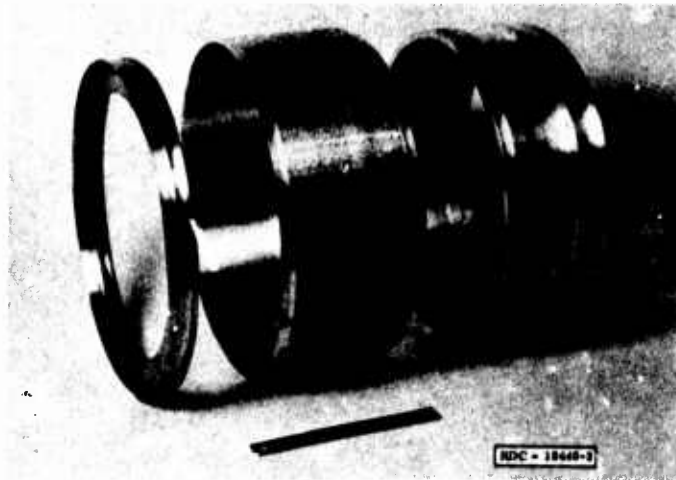


Figure 34. Four-Piece Structural Housings



**Figure 35. Outer Housing**

All of these housings were inspected and found to meet all Design tolerances. All surfaces of the rabbet fits have had a microseal lubricant coating applied to facilitate assembly. These parts are now ready for assembly.

#### **FEEDTHROUGH BULKHEADS**

As reported in the Phase E final report (Ref. 2), the feedthrough bulkheads, as shown in Figure 36, have been completed.

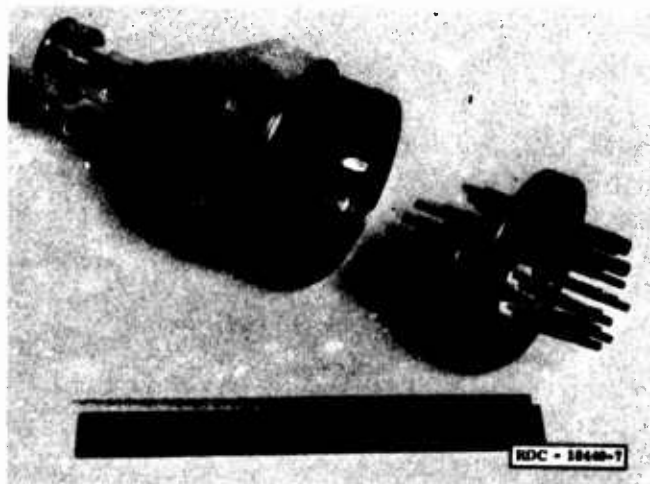


**Figure 36. Feedthrough Bulkheads**

#### **GAS BEARING SIMULATOR HARDWARE**

All of the hardware for the gas bearing simulator, which is described below under "Test Results and Evaluation," is complete (with the exception of

several assembly tools). The intent was to use Module B parts, where possible, for this test assembly. In the case of the bearing pads and stators, the first completed set was to be used for the gas bearing simulator, with the next set of parts being used for the Module A build. Upon completion of the gas bearing simulator test, the hardware from this assembly would have been used, where possible, to build Module B. Initial assembly of the hardware and instrumentation associated with this test had begun.

## **TEST RESULTS AND EVALUATION**

### **THRUST BEARING FLATNESS TESTS AT ELEVATED TEMPERATURES**

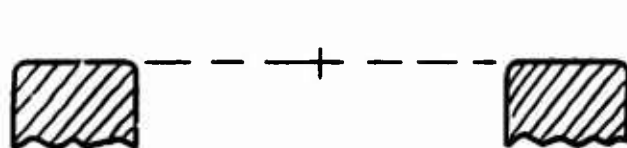
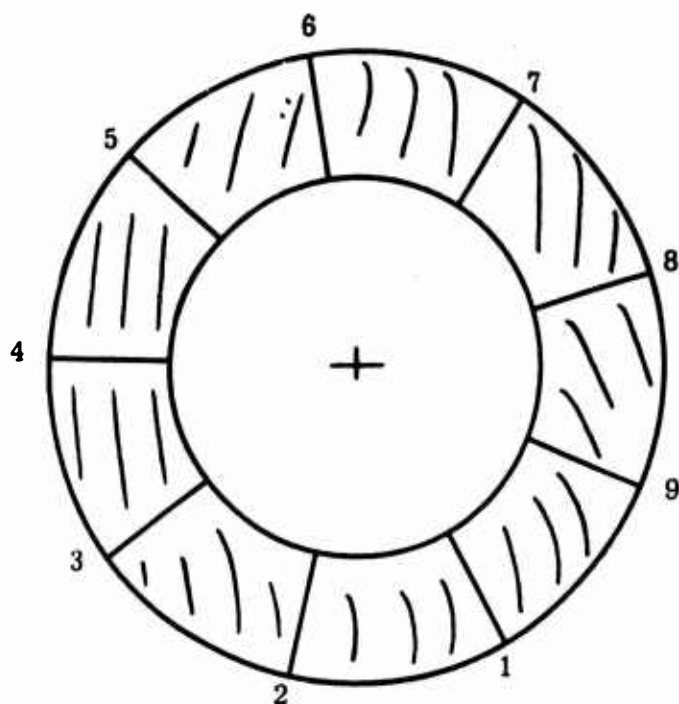
#### **Thrust Bearing 1-2780**

An interferometer setup was built into an oven. Three different flats were taken from room temperature, 78°F (25°C), up to 400°F (204°C). Due to the thickness and poor heat conductivity of the vitreous flats, there was some convex warping of the lower flat, which was closer to the heating element. At equilibrium, there was no warping. This test was conducted at six different stages during the heating cycle. When cooled, the lower flat tended to become concave, but flattened out at equilibrium, usually in less than 5 minutes. At the end of the tests, all of the flats were back to their normal shape. The maximum amount of warping seen at the maximum heating rate of the oven was 3-1/2 fringes, which occurred when the rate was 30°C in 10 minutes or 3°C/min.

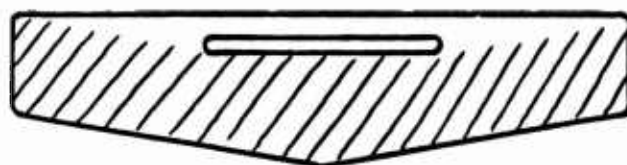
These preliminary tests prove that measurements can be made at the required temperatures and that at equilibrium the flats are good.

The original condition of the bearing is shown in Figure 37. There was a wedge of air between the plate and flat, so sensibly straight fringes were seen. Those fringes in Region 8 were somewhat deformed, showing that the ring is bent down at this point so that as seen from the edge, it would appear as shown in the lower sketch. In addition, most of the rim all the way around is turned down for a distance extending in about 1/16 inch. This condition is normal for any flat surface lapped without a protective surrounding and is due to the weight of the lapping tool being concentrated on the edge at the end of the stroke.

The final small defect is shown in the detail of Figure 38. The fringes bend down near the inner edges of Slots 3 and 4, which indicates that these edges are turned down. The total error in flatness of this bearing does not exceed



Turned Down  
at Edge Approximately  
1/16 Inch About  
3/4-Inch Fringe



CR-3305

Region 8

Figure 37. Original Condition of Thrust Bearing

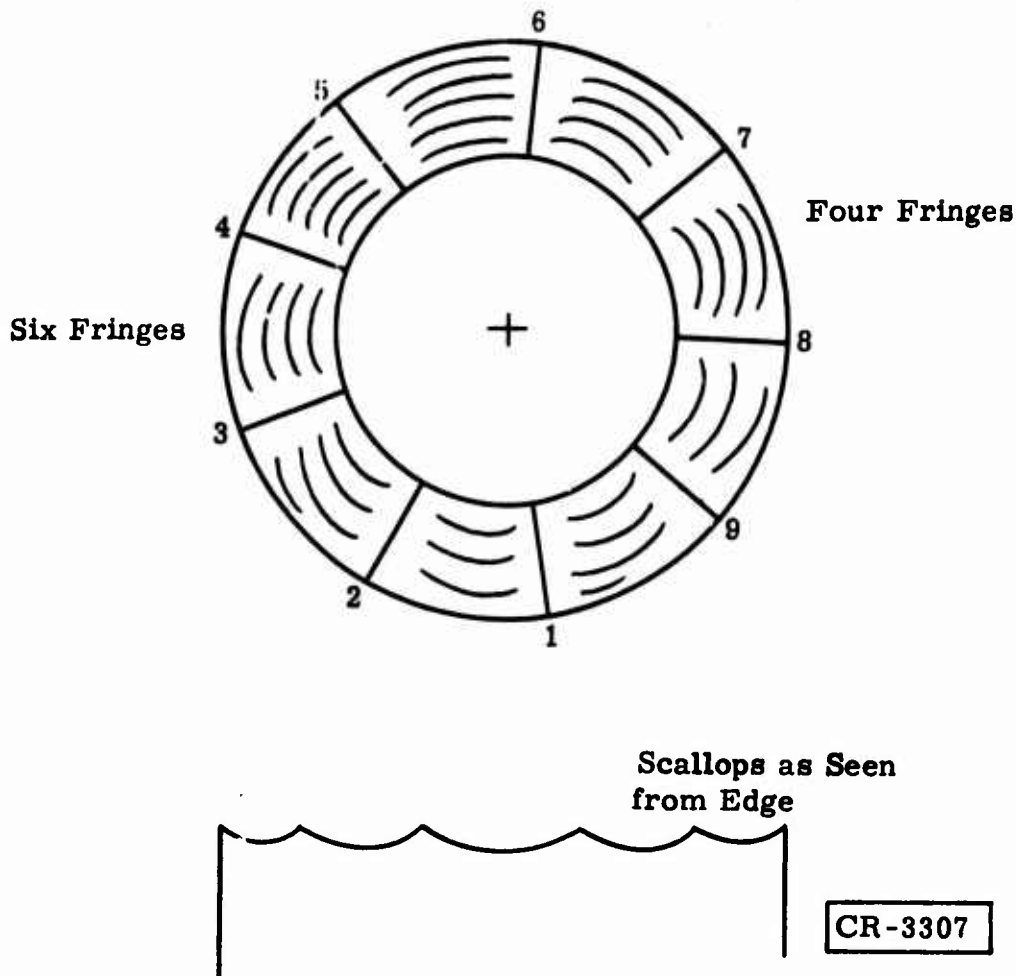


Figure 38. Thrust Bearing at Equilibrium (105°C)

one fringe. In these tests, green thallium light was used with a wavelength of 5350 micrometers, which is 0.535 micron. Because there are two fringes of interference per wavelength, one fringe is equal to 0.267 micron or 9.5 microinches.

As soon as heating was started, the ring as a whole became part of a concave sphere. Even at temperatures as low as 60°C, there was a total of nine fringes across the sphere (Figure 39). The pattern is nearly symmetrical, with an irregularity where the dip occurs near Slot 8. This concavity could be partly due to warping of the flat, but is mainly due to the metal.

The equilibrium condition is shown in Figure 38, which also shows a total of about ten fringes, concave at 105°C. A new effect is also seen: each of the segments of the ring is separately concave, so that as seen from the edge, the ring appears scalloped. Each segment of the ring is scalloped about one fringe deep at this temperature. For some reason, the hooks on the ends of the fringes at Slots 3 and 4 become more noticeable at this temperature and remain so, up to the highest temperature used.

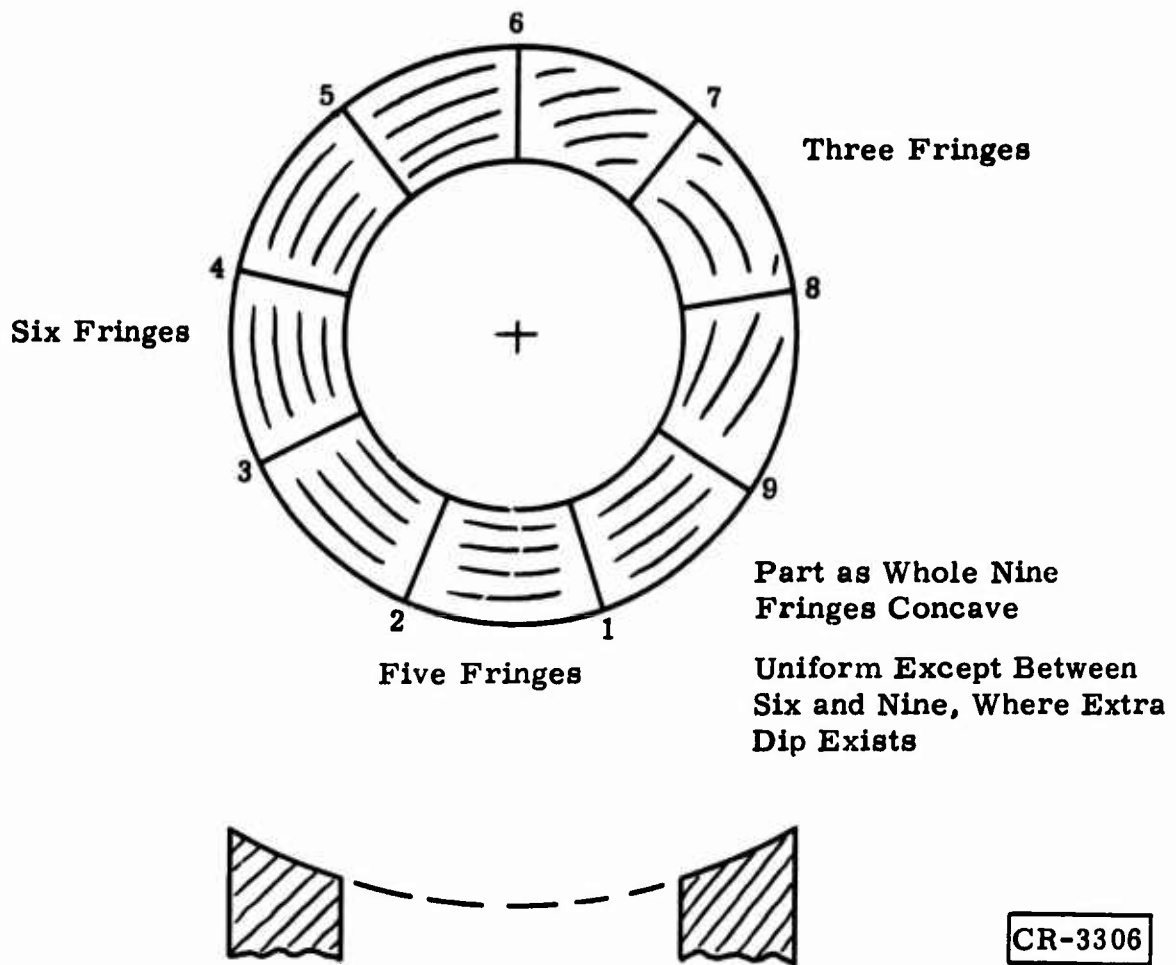


Figure 39. Thrust Bearing at Nonequilibrium (60°C)

These two slightly different patterns continued unchanged up to 400°F, with increasing deformation.

In all of the following examples, the concavity was greater under the heating condition and slightly less at equilibrium (the scalloping was less during heating and greater at equilibrium):

- Nonequilibrium, 262°F (128°C), 13 fringes concave, scalloping less than one fringe
- Equilibrium, 285°F (125°C), 11 fringes concave, scalloping 1-1/2 fringes
- Nonequilibrium, 290°F (143°C), 16 fringes concave, scalloping one fringe
- Equilibrium, 286°F (140°C), 12 fringes concave, scalloping two fringes
- Nonequilibrium, 352°F (178°C), 18 fringes concave, scalloping 1-1/2 fringes

- Equilibrium, 348°F (175°C), 16 fringes concave, scalloping 2-1/2 fringes
- Nonequilibrium, 399°F (204°C), 30 fringes concave, scalloping two fringes
- Equilibrium, 399°F (204°C), 26 fringes concave, scalloping 2-1/2 fringes

If a deformation of 20 microinches is the maximum allowable, then an originally perfectly flat part would be out of specification when 2.1 fringes were visible or a temperature of about 126°F (53°C) existed.

Relative to cooling, the pattern gradually changed from the 26 fringes of concavity to nearly flat at 45°C. While the ring as a whole was nearly flat, the individual sectors were tilted at many different angles (Figure 40). The numbers near the sectors denote the number of fringes. The two sectors between 2-3 and 3-4 are tilted at right angles to each other, as are 3-4 and 4-5.

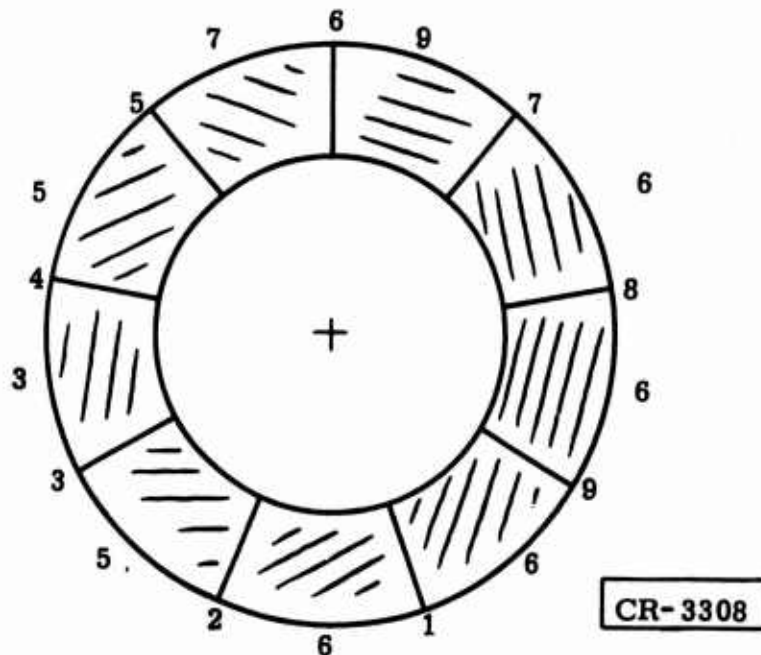


Figure 40. Thrust Bearing Cooling at Equilibrium (45°C)

The final shape after cooling overnight is shown in Figure 41. The ring as a whole is essentially as flat as it was at the beginning. The cross section across the ring is convex, more so than it was at the start. The outside, turned-down edge is less noticeable. The dip in the edge at Slot 8 is still visible. The hooked ends on the fringes at Slots 3, 4, and 5 are still there, but are not shown in the drawing.

It may be summarized that during heating or cooling, the thick vitreous flats may be deformed. The maximum deformation seen was 3-1/2 fringes. At equilibrium, this deformation disappears.

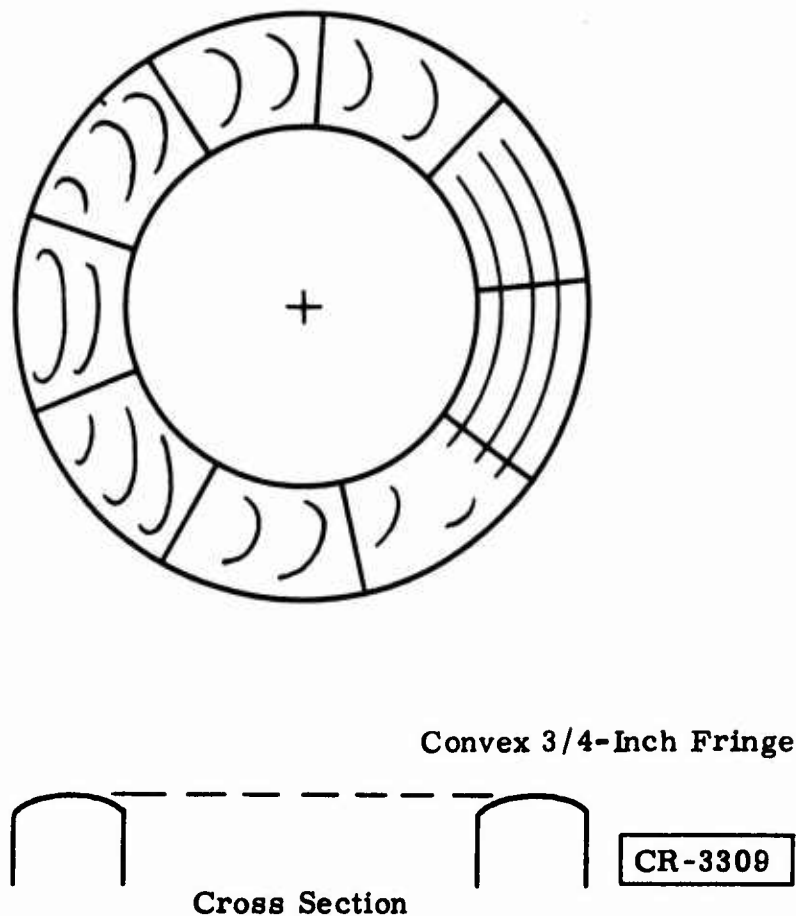


Figure 41. Thrust Bearing Final Shape

Further, starting at very low temperatures, the bearing ring deforms to a concave sphere and the individual facets or sectors become concave, giving the bearing surface a scalloped shape. This shape is probably due to the slots in the surface, which weaken the ring and cause a redistribution of the force, causing the spherical deformation. At 400°F, the spherical deformation over the entire ring was 26 fringes or 247 microinches. After cooling, the ring returned to essentially its original shape. The only noticeable difference was that the cross section was more convex.

#### Thrust Bearing 6-2779

Figure 42 (the original test) shows the plate as a whole to be flat to better than one fringe and to be convex, like a doughnut in cross section, with this convexity about one fringe and uniform around the ring. Unlike the first bearing, which was slightly turned down around the outer edge, this one is turned down on both the inside and outside edges.

As soon as heating was started, the plate became concave about the same amount as the Bearing 1-2780 plate:



- At 60°C (122°F) it showed eight fringes.
- At 100°C (212°F), it showed 12 fringes as practically concentric circles (Figure 43).

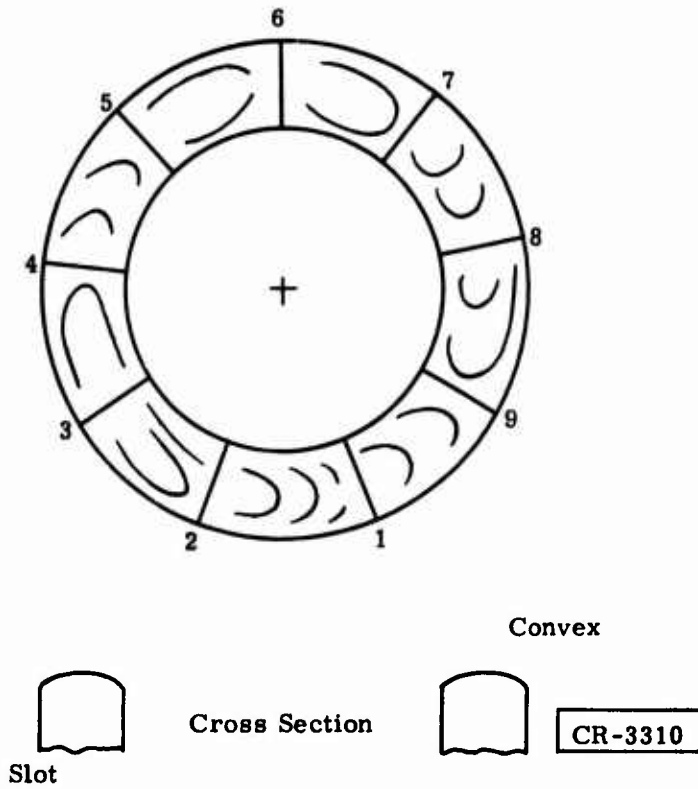


Figure 42. Thrust Bearing Original Shape

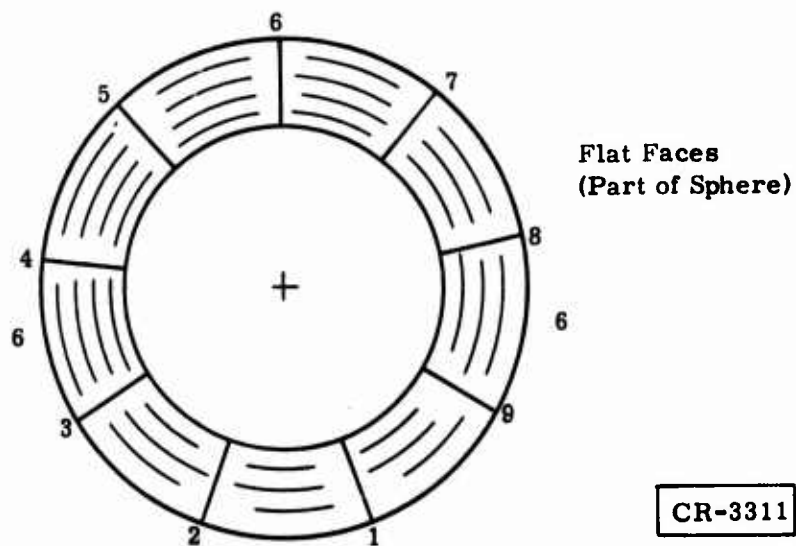


Figure 43. Thrust Bearing (100°C)

At 204°C (400°F), the plate was concave (23 fringes). The scalloping of the faces was less, only about one fringe, and again these were concave. The appearance was practically the same as that shown in Figure 43, except there were more fringes and the inner ones were curved in at the ends of the faces. After cooling, the plate returned to its original shape.

The deformation of this bearing is essentially the same in kind and amount as the deformation of the first one. The total deformation was slightly less, and the concaving of the faces was less.

### COMPRESSOR SHAFT STIFFNESS TESTS

A load deflection test was made on the first compressor shaft. It was supported by its journals on V-blocks and weights suspended from the center. The deflection was measured with a capacitance-type sensing probe. The results are shown in Figure 44. The deflection rate was measured at 3.52  $\mu\text{in./lb}$  of load. The corresponding shaft spring rate is 284,000 lb/in.

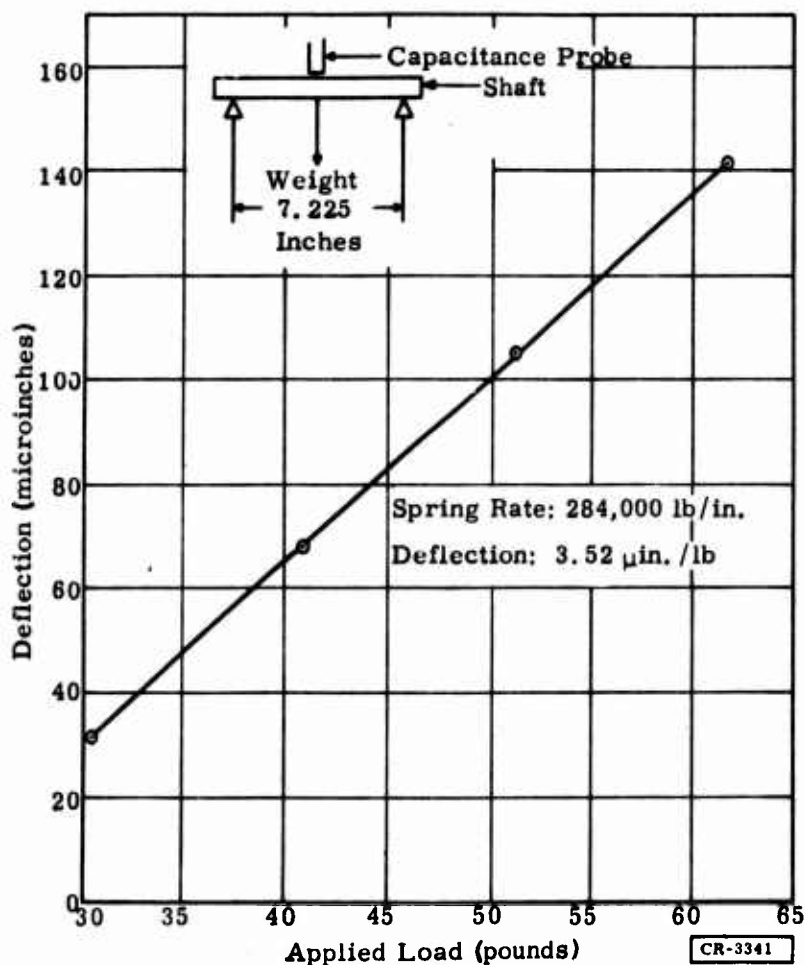


Figure 44. First Compressor Shaft Deflection Versus Load  
(Shaft 588E454, 3B)

Using the simple beam formula, like the conditions of the test, the shaft stiffness is:

$$EI = \frac{SL^3}{48}$$

where:

E = Youngs modulus (psi)

I = Moment of inertia (in.<sup>4</sup>)

S = Shaft spring rate (lb/in.)

L = Span between supports (inches)

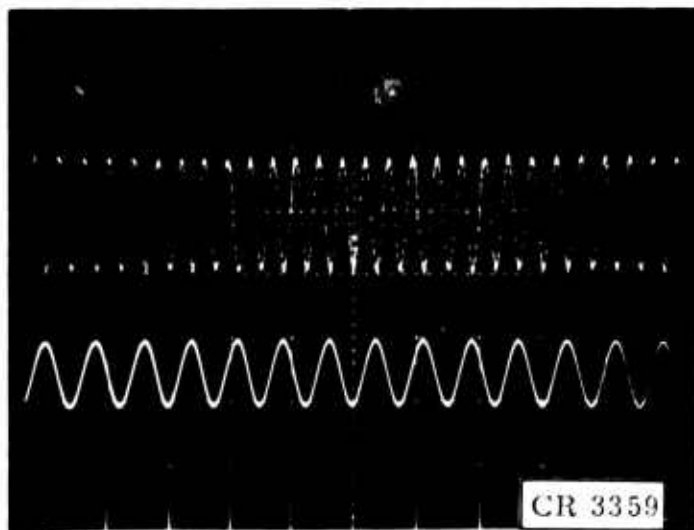
The corresponding shaft stiffness, EI, is equal to  $2.245 \times 10^6$  lb-in.<sup>2</sup>. This value compares with the design value of  $7.28 \times 10^6$  lb-in.<sup>2</sup> used in the original gas journal bearing design.

The original design data were reexamined in light of this variation in shaft stiffness, to determine the effect on the compressor design. Using  $EI = 2.245 \times 10^6$  lb-in.<sup>2</sup>, combined with the original design data, produced a first bending critical speed of 61,076 rpm. This is of particular concern because it falls below the design operating speed. A rule of thumb for gas bearing design is that the first bending critical should be at least 25 percent above the normal operating speed for stable bearing operation.

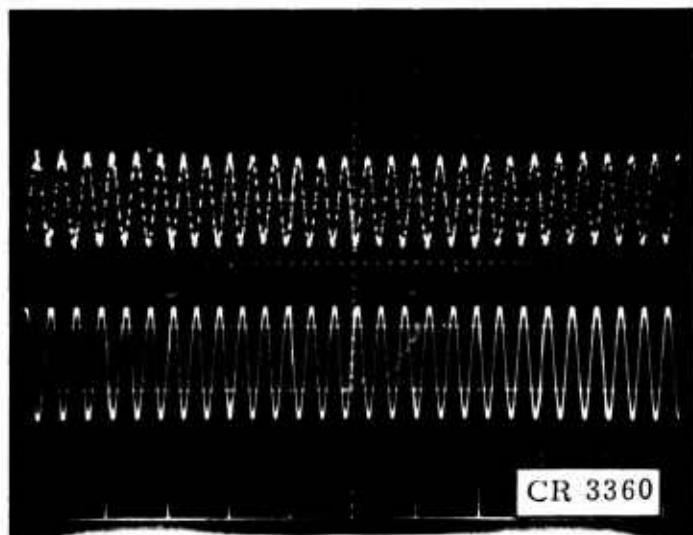
To verify that the shaft stiffness calculated from the load-versus-displacement test was valid, a more reliable test was devised. The shaft, with an accelerometer mounted at midpoint, was hung from two strings so that its axis was in a horizontal plane. An electric coil placed near the shaft was then used to excite the suspended shaft, with the input excitation controlled by a variable frequency oscillator. The output of the accelerometer was displayed on an oscilloscope. Figure 8 is a schematic diagram of the test setup. The results of the testing are shown in Figure 45.

With an input frequency of 78,000 cpm, the shaft was excited; it responded at a frequency of 156,000 cpm (Figure 45a). As the input frequency was increased, the next critical speed was noted with an input frequency of 156,000 cpm. The response from the shaft was at the same frequency (Figure 45b). An additional test was performed by tapping the shaft suspended on the strings and recording the output of the accelerometer mounted on the shaft. The results are shown in Figure 46. Counting the number of cycles and dividing by the time, based on the sweep rate of the oscilloscope, the response of the excited shaft can be determined. The results of this test also show that the natural frequency of the compressor shaft was 156,000 cpm.

The above data indicated that the actual bending critical speed is 156,000 rpm rather than the 61,076 rpm computed. Additionally, the shaft stiffness calculated from the results of the static load deflection test is invalid, and determination of the actual stiffness value from the dynamic test results becomes possible.



- a.   Excitation Frequency   13 Cycles in 10 Milliseconds = 78,000 Cpm  
       Rotor Frequency        26 Cycles in 10 Milliseconds = 156,000 Cpm



- b.   Excitation Frequency   26 Cycles in 10 Milliseconds = 156,000 Cpm  
       Rotor Frequency        26 Cycles in 10 Milliseconds = 156,000 Cpm

Figure 45. Results of Turbocompressor Tests  
 for Natural Frequency of Rotor  
 (Excitation by Electric Coil,  
 1 ms/Division)

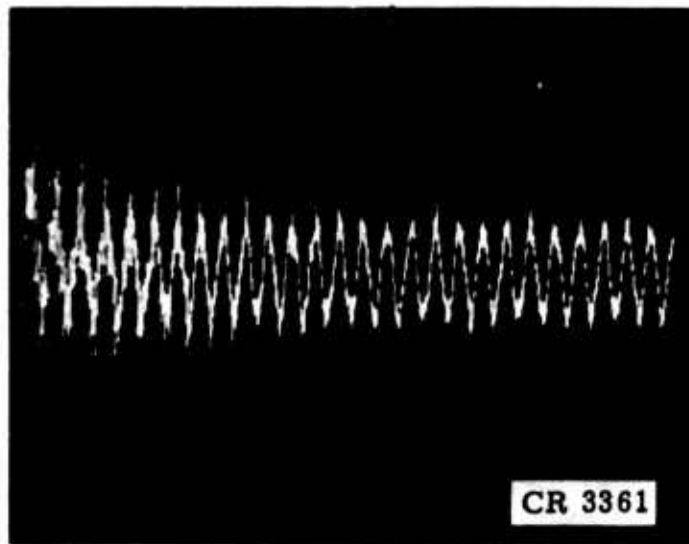


Figure 46. Results of Turbocompressor Tests for Natural Frequency of Rotor, with Suspended Rotor Excited by Striking  
(1 ms/Division, 26 Cycles in 10 Milliseconds = 156,000 Cpm)

Using tilting pad bearing selector program JSELCT to calculate the first bending critical speed, iterations varying the shaft stiffness were made until a first bending critical equal to 156,000 rpm was calculated. This occurred with an  $EI = 1.5 \times 10^7$  lb-in.<sup>2</sup> This value is approximately double that originally calculated.

#### GAS BEARING SIMULATOR

From design analysis and distortion tests, described above, it was apparent that closely monitored tests should be conducted when the gas bearings were first installed. It is only necessary to monitor the thrust bearing and journal bearing at the thrust bearing end, because the other journal bearing would have a less severe temperature distribution. The 25 watts from the motor end turns would not be experienced in initial tests, because the motor would not be at full power.

The interstage leakage flow of 0.19 grams/sec would not be experienced, because the impellers would not be installed during initial tests. However, as a source of gas flow, a fan might be incorporated to simulate this cooling flow.

An expedient means of performing these gas bearing test evaluations would be to use Module B compressor parts as a gas bearing simulator. This simulator would include both the journal and the thrust bearings. The only new parts that were made were dummy impellers on either end of the shaft, with the same weight and center of gravity as the existing vaned impellers. The other details of the gas bearing simulator rig have been described above in this section under "Design."

The gas bearing simulator test rig consisting of the compressor gas bearing simulator mounted on two milling tables allows the unit to be oriented in any desired position.. Tests would first be conducted at ambient pressure; testing would also be conducted at the design ambient pressure, on the order of 6 psia.

The performance of the bearing system would then be evaluated as a function of the operating variables:

- Orientation
- Heat
- Speed
- Ambient pressure

The orientation of the gas bearing simulator would be set with the pair of milling tables, as used in the cleanup room, to set the bearing clearances. Thermocouples would be located appropriately to determine the actual temperature environment. The speed would be regulated from 0 rpm to the maximum design speed of 95,000 rpm. The gas bearing ambient pressure would be regulated by using a suction blower, on the enclosure, that would pull the pressure down to the nominal 6 psia ambient pressure of the gas bearing system.

When the compressor bearing system had been proven at 1-g loads in different orientations, consideration would be given to testing the gas bearing simulator under shock loads to the 3-g design requirements.

It was anticipated that the gas bearing simulator using Module B parts would be assembled and operated in parallel with the Module A complete compressor, depending on the availability of component parts.

Complete instrumentation was planned to be incorporated into the gas bearing simulator. The initial approaches were:

- Proximity Probes

Mounted on one of the two lower pads, facing the shaft. Three probes would be mounted in a line, just ahead of or just behind a line through the pivot point, to measure close to the actual gas pivot film thickness. This positioning would provide a measurement of the combined pad and shaft distortion and single-pad bearing performance.

Mounted on the upper spring-loaded pad. Two probes would be mounted axially in line with the pivot point, outboard on either end of the pad. This placement would provide the spring pad bearing performance data and would also provide performance assurance of the stem spring rate.

Mounted stationary, facing the outer gimbal ring between gimbal pivots, for gimbal ring oscillation.

Mounted stationary, facing the back of the thrust bearing between the gimbal pivots, for thrust bearing oscillation.

Mounted outboard of the thrust bearing. A probe at a gimbal pivot and a probe 90 degrees from a gimbal pivot would be used to measure any distortion around the thrust bearing. These measurements would also provide load versus film thickness performance data.

Mounted at either end of the shaft. This placement would provide a basis for correlating any axial motion in conjunction with any gimbal or thrust bearing motions. Special probe supports would be made, because the scrolls that normally support these probes would not be installed.

Mounted (a pair of X-Y probes) on the motor side of the thrust bearing, as in the prototype unit.

Mounted (a pair of X-Y probes) on the non-thrust-bearing end of the shaft, as in the prototype.

Mounted (one probe) on the leading edge of a pad, as in the prototype compressor.

- Thermocouples

Mounted at the inside and outside diameters of the thrust bearing, both at the pivot points and between pivot points.

Mounted at the gimbal ring, at pivot points and between pivot points.

Mounted on the inside of the housing and on both cooling fins at three radii.

Mounted on the pad near the pivot point.

Mounted on the stem near the pivot point.

NOTE: The temperature-sensitive point would be used on the shaft to obtain approximate maximum operating temperatures and maximum temperature gradients.

Two new capacitance probes had to be designed for monitoring the thrust bearing and the thrust bearing gimbal motion. Size and temperature requirements precluded the use of existing probes. The mounting of capacitance probes onto journal pads was abandoned because of the long installation time required. The remainder of the instrumentation was as outlined above.

The first compressor module was to be assembled in the clean room, without the thrust bearings installed. The journal bearings and motor drive

would be test-evaluated at low speed. Then the dummy wheels and thrust bearings would be installed, and this complete assembly would be operated at low speed. This assembly would then be installed and operated outside the clean room at the gas bearing simulator test station. The assembly would be operated up to full design speed.

### CLOSED CYCLE COMPRESSOR TEST LOOP

The closed cycle compressor test loop assembly (Figure 47) was nearly complete when work was stopped. Figure 48 shows a mockup of the compressor module in place in the loop. After completion of the assembly, the instrumentation was to have been installed in conjunction with the data acquisition system.

The compressors would be assembled and given a preliminary rotational test in a clean room. With the clean air, running the machine at certain stages in the assembly will be feasible. Appendix II, "Assembly Procedures for U.S. Air Force High-Speed, Two-Stage, Centrifugal Compressor," of the Phase B final report is the basis for the sequence to be used.

The first test would have been made without the thrust bearings and impellers. To limit axial motion, special nylon stops would be mounted in the scrolls in place of the axial proximity sensors. Behavior of the rotor and journal bearings would be monitored at speeds up to 30,000 rpm. Pad motion

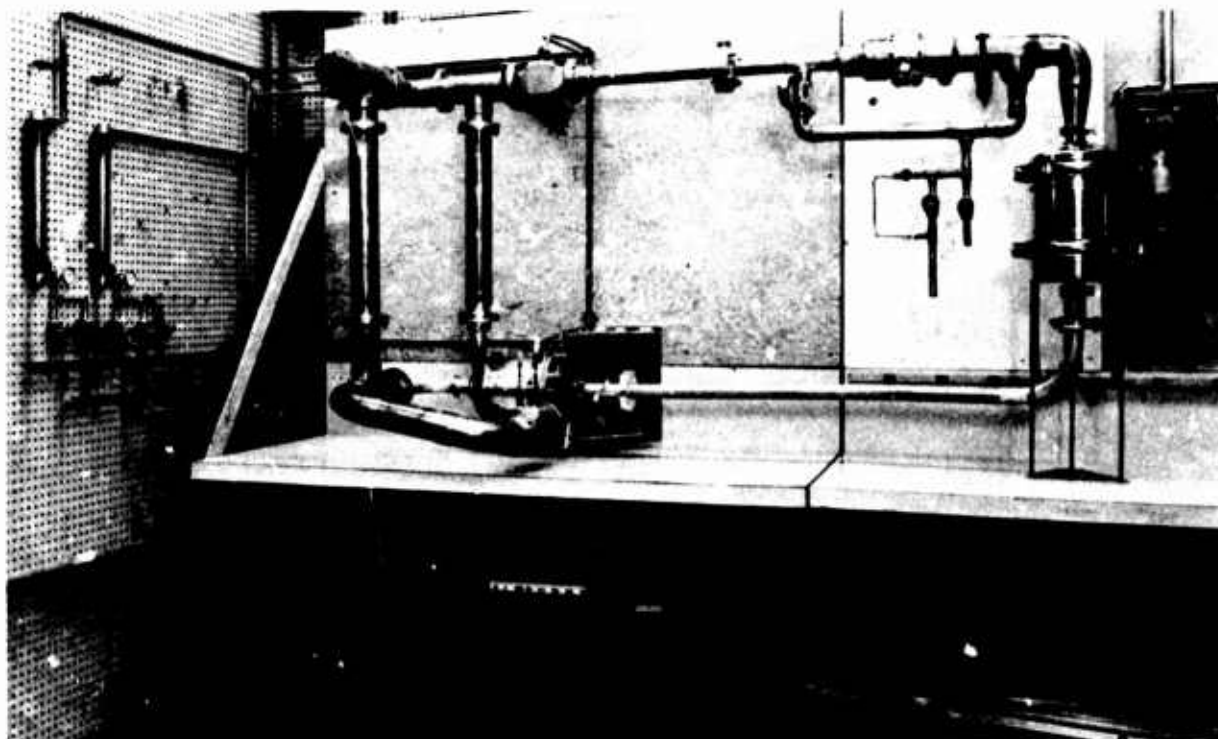
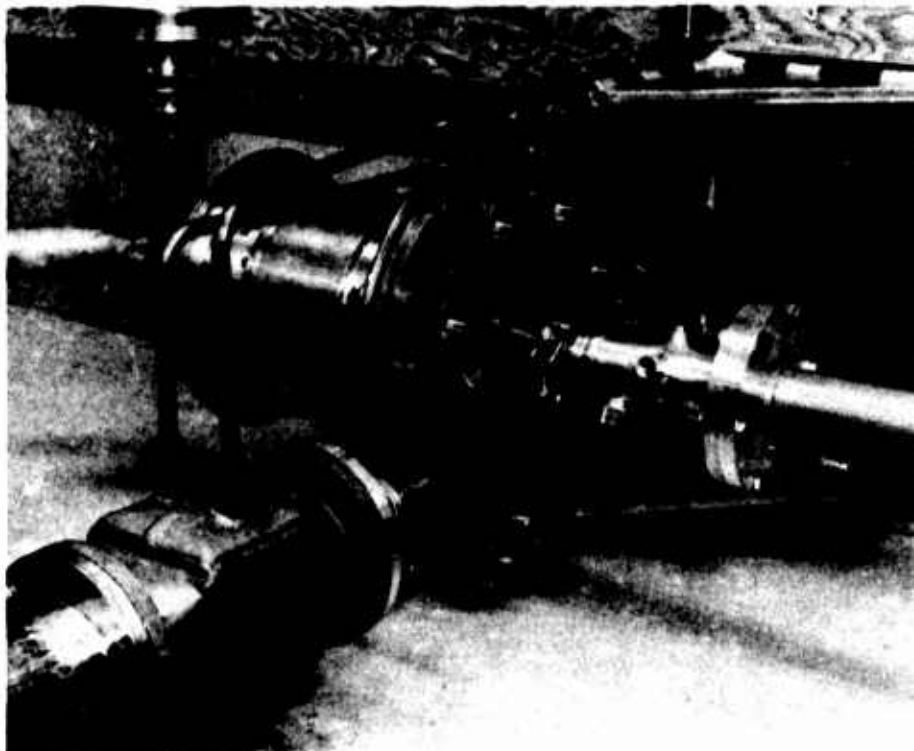


Figure 47. Closed Cycle Test Loop Assembly





**Figure 48. Mockup of Compressor Module in Place in Loop**

of the rotor and journal bearing would be monitored with capacitance, non-contacting sensors. Speed would be measured using a magnetic probe transducer, sensing notches on the periphery of the thrust runner. Any adjustments to the bearing clearance could be made at this time. The electrical control performance would be assessed at this time, and instrumentation to measure voltage, current, and frequency would be used.

The next test step would be to install the thrust bearings and repeat the operational checks outlined above. In addition, with the thrust bearings in place, behavior could be observed with the compressor mounted with the rotor in a vertical orientation. Successful operation of the compressor under the above conditions would complete the planned running in the clean room. The impellers would be assembled on the rotor, and testing would be continued with the compressor installed in the closed loop of the compressor test station. The latest arrangement of the compressor test station is shown in Figure 49. The actual test loop is shown in Figure 47, and a closeup of the compressor connections is shown in Figure 48.

Helium gas enters the first stage of the compressor through a filter, and the heat added is removed by an aftercooler. The flow passes to the second-stage compressor, and the heat added by the second-stage compressor is again removed by an aftercooler. The flow leaves the second-stage aftercooler and enters a flow-straightening element upstream of a square-edged orifice metering element. The flow passes through the orifice and throttle valve and

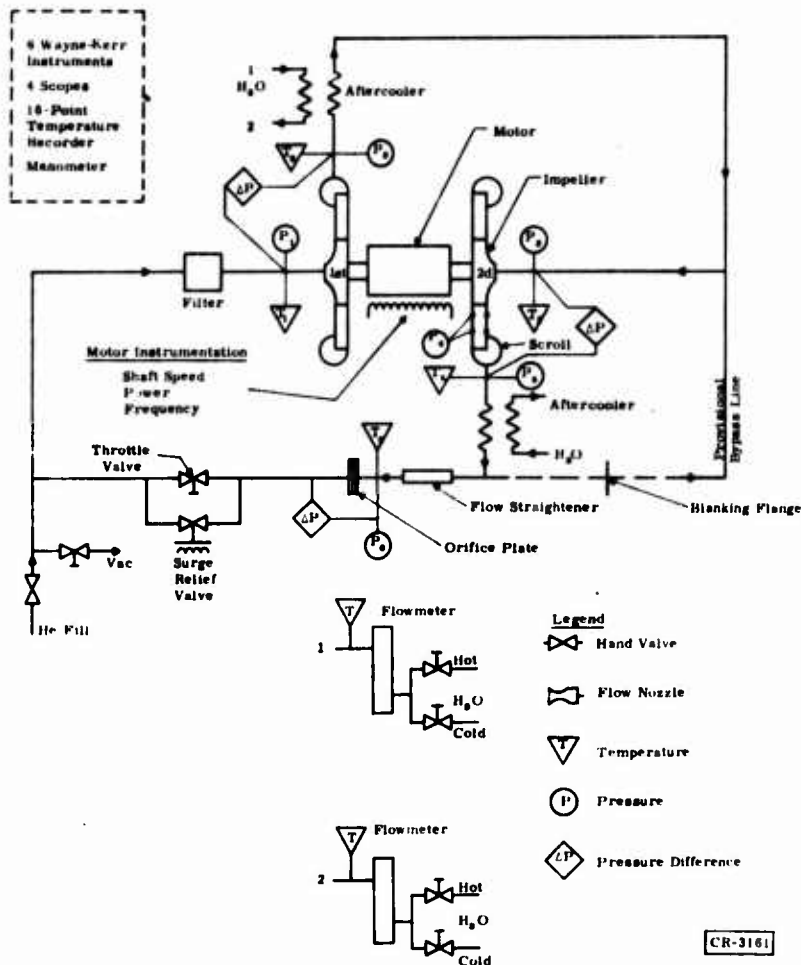


Figure 49. Motor-Compressor Test Station

returns to the first-stage duct. A solenoid surge relief valve has been introduced to provide instant correction of any accidental excursion into the surge region of the compressor.

The loop will be evacuated by a diffusion and roughing pump system operating through a cold trap to prevent backstreaming of pump oil from contaminating the system. The purity of the helium gas admitted to the system will be monitored by oxygen and moisture analyzers.

The first runs of the compressor in the loop would affirm the starting and mechanical operation, as established by the preliminary tests conducted in the clean room. Then full performance testing would be undertaken.

Both functional and performance tests would be conducted. The tests fall into three general categories:

- Bearing Tests

Establish bearing stability along the line of the design specific speed, with the shaft in both the horizontal and vertical positions (horizontal first).

Investigate the rotor critical speeds. All of the critical speeds in the running range (0 to 95,000 rpm) were predicted to be rigid rotor (bearing system) criticals.

- Aerodynamic Tests

Establish a performance map for each stage, as shown in Figure 50. Establish the design specific speed line first, then probe

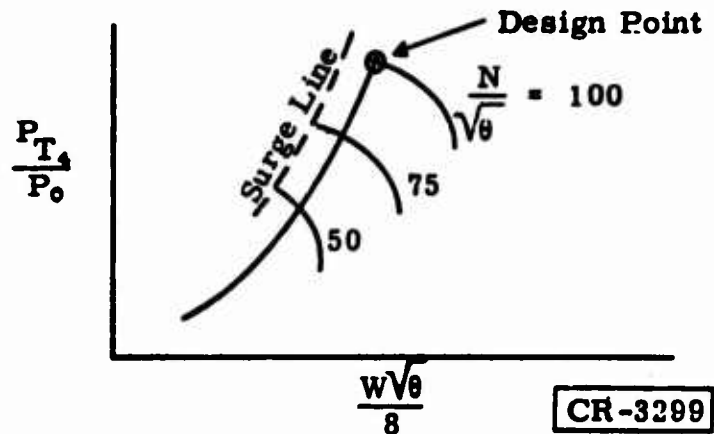


Figure 50. Performance Map

to the right (higher mass flow) on the 50-percent speed line, and then repeat at the 75- and 100-percent lines. Finally, probe cautiously to the left to experimentally establish the surge line. Use will be made of a quick opening bypass valve, around the throttle valve, to allow rapid escape from the surge region.

- Electrical Tests

Establish motor performance by measuring voltage, current, frequency, and phase angle for each operating point.

The following data would be recorded:

<u>Parameter</u>	<u>Symbol</u>
<b>Pressures</b>	
First-stage inlet	P1
First-stage pressure rise	P1-2
Second-stage inlet	P3
Second-stage pressure rise	P5-3
Internal, second stage	P4A, P4B, P4C, P4D
Orifice, inlet	P6
Orifice, $\Delta P$	P7-6

<u>Parameter</u>	<u>Symbol</u>
<b>Temperatures</b>	
First-stage inlet	T1
First-stage discharge	T2
Second-stage inlet	T3
Second-stage discharge	T5
Orifice, inlet	T6
First-stage aftercooler	
Inlet	T11
Outlet	T12
Second-stage aftercooler	
Inlet	T13
Outlet	T14
Motor coolant	
Inlet	T15
Outlet	T16
<b>Coolant Flow</b>	
First-stage aftercooler	Q1
Second-stage aftercooler	Q2
Motor	Q3
Speed (rpm)	N

Using the position probes listed below, the following would be recorded with a scope camera:

- Orbit type
- Orbit diameter

Major  
Minor

- Thrust bearing

Peak-to-peak excursion  
Oscillation frequency

The proximity probes to be used would be:

<u>Probe</u>	<u>Symbol</u>
Shaft, first-stage end, radial	X1
Shaft, first-stage end, radial	Y1
Shaft, second-stage end, radial	X2
Shaft, second-stage end, radial	Y2
Shaft, first-stage end, axial	A1

<u>Probe</u>	<u>Symbol</u>
Shaft, second-stage end, axial	A2
Impeller, first-stage, axial	I1
Impeller, second-stage, axial	I2
Pad, radial	P

The following performance parameters would be calculated:

<u>Component</u>	<u>Parameter</u>
Compressor	Head, isentropic
	Flow, normalized mass
	Speed, normalized
	Efficiency, overall
	Efficiency, aero
Motor	Pressure ratio
	Electromagnetic efficiency
	Motor losses
	Input power
	Output power

A major effort of this program has been to design an efficient motor-compressor to minimize the required electrical input power. An analysis has been made to determine the degree of accuracy required for pressure instrumentation.

Adiabatic gas power is of basic concern to the system. The work per pound to compress the gas is proportional to  $P_r^{(k-1)/k}$ , where  $P_r$  is the pressure ratio and  $k$  is the ratio of the specific heats for the gas. For helium,  $k = 1.665$ .

To illustrate the sensitivity of the power-to-pressure measurement, the following representative values are assumed:

$$P_{in} = 5 \text{ psia}$$

$$P_{out} = 6 \text{ psia}$$

Errors = 0.03 psia, maximum (typical of a 0- to 35-psia Heise pressure gage)

$P_{in}$  and  $\Delta P$  must be measured. Both have maximum error in opposite directions. Thus:

$$P_{in} = 5.03$$

$$\Delta P = 0.97$$

$$P_r = 6.00/5.03 = 1.1928$$

$$\text{Error in } P_r = 0.0072$$

$$\text{Percent of error in } P_r = 0.60$$

This does not appear to be too bad, but the percent of error in indicated power becomes:

$$\text{Percent of error in power} = 100 \frac{\left( \frac{1.1928^{\frac{k-1}{k}}}{1.2^{\frac{k-1}{k}}} - 1 \right)}{1.2^{\frac{k-1}{k}} - 1}$$

$$\frac{k-1}{k} = \frac{1.665 - 1}{1.665} = \frac{0.665}{1.665} = 0.3992$$

$$\text{Percent of error} = 100 \left[ \frac{(1.0227 - 1) - (1.0234 - 1)}{1.0234 - 1} \right] = 3.0 \text{ percent}$$

This percent is very substantial; therefore, it is planned to use pressure transducer instruments with maximum errors of 0.01 psi. These pressure transducers will have a voltage output that can be recorded directly on the teletype data logging system.

## **TURBOCOMPRESSOR HARDWARE STATUS**

All work was stopped on the manufacture of hardware for the turbocompressor. The status described below reflects parts presently complete and the estimated percent of completion of the incomplete hardware.

### **MODULE A**

All hardware is available for the Module A build, if the initial hardware were used for Module A in lieu of the gas bearing simulator.

### **MODULE B**

One shaft is required; the work on three shafts was stopped in process. The shaft center sections have been balanced, and one journal end has been welded to each shaft. Work remaining includes welding the other journal end to the shaft, nitriding, final machining and grinding, and final balancing. The estimated stage of completion is 50 percent.

The third- and fourth-stage scroll housings have been cast and have satisfactorily passed receipt inspection. No machining has been performed. The estimated stage of completion is 25 percent.

Four more journal bearing pads are required for Module B; work on 11 pads was stopped in process. The journal surfaces have been flame-sprayed with tungsten carbide. Final grinding and lapping was not begun. The estimated stage of completion is 75 percent.

One more solid bearing stem is required for Module B; work on three was stopped in process. These three stems were found to have soft tips on the balls, caused by defective nitriding. The nitriding must be stripped, and the parts must be replated and then reground and polished. The estimated stage of completion is 25 percent.

Two thrust bearings are required for Module B; work on three was stopped in process. Plating is complete, and lapping and grinding of the pockets was not begun. The estimated stage of completion is 50 percent.

The core of the stator has been manufactured, but no windings have been made. The estimated stage of completion is 25 percent.

### GAS BEARING SIMULATOR

All of the hardware for the gas bearing simulator is complete, with the exception of several assembly tools. The intent was to use Module B parts, where possible, for this test assembly. In the case of the bearing pads and stators, the first completed set was to be used for the gas bearing simulator, with the next set of parts being used for the Module A build. Upon completion of the gas bearing simulator test, the hardware from this assembly would be used, where possible, to build Module B.

## **Section 3**

### **TURBOALTERNATORS**

#### **FABRICATION**

All of the original design components required for the Module A turboalternator have been completed, and preliminary evaluation tests on the first and second stages were made individually by operating single-stage turboalternator assemblies in the open cycle test station.

The only parts not manufactured for the Module B turboalternator are the turbine wheels and nozzles for the third and fourth stages.

Some additional redesigned or modified parts were also manufactured to improve problem areas in manufacturing and difficulties encountered in the operation of the turboalternator assemblies.

The status of turboalternator parts that were being manufactured are described in the following paragraphs.

#### **SHAFTS**

Five new shafts were in process during this reporting period. One of the five shafts being machined in preparation for copper plating, prior to nitriding, separated at the braze joint between the magnet and the stainless steel. The brazed joints on all five shafts were inspected and subjected to a 120-pound axial load pull test when they were received from the Hamilton Watch Company. The brazed joints appeared to be sound. However, examination of the separated joint showed little evidence of any braze material present, indicating that machining the shaft diameter to size must have removed all of the brazing material that was initially present on the outer diameter.

Other methods of testing the shaft-to-magnet brazed joints were explored to ensure that the remaining shafts have satisfactory brazed joints.

Three old, obsolete turboalternator shafts, of 0.261-inch diameter, made of the same materials and with nitride-hardened cases, were subjected to bend tests. The shafts were placed on a fixture with the magnets centered between two cradle supports, spaced 1.125 inches apart. Bending loads were applied to the top of the shafts at the center of the magnets by an Instron Tensile Testing Machine from which the loading could be applied in a pulling or pushing direction. The rate of the loading applied to the shafts by the Instron Machine could be controlled to very slow speeds, and the loads applied were measured by a calibrated pressure transducer and recorded on a strip chart



recorder. Deflection of each shaft was measured in microinches by a Federal Products Corporation electronic indicator as loads were applied.

The objectives of the tests were to:

- Determine the elastic limit of the materials in the shafts.
- Establish uniformity of the brazed joints in the three samples.
- Examine the condition of the brazed joints in the test shafts.

Each of the three shafts was individually loaded in four positions, 90 degrees apart, for detection of any variations in the brazed joints around the circumference of the shafts. Loads were applied gradually, up to maximums of 20, 40, 100, 140, and 200 pounds. During loading, the linearity of the deflections was examined. After a maximum load was reached, the load was removed, and the shaft deflection was measured to ensure that the initial zero position repeated. Measured runout of the shafts was also tested after each loading by rotating the shafts, supported on small V-blocks, with a 0.0001-inch indicator to measure any variation in the shaft at the center of the magnet.

All three samples tested satisfactorily up to the 200-pound loading. The deflections on each shaft agreed very closely in all four positions, and there were no indications of permanent deformation. The deflection at 200 pounds was 0.0012 inch.

One sample was then loaded slowly to 275 pounds, in one position. The chart recording the load showed a variation in the rate of loading near 250 pounds, indicating a yield point had been reached, and the initial zero load deflection did not repeat when the load was removed. This was also confirmed by measuring a 0.0004-inch runout at the center of the magnet.

The same shaft was then subjected to a breaking test, in an effort to expose one of the brazed magnet joints to determine the quality of the braze. A more heavily constructed fixture was designed to maintain the 1.125-inch spacing, and the load was applied at a rate of 0.002 in./min until the breaking point was reached at 912 pounds. The break was uniform at one of the brazed magnet joints. Examination of the broken joint showed a uniform brazed area approximately 1/32 inch wide around the outer circumference and deterioration toward the 0.1254-inch-diameter magnet pilot in the center of the shaft. There was an unbrazed, oxidized area approximately 1/64 inch square near the pilot hole, and there was no braze on the pilot portion of the assembly. The broken magnet pilot was loose in the stainless steel section of the shaft. However, this brazed joint withstood much greater bending forces than a turboalternator shaft would ever be subjected to in actual use. Therefore, tests on the other two sample shafts were not continued, because they appeared to be nearly as strong as or stronger than the broken shaft.

The four new turboalternator shafts were then machined to a diameter 0.010 inch oversize, to remove the major part of the material from the outer diameter and still allow removal of material to clean any dents that might be incurred in the soft material during the bend tests prior to nitriding. Each shaft was then subjected to the bending tests described above, with a maximum loading of 130 pounds in four positions 90 degrees apart. All four shafts successfully passed the bend tests and have been processed through nitriding.

The bend tests were to be repeated after nitriding to ensure that the brazed joints were not damaged during the nitriding process.

### FIRST-STAGE ALUMINUM TURBINE WHEEL

Inspection of the first-stage aluminum turbine wheel used in several turboalternator assemblies has indicated slight galling and possible out-of-roundness of the wheel bore after many wheel-to-shaft assemblies. The air gage used to measure the bore diameter indicates the required minimum interference fit of 0.0003 inch; however, the air gage gives an average measurement and does not measure out-of-roundness. Therefore, the actual surface contact may be less than indicated by the measurements, and the holding force may not be sufficient to maintain the wheel position on the shaft at lower temperatures. An order was placed with the Andrews Engineering Company to machine a new first-stage, aluminum turbine wheel.

The new first-stage aluminum turbine wheel from the Andrews Engineering Company has been received and inspected. The wheel dimensions and the blade geometry were measured and found to be within the drawing specifications. The turbine wheel was then deburred, principally at the blade trailing edges, and the chemical protective coating and the lubricative plating were applied to the bore. This wheel is now available to replace the existing first-stage turbine wheel.

### JOURNAL BEARING PADS

Because problems have been encountered in the operation of turboalternators using journal bearings with spherical pivot sockets, two experimental pieces were made to determine the feasibility of grinding flat surfaces at the bottom of the 0.078-inch-diameter pivot hole. Both pieces proved satisfactory. Special grinding techniques were established to produce satisfactory methods for grinding and polishing the flat-bottom and cylindrical walls of the pivot sockets.

A lot of 30 tilting pads of the new flat bottom pivot socket design (Figure 51) were machined for nitriding.

Three sample pads were sent for nitriding, to evaluate the hardness of the pivot holes. All three pads meet hardness specifications. Dye tests

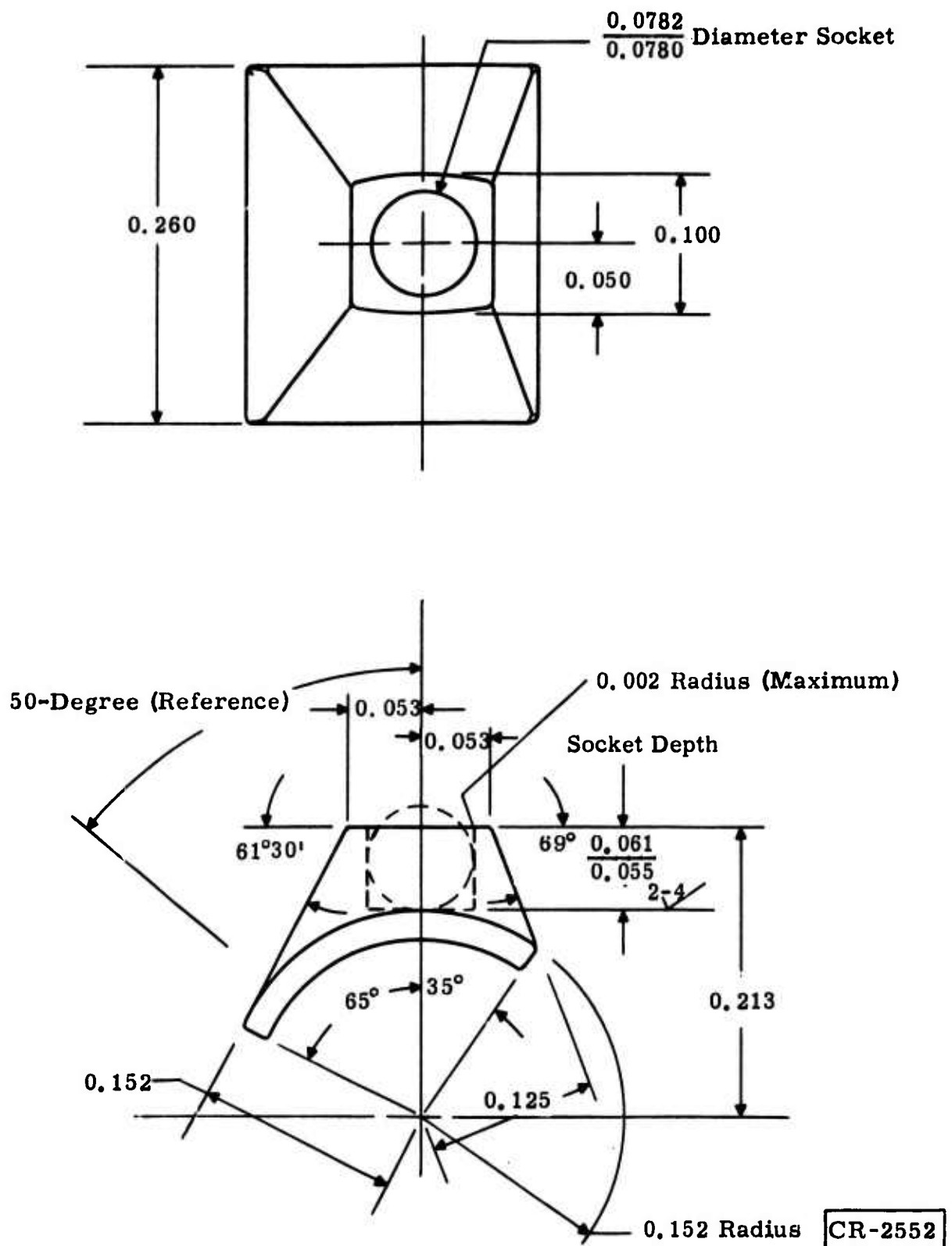


Figure 51. Modified Tilting Pad Journal Bearing (All Dimensions in Inches)

were also made on the critical surfaces of the pads, revealing no indication of cracking. Then 15 of the 30 bearings were nitrided. Inspection of the nitrided pads showed that cracks had developed at the corners. Further inspection showed the nitrided case depth was 4 mils thick, which is thicker than specified and undoubtedly contributed to this cracking at the corners. To remove the corner cracks, the outer edges of all 15 of these journal bearing pads were ground to remove 0.006 inch of material from each of the four edges.

The journal bearing surfaces were then rough-lapped prior to final polishing. During the lapping operation, it was noted that the radius of the journal surface had increased more than expected after nitriding. This effect is normally a function of the nitrided case depth; it was believed that there was a sufficient case depth to correct the radius within the drawing specifications without breaking through the case. The journal bearings appeared to be satisfactory after rough lapping, but inspection of the journal surfaces after polishing showed that the case had been broken through on eight of the pads and they had to be rejected.

The pivot holes in the remaining seven journal bearing pads were ground and lapped. During the grinding and lapping process, it was observed that there are minute cracks on the surface of the pivot socket flat. Attempts were made to dislodge the nitride case, but it could not be chipped off. Nevertheless, these cracks represent a potential contamination hazard in a very sensitive area near the pivot ball in addition to the general particulate contamination problem.

The vendor, Owego Heat Treat Company, had been contacted several times, and engineers there believed the case depth could be controlled. However, when the above lot of 15 journal bearing pads were nitrided, with specification to provide a uniform case depth of 0.0025 to 0.0030 inch, the pads were received with case depths over 0.004 inch on the journal surfaces but considerably less in most of the pivot sockets. Corporate Research and Development manufacturing was unable to salvage six usable journal bearing pads out of the 15 for a turboalternator assembly.

One of Corporate Research and Development's manufacturing engineers visited the nitriding vendor to discuss the problems experienced with the above nitrided journal bearing pads and arrive at a solution. One pad was left to be processed, as a sample to prove that a uniform case and exact depth could be obtained. When the pad was received, the journal surface was satisfactory, but the pivot hole was soft on the bottom.

In view of the above difficulties, with nitrided stainless steel pads, alternate bearing pad materials were considered that would provide the hardness without a separate coating or plating process. A promising candidate is Kintanium -- a sintered powdered metal consisting of titanium carbide as the principal ingredient and nickel and nickel-molybdenum as the binder materials.

Since Kentanium has a lower coefficient of thermal expansion, the machined-in clearance will be larger at low temperatures in comparison to stainless steel pads, because the pad radius will not shrink as much. This is the proper direction for increased stability and increased load capability for the low viscosity to be experienced at low temperatures, because the non-dimensional film thickness is decreased for the same actual pivot film thickness. With this trend, and with the load capability increase, a slight increase in bearing friction will be experienced.

Three samples of Kentanium recommended for use at extreme temperatures were obtained: grades K-151A, K-162B, and K-165. The hardness of these materials ranges from 90.0 to 93.5 Rockwell A.

Test samples of each grade were prepared for cryogenic testing by grinding a V-notch across one surface and shocking the materials by quenching repeatedly in liquid nitrogen from room temperature. No fractures or cracks were visible upon examination of the samples under a 60-power microscope.

Friction and wear tests were also made on the Kentanium samples and on a sample of nitrided 316 stainless steel in a Dow Corning testing machine. The samples were all in the form of blocks measuring  $3/8 \times 5/8 \times 0.212$  inch with one face  $5/8$  inch  $\times$   $0.212$  inch polished to a No. 2 finish, representative of the bearing surface of a finished tilting pad bearing. The samples were all tested under the same conditions, riding against a rotating ring of 316 stainless steel  $1-3/8$  inches in diameter, nitrided and ground on the outside diameter to a 2-rms finish, representative of the journal surface on a finished shaft.

Each material sample was tested against its own individual nitrided ring under clean conditions. All tests were run dry. Each test block was held against the ring, producing a line contact by a holder designed to equalize the pressure across the contact surface. The applied load ranged from a minimum of 2 pounds to a maximum of 10 pounds. The speed of the rotating ring could be varied from 0 to 1300 rpm. Tests were made at 500 and 1300 rpm. The testing machine is not designed for light load conditions. The friction force is measured through a transducer and recorded on a Hewlett-Packard recorder calibrated for this application. The unit force is measured in pounds. Therefore, the dynamic coefficient of friction can be calculated:

$$\frac{\text{Friction load (pounds)}}{\text{Applied load (pounds)}} = \text{Dynamic coefficient of friction}$$

Surface speed (ft/min) can be calculated:

$$N_s = \frac{(\text{rpm}) (\pi) (D \text{ inches})}{12} = D = \text{test-ring diameter}$$

$$N_s = \frac{(1300) (\pi) (1.38)}{12} = 470 \text{ (ft/min)}$$

The equivalent turboalternator shaft speed is 6873 rpm.

The dynamic coefficient of friction calculated from testing is:

Speed (rpm)	Load (pounds)	Dynamic Coefficient of Friction			
		Nitrided 316 Stainless Steel	Kentanium		
			K-165	K-151A	K-162B
500	10	1.2	0.8	1.2	0.75
1300	10	1.2	0.55	0.5	1.0

In summary:

- The nitrided stainless steel scored first under the light load conditions.
- The nitrided stainless steel eroded away more material than any of the other materials.
- Kentanium K-165 showed only a shiny wear line at the contact, with little debris compared to the K-151A and K-162B samples.

Based on the above test results, an order was placed for 15 Kentanium K-165 journal bearing pads, to be sintered in molds of appropriate dimensions to reduce the total amount of machining and provide sufficient material to finish machine the pads within drawing specifications. Dimensional inspection of the pads received showed the dimensions to be greater than anticipated. This could be corrected in the future, however, if the pads prove to be satisfactory.

Machining of the 15 Kentanium K-165 journal bearing pads of the flat-bottom pivot socket design has been completed. Three of the 15 pads cracked during machining, leaving 12 usable pads. The first set of six journal bearing pads has been completed, with the journals and pivot sockets finish-lapped.

#### JOURNAL BEARING SPRING STEMS (DOUBLE-SPRING DESIGN)

The spring thickness on the weaker spring of two journal bearing double-spring stems was adjusted to approximately 0.008 inch. This adjustment produced spring constants of 280 lb/in.,  $\pm 5$  percent, well within design specifications.

To complete the stems, a 0.001-inch slot must be machined in the second stiffer spring stop, to limit the spring travel. The second spring would have to be calibrated and adjusted as required to meet the design specification spring constant of 800 to 1050 lb/in.

#### JOURNAL BEARING PIVOT STEMS

Sixteen bearing stems with the 0.077-inch-diameter pivot balls developed spalling during the final grinding operation on the stems. Because spalling of

the nitrided case on the stems could generate particulate contamination in the turboalternators, the bearing stems have been rejected. A new set of 16 bearing stems was started in manufacturing. The new stems were dimensioned to allow removal of the nitrided case on the stems, in order to eliminate this problem.

Fifteen tungsten carbide balls, 0.077 inch in diameter, were purchased and copper-brazed to 304L stainless steel stems. The excess braze was removed from the balls, and the stems were ground concentric to the ball end. This new design of journal bearing pivot stems will be used with the above Kentanium journal bearing pads. Six stems were completed. Two of the completed stems were modified and assembled in two of the journal bearing single-spring stems.

#### THRUST BEARING GIMBAL PIVOTS

The present design of the thrust bearing gimbals use pivot balls 0.013 inch smaller than the mating socket diameter. Slight variations in the relative position of the thrust bearings have been noted in the turboalternator assemblies. To reduce the motion of the pivot balls in the socket, eight of the nitrided journal bearing stems with the 0.063-inch-diameter pivot balls were modified for use as thrust bearing pivots. This reduction will reduce the difference in diameter between the pivot ball and socket to 0.005 inch and should make the thrust bearing axial assembly dimensions considerably more stable.

#### WELDABLE LEAD FEEDTHROUGHS

Additional tests have been made on the weldable proximity probe lead feedthroughs received from Microdot, Inc., because the initial assemblies leaked after welding. A single feedthrough was successfully welded into a header plate, using special chill blocks and a minimum current in the electron beam welding machine. Then a header for the open cycle test can, containing five feedthroughs, developed leaks after welding in the  $10^{-8}$  cm<sup>3</sup> He/sec range. The feedthroughs were mass spectrometer leak-tight as received and after cooling to liquid nitrogen temperatures before welding.

Microdot, Inc. was contacted again and quoted on building the complete header plates. The feedthroughs would have been assembled in the machined header plates, and the insulating beads would be fired in the assembly. This method would eliminate welding of the individual feedthroughs. This type of feedthrough was not ordered.

Two feedthroughs to be used for the turboalternator electrical connections and stator thermocouples, purchased from the Borders Electronics Company, failed in leak testing. The Borders Electronics Company was in the process of building a modified design. The order was cancelled.

Twelve similar feedthroughs were purchased from the Hermetic Seal Corporation. Ten feedthroughs were leak-tight as received and after cycling four times to liquid nitrogen temperature. Two feedthroughs leaked as received and were returned to the vendor.

## **TEST AND EVALUATION**

### **TEST OBJECTIVES AND PLANS**

The complete test objectives and test plans have been outlined in the Phase B final technical report (Ref. 2). More detailed test plans and the implementation of both one- and two-stage test plans are described below. Also, the data required of the single-stage tests are identified; these data are required to interpret some of the subsequent two-stage performance operation and test evaluation procedures.

#### **Open-Cycle, Single-Stage Turboalternator Test Plans**

The turboalternators would be tested at various levels of assembled completion, at temperatures and pressures different from room temperature ambient, and at 1-atmosphere exhaust conditions, up to temperatures and pressures approaching the individual turbine stage design conditions.

Tests would first be conducted with the individual stages operating with helium and nitrogen gas, at both room and cryogenic temperatures. Single-stage performance test results would be reduced by data reduction program OCTRMT, for room temperature data, and OCTCRT, for cryogenic temperatures, based on the turboalternator instrumentation schematic (Figure 52). Then performance tests, with two stages on a shaft, will be conducted.

Following are the turboalternator test procedures that were planned:

#### **• Nozzle Performance Test**

1. **Nozzle Seal Inspection.** The two sections of the nozzle are assembled with the outer-flange C-seal and with a light coating of high-spot bluing on one of the surfaces of the inner metal-to-metal seal surfaces surrounding the nozzle channels. The outer flange assembly screws, size 4-40, are torqued to 5.5 in. -lb. The nozzle is then disassembled, and the inner metal-to-metal seals are inspected to ensure that uniform contact has been made to provide the required metal-to-metal seal at the nozzle diameter.
2. **Nozzle Flow Test Without Turbine Wheel.** After successfully completing the above inner seal test, the nozzle is cleaned and reassembled with the inlet gas test fixture shown in Figure 52. The inlet gas test fixture provides the means of ducting gas to the nozzle and also provides a pressure tap to measure the gas inlet pressure to the nozzle.



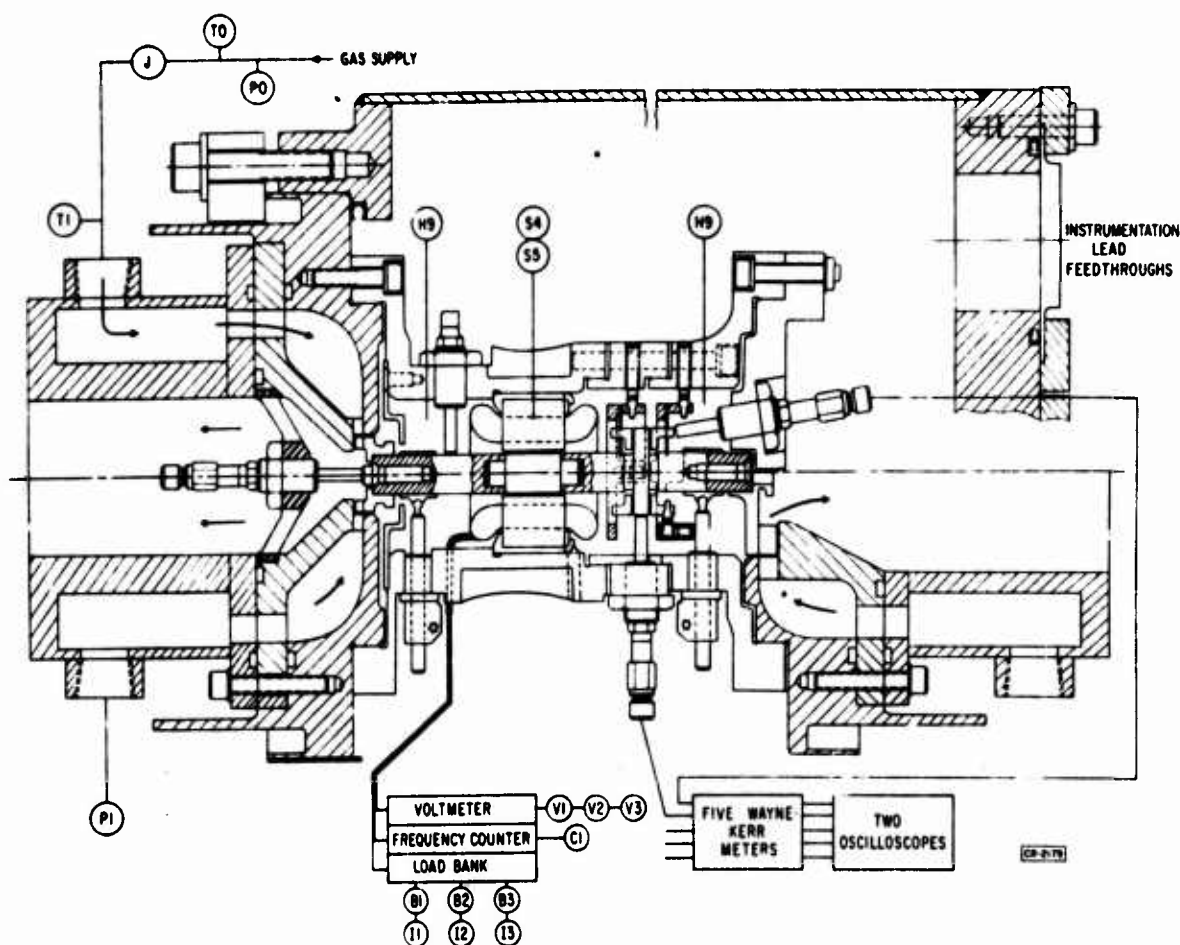


Figure 52. Principal Turboalternator Instrumentation

Gas flow measurements are made over a range of nozzle pressure ratios for both helium and nitrogen gas at room temperature.

3. **Housing Leak Rate Test.** After the assembly of a single-stage turboalternator has been completed, with the correct shimming to provide the specified clearances and with all the housing proximity probes installed, a housing pressure tap is installed in the housing adjacent to the stage under test. The housing pressure tap at the opposite end is temporarily sealed with a gasket under the head of a screw.

The turboalternator shaft is kept from rotating by a length of 4-40 threaded rod installed into one end of the shaft and held securely outside the housing. The stage at the opposite end of the housing, the end not being tested, is sealed with a temporary end cover. A silicone rubber sealant is used to make temporary seals between the 4-40 threaded rod and the housing.

As gas is applied to the nozzle inlet gas test fixture, the turbine wheel is kept from rotating, and the gas flows across the turbine

wheel. Some flow leaks from the nozzle exhaust through to the housing leakage paths.

By installing a rubber stopper into the exhaust of the nozzle gas test fixture and clamping it in place, the gas flow is directed through the housing leakage paths. Therefore, the housing leak rate can be determined by measuring the gas flow, which is related to the housing pressure. Both helium and nitrogen gas at room temperature are used for these calibration tests.

4. Nozzle Flow Test with Turbine Wheel. Removing the above rubber stopper from the gas test fixture exhaust allows the gas to flow both through the nozzle exhaust and to the housing. Measuring the total gas flow, nozzle inlet pressure, and housing pressure, the housing leak rate can be determined from the housing pressure, as obtained in the above tests, and the leakage gas flow around the turbine wheel out the exhaust can be calculated versus the nozzle inlet pressure.

The results of the nozzle performance tests would be used for possible future nozzle channel modifications if the flow rates were not as required to meet design conditions, and the data would also be used to determine performance evaluation of the individual stages.

After completion of the above tests, the shaft holding fixtures would be removed and the shaft would be magnetized.

- Open-Cycle Single-Stage Tests. These tests provide both functional assurance and initial overall performance test results.

1. Warm Tests. With the shaft magnetized, the turboalternator is tested at various resistance loads at design speed and at speeds above and below design speed. Tests are conducted at room temperature with helium and nitrogen gas. Because the rotating speed is limited, the velocity ratio with helium gas is low. With nitrogen gas, a wider range of velocity ratios can be obtained.
2. Test with Sealed Housing. After the above tests have been completed, the turboalternator housing will be installed into a sealed housing with feedthroughs for the electrical proximity probe, and pressure measurements. The turbine exhaust gas will still expand to atmosphere.

With this assembly, performance measurements will be obtained and the effective average nozzle pressure will be measured in conjunction with other performance factors. This effective average nozzle pressure is the pressure in the sealed housing. However, the axial thrust from pressure differences may be a problem for large-diameter turbine wheels. The three pressure ratios obtained from combinations of the inlet, nozzle, and exit pressures will vary with the velocity ratio in a characteristic manner, suitable for comparison with similar characteristics of other turbine stages.

3. Cryogenic Liquid Nitrogen Test. The above warm temperature test procedures are repeated by precooling the gas supplied to the turboalternator with a liquid nitrogen heat exchanger. Tests are performed at temperatures approaching liquid nitrogen temperatures, as required to obtain additional performance data for future application to two-stage turbine tests.

### Closed-Cycle, Two-Stage Turboalternator Test Plans

Detailed plans have been formulated for tests to evaluate functional and performance characteristics of both of the two-stage turboalternator modules, prior to complete cryosection system testing.

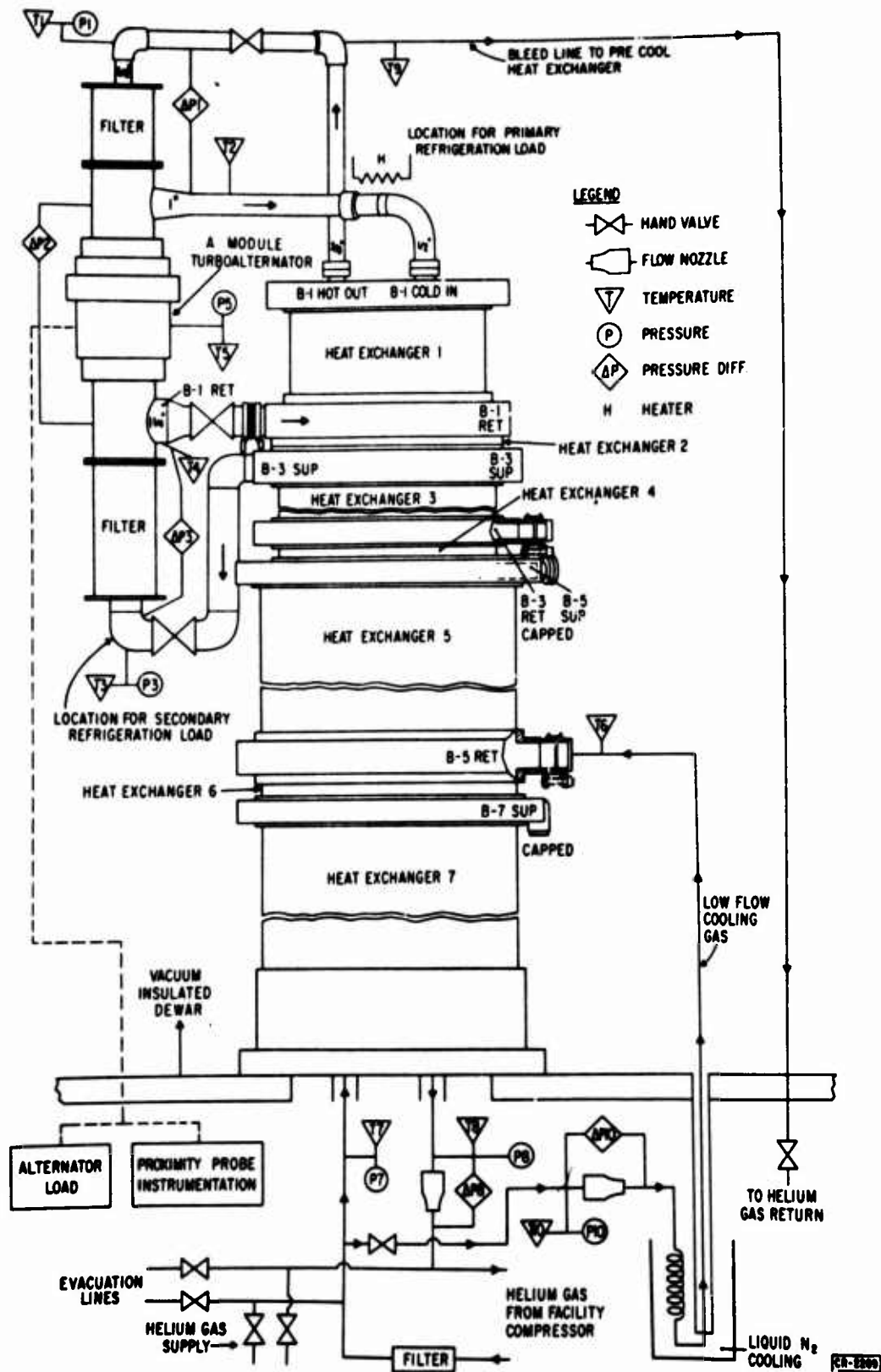
The General Electric facility compressor can operate at an inlet pressure slightly above atmospheric pressure. Any pressure below atmospheric pressure would result in air leakage into the compressor and hence to the cryogenic heat exchanger. Hence no component tests are planned at the low design ambient pressure of the turboalternators, which is approximately 5 psia. The first low-ambient-pressure tests planned for the turboalternators will be made with the complete cryosection assembled.

Room temperature tests could be conducted on the gas bearings at low ambient pressure with an enclosure and suction blowers; however, at this stage in the development cycle, these types of tests are considered unwarranted.

The closed cycle test station would be used to test turboalternator modules with two turbine stages per module. A schematic diagram of the station for testing the Module A turboalternator, which includes the two lowest temperature stages, is shown in Figure 53. Tests would be conducted toward 12.46° and 59.49°K turbine inlet temperatures of the first and second stages, respectively. Tests would be conducted with the cryosection installed in a vacuum dewar. Helium gas would be supplied to the closed test loop by the facility compressor.

Complete instrumentation would be incorporated to measure turboalternator speed, gas flow rate, pressures, temperatures, and gas bearing and rotor dynamic characteristics. Noninductive load banks would be used to load the turboalternator, and the electrical power output would be measured.

The cryogenic heat exchanger would be mounted in a vertical position above a header plate, as shown in Figure 53. The Module A turboalternator would be connected to the heat exchanger in a manner similar to the connection in the final refrigerator system, except manual valves would be installed in the first- and second-stage supply lines and in the second-stage return line. Valves with extended stems would be used to control the gas flow to the turbine stages and to balance the turboalternator nozzle exit pressures, to eliminate gas flow through the housing during operation of the turboalternator.



The piping between the heat exchanger and the valves would be the actual lines to be used in the final cryosection assembly and would contain sections with bellows to compensate for thermal contraction during cooling. Bellows would be installed in the first- and second-stage gas supply lines to the turbines and in the first-stage return line. Flanges are provided to remove the valves before final cryosection assembly.

When the system is completely assembled and leak-tested, the closed loop station would be valved off from the facility compressor and would be evacuated and charged with a clean, dry source of helium gas, to a pressure of 2 psig.

To operate the Module A turboalternator at temperatures on the order of 20°K, the higher temperature sections of the heat exchanger must be cooled to near liquid nitrogen temperature, 77°K. This cooling would be accomplished by sealing off the heat exchanger connections normally used for the Module B turbolator, except for the B-5 return connection. A low flow of helium gas would be cooled to near liquid nitrogen temperature by a cooling coil immersed in liquid nitrogen. The line to the heat exchanger would be thermally isolated by the dewar vacuum. The cold helium gas would flow through Heat Exchangers 6 and 7, cooling the sections.

Before operating the turboalternator, the valves in the lines between the heat exchanger and the turboalternator would be closed. Then the valve in the bleed line, connected to the first-stage turbine inlet, would be opened, allowing the helium gas to flow through the complete heat exchanger and cooling all sections. The temperature of the gas coming out of the heat exchanger would be measured to determine when the heat exchanger has been completely cooled.

The above method of precooling the heat exchanger before starting the turboalternator will improve the operating conditions for the turbines, because any volatile materials that may be present in the helium gas from the system will be collected in the heat exchanger.

After the heat exchanger has been cooled, the helium gas flowing through the heat exchanger would be momentarily turned off, the valve in the bleed line would be closed, and the turboalternator valves would be opened. Then, as helium gas is circulated through the system, the turboalternator would begin operating. The valves in the turboalternator gas lines would be adjusted to correct the pressure differentials between the turbine stages, if necessary. A low flow of the helium cooling gas would continue to circulate through Heat Exchangers 6 and 7, to maintain temperatures near 77°K, simulating the operation of the Module B turboalternator in the final refrigerator system.

As the Module A turboalternator is operated, the system would be cooled to a minimum temperature below the 77°K starting temperature.

Adjustment of the two exit valves and one inlet valve to the two turbine stages would be the mechanism used to prevent interstage leakage. Table 3

Table 3  
MODULE A DESIGN POINT PERFORMANCE CONDITIONS

Characteristic	Stage 1	Stage 2
Inlet temperature ( $^{\circ}\text{R}$ )	22.40	107.1
Inlet temperature ( $^{\circ}\text{K}$ )	12.46	59.49
Inlet pressure (psia)	9.111	9.156
Outlet pressure (psia)	5.384	5.305
Pressure ratio	1.692	1.726
Speed (rpm)	80,000	80,000
Flow (lb/hr)	6.156	12.89
Velocity ratio	0.3400	0.3365
Flow factor	1.570	7.152
Corrected speed (rpm/ $\sqrt{^{\circ}\text{R}}$ )	16,930	7,740
Difference in inlet		
Pressure	0.045 psia	
In. of $\text{H}_2\text{O}$	1.25	
Difference in exit		
Pressure	0.079 psia	
In. of $\text{H}_2\text{O}$	2.20	

CR-2239

shows the principal design stage points of the first two stages (note the very low design pressure differences between the stages, based on the cycle design). The actual cryogenic heat exchanger pressure drop characteristics will also affect the potential interstage turbine leakage problem. The instrumentation shown would be used to determine the adjustments required. The instrumentation would provide, either directly or indirectly, the basis for determining performance parameters, as follows:

- Inlet temperature
- Inlet pressure
- Nozzle pressure
- Exit pressure
- Exit pressure difference, between stages
- Rotational speed
- Electrical power output
- Alternator stator temperature

From these, the following performance parameters would be determined:

- Overall pressure ratio
- Inlet-to-nozzle pressure ratio
- Nozzle-to-exit pressure ratio
- Mass flow
- Overall efficiency
- Flow factor
- Velocity ratio
- Temperature drop
- Electromagnetic efficiency
- Corrected torque
- Corrected speed
- Power to each stage

The last item may be difficult to obtain uniquely, because it would have to be obtained principally from performance data obtained from single-stage, open cycle test results at room and liquid nitrogen temperatures. The performance data needed include:

- Flow factor and overall efficiency versus velocity ratio, at constant overall pressure ratios
- Flow factor versus pressure ratio, at constant values of corrected speed
- All three pressure ratios incorporating inlet, nozzle, and exit pressures versus velocity ratio
- Bearing settings to directly calculate the approximate bearing power losses, and the gas friction losses, along the shaft

A special data reduction and analysis computer program would have been prepared to accomplish the above performance evaluation.

The Module B turboalternator would be tested in a manner similar to testing of Module A, down to the target design temperatures of 100.0° and 190.0°K for the third and fourth stages, respectively.

Figure 54 is a schematic diagram of the system for testing Module B. The heat exchanger connections previously used for Module A are sealed. Because the heat exchanger will not be precooled in this test, the low-flowing cooling gas and the bleed lines are valved off and disconnected from the heat exchanger. Charcoal filters would have been installed in the gas supply lines to the turbines.

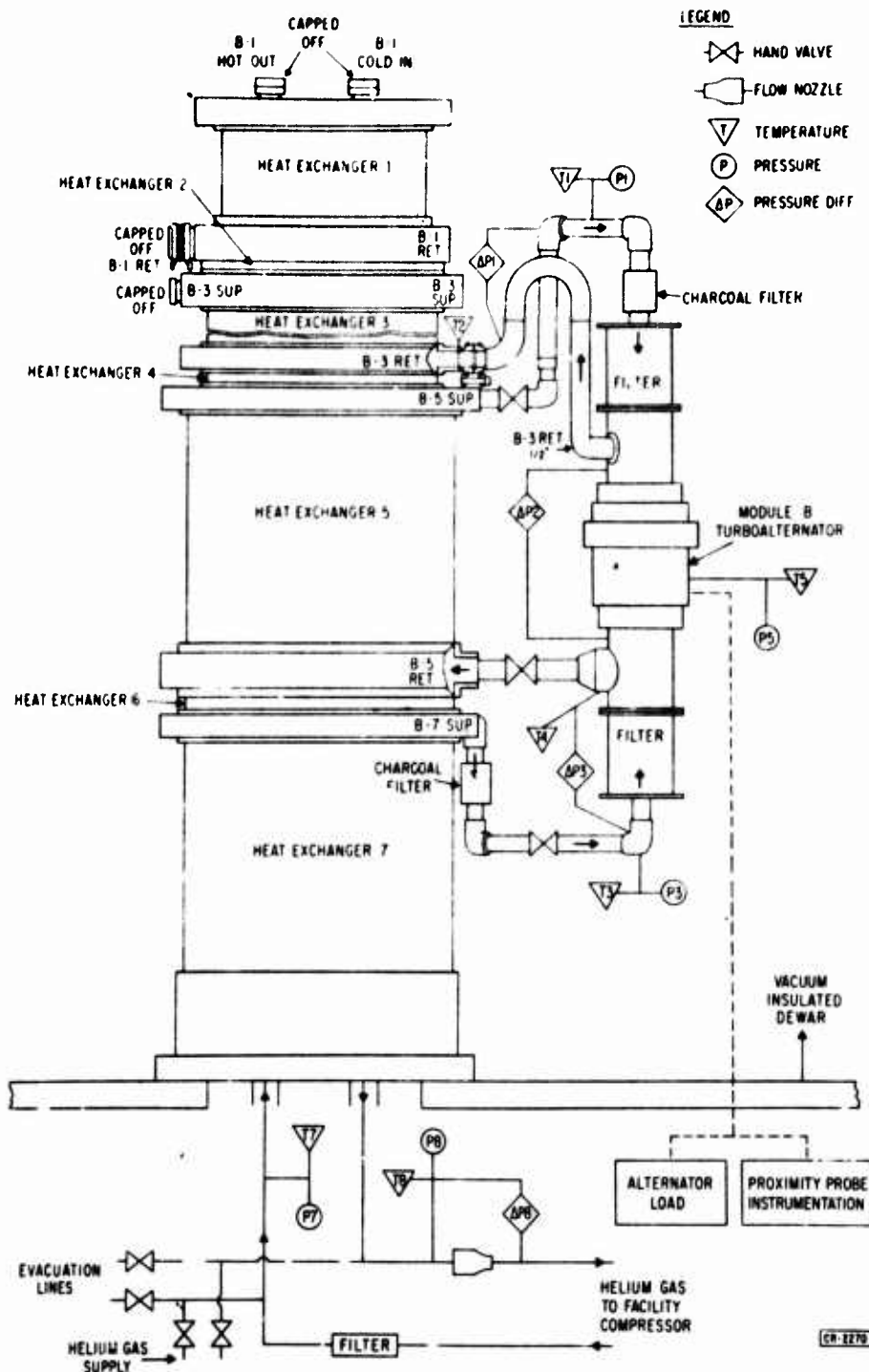


Figure 54. Closed Cycle Turboalternator Test Station for Module B

Manual valves would also be installed in the first- and second-stage gas supply lines and in the second-stage return line, to control the gas flow to the turbine stages and to balance the nozzle exit pressures to eliminate gas flow through the housing during operation of the turboalternator.



The piping used to connect the Module B turboalternator to the heat exchanger would be very similar to the piping described above for Module A. Bellows would be installed in the first- and second-stage gas supply lines to the turbines and in the first-stage return line, to compensate for thermal contraction. Flanges are provided to remove the valve sections before final cryosection assembly.

After the system is assembled and leak-tight, the closed-loop station is valved off from the facility compressor and is evacuated and charged with a clean, dry source of helium gas to a pressure of 2 psig.

Then, as helium gas is circulated through the system from the facility compressor, the turboalternator would start operating. The valves in the turboalternator gas lines would be adjusted to correct the pressure differentials between the turbine stages, if necessary.

As the turboalternator operates, the system would cool to a minimum temperature, depending on the given load conditions. Data would be recorded with the turboalternator operating under various load conditions.

### FUNCTIONAL TESTS

During this reporting period, preliminary shakedown tests were made on five turboalternator assemblies, as outlined below.

#### Turboalternator Build 6

Build 6 consisted of the first-stage, 0.5-inch-diameter, aluminum turbine wheel and nozzle. The electroless, nickel-plated, tilting pad bearings of the flat-bottom pivot design described in the Phase II final report (Ref. 2) were used for the first time. A 910-lb/in.,  $\pm 3$ -percent, spring stem was installed in each of the journal bearing assemblies. The journal bearing radial clearances were adjusted to 250 microinches by adjusting the spring stems; after initially setting the journal bearings to a gage shaft, which is 400 microinches larger in diameter than the turboalternator shaft. The thrust bearings were shimmed to give the shaft a total axial travel of 0.0008 inch and a wheel-to-nozzle clearance of 0.0015 to 0.0025 inch, axially.

The turboalternator seemed to operate satisfactorily. Tests were made at speeds up to 120,000 rpm. The proximity probe signals indicated stable operation. The shaft orbit probe signals produced relatively small orbits of 120 microinches at the first-stage end of the shaft and 80 microinches at the second-stage end. The thrust proximity probe viewing the end of the shaft, monitoring the axial motion, had a once-per-revolution ripple of less than 10 microinches, representing a very stable thrust bearing operation.

Flow tests were made on this assembly, to confirm earlier data pertaining to the relationships between the nozzle pressure, housing pressure, housing leak rate with the nozzle sealed, and the total nozzle gas flow with the nozzle open and the turbine wheel in position but not turning. Flow measure-

ments were made with both helium and nitrogen gas at room temperature. The data obtained agreed very closely with that obtained from the earlier tests. Several additional data points were taken to extend the ranges of flow and pressures.

After the flow measurements were completed, the shaft holding fixture was removed and the turboalternator was retested. The journal bearing clearances remained the same. The thrust bearing clearance increased 0.0003 inch. Shims for the thrust bearings were readjusted to allow the shaft 0.0008-inch total axial travel. The turboalternator was then operated satisfactorily again, as in the original test.

Because the turboalternator was initially assembled with the shaft permanent magnet unmagnetized, the unit was disassembled to remove the shaft and magnetize the magnet. As the shaft was removed from the assembly, discoloration was noted at the first-stage journal bearing area. The turboalternator was then completely disassembled, and the parts were carefully examined under a microscope. Inspection of the parts showed adverse wear conditions, after an estimated 12 to 15 stop-starts of this turboalternator assembly.

No indications of wear or discoloration were evident on the shaft or journal bearing surfaces at the second-stage end of the assembly.

The first-stage journal bearing area of the shaft was discolored at the outer extremes for approximately 180 degrees around the circumference. Figure 55 shows the shaft with a mirror located below it, to show the difference around the circumference. There were no other indications of wear or material buildup on the nitrided shaft at either journal surface.

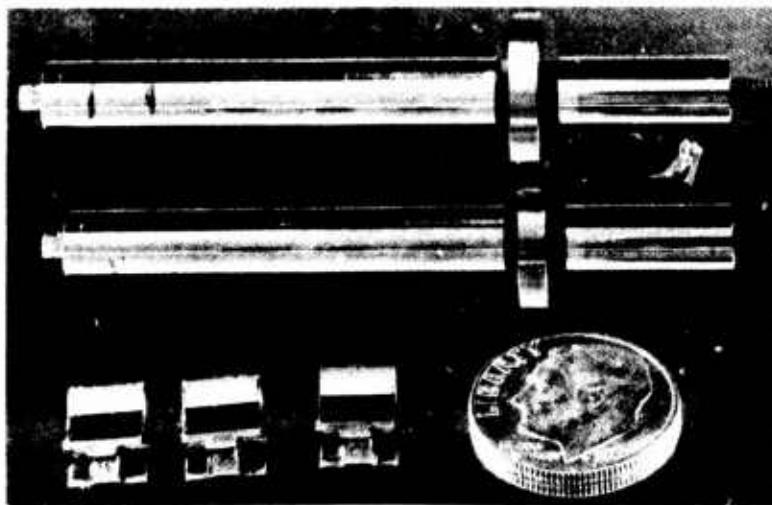


Figure 55. Turboalternator Shaft and First-Stage Journal Bearings from Build 6 (Photographed Above Mirror to Show Discoloration of First-Stage Journal Bearing Surface)

Figure 55 also shows the journal bearing pads from the first-stage end. The journal bearing pad at the left was supported by the spring stem, and only a slight indication of discoloration was noted at the upper right leading edge of the journal surface. The other two bearings shown in Figure 55 were supported by the solid pivot stems in the first-stage journal bearing assembly. Considerable discoloration was noted at the outer edges of the two journal surfaces. The discoloration was approximately 0.013-inch wide along the outer edges, starting at the leading edge of the pad and continuing to near the center of the bearing surfaces. Slight indications of wear were also noted in the discolored areas.

Figure 56 shows another view of the three journal bearing pads from the first-stage end. The pad on the left was supported by the spring stem, and the pad on the right was supported by the solid stem. The pad in the center of Figure 56 was positioned to show the dent formed at the bottom of the previously flat-bottomed pivot socket. This pad was also supported by a solid stem. The dent was approximately 0.0002 inch deep. Slight roughness in the dent also indicated wear. The condition of all six journal bearing pad pivot sockets varied from the large dent shown in Figure 56 to very faint indentations; however, the bottom of all pivot sockets definitely showed signs of wear, to some degree, by the roughness of the previously flat surfaces, and there were signs of particles being generated.



Figure 56. Closeup of Journal Bearing Pads from First-Stage End of Turboalternator Assembly, Build 6

No indications of wear were evident on any of the nitrided pivot balls. The discoloration on the shaft and journal bearing pads was probably caused by a heating effect due to the pads not riding smoothly, in the pivots, as wear occurred.

A spare, unused, electroless nickel pad was tested by applying the normal pressure required on the pivot stem to preset the journal bearing pad against the gage shaft during assembly. The results of this test definitely

indicated that the dents at the bottom of the pivot sockets could have been formed during assembly. Earlier tests on samples of electroless nickel plating showed the hardness to be in the order of 70 Rockwell C. Perhaps increasing the thickness of the plating would prevent denting at the bottom of the sockets. Tests made on one of the pads indicated a 0.0017-inch-thick plating on the bottom of the pivot socket and 0.0022- to 0.0026-inch-thick plating on the journal surface after lapping. However, because the wear characteristics of electroless nickel appear relatively poor, based on the short operating period and few stop-starts of this assembly, further tests with electroless nickel-plated pads are not planned.

#### Turboalternator Build 7

This assembly consisted of the 0.5-inch-diameter, first-stage, aluminum turbine wheel and the conforming journal bearing pivot design with the journal bearing pivot balls machined 2 percent smaller than the pad socket diameter. Test data were obtained at room temperature, with the turbine operating in a vertical position at a speed of about 100,000 rpm. Tests were made using both helium and nitrogen gas. Turboalternator loads ranged from no load to approximately 20 watts total. Test data were reduced and plotted, and are discussed below under "Performance Results."

The turboalternator operated very well during these tests. The proximity probe signals observed on the oscilloscopes were very similar to signals shown in Phase II final report (Ref. 2). The shaft orbits were approximately 70 microinches at the first-stage end and 110 microinches at the second-stage end. A once-per-revolution oscillation on the order of 100 microinches was observed by the proximity probe viewing a journal bearing pad at the second-stage end of the assembly. The proximity probes viewing the axial motion of the shaft and the motion of the outer thrust bearing also showed a once-per-revolution oscillation of approximately 60 microinches.

The only variation noted in the operation of the turboalternator was that the shaft moved closer to the outer thrust bearing as the load was increased on the alternator. The shaft did not appear to touch the outer thrust at the maximum load tested. This condition was undoubtedly caused by the increased axial force on the turbine as the gas flow was increased to maintain the speed at 100,000 rpm with increased loads. The effects of this axial force on the thrust bearings cannot be fully determined until the turboalternator is tested with both turbine stages operating.

The next series of tests planned for this turboalternator required installation of the turboalternator housing into a sealed housing, with feedthroughs for the electrical connections and with the turbine exhaust gas still expanding to the atmosphere. In this assembly, the performance measurements could be obtained, and the effective average nozzle pressure could be measured in conjunction with other performance factors. The effective average nozzle

pressure would be the pressure in the sealed housing. The three pressure ratios obtained from combinations of the inlet, nozzle, and exit pressures will vary with the velocity ratio in a manner suitable for comparison with similar characteristics of other turbine stages.

Because the feedthroughs received from the vendors have leaked to some degree, tests were made to measure the total leak rate of the sealed housing, in order to determine the accuracy of measuring the housing pressure. The feedthroughs were assembled to the sealed housing with metal C-seals and clamping rings. The total leak rate was measured by pressurizing the housing with helium gas and measuring the pressure decay rate. Results of the leak rate tests are shown in Figure 57. This very low leak rate should not significantly affect the average nozzle pressure measurements.

The turboalternator housing was then assembled into the sealed housing. Several test runs were made by operating the turboalternator in a vertical position, with the nozzle-inlet-to-exhaust-pressure ratios ranging from 1.1 to 1.7. Each test run was made at a specific pressure. Tables 4 and 5 list the test runs made at room temperature with both helium and nitrogen gases. These tables list some of the most pertinent performance data obtained and give the extreme ranges covered in each test run. The limitations of the tests are shown in the last columns.

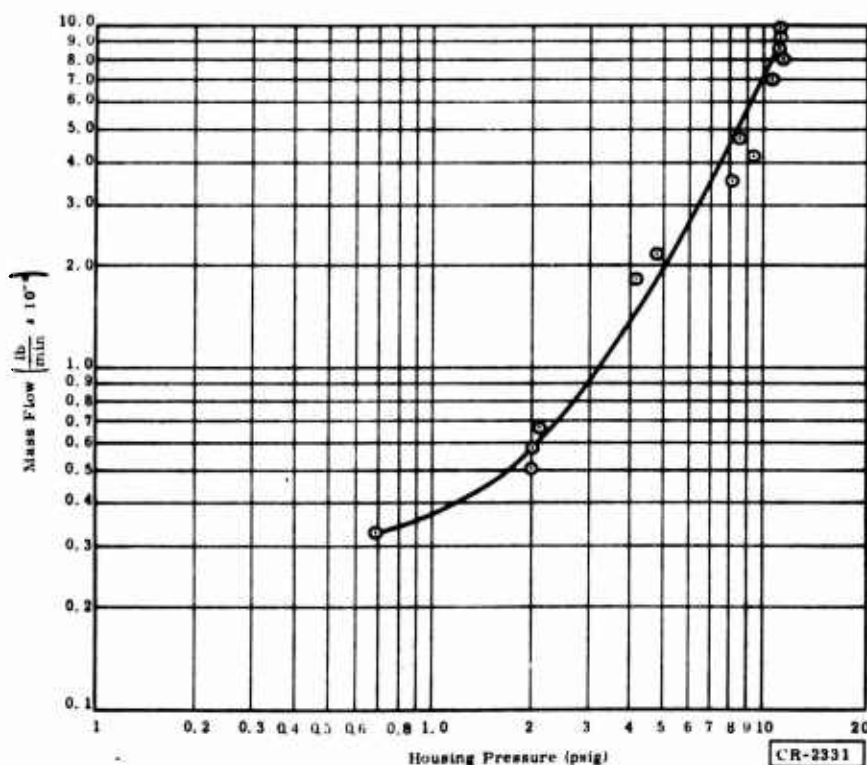


Figure 57. Open Cycle Sealed Housing Leak Rate with Feedthroughs Assembled

Table 4

### SUMMARY OF TURBOALTERNATOR PERFORMANCE RESULTS (Room Temperature with Helium Gas)

Run No.	Number of Data Points	Overall Pressure Ratio	Ambient Pressure (in. hg)	Extreme Ranges of Results						Limitations of Test			
				Electrical Power (watts)	Speed (rpm)	Overall Efficiency (fr)	Corrected Speed (rpm / °R)	Wheel Efficiency (fr)	Velocity Ratio (N.D.)	Corrected Torque (in.-lb/in. hg A)	High Speed	Low Speed	Maximum Electrical Load Available
106	5	1.1	30.169	0.0 0.8670	36,120 109,120	0.0 0.0715	1,557.3 4,715.2	0.0870 0.2428	0.0704 0.2139	0.0 $0.4992 \times 10^3$		X	
109	4	1.2	29.457	2.6107 3.2275	54,960 137,280	0.0908 0.1145	2,369.5 5,918.9	0.1240 0.2905	0.0780 0.1947	$0.4728 \times 10^3$ $0.1133 \times 10^3$	X	X	
111	7	1.3	29.587	3.3415 6.8132	39,300 108,660	0.0753 0.1414	1,908.3 4,699.9	0.0812 0.2135	0.0469 0.1302	$0.1376 \times 10^3$ $0.1865 \times 10^3$	X	X	
112	10	1.4	29.588	4.3092 10.5766	37,380 111,120	0.0606 0.1513	1,610.1 4,788.5	0.0715 0.2049	0.0397 0.1151	$0.1939 \times 10^3$ $0.2350 \times 10^3$	X	X	
113	10	1.5	29.590	6.3504 14.3658	44,040 113,500	0.0656 0.1630	1,898.4 4,896.6	0.0779 0.1928	0.0429 0.1107	$0.2400 \times 10^3$ $0.2756 \times 10^3$	X	X	
114	10	1.6	29.598	8.6904 18.1654	49,980 115,140	0.0713 0.1526	2,195.2 4,964.3	0.0839 0.1893	0.0456 0.1049	$0.2810 \times 10^3$ $0.3114 \times 10^3$	X	X	
115	11	1.7	29.614	10.5558 21.9870	52,020 116,280	0.0718 0.1523	2,241.8 5,014.3	0.0855 0.1881	0.0449 0.1004	$0.3171 \times 10^3$ $0.3426 \times 10^3$	X	X	

Table 5

### SUMMARY OF TURBOALTERNATOR PERFORMANCE RESULTS (Room Temperature with Nitrogen Gas)

Run No.	Number of Data Points	Overall Pressure Ratio	Ambient Pressure (in. hg)	Extreme Ranges of Results						Limitations of Test			
				Electrical Power (watts)	Speed (rpm)	Overall Efficiency (fr)	Corrected Speed (rpm * R)	Wheel Efficiency (fr)	Velocity Ratio (N.D.)	Corrected Torque (in. -lb in./hg A)	High Speed	Low Speed	Maximum Electrical Load Available
107	5	1.1	30.102	0.0 1.1424	37,860 81,240	0.0 0.2457	1,631.16 3,501.28	0.3142 0.3830	0.1945 0.4163	0.0 0.7686 * 10 <sup>-4</sup>		X	
110	10	1.2	29.449	0.0 2.6082	30,900 124,680	0.0 0.2357	1,332.82 5,376.55	0.1903 0.4497	0.1155 0.4658	0.0 0.1421E-03		X	
116	13	1.3	29.603	2.6568 5.0544	28,260 117,780	0.1331 0.2694	1,221.72 5,090.12	0.1577 0.4701	0.0890 0.3694	0.7435E-04 0.2048E-03	X	X	
117	18	1.4	29.772	3.2834 8.0346	26,400 115,560	0.1126 0.2927	1,139.10 4,996.66	0.1342 0.4388	0.0736 0.3231	0.1360E-03 0.2640E-03	X	X	
118	10	1.5	29.724	4.6258 11.0664	29,700 113,460	0.1197 0.3032	1,280.27 4,894.32	0.1442 0.4223	0.0757 0.2894	0.1844E-03 0.2908E-03	X		
119	10	1.6	29.693	6.6000 14.3748	36,660 129,480	0.1362 0.3177	1,585.26 5,598.92	0.1643 0.4396	0.0875 0.3089	0.1871E-03 0.3204E-03	X		
120	18	1.7	29.677	8.5842 17.6946	42,120 126,420	0.1458 0.3189	1,816.18 5,454.50	0.1740 0.3970	0.0948 0.2846	0.2340E-03 0.3441E-03	X		X

Tests were conducted by adjusting the gas flow through the nozzle to obtain a given pressure ratio, and the turboalternator speed was controlled by varying the resistive load on the alternator. At the low pressure ratios, the turboalternator test runs were started at no load. Then additional data points for a test run at a given pressure ratio were obtained by increasing the turboalternator load and readjusting the nozzle inlet pressure to maintain the pressure ratio as the turbine speed decreased. The resistive loads were increased by switching a Y-connected, three-phase, pure resistive load bank in fixed steps. As the loads were increased, the turbine speed decreased to a point where the thrust bearings would not support the shaft and the turboalternator would stop. Test data were obtained at low speeds of 20,000 to 30,000

rpm, depending on the type of gas, the pressure ratio, and the next fixed resistance. Results of the above test data were reduced and plotted, and are discussed below under "Performance Results."

During an initial test with helium gas for a test run at a pressure ratio of 1.3, the turboalternator was adjusted to a speed of 100,000 rpm and allowed to run for approximately 35 minutes, in order to purge the system. Then, as the gas flow was adjusted for the pressure ratio of 1.3, the turboalternator speed increased to 180,000 rpm; suddenly the second-stage shaft orbit became rough, so the turboalternator was stopped. A short time later, an attempt to restart the turbine showed the same rough orbit operation.

The turboalternator was partially disassembled and examined. Slight wear marks were noted on the shaft at the outer edges and on both sides of the second-stage journal bearing area. This slight amount of wear did not seem to affect the smooth rotation of the shaft. Therefore, the turboalternator was reassembled and operated satisfactorily at speeds of up to 100,000 and 120,000 rpm.

The rough operation described above was probably caused by the bearings heating at the higher speeds, especially with the housing sealed, thereby not allowing a flow of cooling gas to remove the heat. Figure 58 is a plot of data

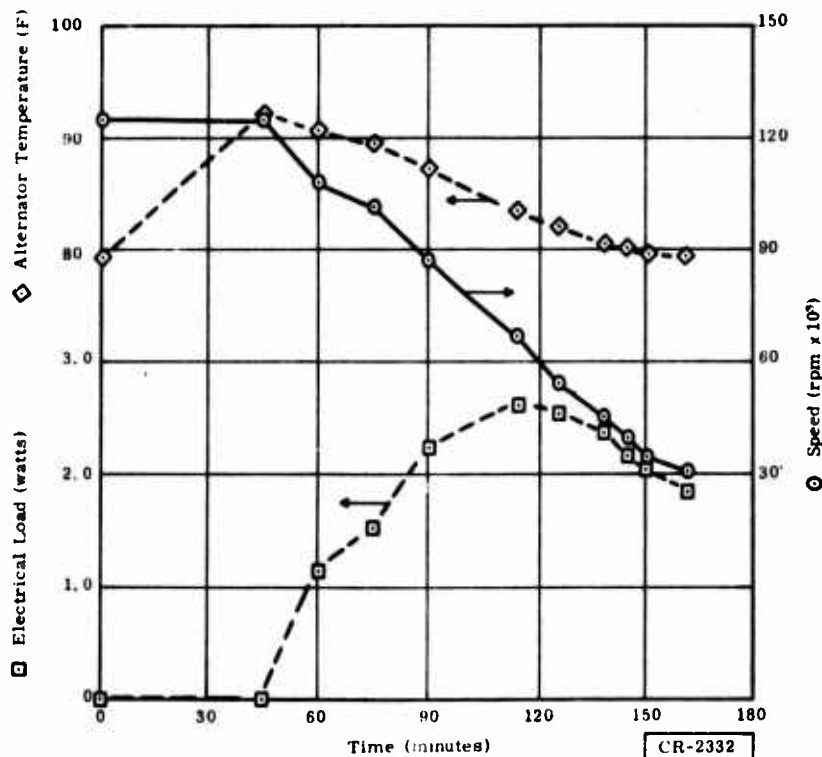


Figure 58. Turboalternator Heating Effects Noted During Run 110 with Nitrogen Gas at Pressure Ratio of 1.2

points taken during Run 110, showing the relation of time, stator temperature, speed, and alternator load. The test run was started by operation of the turboalternator at 125,000 rpm, at no load, for 45 minutes -- with nitrogen gas to purge the system. During the 45-minute period, the alternator winding temperatures increased 13° F above ambient. Raising the alternator temperature 13° F at no-load conditions definitely showed that the bearings were operating at much higher temperatures. Therefore, during the previous test, when the journal bearings apparently rubbed (the turboalternator was operating at 180,000 rpm with a light alternator load), the bearing temperatures must have been considerably higher.

The thickness of the journal bearings used in this assembly is approximately 0.020 inch at the outer edges, with a thicker rib through the center to contain the pivot socket. The journal bearing pads were designed in this manner to reduce the pad weight and produce more stable operation. The spring stems in the journal bearing assemblies were designed to compensate for thermal expansion of the bearing assemblies while operating at high temperatures. A possibility exists that the thin outer edges of the journal bearing pads warped at the high temperatures, thereby causing the rub, because there was no evidence of wear through the center sections of the bearings.

Problems were encountered when the pads warped during nitriding. Therefore, the new flat-bottom socket journal bearing pads were designed to be thicker, to improve the nitriding process. This design should also reduce the possibility of the leading and trailing edges warping at elevated temperatures.

The turboalternator continued to operate satisfactorily during the remaining test runs, by limiting the maximum speed to approximately 120,000 rpm, although the inner thrust bearing appeared to shift position during operation of the turboalternator. This condition did not affect operation of the turboalternator during the above test runs, but it must be corrected to maintain the thrust bearing stiffness over the operating temperature range. The total travel of the shaft between the thrust bearings was initially adjusted to 0.0008 inch.

During the test runs, the position of the inner thrust bearing varied approximately  $\pm 0.0004$  inch. Further examination showed that with the turboalternator in a vertical position, thrust end up, gently tapping the top end of the shaft would move the inner thrust bearing down approximately 0.0004 inch from the original 0.0008-inch setting. Then, tapping the housing would move the shaft and the inner thrust bearing back up 0.0004 to 0.0008 inch.

Figure 59 shows the inner thrust bearing assembly. This assembly consists of a housing flange section (Part 1) that supports a gimbal ring (Part 3) by two pivots. The thrust bearing (Part 2) is supported by two other pivots mounted from the gimbal ring. Springs are incorporated in the gimbal ring and the thrust bearing to maintain tension on the pivots. During assembly, the pivots



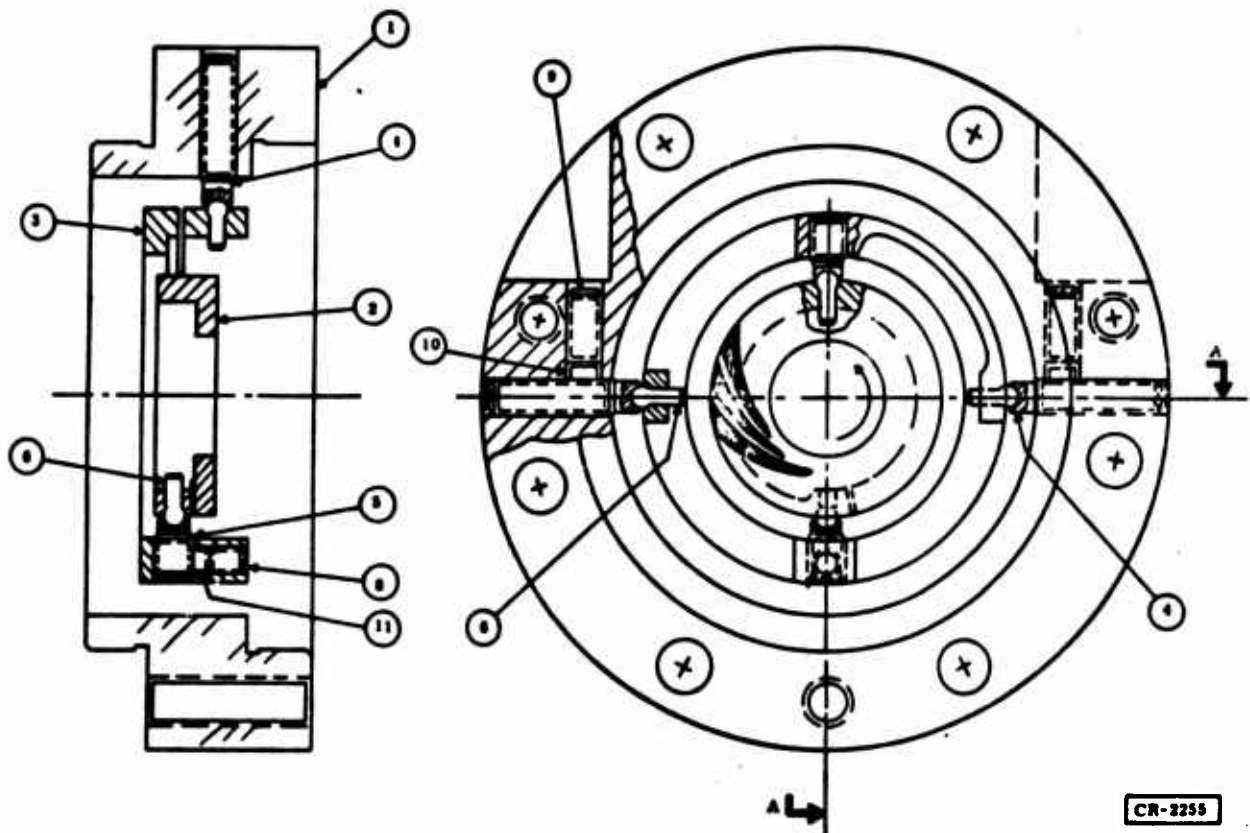


Figure 59. Two-Stage Turboalternator Inner Thrust Bearing Assembly

are adjusted to produce a tipping force of 1.5 to 2.0 grams. In the design of the ball and the socket pivots (Parts 5 and 6), the ball was made 0.055 inch in diameter, 0.014 inch smaller in diameter than the pivot socket. This arrangement was done because it was believed the spring tension would force the pivot ball to ride in the center of the socket and the clearance would reduce the possibility of particles generated from wear building up and binding. However, from the above observations, the pivot ball must ride up on the socket radius, thereby shifting the thrust bearing position. The pivot design will be reviewed, and the most convenient modification of either increasing the pivot ball diameter or decreasing the socket radius will be made to correct these undesirable shifts in thrust bearing clearances.

The turboalternator assembly was then prepared for cold open cycle testing at liquid nitrogen temperature. In this test, the helium gas to the turbine was precooled by flowing the gas through a coil immersed in liquid nitrogen. Strips of plastic material were attached to the turboalternator support stand, to direct the cold nozzle exhaust gas around the turboalternator sealed housing, cooling the whole assembly. A bell jar was placed over the turboalternator assembly, to isolate the system from ambient moisture.

After the above preparations, the turboalternator was operated for 1 hour at room temperature, 100,000 rpm, and no load to purge the system with

dry (5-ppm moisture content) helium gas. The gas pressure tap connected to the sealed housing was disconnected to purge the turboalternator housing and the sealed housing. Then, in order to cool the turboalternator assembly at a slow rate, liquid nitrogen was slowly added to a dewar containing the cooling coil. Cold tests in the past on turboalternator assemblies, Builds 4 and 5, using the same type of journal bearing have operated roughly and been damaged as the gas inlet temperature approached 100° K.

The test plan was to cool at a much slower rate, thus reducing thermal gradients and possibly improving the operation of the turboalternator at the low temperatures. The turboalternator was cooled for two hours, but again, as the inlet gas temperature to the nozzle reached 105° K, the proximity probes monitoring the shaft orbits indicated rough operation. Varying the turboalternator speed and load had no effect, and the turbine was quickly shut down. The alternator winding temperature was approximately 180° K.

After the turboalternator warmed up to room temperature, it operated satisfactorily again, with no indication of the bearings being damaged during the above rough operation. All of the proximity probe signals were the same as they were before the cold test.

The rough cold operation of the turboalternator was very similar to the rough operation experienced during the room temperature tests when the turbine was operated at higher speeds, as described above. Both conditions could have been caused by distortion of the 0.020-inch-thick outer edges of the journal bearing design.

While journal bearings with the new flat-bottom pivot socket of the thicker design were being manufactured, the following tests were made, to obtain test data on the turboalternator at the lowest cold temperature that would allow satisfactory operation.

A bypass line and valve were installed across the liquid nitrogen cooling coil, to provide a better control of the gas temperature supplied to the turbine nozzle. Adjustment of the bypass valve controls the mixture of warm, room temperature gas and the cold gas supplied from the liquid nitrogen cooling coil.

The cold tests were started by operating the turbine at no load and 100,000 rpm for 1 hour, to purge the system with the dry helium gas. Then, the pressure ratio across the nozzle was adjusted to 1.5 by increasing the gas flow and limiting the turbine speed to 120,000 rpm (by increasing the resistive load on the alternator). Liquid nitrogen was added to the dewar containing the cooling coil, and the bypass valve was adjusted to provide a moderate rate of cooling. As the turboalternator cooled, slight roughnesses of the shaft orbits were noted occasionally, but minor adjustments in the speed corrected the operation.

After 1-1/2 hours of cooling, the gas inlet temperature reached 178° K and the alternator winding temperature was 214° K. The turboalternator operated

satisfactorily at speeds in the order of 100,000 rpm. However, further decrease in the gas inlet temperature caused roughness in the shaft orbits that could not be corrected by speed adjustments. Therefore, the gas inlet temperature was readjusted to 177°K and the sealed-housing pressure tap was connected. The turboalternator operated satisfactorily as several data points were taken for test runs 121 and 122, with nozzle pressure ratios of 1.5 and 1.6. Only one data point was obtained for test run 123, with a nozzle pressure ratio of 1.7. The shaft seemed to be riding very close to the inner thrust bearing at 100,400 rpm for this single data point. As the turbine speed decreased with increased alternator load for the next data point, the shaft thrust touched the inner thrust bearing and stopped the turbine.

Attempts to operate the turboalternator at higher temperatures with a nozzle pressure ratio of 1.7 produced the same results. It appears that the gas flow through the nozzle at a pressure ratio of 1.7 creates a force greater than the inner thrust bearing when the turbine speed is adjusted below 100,000 rpm. This force pulls the shaft thrust against the inner thrust bearing and stalls the turbine. The turboalternator operates satisfactorily with a nozzle pressure ratio of 1.7 when the sealed housing pressure tap is open. This situation decreases the housing pressure and reduces the total flow through the nozzle.

All of the above test runs were made with the turboalternator in a vertical position, with the thrust end up. In this position, gravity on the shaft would also pull the shaft thrust toward the inner thrust bearing. Therefore, it was decided to invert the turboalternator assembly and repeat the 1.7 nozzle pressure ratio tests with gravity pulling the shaft toward the outer thrust bearing. The results of this test were the same as above. Only one data point could be obtained at 100,000 rpm, with the inlet temperature at 177°K. At lower speeds the shaft thrust runner would still touch the inner thrust bearing and stop the turbine.

During the last series of tests, wear on the shaft journal surfaces and the journal bearings increased to a point where this assembly would no longer operate.

The problem of the shaft thrust runner touching the inner thrust bearing may not be serious when the second-stage turbine wheel is installed on the opposite end of the shaft. The second-stage wheel will create a counter force to reduce this effect.

The turboalternator was disassembled, and examination of the parts showed the following conditions:

- Thrust Bearings. Some wear marks and fine scratches were noted on the inner thrust bearing surfaces, on both the shaft and the thrust bearing. Most of this wear undoubtedly occurred during low-speed tests at the various pressure ratios, with the turboalternator mounted in a vertical position, thrust end up. In this position, at low speeds,

the shaft tended to ride on the inner thrust bearing. The amount of wear noted did not appear to be sufficient to affect the operation of the turbine. No indication of wear on the outer thrust bearing surfaces was evident.

- Journal Bearings. The first-stage journal bearings showed the most wear, with heavier score marks noted on the shaft journal and on all three journal bearing pads, as compared to the journal bearings at the thrust end of the housing. No wear was indicated through the center area of the journal bearings at either end. The wear marks were within 1/16 inch from the outer edges of the pads at the first-stage end and within 1/32 inch from the outer edges of the pads at the thrust end of the housing. This situation tends to confirm the earlier suspicions that the 0.020-inch-thick outer edges of this journal bearing design are distorting with changes in temperature, reducing the journal bearing clearances until the pads touch the shaft, causing the rough operation observed.
- Journal Bearing Pivots. Only faint indications of wear were noted in the journal bearing pivot sockets and on the pivot balls.
- Thrust Bearing and Gimbal Pivots. No actual wear was noted in the gimbal pivot sockets or on the pivot balls. Only a slight discoloration was noted on the ends of the pivot balls and in the bottom of the sockets, indicating a burnishing effect of the balls riding in the sockets.

#### Turboalternator Build 8

Six new Kentanium-grade K-165 journal bearing pads were completed (Figure 60). The new Kentanium journal bearings with the flat-bottom, pivot

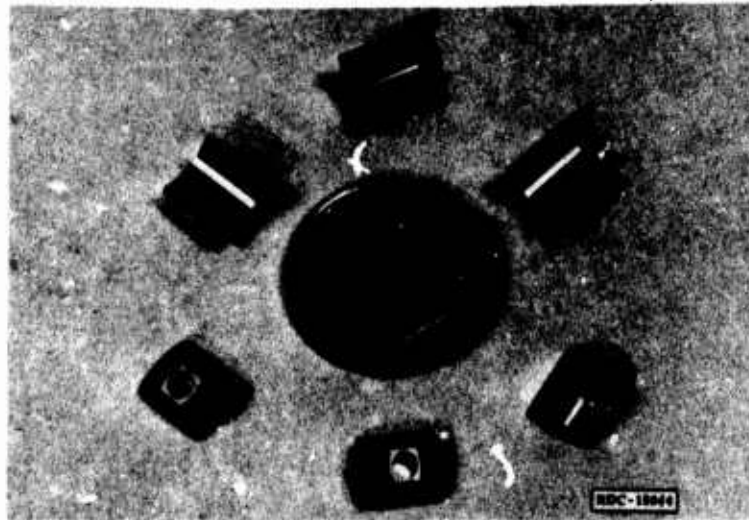


Figure 60. Kentanium-Grade K-165 Journal Bearing Pads  
(Flat-Bottom, Pivot Socket Design)

socket design were installed in turboalternator assembly Build 8. This assembly consisted of the 1.1-inch-diameter, second-stage, titanium turbine wheel and nozzle. New tungsten carbide journal bearing pivot balls, 0.077 inch in diameter, were also used in this assembly. The tungsten carbide balls were copper-brazed to the end of the 304L stainless steel pivot stems, to provide a hard homogeneous material that will withstand the comparatively high-hertz stress incurred on the tip of the pivot ball by the new flat-bottom journal bearing pivot sockets. The journal bearing radial clearances were adjusted to 250 microinches. The thrust bearings were shimmed to give the shaft a total axial travel of 0.0007 inch and a wheel-to-nozzle axial clearance of 0.0015 to 0.0022 inch.

As the new turboalternator assembly was operated, the shaft orbit proximity probes viewing the radial motion of the shaft showed a much larger than normal orbit at the first-stage end of the shaft. The turbine was shut down immediately. Alignment of the wheel-to-shaft match marks used to align the turbine wheel on the shaft after balance corrections, when examined, appeared very close to normal, although it is difficult to accurately view the fine scribe marks behind the turbine wheel in the assembly. The turbine wheel was then removed from the shaft and reassembled. When the turbine was again operated, the size of the first-stage shaft orbit improved slightly, but it was still approximately twice as large as that obtained in previous assemblies. Figures 61 and 62 show the proximity probe signals obtained. A slight roughness was also noted in the first-stage shaft orbit as the speed approached 100,000 rpm. The thrust proximity probe showed stable operation of the shaft between the thrust bearings.

Difficulties were encountered in the initial balance tests with the above shaft. The first wheel-to-shaft assembly was made with the first-stage, 0.5-inch-diameter wheel, and tests indicated more material than normal would have to be removed to make the necessary balance corrections. Therefore, the first-stage wheel was removed, and balance tests were made with the second-stage turbine wheel. This combination appeared to balance more normally. However, there may be an imperfection in this shaft assembly, making the balance of the assembly more critical than usual.

Rather than risk damaging the new parts, it was decided to disassemble the turboalternator and make a new assembly with another wheel/shaft combination.

The turboalternator parts were examined under a microscope after disassembly. The only indication of wear was at the first-stage journal bearings. The extreme outer edges of the two journal bearing pads supported by the solid pivot stems showed slight burnishing, and the corresponding journal surface on the shaft was discolored. This slight indication of wear was undoubtedly caused by the large first-stage orbit. Otherwise, the only noticeable change in the parts was a more highly polished spot in the center of each flat-bottom pivot socket of the journal bearings, where the tungsten carbide ball was touching.

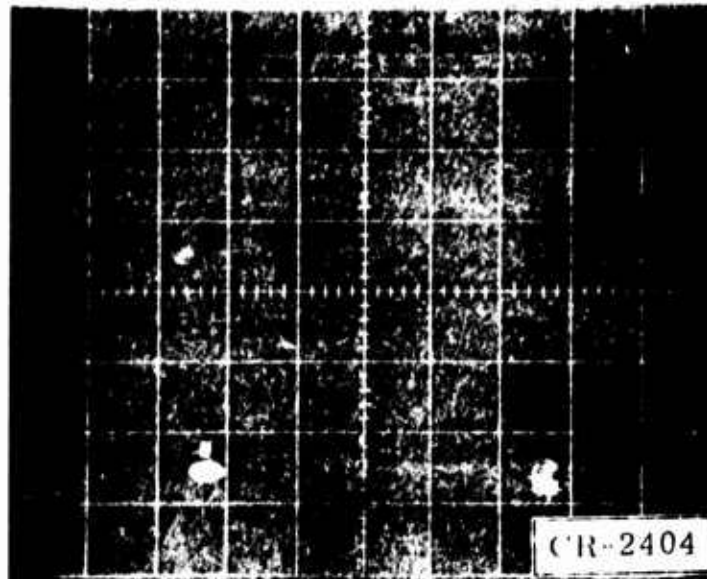


Figure 61. Shaft Orbits of Second-Stage Turboalternator Assembly, Build 8, Operating at 100,000 Rpm (Oscilloscope Sensitivity of Proximity Probe Signals = 400  $\mu$ in./cm)

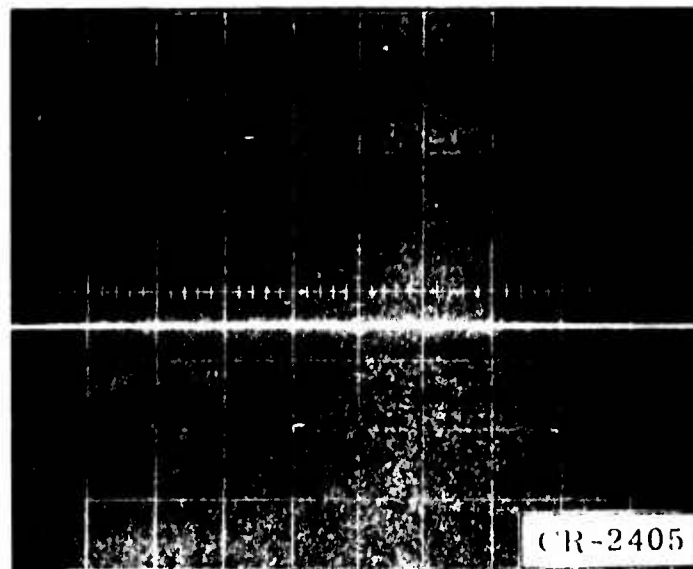


Figure 62. Shaft Axial Motion Between Thrust Bearings of Turboalternator Assembly, Build 8, Operating at 100,000 Rpm (Oscilloscope Sensitivity of Proximity Probe Signal = 400  $\mu$ in./cm Vertically; Horizontal Sweep = 1.0 ms/cm)

Because the titanium turbine wheel used in this assembly was assembled and disassembled at least nine times (with an interference fit of 0.00055 inch), the wheel bore should be recoated with the chemical conversion coating and should be lubricative-plated with molybdenum disulfide, to prevent damage to the bore. A new first-stage, 0.5-inch-diameter aluminum turbine wheel recently received from the Andrews Engineering Company had been lubricative-plated and was available for use in the next turboalternator assembly.

#### Turboalternator Build 9

The Kentanium journal bearing pads and the new tungsten carbide journal bearing pivot balls used in Build 8 were relapped and assembled in turboalternator Build 9. This assembly consisted of a new shaft balanced with a new first-stage, 0.5-inch-diameter, aluminum turbine wheel. New 0.063-inch-diameter pivot balls were also installed in the thrust bearing gimbal assemblies, to reduce the axial shift noted in the previous thrust bearing assemblies. The 0.063-inch-diameter balls are 0.005 inch smaller in diameter than the mating sockets. The original gimbal pivot design had a 0.014-inch difference in the ball socket diameters. The journal bearing radial clearances were adjusted to 250 microinches. The thrust bearings were shimmed to give the shaft a total axial travel of 0.0007 inch and a wheel-to-nozzle axial clearance of 0.0015 to 0.0021 inch.

The turboalternator seemed to operate satisfactorily. Tests were made at speeds on the order of 100,000 rpm, and the proximity probe signals indicated stable operation. The shaft orbit probe signals produced relatively small orbits of 80 microinches at the first-stage end of the shaft and 100 microinches at the second-stage end. The thrust proximity probe viewing the end of the shaft, monitoring the axial motion, had a once-per-revolution ripple of approximately 20 microinches, representing very stable thrust bearing operation.

The turboalternator was operated in a vertical position, only thrust end up, at 100,000 rpm for 1/2 hour and was subjected to six start-stop operations as a preliminary test on the Kentanium journal bearing pads, before disassembly to magnetize the shaft magnet. During the tests, the turboalternator operated smoothly, starting at a low nozzle inlet pressure of 2.5 inches of mercury. After the inlet gas was turned off, the turbine coasted to a smooth stop, with the shaft gently settling on the inner thrust bearing as the speed decreased.

The turboalternator was partially disassembled, to magnetize the shaft. Two dark, discolored areas were noted on the shaft at the outer edges of the second-stage journal bearing surfaces. The discolored areas were very similar in size and relative position and continue approximately one-third of the way around the circumference of the shaft.



Examination of the discolored areas on the shaft, under an 80-power microscope, indicated a smearing of a resin material subjected to heating, causing a variation in color. The first-stage journal bearing surface on the shaft did not show the discoloration or any signs of wear.

The journal bearing pads were also inspected. All of the pads from both stages showed traces of a translucent material on the journal surfaces. One journal bearing pad from the second-stage end, supported by a solid pivot stem, showed slight, burnished rub marks along the outer edges of the journal surface. More of the translucent material appeared to be on this pad.

The Kentanium journal bearing pads were sintered in molds slightly oversize, to allow finish machining within drawing tolerances. Therefore, all surfaces had to be ground. Stems were epoxied in the pivot holes to hold the pads during the initial machining operations. After completion of the initial machining, the stems were removed by heating them to soften the epoxy. The epoxy possibly impregnated into the microporous Kentanium material, and during the operation of the turboalternator, sufficient heat could have been generated in the bearing pads to cause the epoxy to seep out of the pores onto the journal surfaces. The larger, second-stage orbit would cause more heating of the journal bearings and affect the second-stage pads more than the first-stage pads.

To confirm that the discolored areas on the shaft were epoxy, the shaft was subjected to several commercial epoxy remover solvents. The solvents tended to affect the discolored areas to some degree, indicating the material was epoxy. However, the solvents also damaged the nitrided surfaces on the shaft, turning it into a soft black substance.

To ensure that the epoxy remover solvent recommended for the epoxy used on the pads would not damage the Kentanium, a sample of Kentanium was placed in the solvent for several hours, without any effects noted. The Kentanium pads were then placed in the solvent, to remove as much of the epoxy as possible. Then the six Kentanium bearing pads were subjected to a vacuum bake up to 350°C, to remove the majority of epoxy in vapor form and carbonize the remaining substances in the pores. The furnace vacuum system was evacuated to a pressure of  $8 \times 10^{-7}$  millimeters of mercury at room temperature. The furnace temperature was increased slowly, in steps of 50°C, up to the maximum temperature of 350°C over a seven-hour period. During the heating cycle, the vacuum pressure remained low, varying between  $10^{-7}$  to  $10^{-6}$  millimeters of mercury. The pads were cooled in the vacuum atmosphere to prevent oxidation.

After the vacuum bake, the journal bearing surfaces and the pivot sockets were relapped to ensure clean surfaces.



### Turboalternator Build 10

After relapping, the above Kentanium journal bearing pads were assembled in turboalternator Build 10. The tungsten carbide journal bearing pivot balls were also relapped before assembly, to ensure clean surfaces. A new shaft was balanced with the above first-stage, 0.5-inch-diameter, aluminum turbine wheel. All other parts used in this assembly were taken from the Build 9 assembly. The journal bearing radial clearances were adjusted to 250 micro-inches, and the thrust bearings were shimmed to give the shaft a total axial travel of 0.0008 inch and a wheel-to-nozzle axial clearance of 0.0015 to 0.0023 inch.

The turboalternator operated very well. Tests were made at speeds in the order of 100,000 rpm. The proximity probe signals indicated very stable operation, and the shaft orbit probe signals produced exceptionally small orbits of 30 to 40 microinches at each end of the shaft. The thrust proximity probe viewing the end of the shaft, monitoring the axial motion, also showed very stable operation. Figures 63 and 64 show the proximity probe signals obtained.

This turboalternator assembly was also operated in a vertical position, only thrust end up, at 100,000 rpm for 1/2 hour and was subjected to six start-stop operations, as a preliminary test on the Kentanium journal bearing pads before disassembly to magnetize the shaft magnet. During the tests, the turboalternator operated very smoothly, starting at a low nozzle inlet pressure of 2.5 to 3.0 inches of mercury. After the inlet gas was turned off, the turbine coasted to a smooth stop, with the shaft gently settling on the inner thrust bearing as the speed decreased.

The turboalternator was then partially disassembled, to magnetize the shaft magnet. A careful examination of the shaft journal surfaces under a 60-power microscope gave no indication of any wear or discoloration as experienced in the Build 9 assembly. Therefore, the shaft magnet was magnetized, and the turboalternator was reassembled.

The operation of the turboalternator, after reassembly, was identical to the initial tests. A proximity probe was installed to monitor the outer thrust bearing motion. The pad proximity probe used in some of the previous assemblies was not installed, because the new design of journal bearing pads with the flat-bottom pivot sockets required an 11-degree change in the angle of the probe viewing surface, and this would not allow positioning of the probe without interfering with the pad motion.

Six start-stops were repeated, to test the operation of the turboalternator after reassembly and to check the position of the outer thrust probe during operation. The turboalternator was then prepared for cold, open cycle testing, to evaluate operation with the Kentanium pads at temperatures approaching

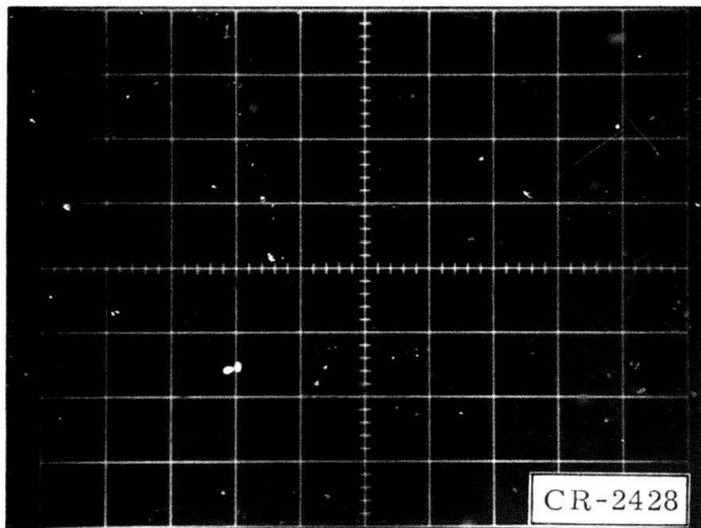


Figure 63. Shaft Orbits of First-Stage Turboalternator Assembly, Build 10, Operating at 100,000 Rpm (Oscilloscope Sensitivity of Proximity Probe Signals =  $400 \mu\text{in./cm}$ )

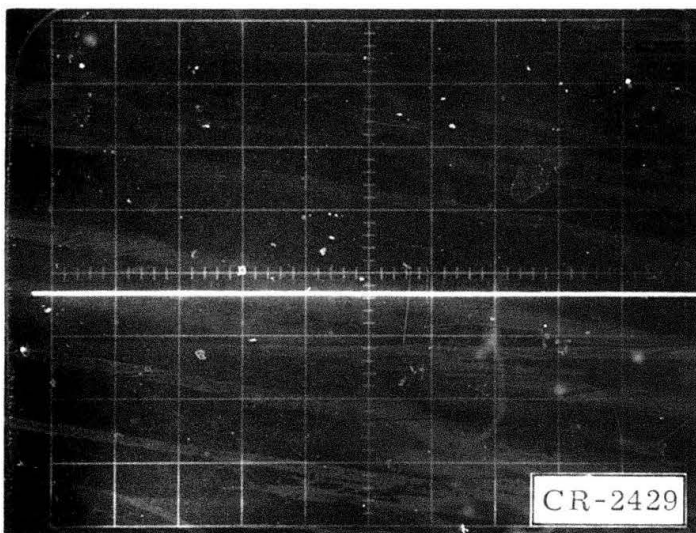


Figure 64. Shaft Axial Motion Between Thrust Bearings of Turboalternator Assembly, Build 10, Operating at 100,000 Rpm (Oscilloscope Sensitivity of Proximity Probe Signal =  $400 \mu\text{in./cm}$  Vertically; Horizontal Sweep =  $1.0 \text{ ms/cm}$ )

liquid nitrogen temperature. The sealed housing was not assembled onto the turboalternator, because performance data were not taken during this preliminary test run.

The turboalternator was operated for 1 hour at room temperature, 100,000 rpm, and no load, to purge the system with dry (5-ppm moisture content) helium gas. Then liquid nitrogen was gradually added to the dewar containing the cooling coil, to slowly cool the turboalternator assembly. Cold tests on turboalternator Builds 4, 5, and 7, using the original design journal bearings, operated roughly and were damaged as the gas inlet temperature approached 100°K.

After 2-1/2 hours of cooling and gradually increasing the alternator load to 165.5 ohms (approximately 16 watts) at 100,000 rpm, the turboalternator continued to operate very well with the gas inlet temperature at 93°K and an average stator temperature of 102°K. The only problem encountered was one of the orbit proximity probe connections opened so that only the first-stage shaft orbit could be monitored. Otherwise the turboalternator operation was essentially the same as operation at room temperature.

The first-stage orbit remained the same. A slight increase in the axial motion of the shaft and outer thrust bearing was noted. As the next load point of 142 ohms was applied to the alternator, the turbine operation became unstable in the axial plane. The proximity probes viewing the shaft and the outer thrust showed comparatively large oscillations and indicated that the shaft was touching the thrust bearings. The alternator load was reduced immediately, and smooth operation was again obtained. The unstable operation may have been caused by the outer thrust bearing touching the proximity probe as the gas flow to the turbine was increased to maintain the speed at 100,000 rpm, with the increase in the alternator load.

Because the operation of the turboalternator seemed to be limited to the above conditions, it was decided to remove the alternator load and test the journal bearing, at temperatures of approximately 100°K, with start-stop tests. Ten start-stop tests were successfully made, with the turbine starting at nozzle inlet pressures ranging from 3.2 to 3.8 inches of mercury and coasting to smooth stops when the gas was turned off.

The assembly was allowed to warm up to room temperature, and the turboalternator continued to operate satisfactorily. The proximity probe viewing the outer thrust bearing definitely appeared to be positioned closer to the bearing than during the initial adjustment, indicating the diameter of the gimbal pivot balls should be increased further to eliminate this type of shift in the thrust bearings.

The turboalternator was then partially disassembled, to allow examination of the shaft journal surfaces by viewing them between the journal bearings under a 60-power microscope. No indications of wear or discoloration were evident on the shaft journal surfaces.

Results of the above tests with the Kentanium journal bearings have shown considerable improvement in the operation of the turboalternator at the lower temperatures and should be investigated further.

## PERFORMANCE TESTS

### First-Stage Open Cycle Tests

Details of first-stage open cycle performance tests are included above in the description of functional tests under "Turboalternator Build 7."

### First-Stage Performance Test Results

The performance tests were conducted at both room temperature and at cryogenic temperatures with both helium and nitrogen gases, in order to provide a broad range of performance test results for the first-stage turboalternator. Only limited data were obtained at cryogenic temperatures and will not be reported until more data are obtained. However, considerable meaningful data have been obtained from the room temperature tests and will be discussed.

The data reduction computer program output sheet was changed from the one described in Contract Status Report No. 26. "Pressure Ratio" was changed to "Inlet/Exhaust Pressure Ratio," which is the total pressure ratio across the turbine. "Wheel Flow" was no longer needed with the enclosure can, because it is the same as "Total Flow." Accordingly, this entry was changed to "Inlet/Nozzle Pressure Ratio," which is the inlet-pressure-to-nozzle-exit pressure ratio. Also with the can, "Alternator Leakage Flow Fraction" was no longer needed, so it was replaced with "Nozzle/Exhaust Pressure Ratio" was no longer the ratio of the nozzle exit pressure to the turbine exit pressure.

Figure 65 shows the overall efficiency versus the velocity ratio for helium gas at room temperature. The limitations of these tests, in addition to the extremes of the test operating data obtained, are shown in Table 4. The various constant pressure ratios were tested from 1.1 up to the approximate design pressure ratio of 1.692. The performance results are limited with the higher pressure ratios, due to the high spouting velocity at the ambient-temperature test conditions.

More meaningful overall performance test results are shown in Figure 66, in which the overall efficiency is shown as a function of the velocity ratio for the set of pressure ratios in which nitrogen gas was used. A peak efficiency is obtained with a velocity ratio near the design point value of about 0.340, for a pressure ratio of 1.7. Of course the bearing, windage, and electromagnetic losses at room temperature are much greater than at the design cryogenic temperatures; thus the peak efficiency is below the design value of 0.4128. However, this curve does establish credibility that the peak efficiency will be on the order of the design point velocity ratio.

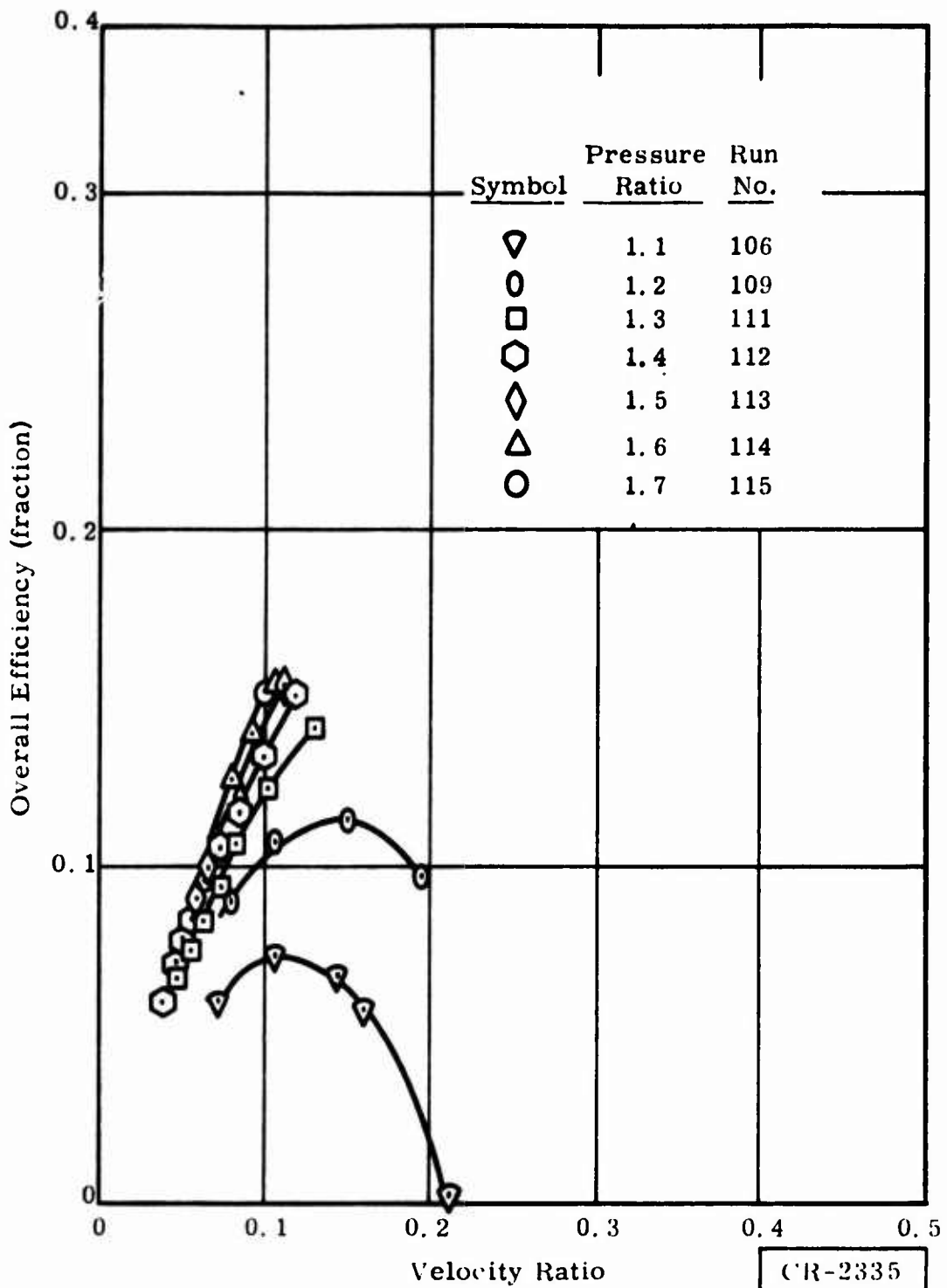


Figure 65. Turboalternator Performance -- Overall Efficiency Versus Velocity Ratio for Helium Gas at Room Temperature

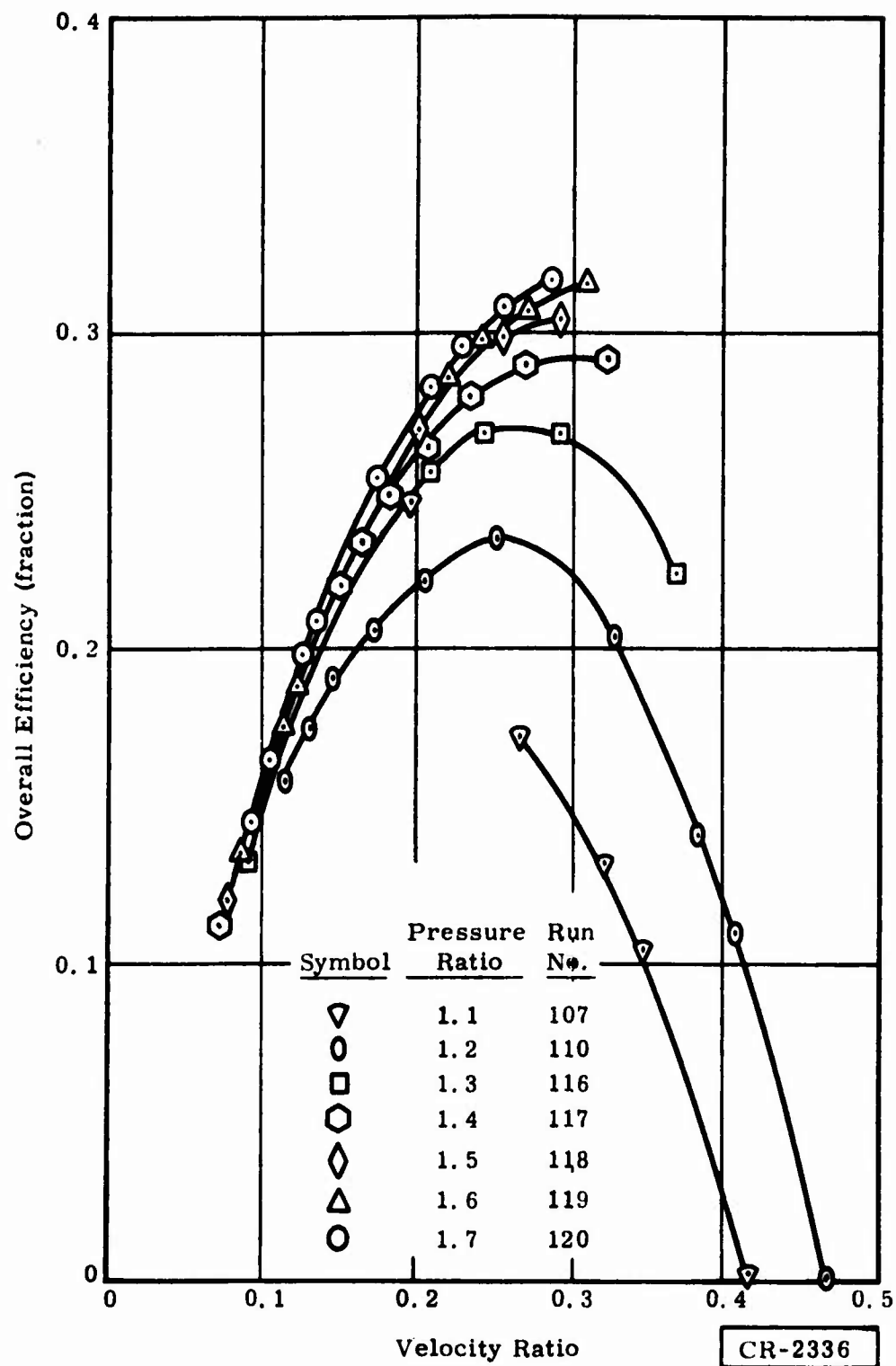


Figure 66. Turboalternator Performance -- Overall Efficiency Versus Velocity Ratio for Nitrogen Gas at Room Temperature

The largest efficiency measurement obtained is represented by the wheel efficiency shown in Figure 67. This efficiency represents the total efficiency

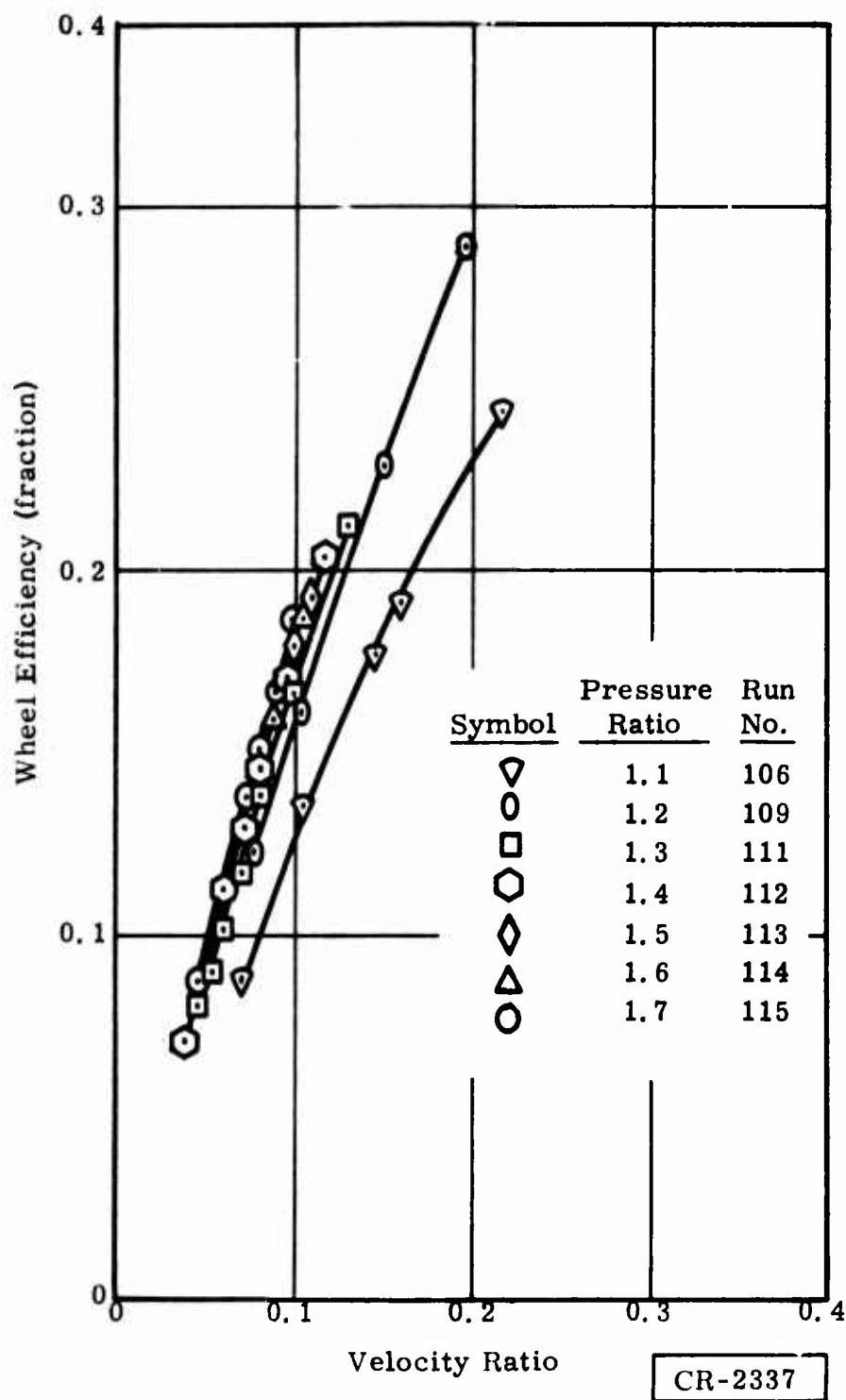


Figure 67. Turboalternator Performance -- Wheel Efficiency Versus Velocity Ratio for Helium Gas at Room Temperature

less the windage, bearing, and electromagnetic losses. In this particular figure, the same limitations are shown with helium gas at room temperature testing; hence the test velocity ratio did not come close to the design point velocity ratio.

The wheel efficiency obtained during operation with nitrogen gas at room temperature is shown in Figure 68. In this case, the design point efficiency

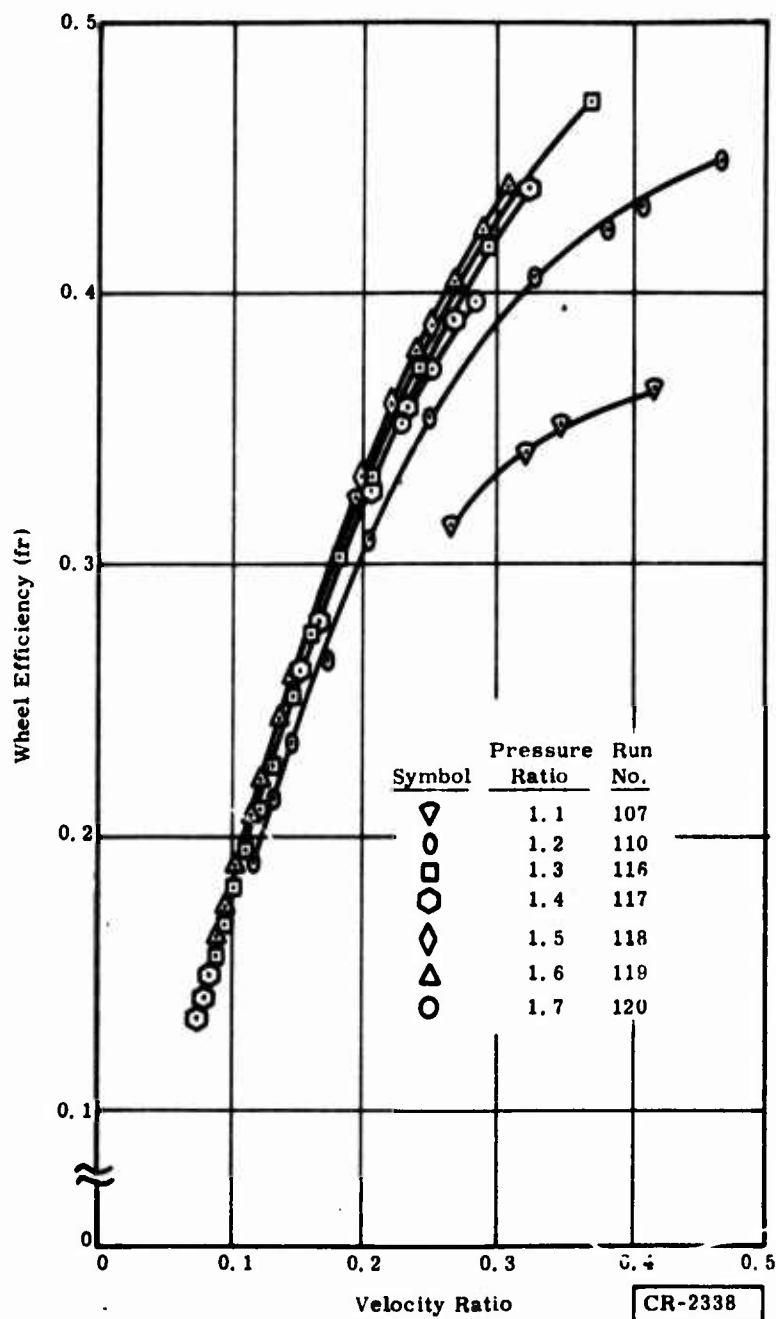


Figure 68. Turboalternator Performance -- Wheel Efficiency Versus Velocity Ratio for Nitrogen Gas at Room Temperature



exceeds the required value. The best efficiency is achieved at approximately a pressure ratio of 1.6, and a slight decrease in efficiency appears with a pressure ratio of 1.7. Up to the 1.6 pressure ratio, the efficiency increased with the pressure ratio.

Figures 69 and 70 show the flow factor, which is a function of nozzle sizing, for the first-stage test results obtained at room temperature for helium

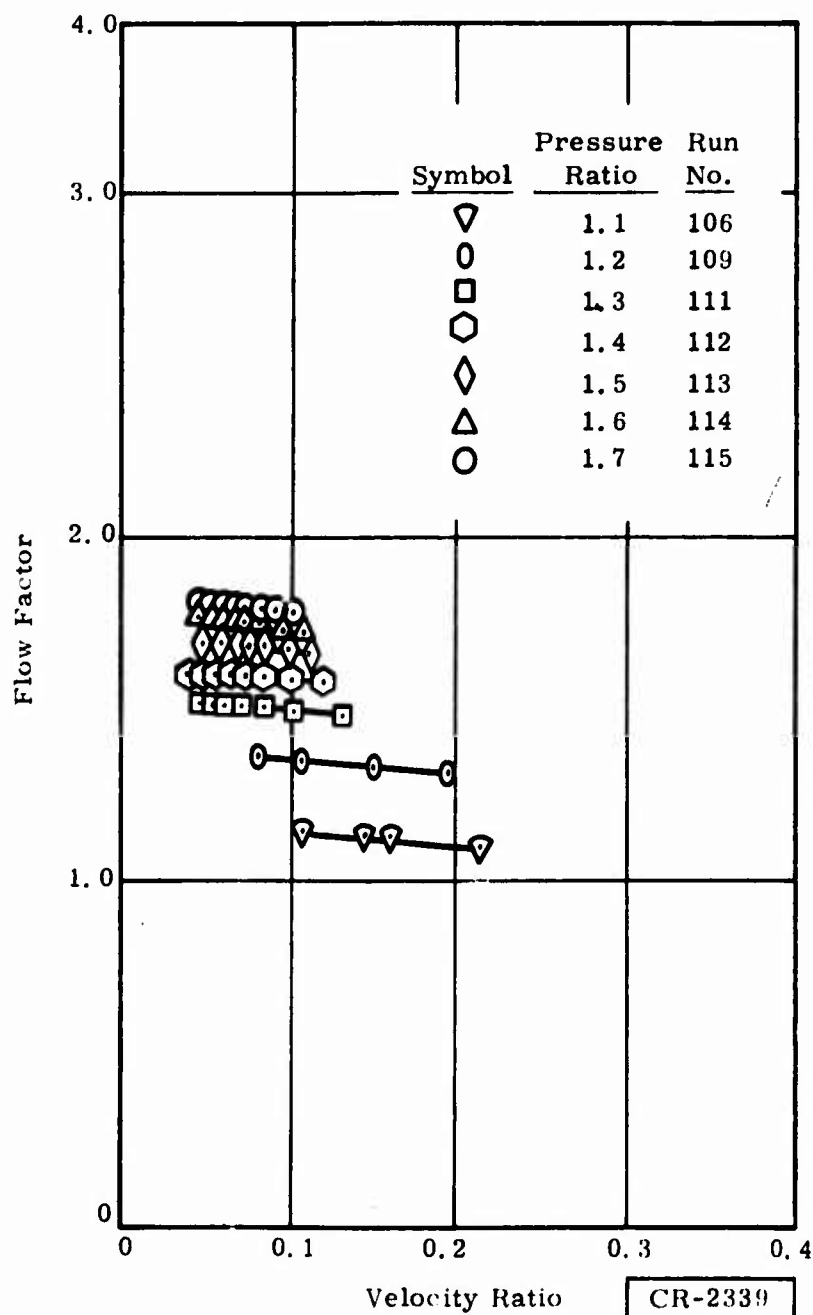


Figure 69. Turboalternator Performance -- Flow Factor Versus Velocity Ratio for Helium Gas at Room Temperature

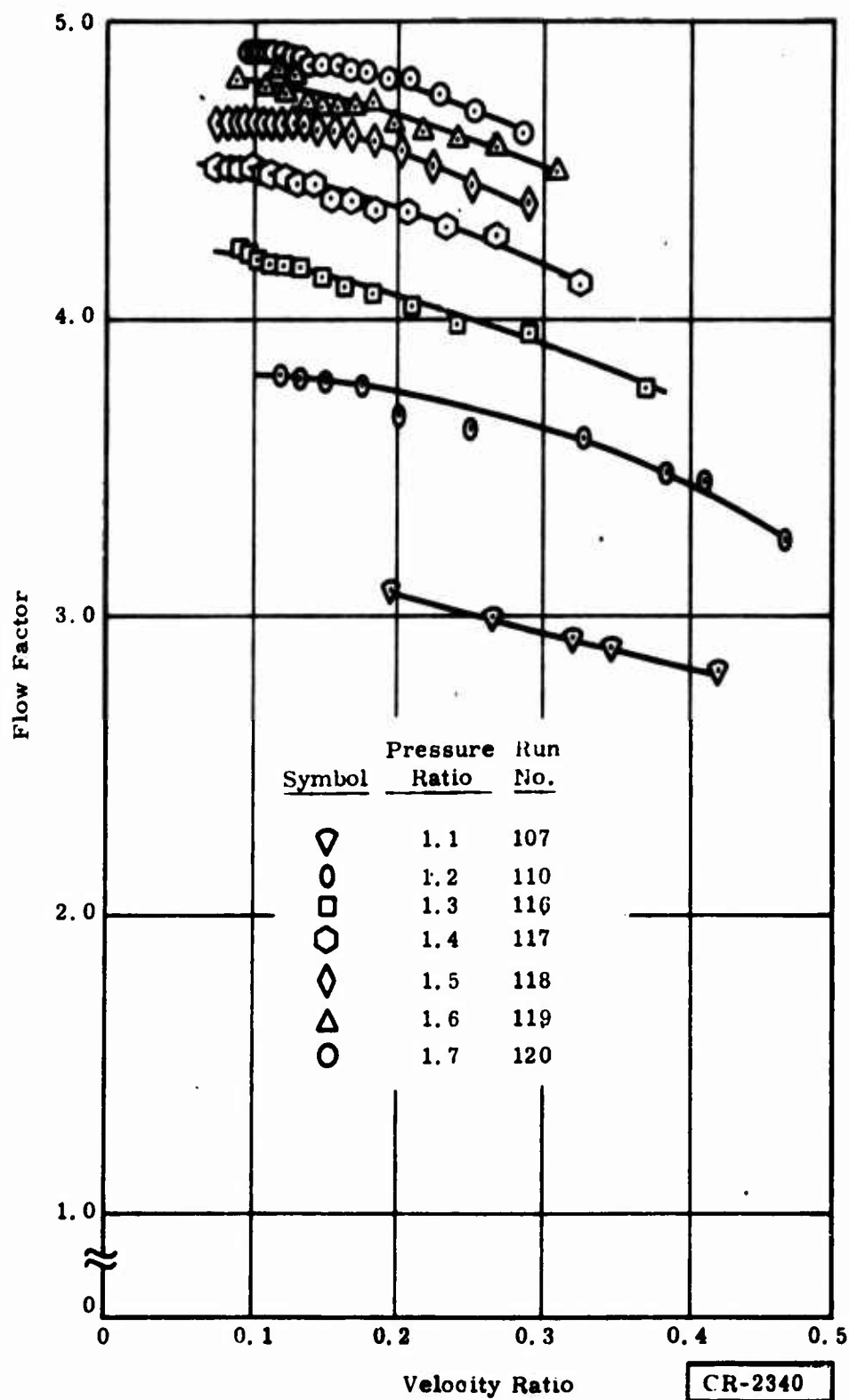


Figure 70. Turboalternator Performance -- Flow Factor Versus Velocity Ratio for Nitrogen Gas at Room Temperature

and nitrogen gas operation as a function of velocity ratio across the turbine. This information would be incorporated, as required, in the analysis and possible redesign of the nozzles for suitable refrigerator cycle matching.

The three measured pressure ratios across the turbine for the performance runs conducted with helium gas are shown in Figure 71. For essentially

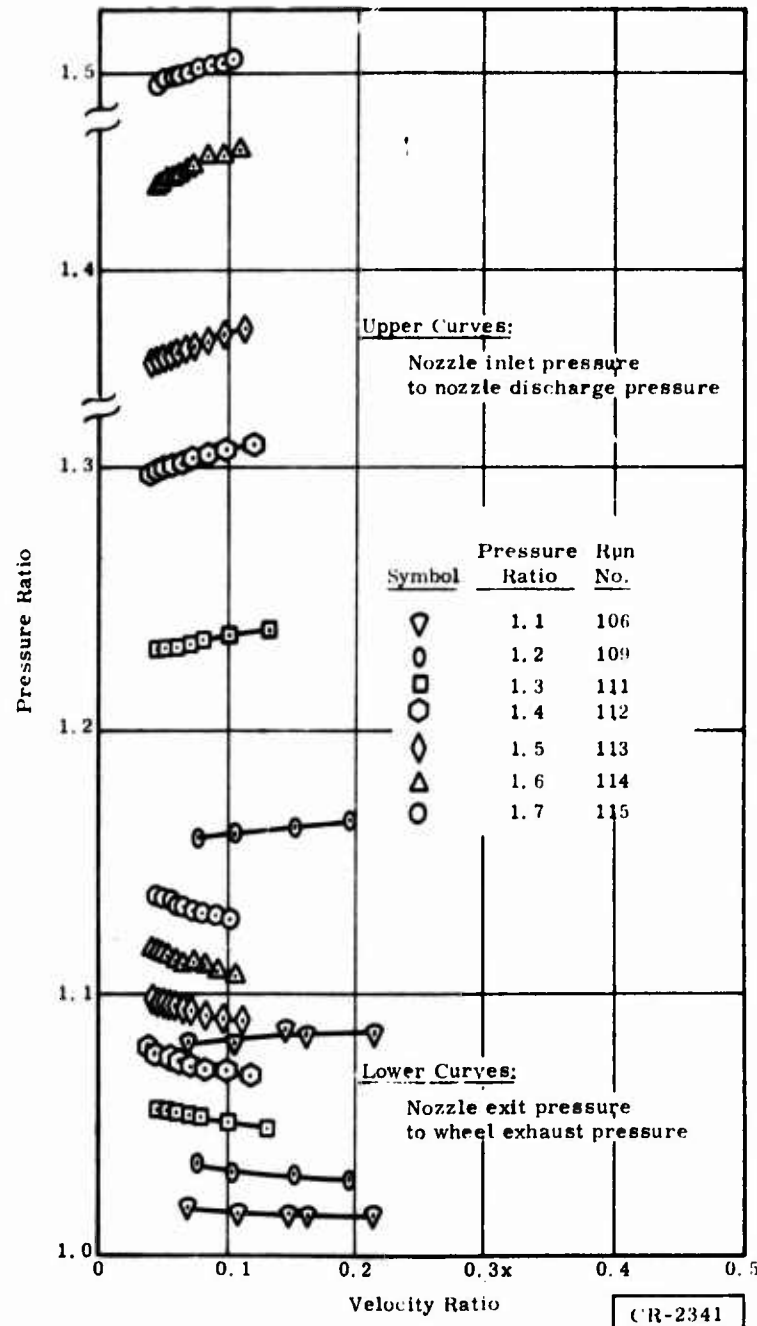


Figure 71. Turboalternator Performance -- Pressure Ratio Versus Velocity Ratio for Helium Gas at Room Temperature

the same constant pressure ratios shown across the entire turbine stage, the two pressure ratios of interest are shown to determine the actual reaction and nozzle pressures of the unit. The upper set of curves show the nozzle inlet pressure to the nozzle discharge pressure. The lower set of curves show the nozzle exit pressure to the wheel exhaust pressure. Similar performance using nitrogen as the test gas in the turbine is shown in Figure 72.

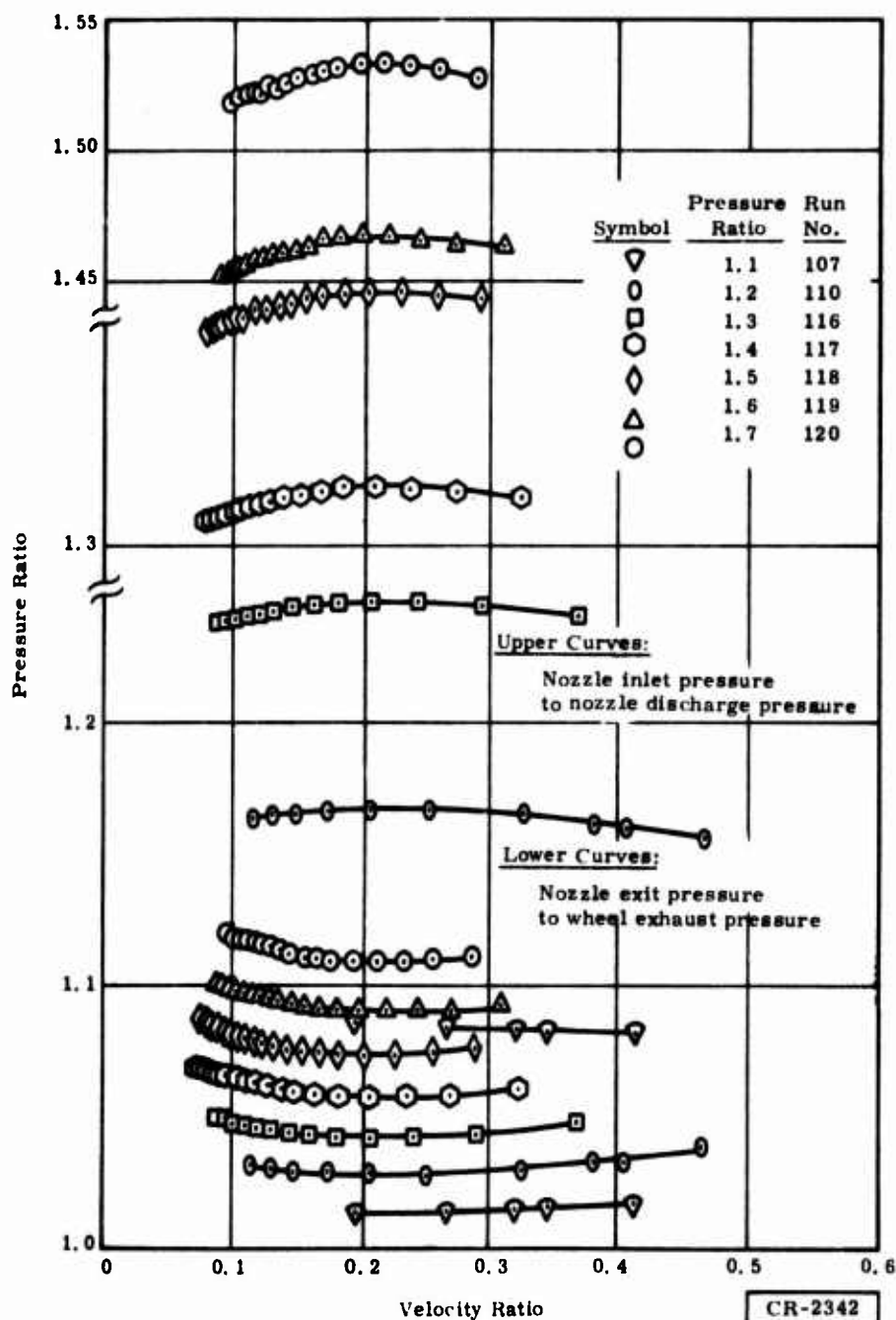


Figure 72. Turboalternator Performance -- Pressure Ratio Versus Velocity Ratio for Nitrogen Gas at Room Temperature

These sets of curves will be used to analyze and correlate the potential of flow leakage from one nozzle to the other. Hence, when the second-stage tests are available under similar conditions, the possible interstage flow leakage will be analyzed and established.

Another operating characteristic is shown by a set of curves of corrected torque versus velocity ratio. The performance data were reduced, as shown in Figure 73, for the different constant pressure ratio runs using helium gas

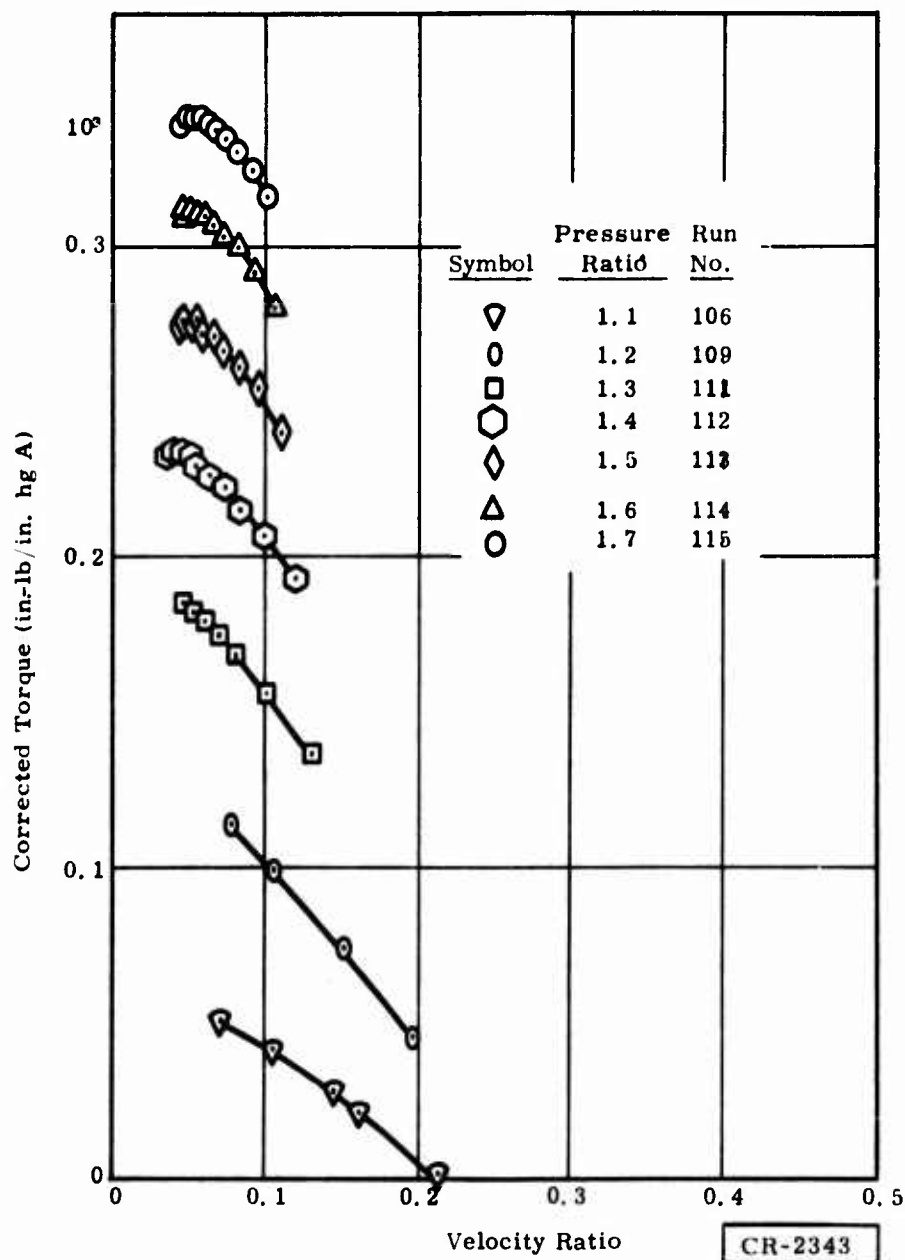


Figure 73. Turboalternator Performance -- Corrected Torque Versus Velocity Ratio for Helium Gas at Room Temperature

at room temperature. The corresponding performance data using nitrogen gas at room temperature are shown in Figure 74. These curves will be valuable for analysis and design of the final refrigeration control system.

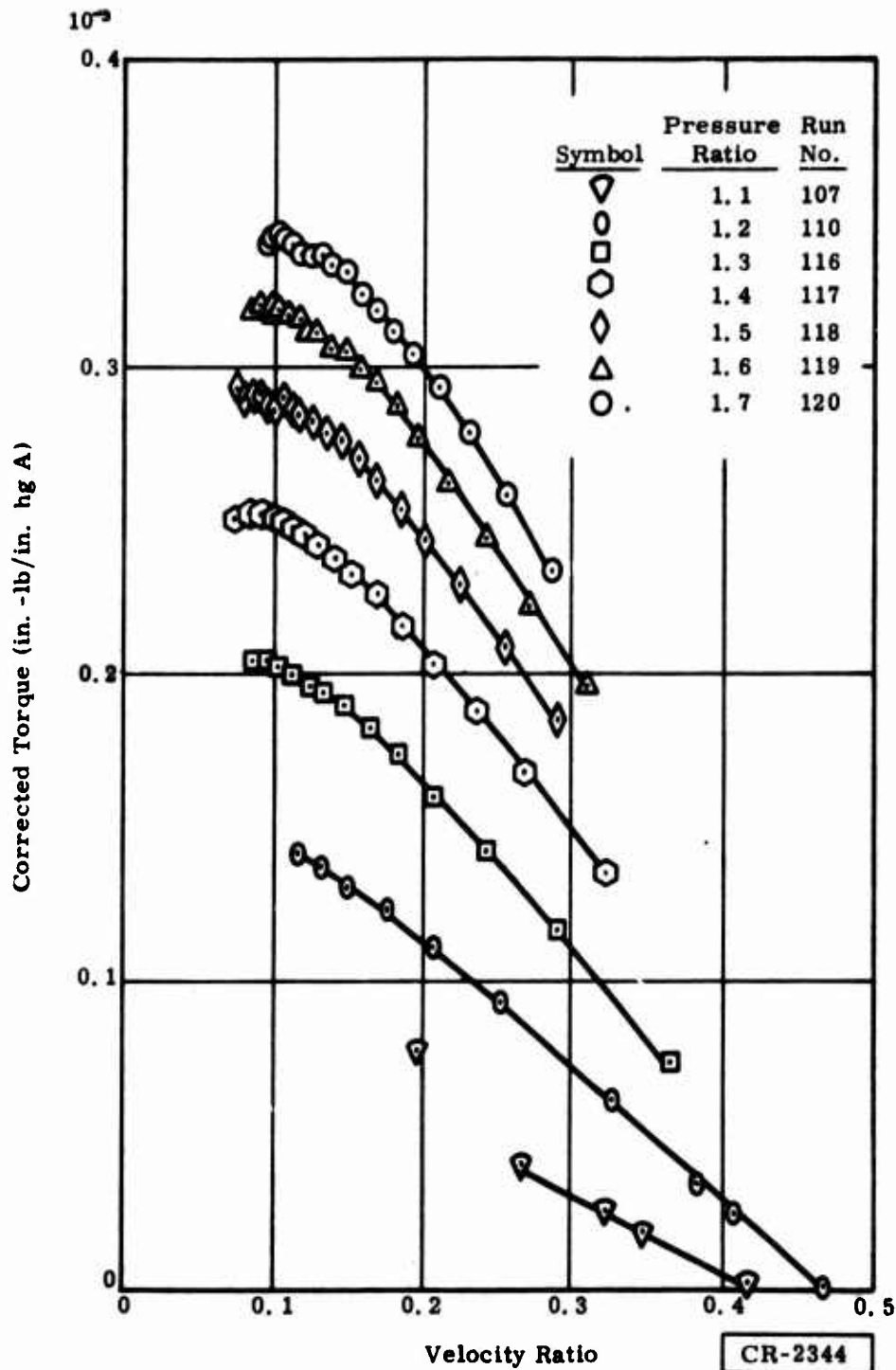


Figure 74. Turboalternator Performance -- Corrected Torque Versus Velocity Ratio for Nitrogen Gas at Room Temperature

## PERFORMANCE RESULTS

Initial room temperature, single-stage test results for the second-stage 1.1-inch-diameter wheel were reported in Contract Status Report 27. Similar room temperature test results for the first-stage, 0.5-inch-diameter wheel are described below.

Because of the relatively high bypass flow rates resulting from first-stage Runs 100 and 101, calibration of the housing leak rate characteristic was repeated. It was found that there was no significant difference in the leak rate characteristics.

There was a difference, however, in the reference point for this leakage. The first runs, 100 and 101, used the turbine exhaust as the leak rate reference ambient pressure. The more recent runs, 104 and 105, used the ambient pressure just outside the housing; this reference is more consistent with the housing leak rate calibration basis.

Figures 75 and 76 show the flow factor performance test results versus the overall pressure ratio for three conditions:

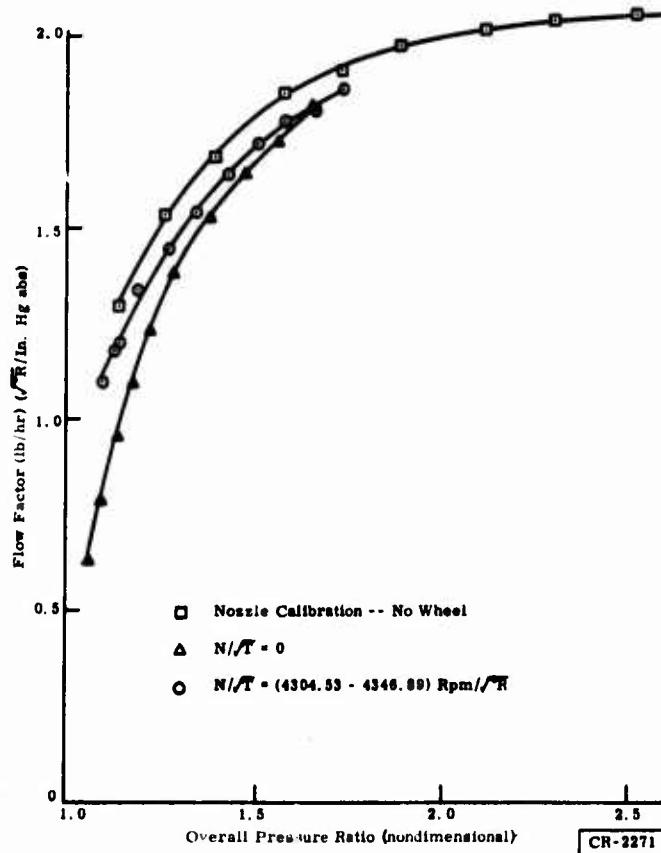


Figure 75. Flow Factor Versus Overall Pressure Ratio for Helium (Run 104)

- Nozzle calibration and no wheel installed
- Wheel installed, but the shaft kept from turning so the corrected speed is zero
- Constant mechanical rpm of about 100,000, which resulted in a corrected speed,  $N/\sqrt{T}$ , of about 4300 rpm/ $\sqrt{^{\circ}\text{R}}$

Figure 75 shows the results with helium gas, while Figure 76 shows the results with nitrogen gas. These characteristic results will be supplemented by

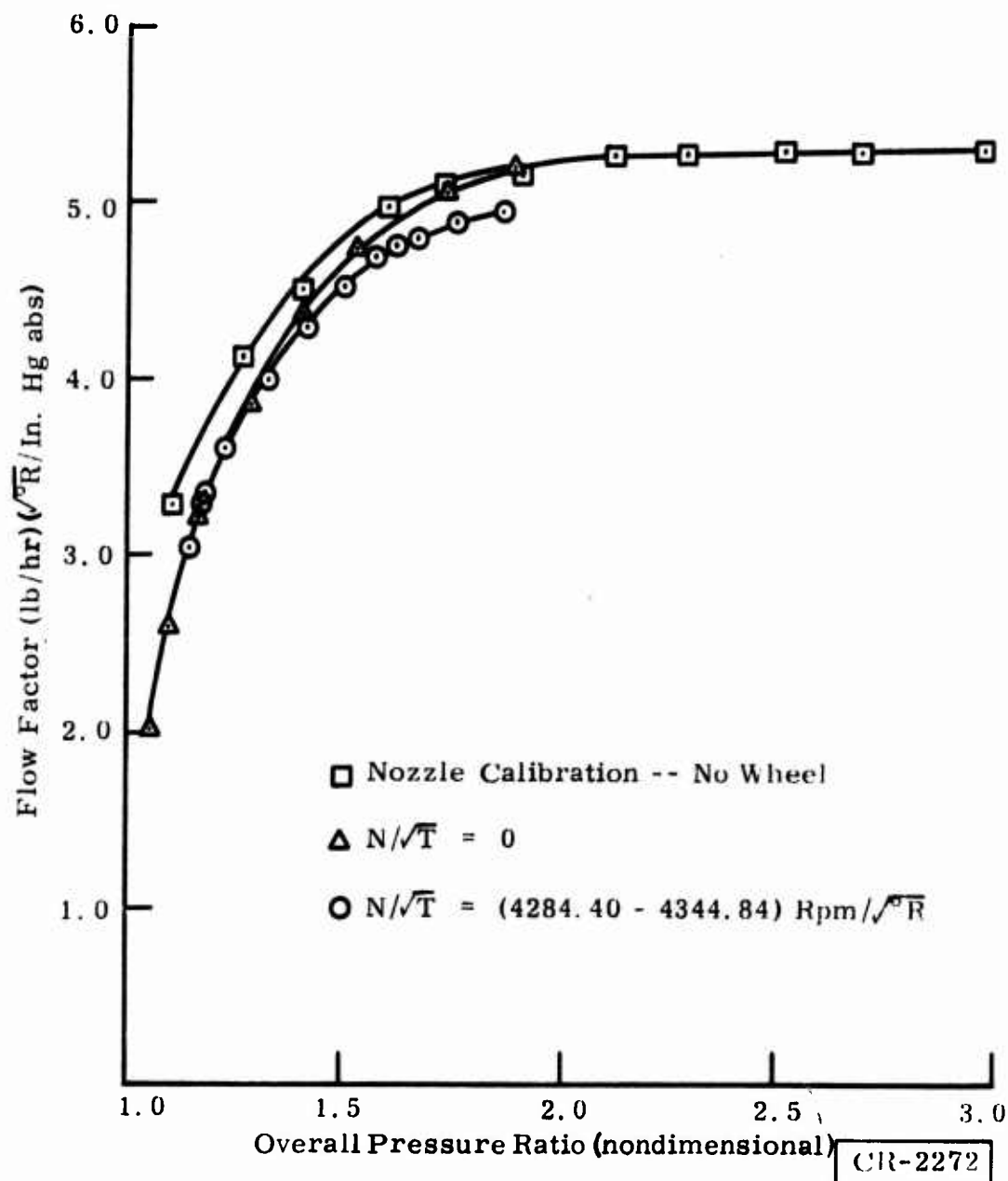


Figure 76. Flow Factor Versus Overall Pressure Ratio for Nitrogen (Run 105)



future test results and will be used in conjunction with the sizing of the turbine nozzle areas to assure that proper flow to each nozzle in the refrigerator system has been obtained.

Overall performance test results were obtained at a temperature-corrected speed of about 4300 rpm/ $\sqrt{^\circ\text{R}}$  and Figure 77 shows the flow factor and efficiency-versus-velocity ratio. The flow factor characteristics are typical for this type of operation. Figure 78 shows the leakage flow and corrected torque versus the velocity ratio. The leakage flow ratio is the fraction of the total flow to the alternator housing, where the leakage is measured from the precalibrated housing leakage characteristic. The corrected torque shown is based on the measured electrical power output and is a function of the inlet pressure in inches of mercury absolute.

Figure 79 shows the three types of efficiencies derived from the performance test results of the second stage for both helium and nitrogen gas operation.

The wheel power is the power input of the turbine wheel to the shaft. Wheel power is determined by adding the total measured electrical power output to the sum of the parasitic losses, which includes Joule and core losses and windage and bearing friction. The wheel efficiency then is the ratio of the wheel power to the isentropic power available across the turbine wheel. This efficiency measurement is reduced by any flow diverted from the turbine wheel, such as the leakage to the housing. This wheel efficiency would increase directly as the leakage is decreased, because the isentropic power is based on the full measured flow to the turbine nozzle.

The temperature-drop efficiency is the ratio of the calculated temperature drop to the isentropic temperature drop. This ratio represents the potential efficiency if there were no flow leakage losses. The actual temperature drop is calculated from the electrical power output and actual flow across only the turbine wheel. This calculation basis assumes that all electromagnetic, windage, and bearing losses would be absorbed in the turbine gas stream; this will be the case for actual turboalternator design operation. For open cycle tests with flow leaking to the alternator, this leakage flow provides a coolant stream to carry away the heat generated by the parasitic losses.

The overall efficiency shown is based on the actual measured electrical power output and the isentropic power input.

Figures 80 and 81 show the computer program output for the peak efficiency points obtained for the two gases used. All entries were described in Contract Status Report 26.

Table 6 compares the design point from Contract Status Report 25 with the two peak efficiency data points obtained. The nitrogen data show that the

	Helium (Run 104)	Nitrogen (Run 105)
Overall Efficiency	○	△
Temperature-Drop Efficiency	⊙	◇
Wheel Efficiency	□	◇
Flow Factor	□	◇

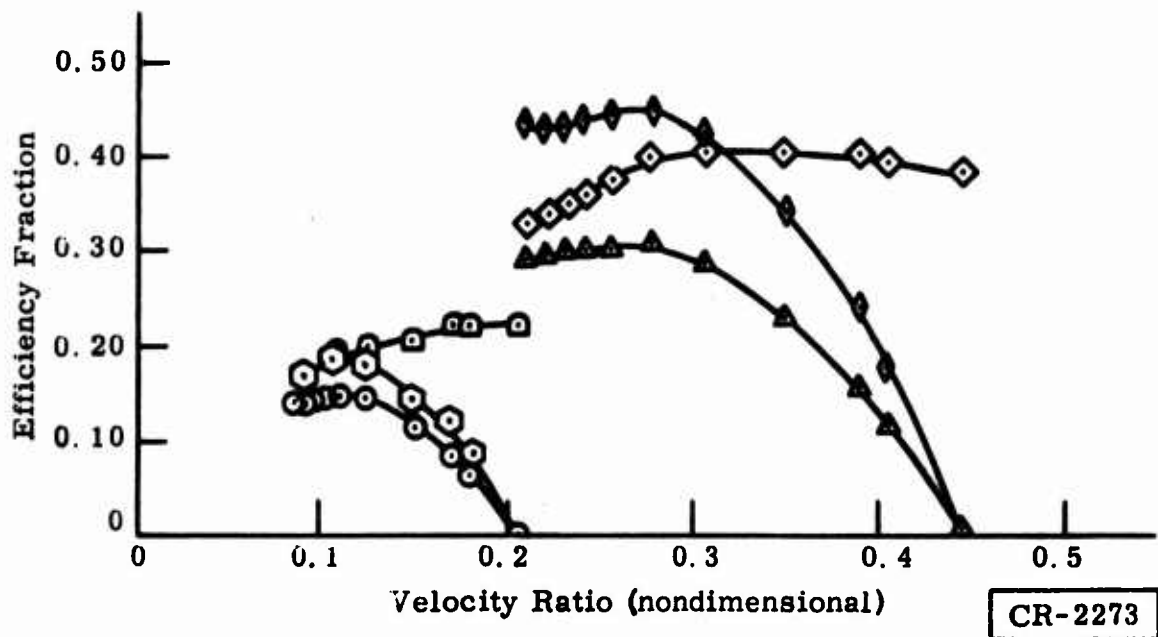
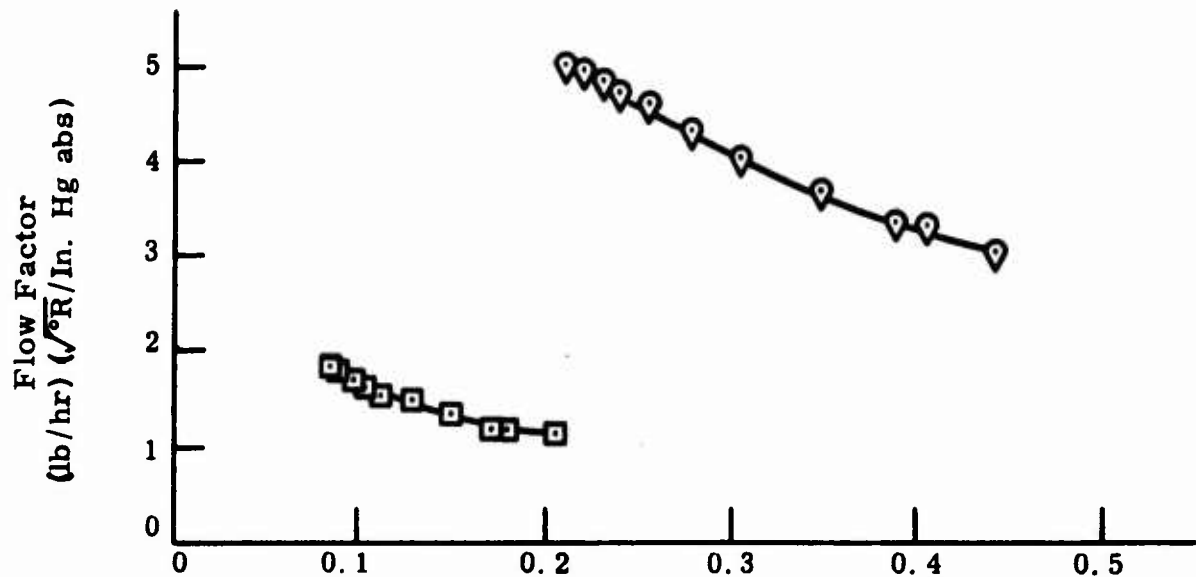


Figure 77. Flow Factor and Efficiency Versus Velocity Ratio

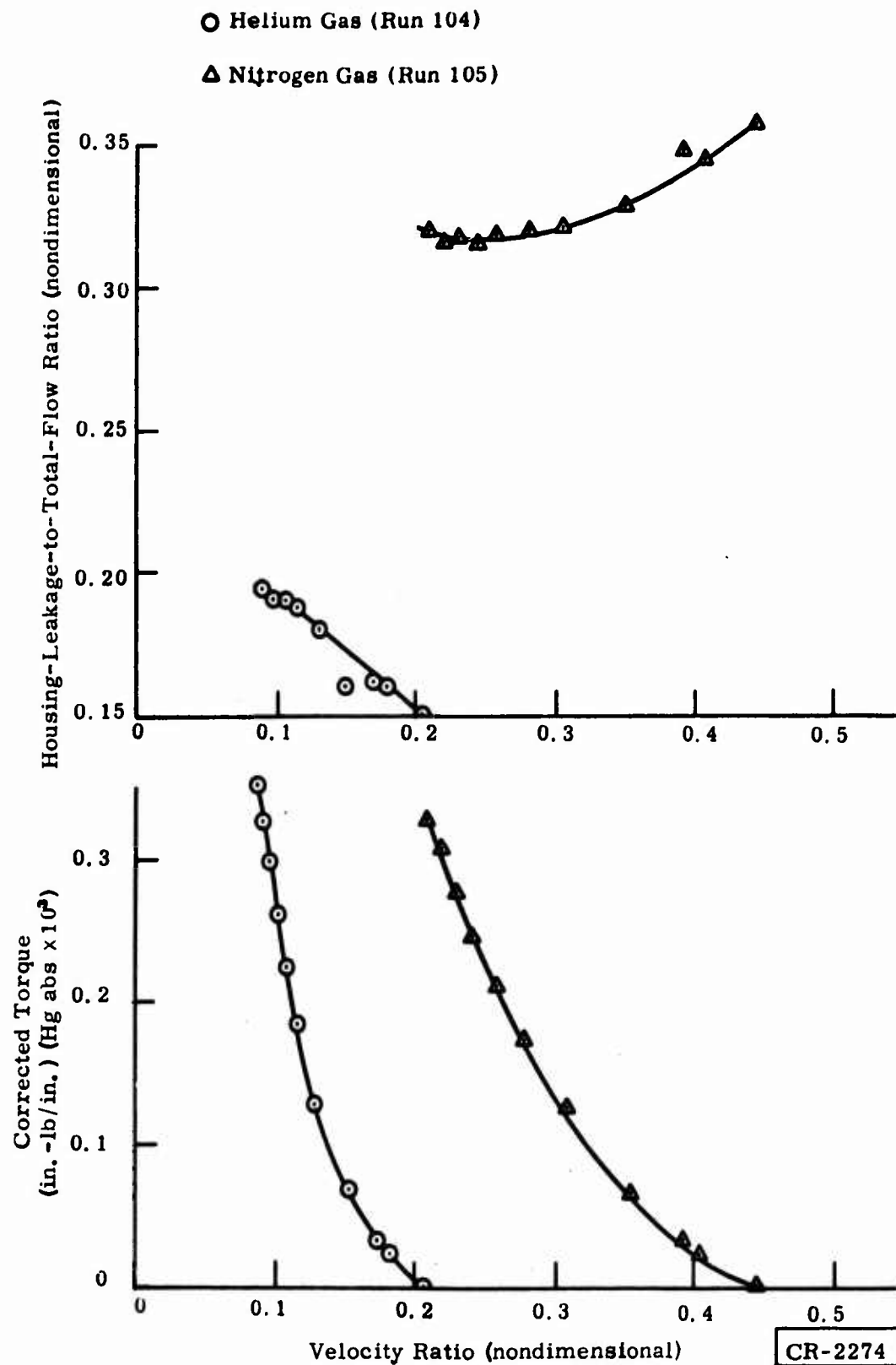


Figure 78. Leakage Ratio and Torque Versus Velocity Ratio

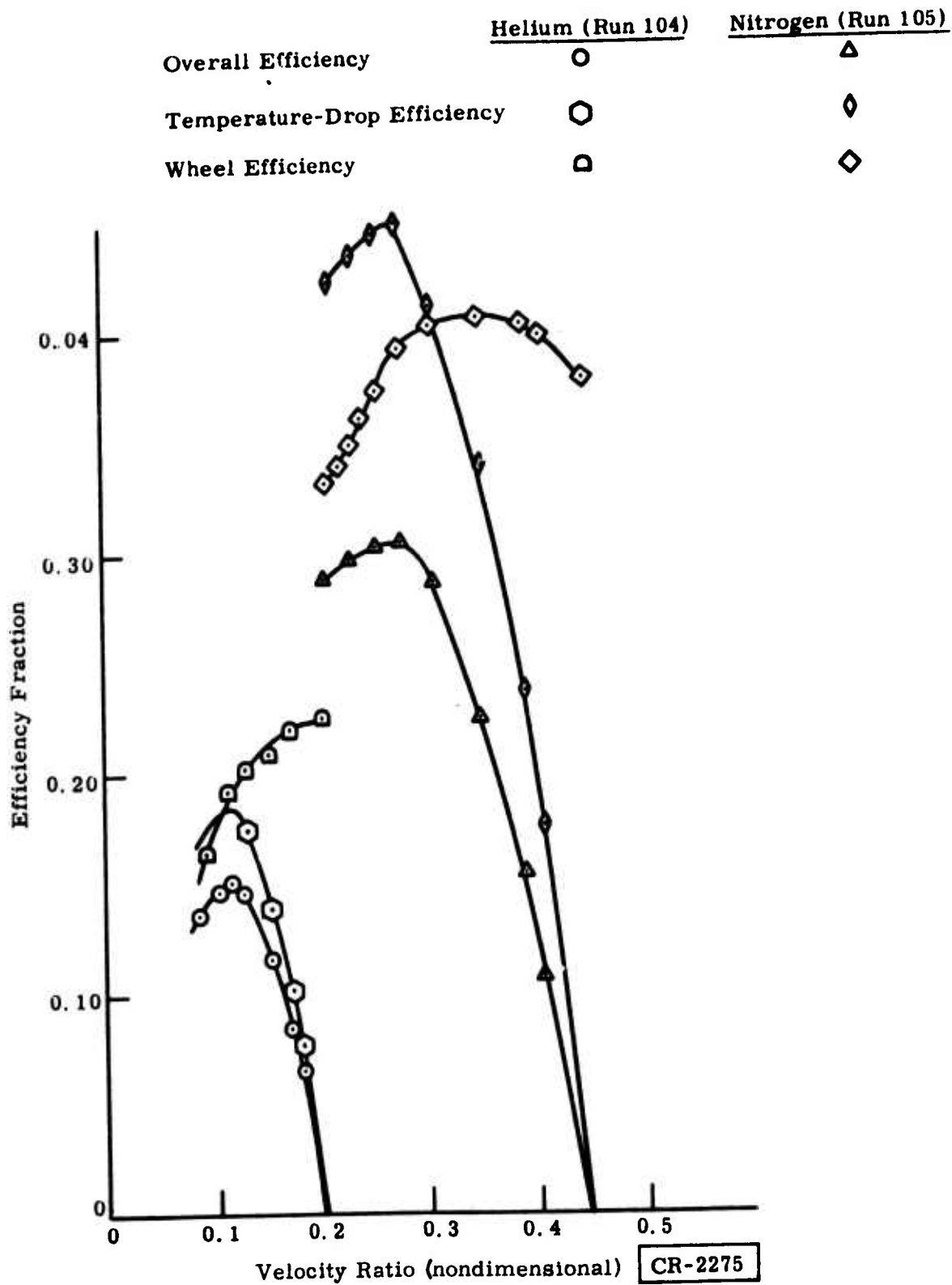


Figure 79. Efficiency Versus Velocity Ratio

\*\*\*\*\*TEST REFERENCE\*\*\*\*\*

POINT	RUN	MONTH	DAY
6	104	11	20

\*\*\*\*\*OVERALL PERFORMANCE\*\*\*\*\*

TOT EL PWR.	SPD, RPM	OVALL EFF.	CORR. SPD.
8.6856	100080.	0.1516	4323.21

\*\*\*\*\*ELECTROMAGNETIC PERFORMANCE\*\*\*\*\*

***PHASE VOLTAGE, VOLTS***,	LOAD RES (L-N)	FREQ, CPS
30.80 30.80 30.80	326.1	1668.0

*****PHASE CURRENT, AMPS*****	CORE LOSS, WATTS
0.0940 0.0940 0.0940	0.168038

*****PHASE PWR, WATTS*****	ELMAG. EFF.
2.8952 2.8952 2.8952	0.9627

*****JOULE LOSS/PHASE, WATTS*****	TOTAL JOULE LOSS, WATTS
0.0562 0.0562 0.0562	0.1687

*****SLØT TEMPS, R*****	AVG SLØT T, R	WDG RES/PH
538.110 538.110 538.110	538.110	6.3631

\*\*\*\*\*TURBINE PERFORMANCE\*\*\*\*\*

TUR IN T, R	TUR EX T, R	ACT T DR, R	PRESS. RATIO
535.90	524.74	11.16	1.3439
WHL. PWR.	WHL. EFF.	WIND PWR.	BRG. PWR.
11.1390	0.1944	0.1040	2.0127
CORR. TORQ.	T.D. EFF.	TIP SPEED	VEL. RATIO
0.1855E-03	0.1867	218.3	0.1133
TOT. FLOW	WHL. FLOW	A/W FLOW	FLOW FACT.
2.633	2.1377	0.1883	1.5446
JNL. PWR.	PIV. FIL. CL.	TH. LØ. PWR.	TH. LØ. CL.
0.4216	250.00	0.5848	450.00

CR-2276

Figure 80. Single-Stage Turboalternator Open Cycle Performance with Helium Gas at Room Temperature

\*\*\*\*\*TEST REFERENCE\*\*\*\*\*

POINT	RUN	MONTH	DAY
6	105	11	20

\*\*\*\*\*OVERALL PERFORMANCE\*\*\*\*\*

TOT EL PWR.	SPD, RPM	OVALL EFF.	CORR. SPD.
8.6574	100080.	0.3069	4327.69

\*\*\*\*\*ELECTROMAGNETIC PERFORMANCE\*\*\*\*\*

***PHASE VOLTAGE, VOLTS***	LOAD RES (L-N)	FREQ, CPS
30.70 30.70 30.70	326.5	1668.0

*****PHASE CURRENT, AMPS*****	CORE LOSS, WATTS
0.0940 0.0940 0.0940	0.168038

*****PHASE PWR, WATTS*****	ELMAG. EFF.
2.8858 2.8858 2.8858	0.9625

*****Joule LOSS/PHASE, WATTS*****	TOTAL Joule LOSS, WATTS
0.0563 0.0563 0.0563	0.1689

*****SLØT TEMPS, R*****	AVG SLØT T, R	WDG RES/PH
539.037 538.640 538.839	538.839	6.3701

\*\*\*\*\*TURBINE PERFORMANCE\*\*\*\*\*

TUR IN T, R	TUR EX T, R	ACT T DR, R	PRESS. RATIO
534.79	512.11	22.68	1.4125
WHL. PWR.	WHL. EFF.	WIND PWR.	BRG. PWR.
11.1015	0.3935	0.3358	1.7714
CORR. TORQ.	T.D. EFF.	TIP SPEED	VEL. RATIO
0.1757E-03	0.4514	218.3	0.2764
TOT. FLOW	WHL. FLOW	A/W FLOW	FLOW FACT.
7.717	5.2465	0.3201	4.2962
JNL. PWR.	PIV. FIL. CL.	TH. LØ. PWR.	TH. LØ. CL.
0.3740	250.00	0.5117	450.00

CR-2277

Figure 81. Single-Stage Turboalternator Open Cycle Performance with Nitrogen Gas at Room Temperature

Table 6  
COMPARISON OF TURBOALTERNATOR DESIGN AND TEST RESULTS  
(First Stage Alone, Open Cycle)

Characteristic	Design Operation*	Warm Operation Data Point 6 (Run 104)	Warm Operation Data Point 6 (Run 105)
Gas	He	He	N <sub>2</sub>
Inlet temperature (°R)	22.40	535.9	534.8
Inlet temperature (°K)	12.46	298.0	296.5
Exhaust pressure (psia)	5.384	14.41	14.47
Pressure ratio	1.692	1.3439	1.4125
Speed (rpm)	80,000	100,000	100,080
Corrected speed (rpm $\sqrt{^\circ R}$ )	16,930	4323.2	4327.7
Velocity ratio	0.3400	0.1133	0.2764
Overall efficiency	0.4128	0.1516	0.3069
Temperature-drop efficiency	--	0.1867	0.4514
Wheel efficiency	0.4727	0.1944	0.3935
Electromagnetic efficiency	0.945	0.9627	0.9625
Flow factor	1.570	1.5446	4.2962
Total mass flow (lb/hr)	6.156	2.633	7.717
Wheel flow (lb/hr)	--	2.1377	5.2465
Leakage-to-total-flow ratio	--	0.1883	0.3201
Net electric power (watts)	4.019	8.686	8.6574
Wheel power (watts)	4.496	11.139	11.102
Windage losses (watts)	0.1350	0.1040	0.3358
Bearing losses (watts)	0.3185	2.0127	1.7714
Core plus Joule losses (watts)	0.2486	0.3367	0.3369
Total parasitic losses (watts)	0.7021	2.4534	2.4441
Wheel axial clearance (mils)	0.001	0.002	0.002

\*From Contract Status Report 25.

CR-2278

design efficiency of 0.4128 can be met with no leakage, because of the high temperature-drop efficiency of 0.4514. This point is near the design velocity ratio of 0.340. Other entries in the table also provide some basis for being optimistic that the design point efficiency can be achieved.

#### CRYOGENIC TEMPERATURE TESTS

Additional performance tests were conducted at cryogenic temperatures, in the vicinity of 177°K (318°R). Table 7 lists the runs completed.

Performance data were obtained and reduced, and curves were plotted, including:

Table 7  
SUMMARY OF TURBOALTERNATOR PERFORMANCE RESULTS  
(Helium Gas at 318°R)

Run	Number of Data Points	Overall Pressure Ratio	Ambient Pressure (inches mercury)	Extreme Ranges of Results						Limitations of Test		
				Electrical Power (watts)	Speed (rpm)	Overall Efficiency (fraction)	Corrected Speed (rpm °R)	Wheel Efficiency (fraction)	Velocity Ratio (nondimensional)	Corrected Torque (in. -lb/in. hg A)	High Speed	Low Speed
121	10	1.5	29.646	6.5844 14.0913	40,800 97,380	0.0920 0.1997	2285.3 5456.5	0.1023 0.2288	0.0516 0.1232	0.2741 × 10 <sup>-3</sup> 0.3059 × 10 <sup>-3</sup>		X
122	8	1.6	29.638	9.2418 16.0632	48,240 88,080	0.1022 0.1782	2704.3 4937.7	0.1135 0.1995	0.0571 0.1043	0.3242 × 10 <sup>-3</sup> 0.3407 × 10 <sup>-3</sup>		X
123*	1	1.7	29.638	20.6580	100,440	0.1896	5623.6	0.2123	0.1125	0.3444 × 10 <sup>-3</sup>		X
											CR-1099	

\*Shaft touched inner thrust and stopped at the lower speed.

CR-1099



- Overall efficiency versus velocity ratio
- Wheel efficiency versus velocity ratio
- Flow factor versus velocity ratio
- Corrected torque versus velocity ratio
- Flow factor versus corrected speed
- Electrical power output versus speed
- Pressure ratio versus velocity ratio
- Flow factor versus pressure ratio

These curves are included as Figures 82 through 105.

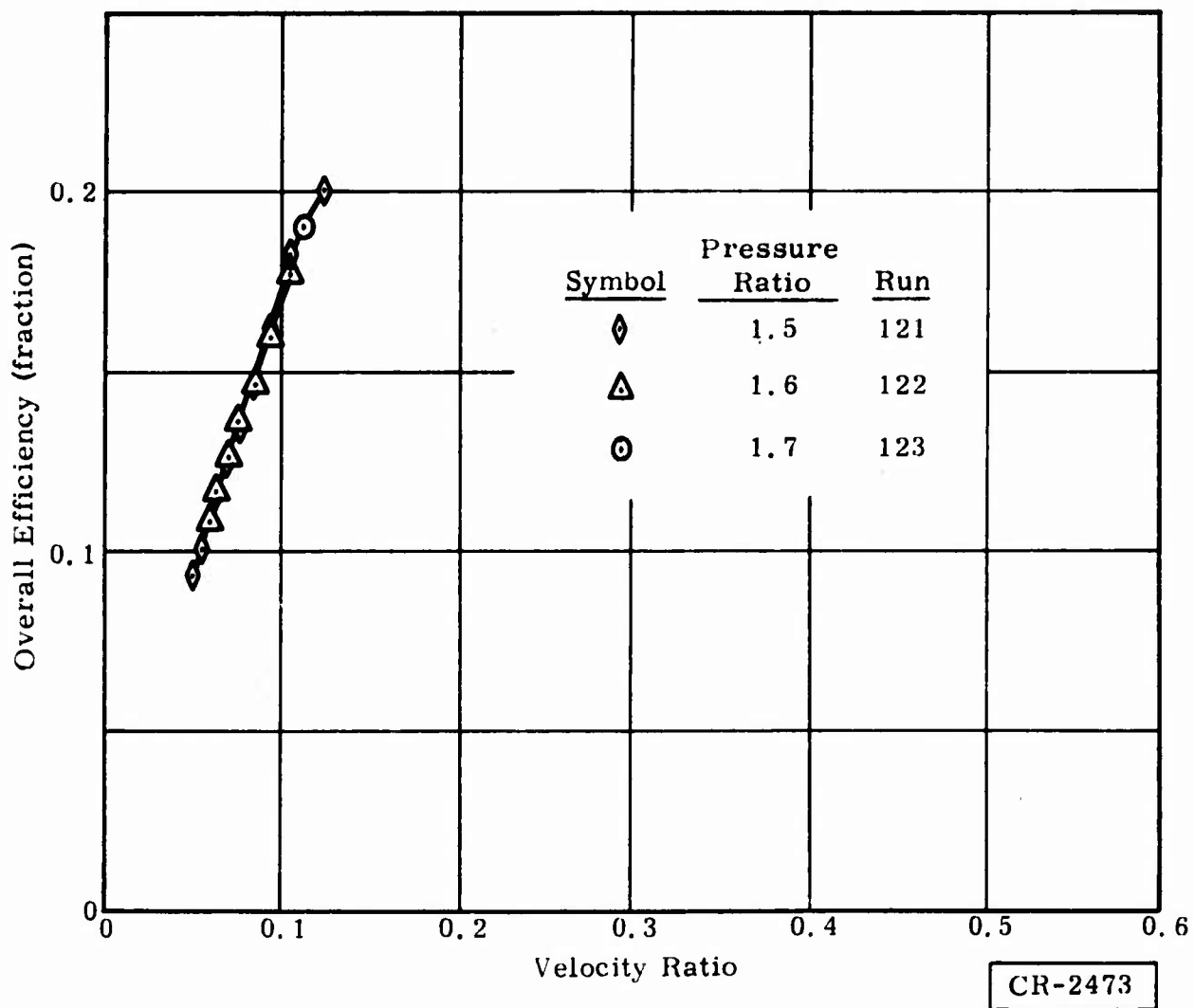


Figure 82. Turboalternator Performance -- Overall Efficiency Versus Velocity Ratio for Helium Gas at 318°R, 177°K

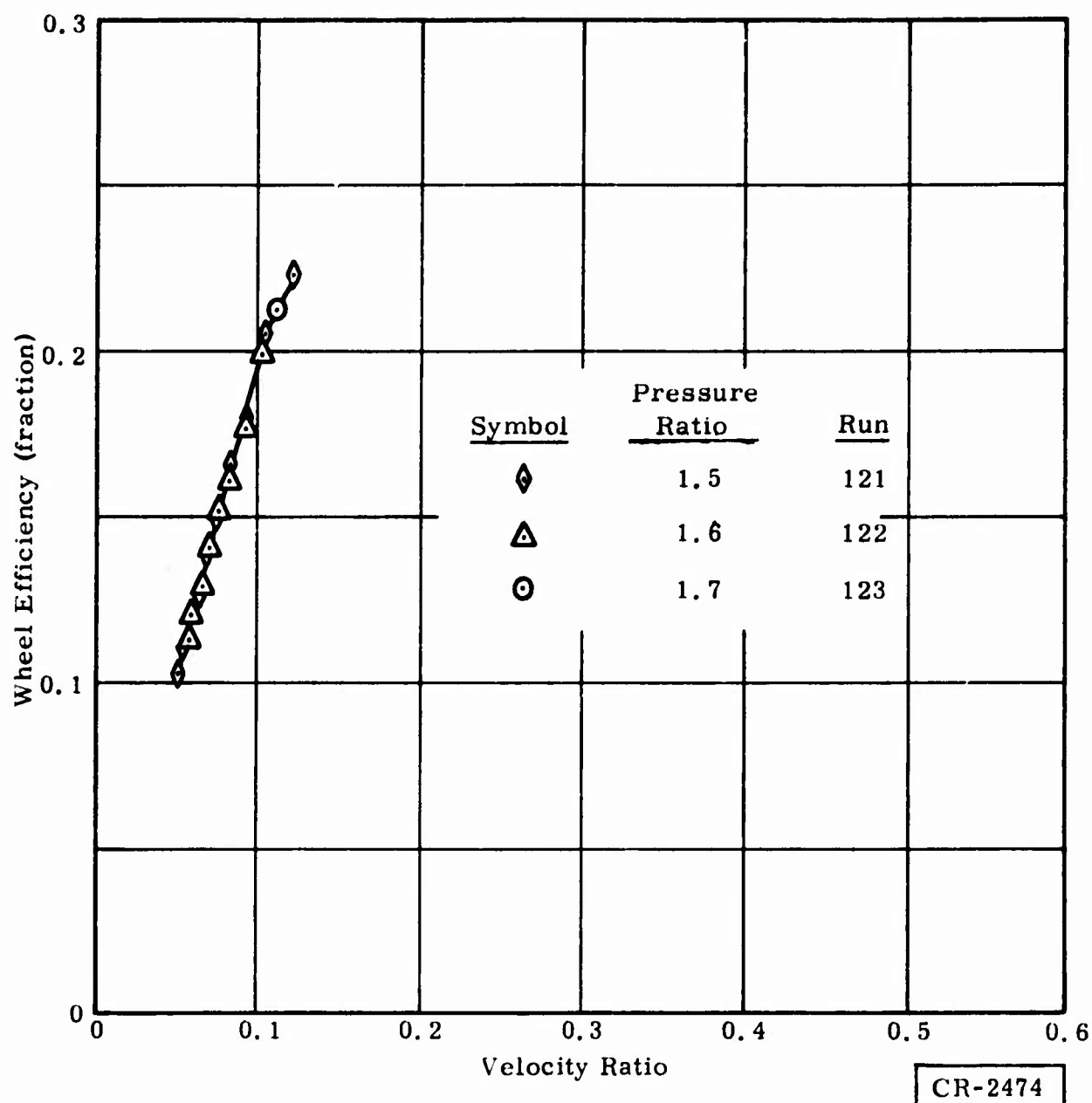


Figure 83. Turboalternator Performance -- Wheel Efficiency Versus Velocity Ratio for Helium Gas at 318° R, 177°K

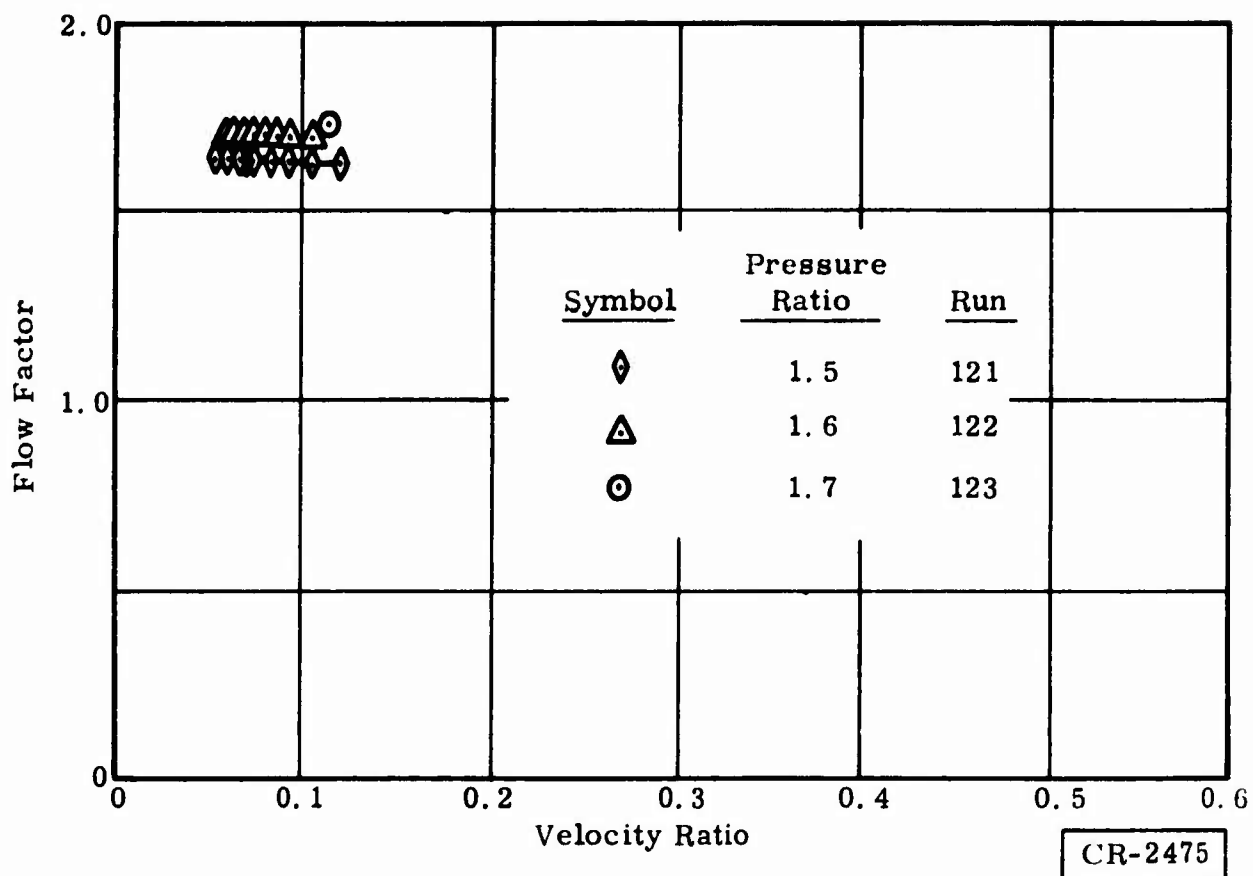


Figure 84. Turboalternator Performance -- Flow Factor Versus Velocity Ratio for Helium Gas at 318° R, 177°K

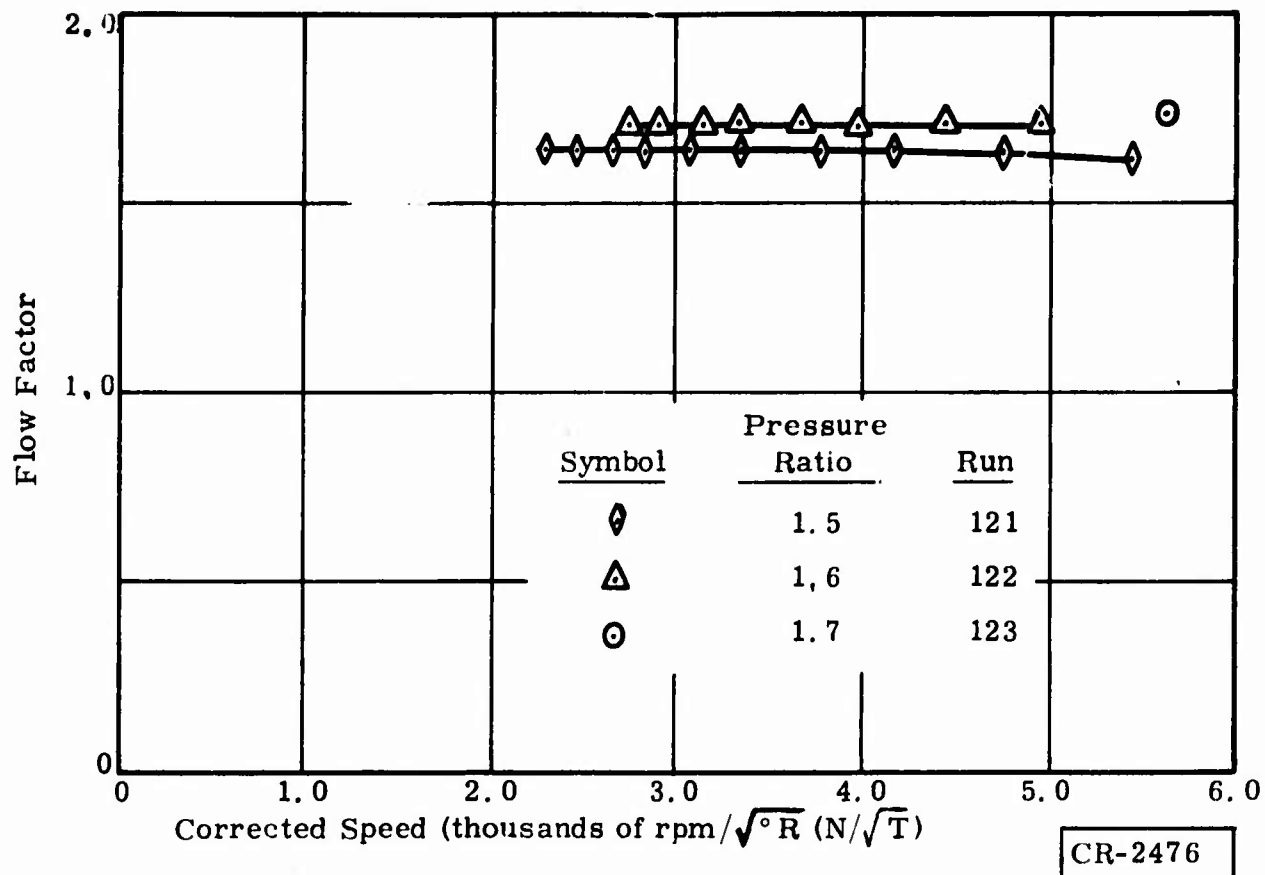


Figure 85. Turboalternator Performance -- Flow Factor Versus Corrected Speed for Helium Gas at 318°R, 177°K

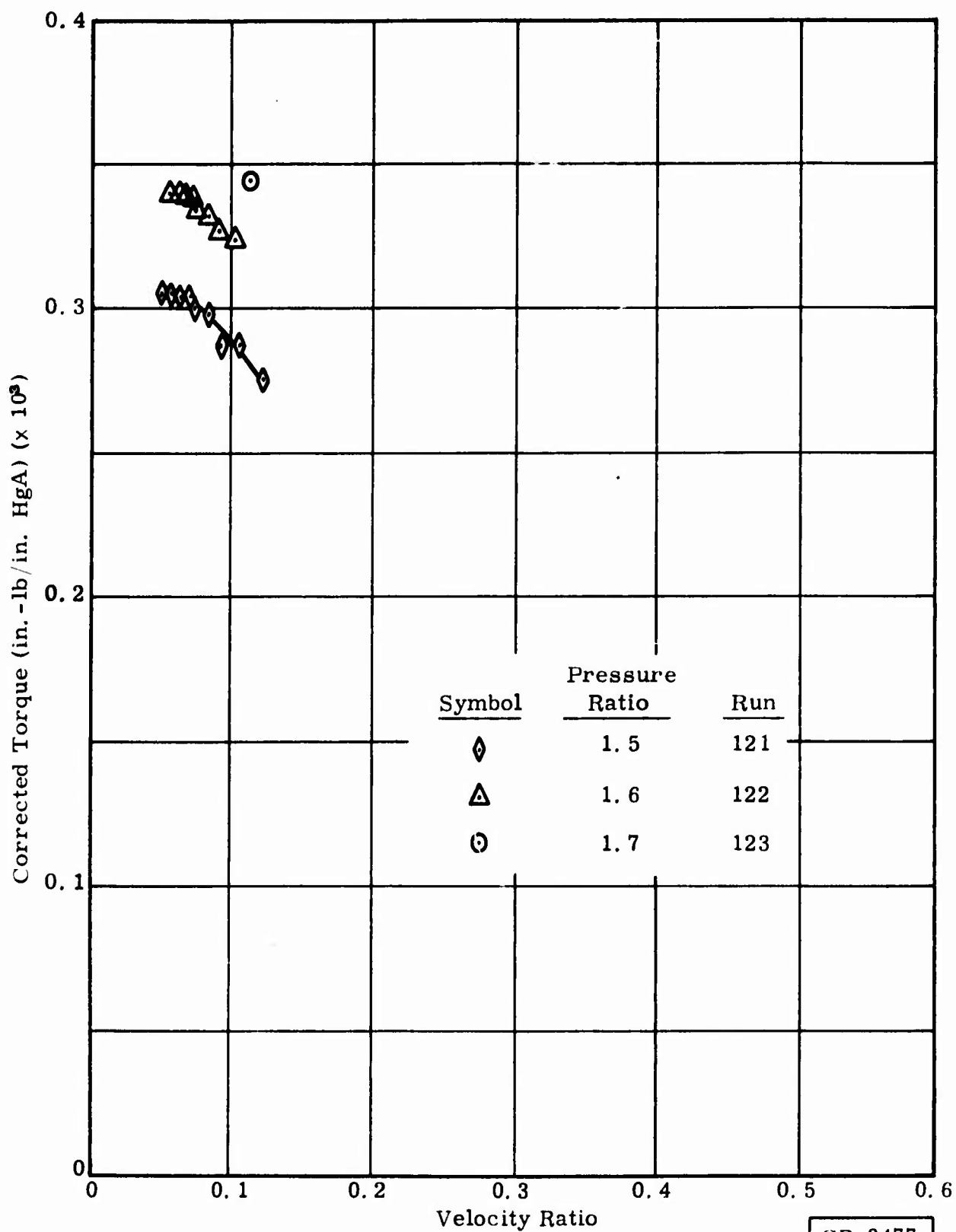


Figure 86. Turboalternator Performance -- Corrected Torque Versus Velocity Ratio for Helium Gas at 318°R, 177°K

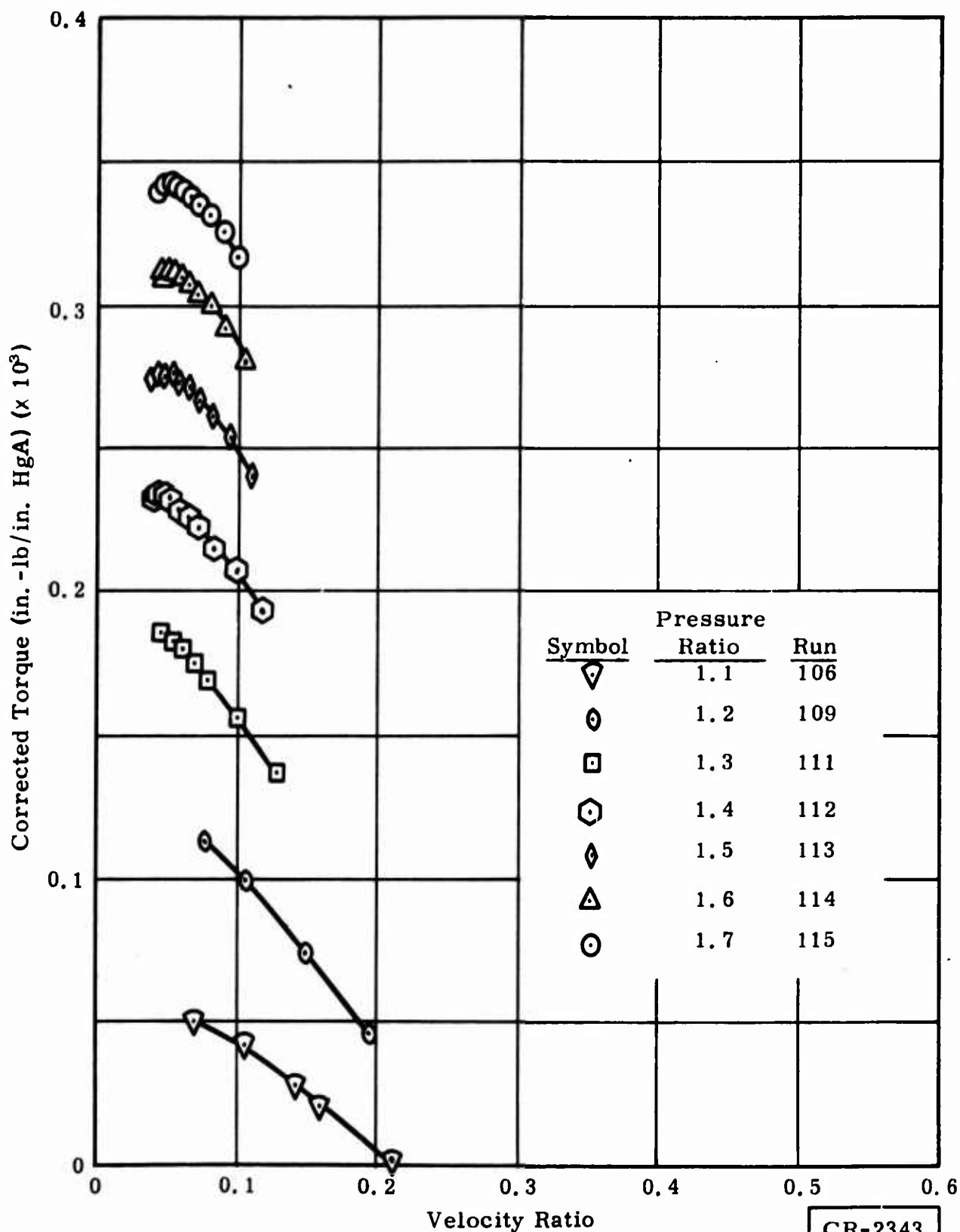


Figure 87. Turboalternator Performance -- Electrical Output Power Versus Speed for Helium Gas at 318°R, 177°K

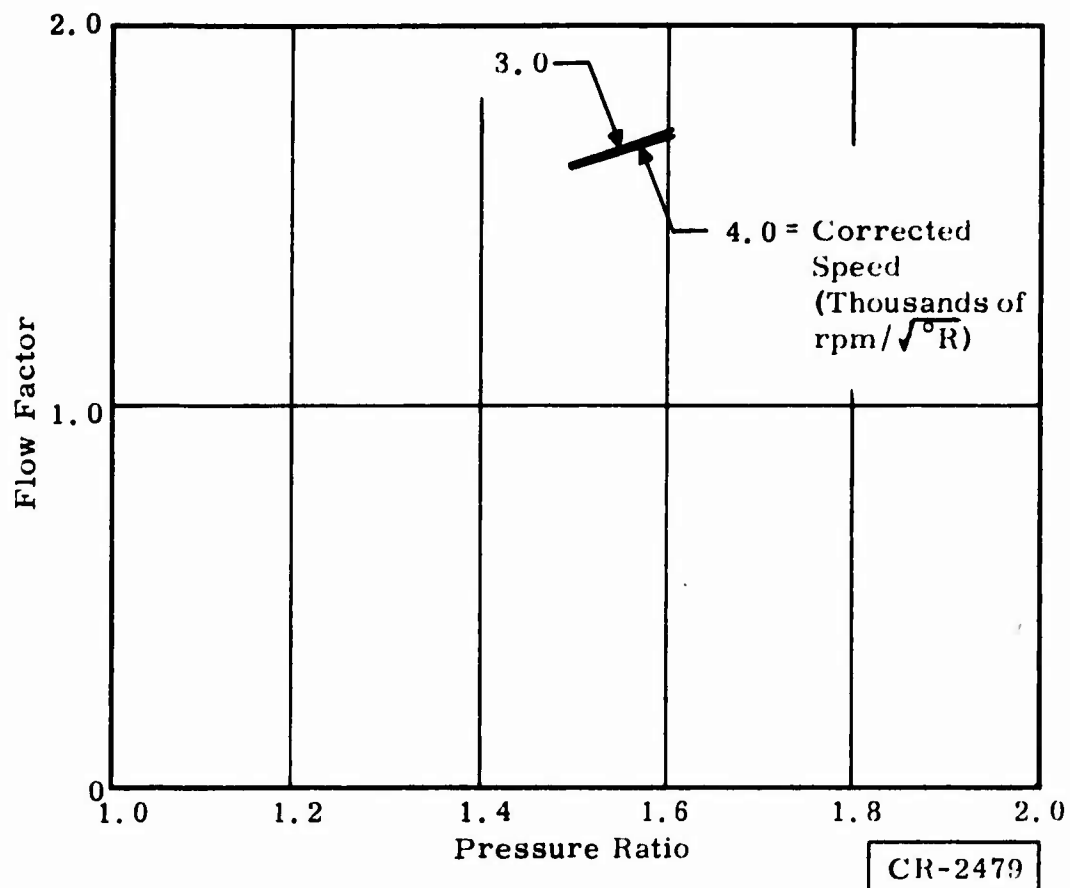


Figure 88. Turboalternator Performance -- Flow Factor Versus Pressure Ratio for Helium Gas at 318°R

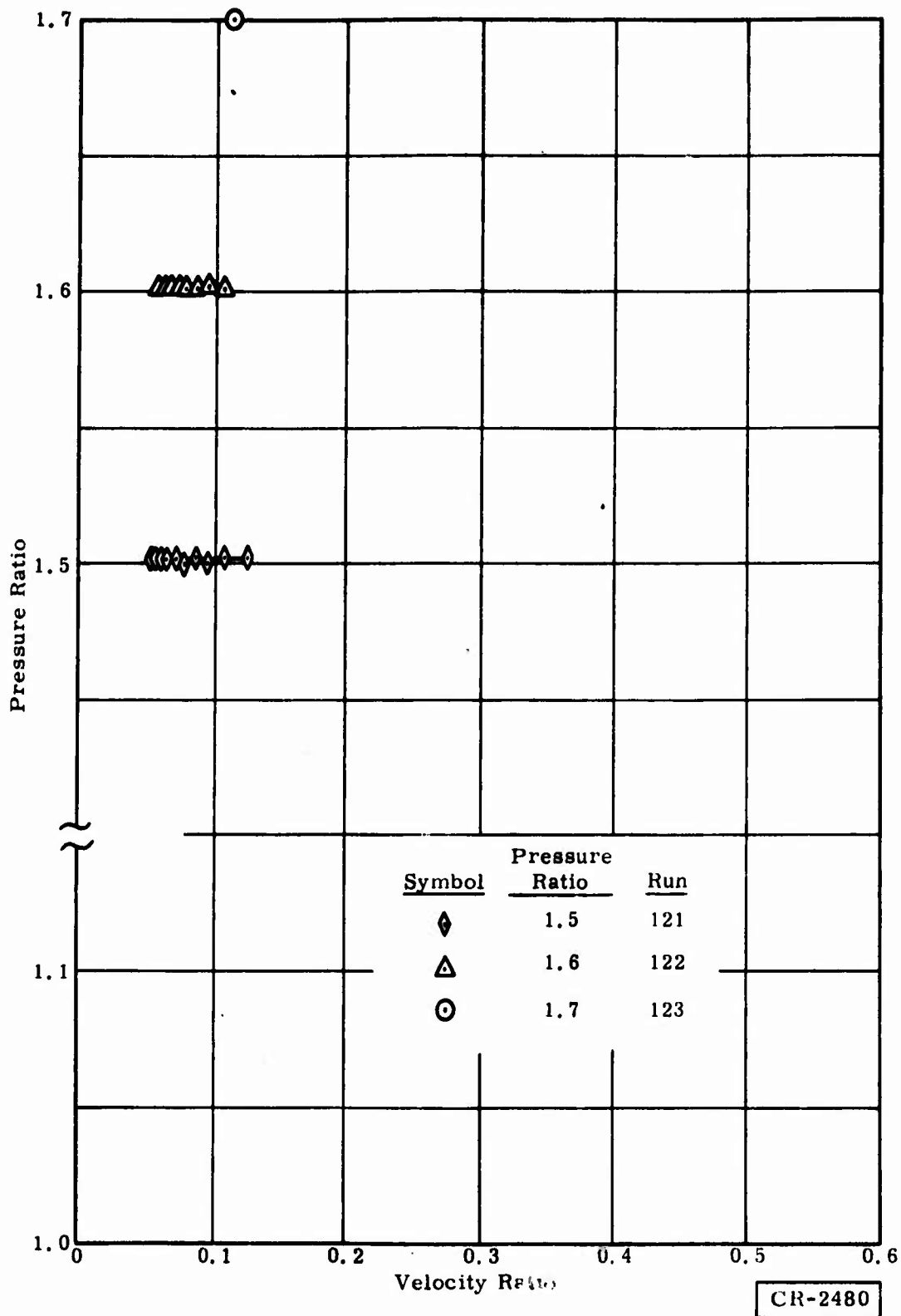


Figure 89. Turboalternator Performance -- Pressure Ratio Versus Velocity Ratio for Helium Gas at 318°R



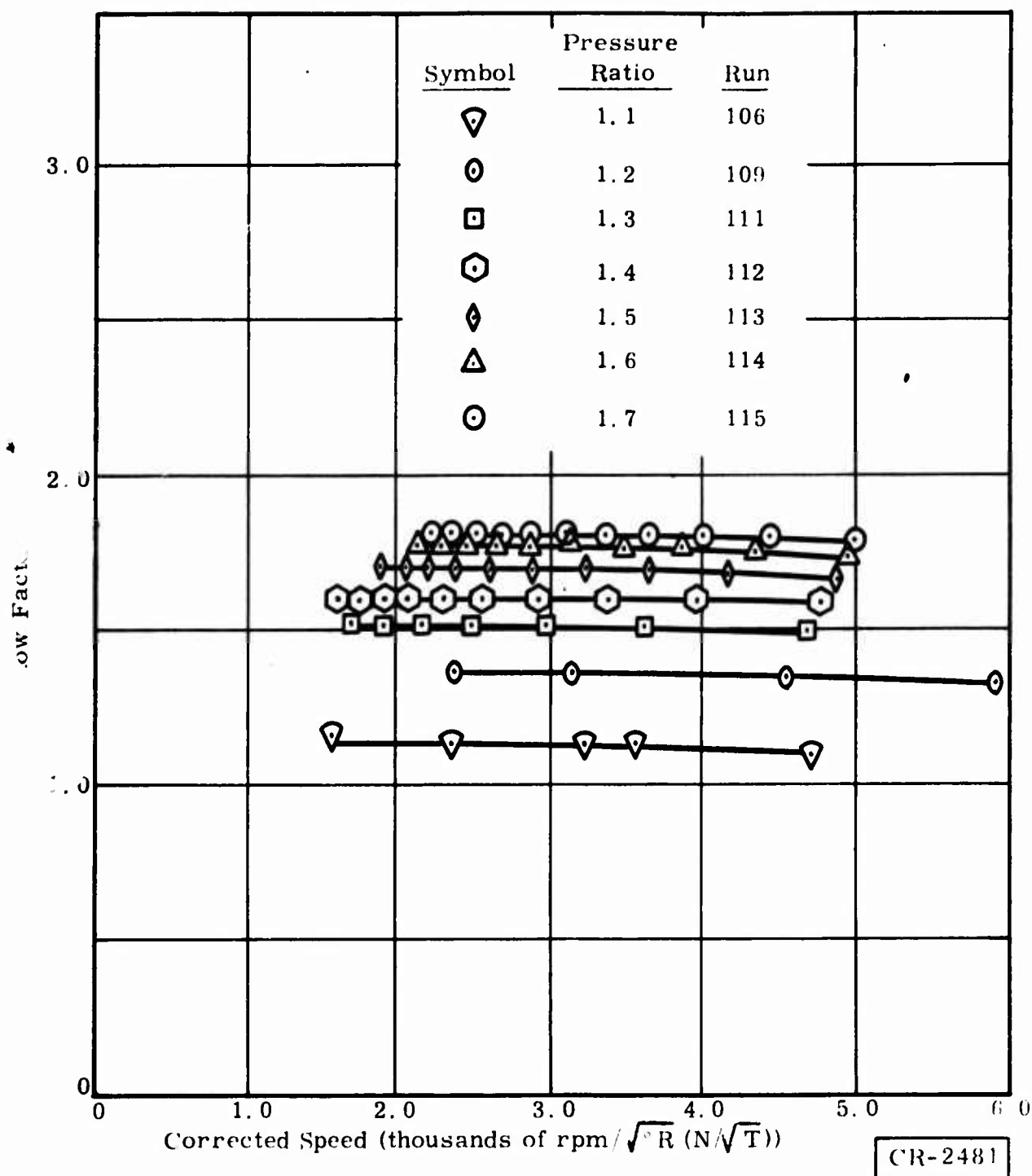


Figure 90. Turboalternator Performance -- Flow Factor Versus Corrected Speed for Helium Gas at Room Temperature

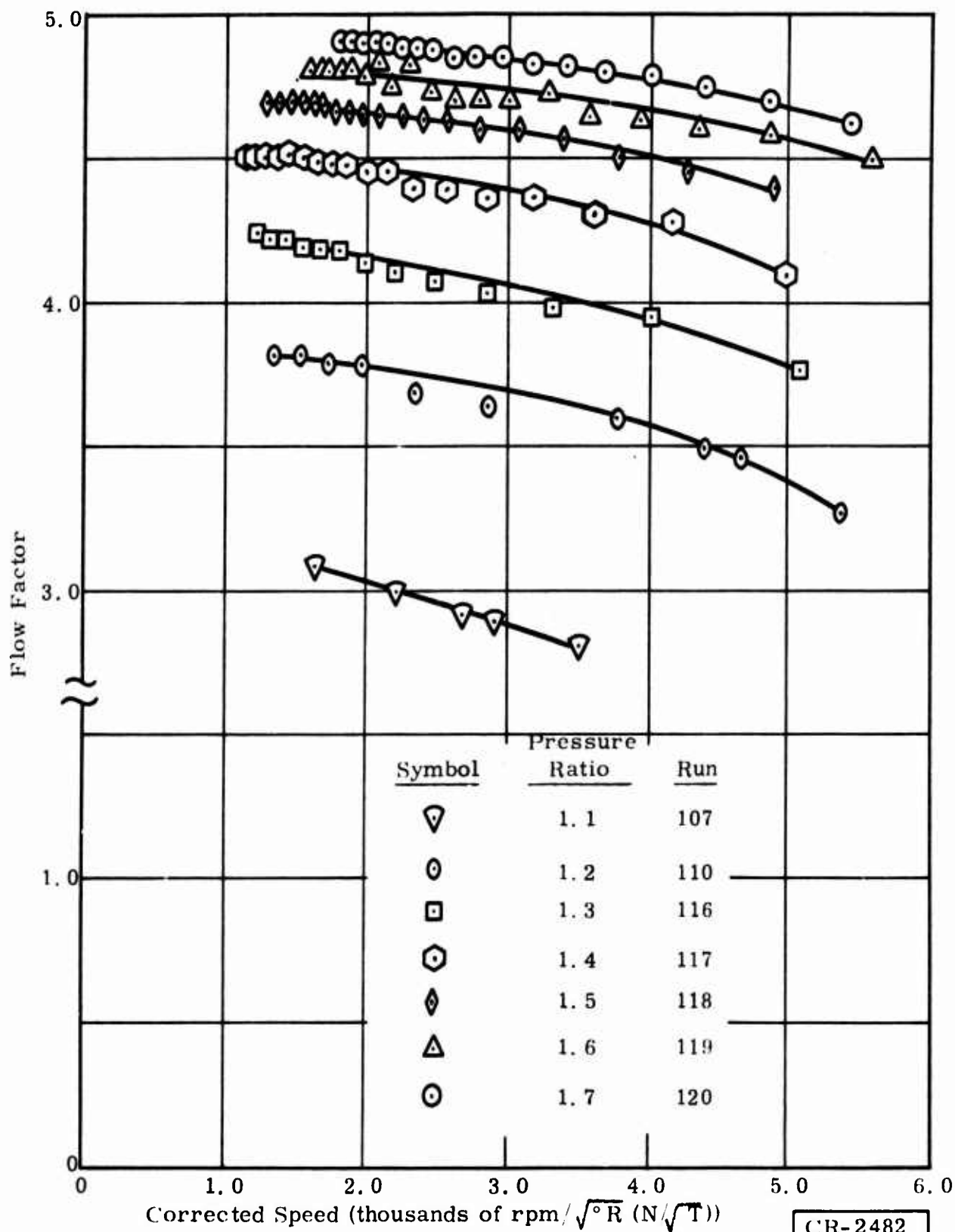


Figure 91. Turboalternator Performance -- Flow Factor Versus Corrected Speed for Nitrogen Gas at Room Temperature

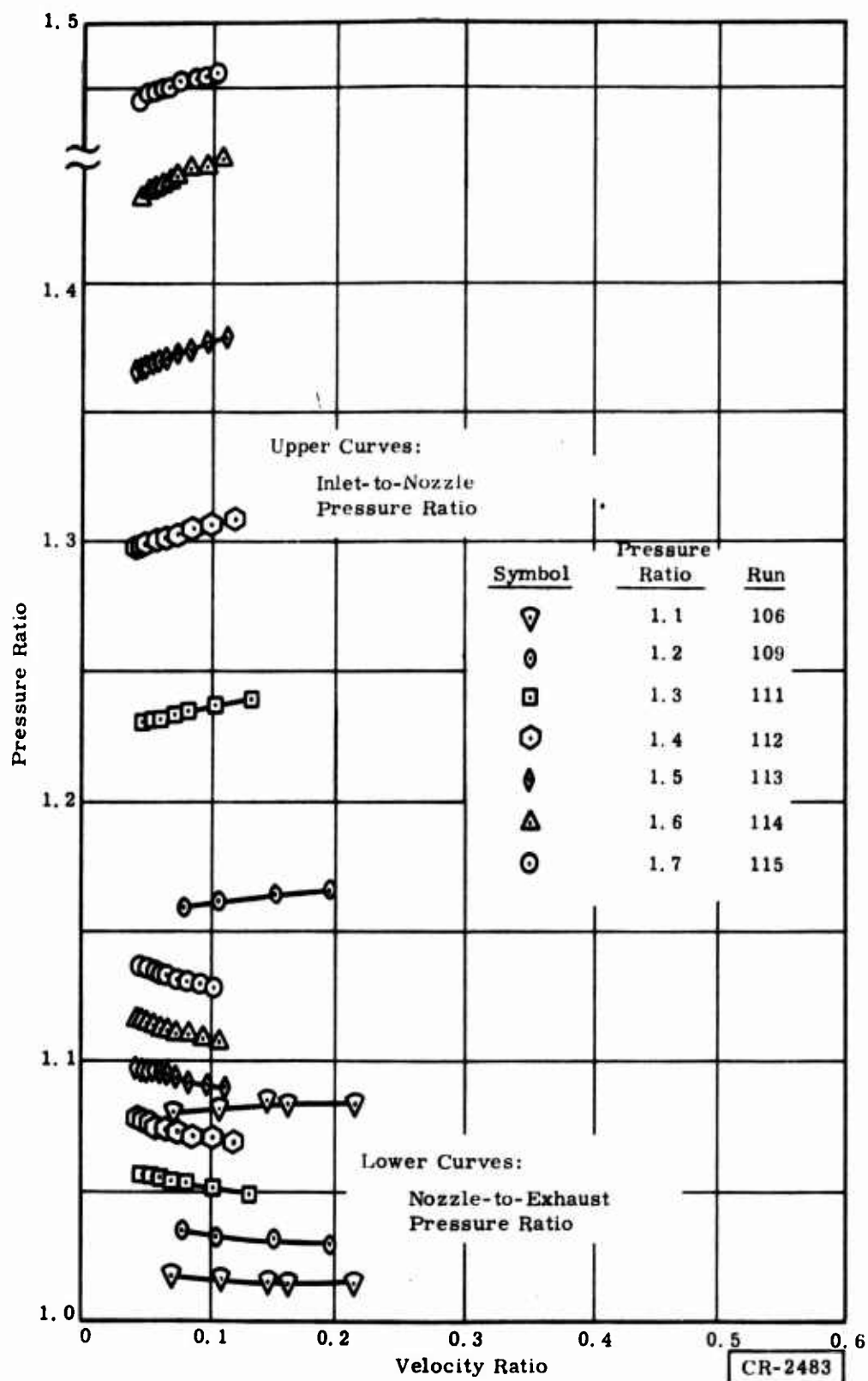


Figure 92. Turboalternator Performance -- Pressure Ratio Versus Velocity Ratio for Helium Gas at Room Temperature

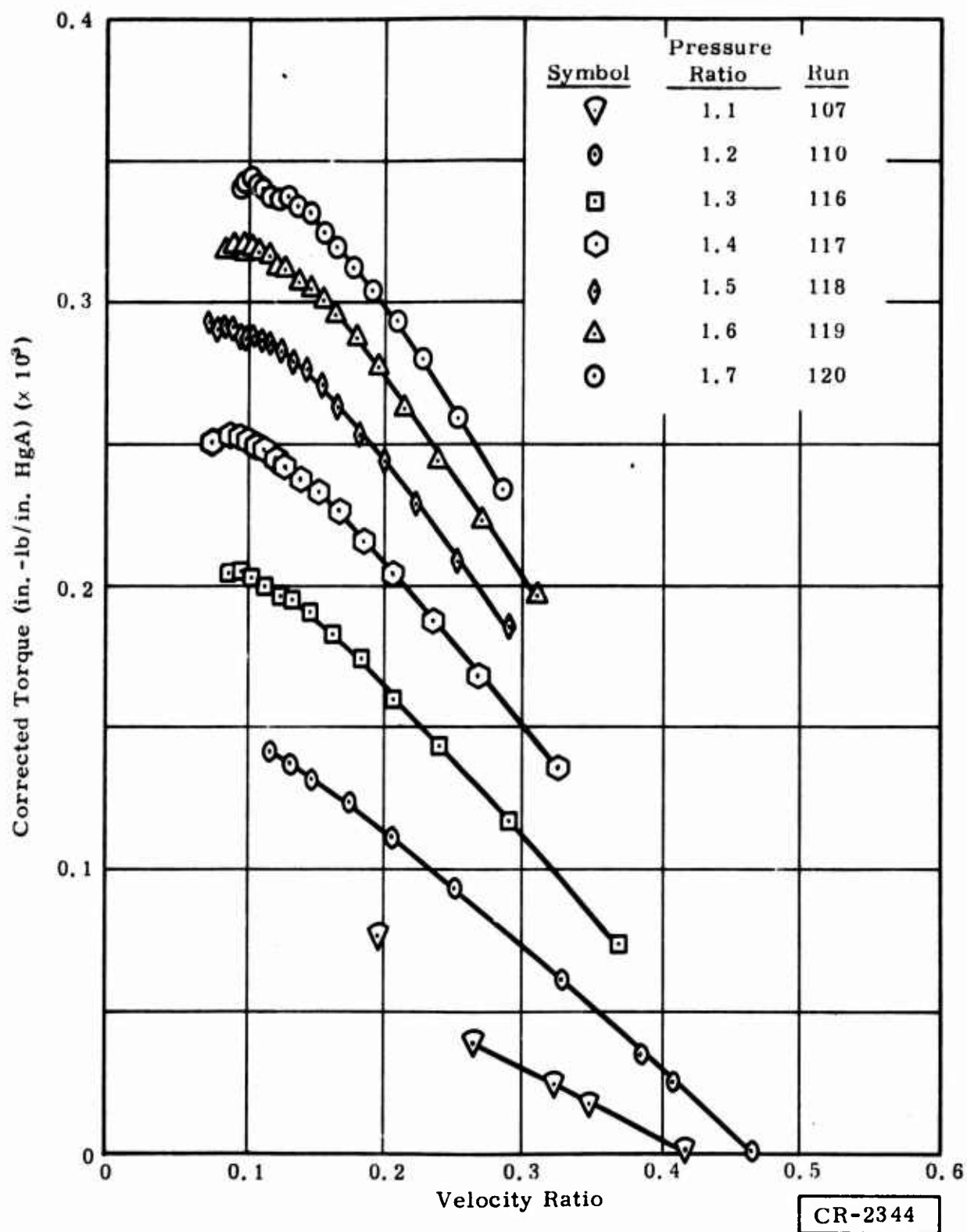


Figure 93. Turboalternator Performance -- Corrected Torque Versus Velocity Ratio for Nitrogen Gas at Room Temperature

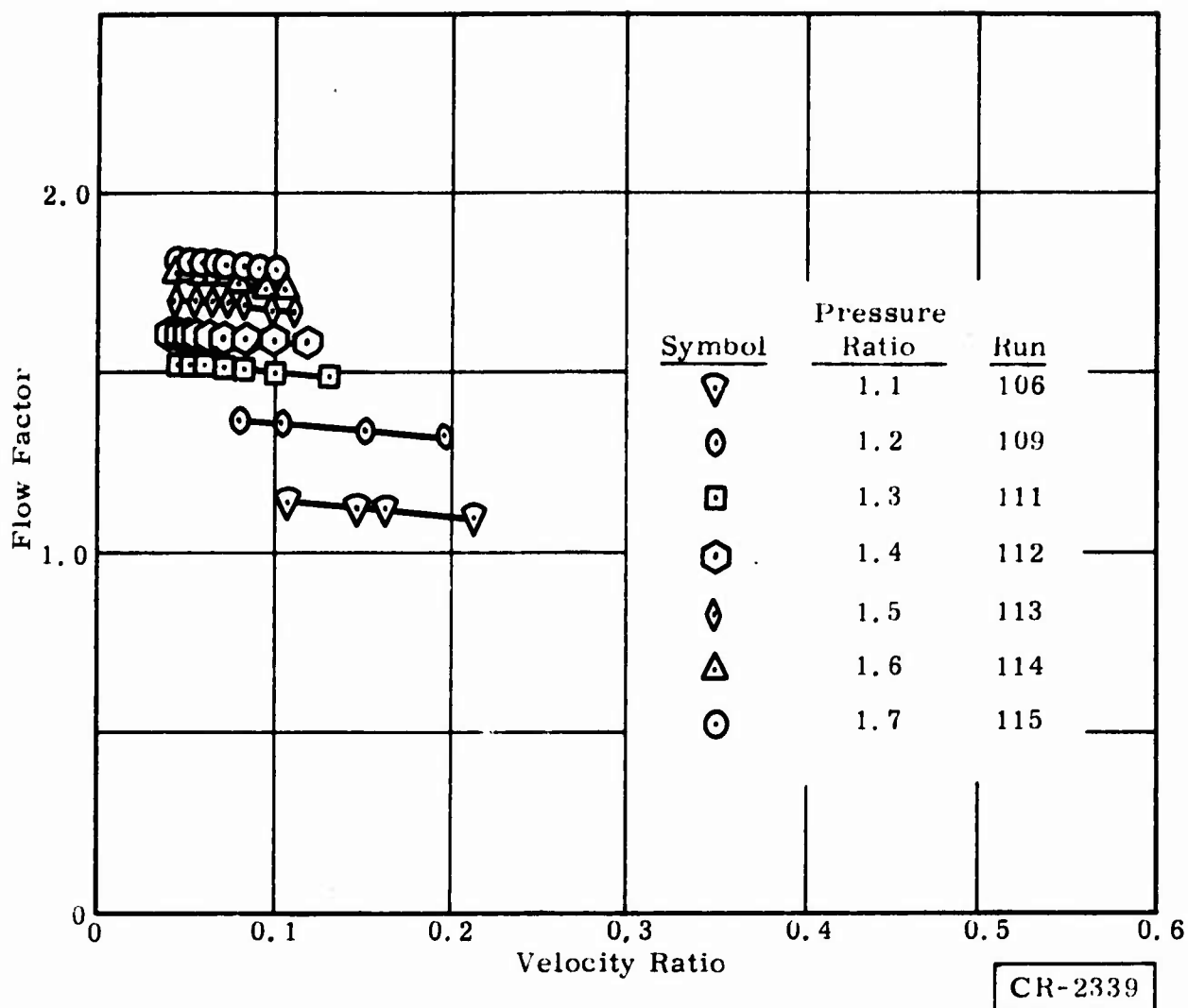


Figure 94. Turboalternator Performance -- Flow Factor Versus Velocity Ratio for Helium Gas at Room Temperature

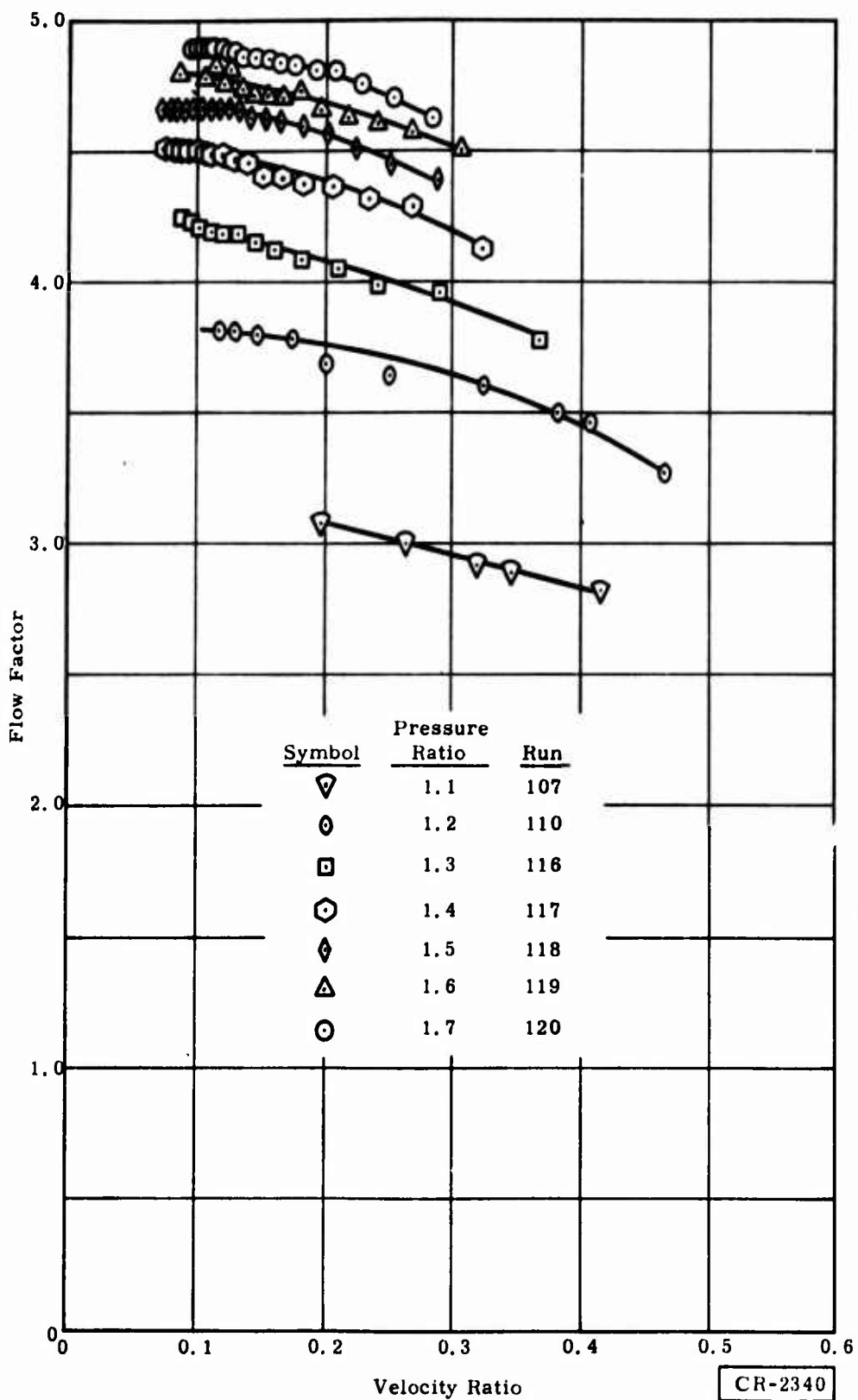


Figure 95. Turboalternator Performance -- Flow Factor Versus Velocity Ratio for Nitrogen Gas at Room Temperature

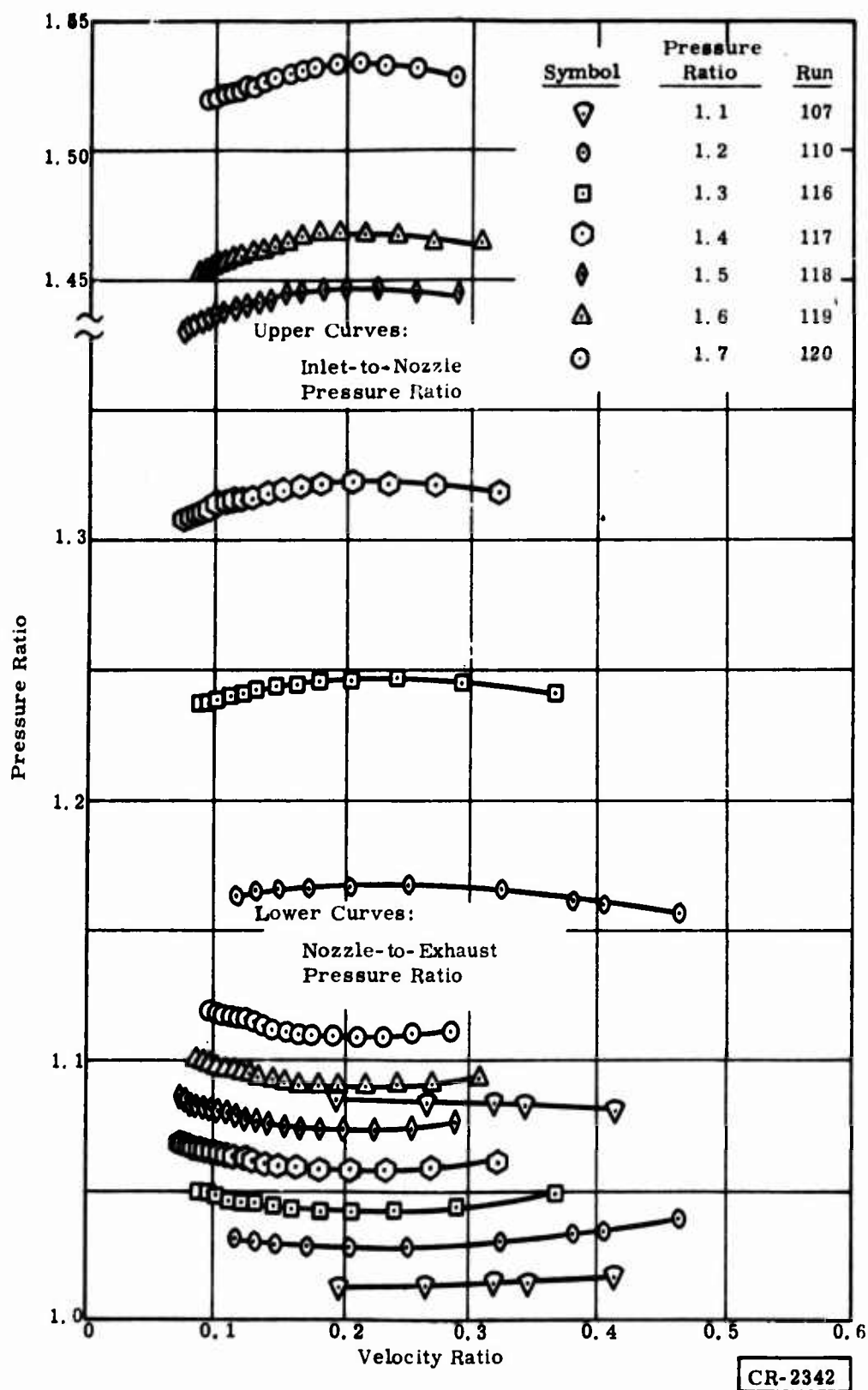


Figure 96. Turboalternator Performance -- Pressure Ratio Versus Velocity Ratio for Nitrogen Gas at Room Temperature

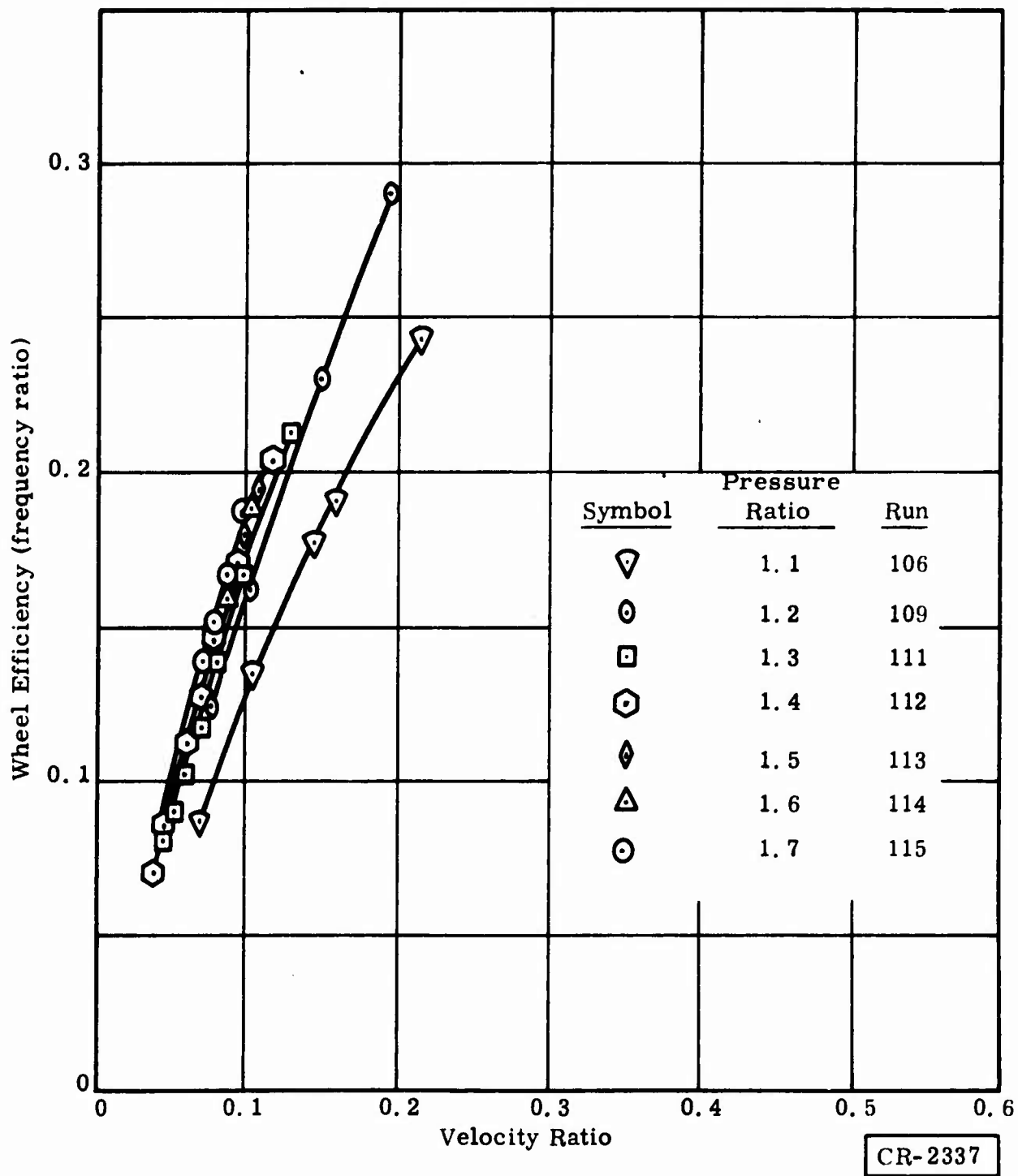


Figure 97. Turboalternator Performance -- Wheel Efficiency Versus Velocity Ratio for Helium Gas at Room Temperature



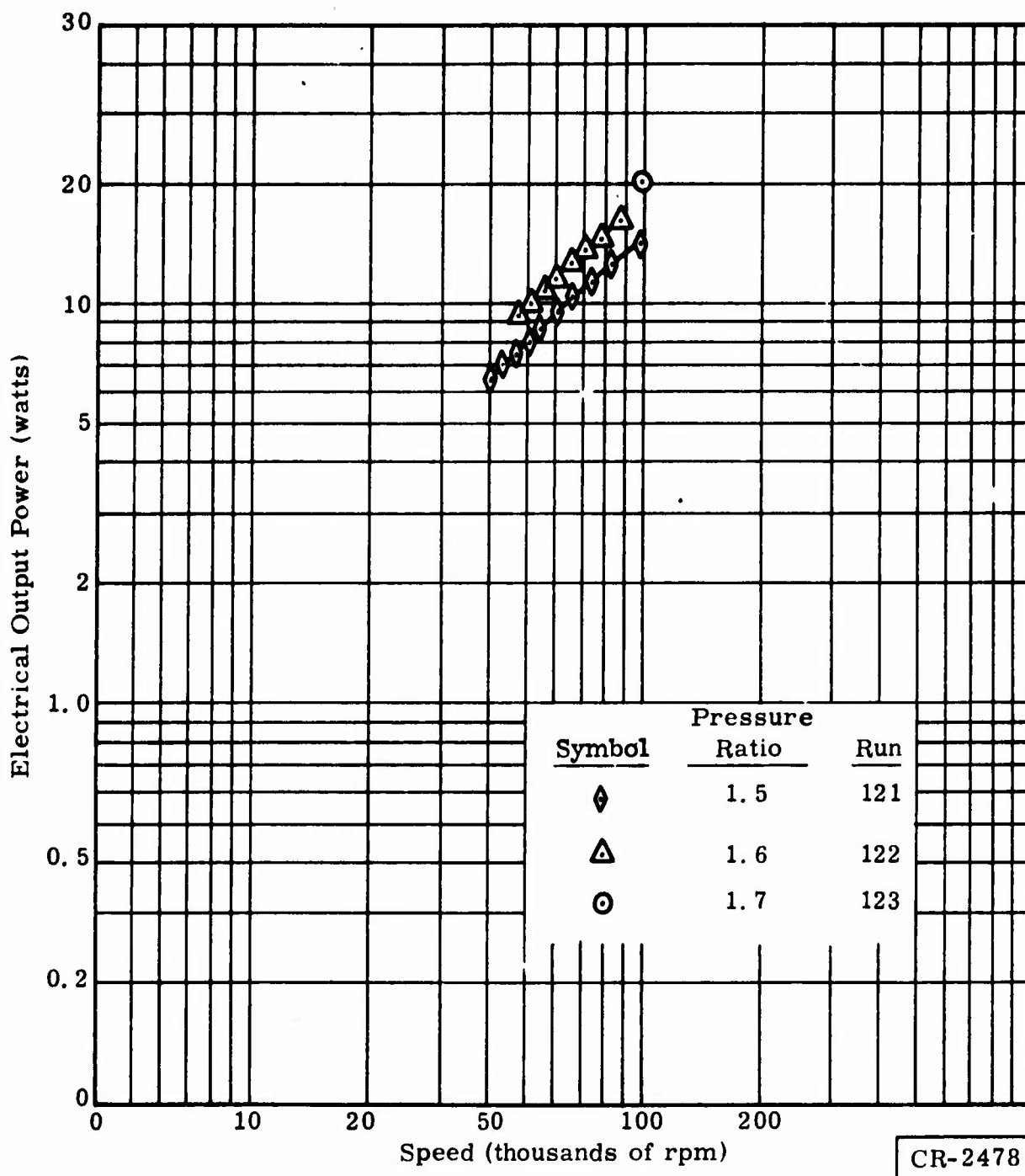


Figure 98. Turboalternator Performance -- Corrected Torque Versus Velocity Ratio for Helium Gas at Room Temperature

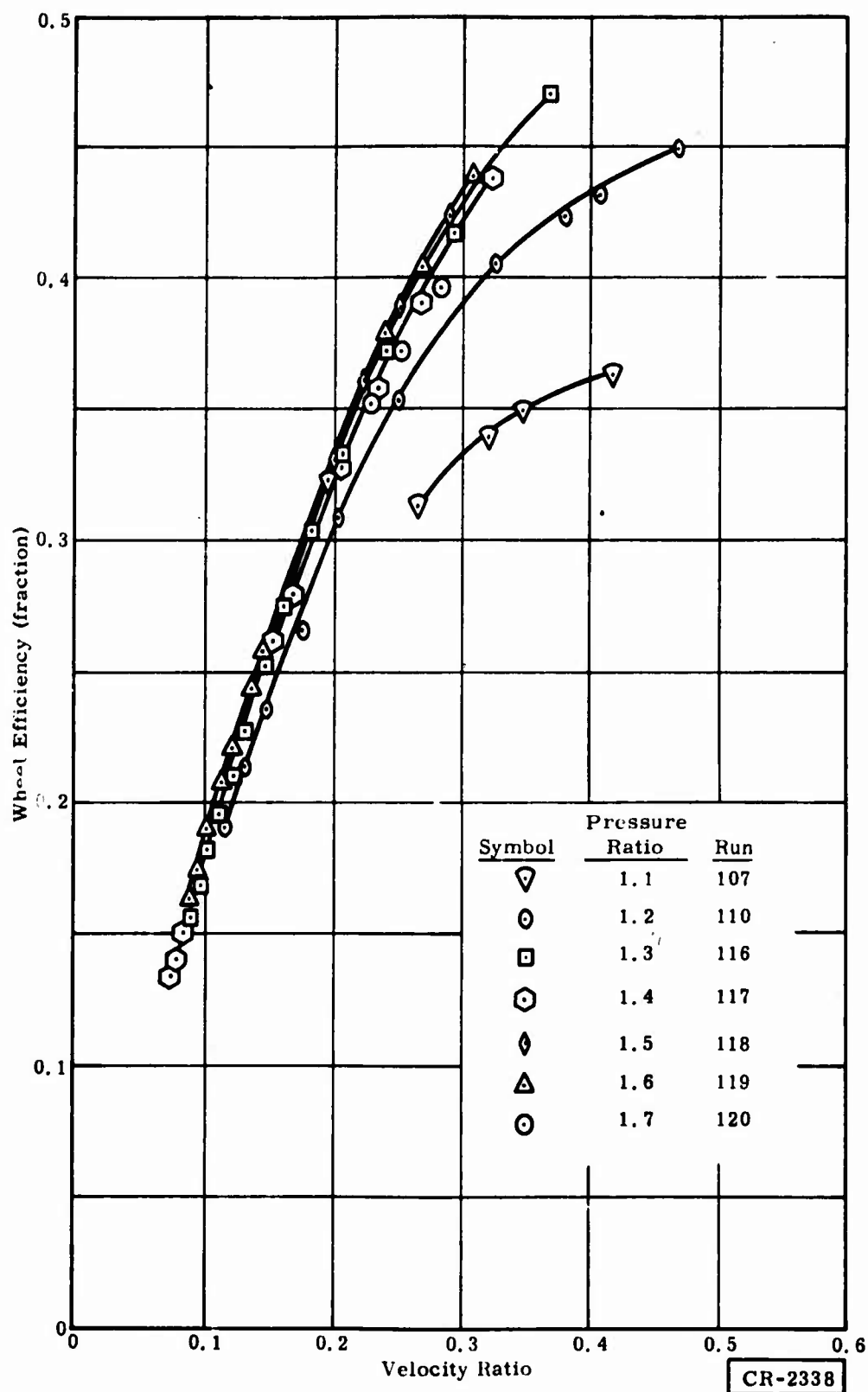


Figure 99. Turboalternator Performance -- Wheel Efficiency Versus Velocity Ratio for Nitrogen Gas at Room Temperature

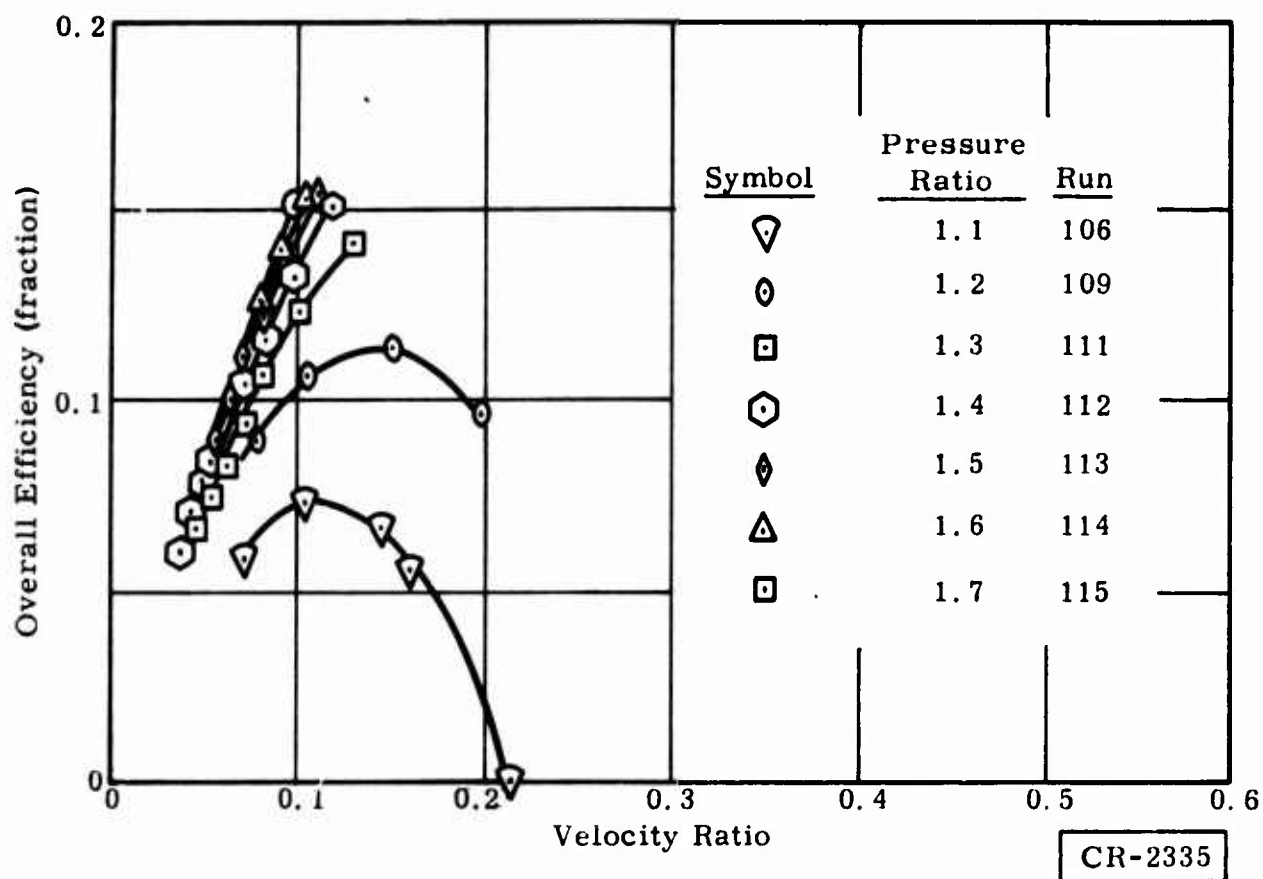


Figure 100. Turboalternator Performance -- Overall Efficiency Versus Velocity Ratio for Helium Gas at Room Temperature

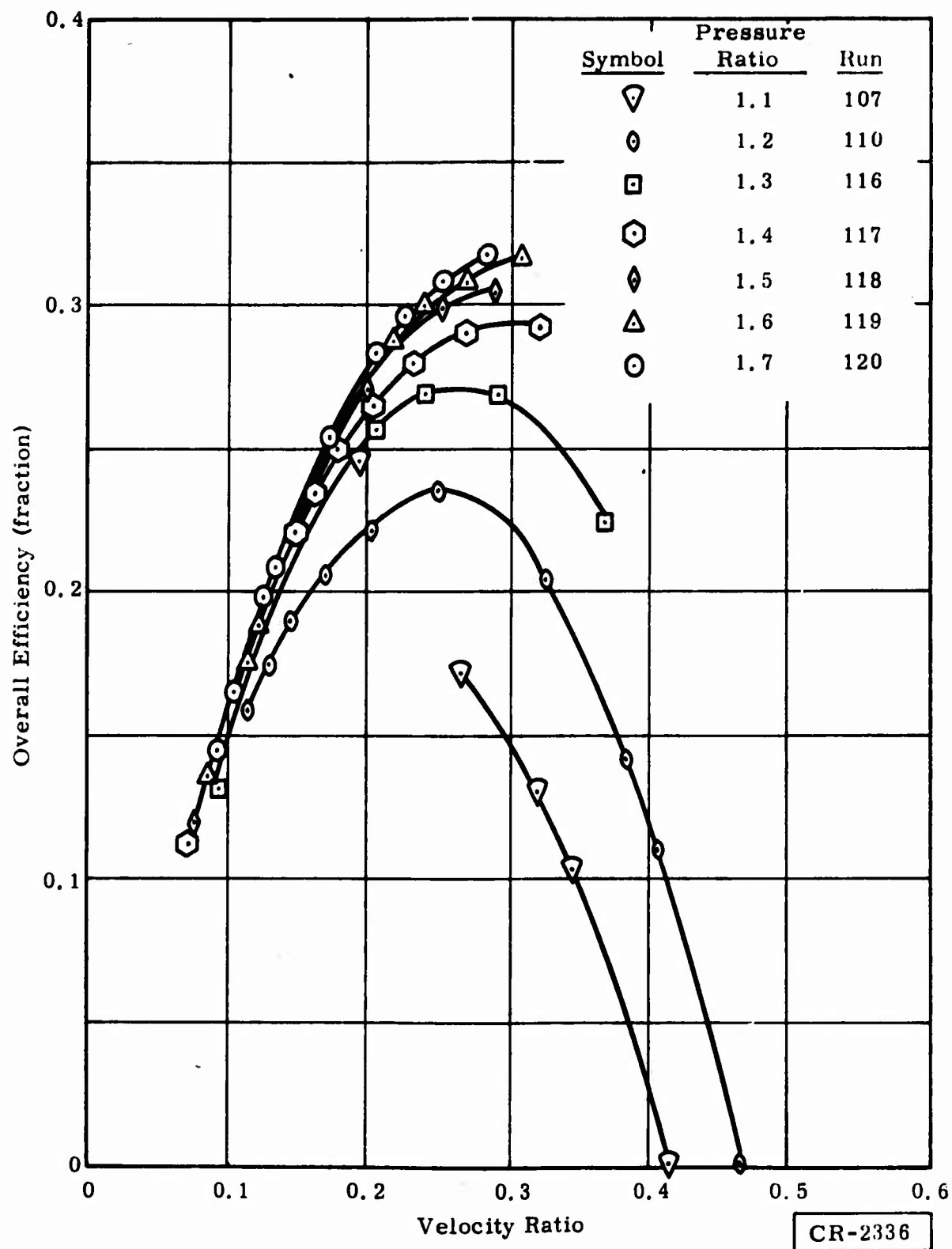


Figure 101. Turboalternator Performance -- Overall Efficiency Versus Velocity Ratio for Nitrogen Gas at Room Temperature

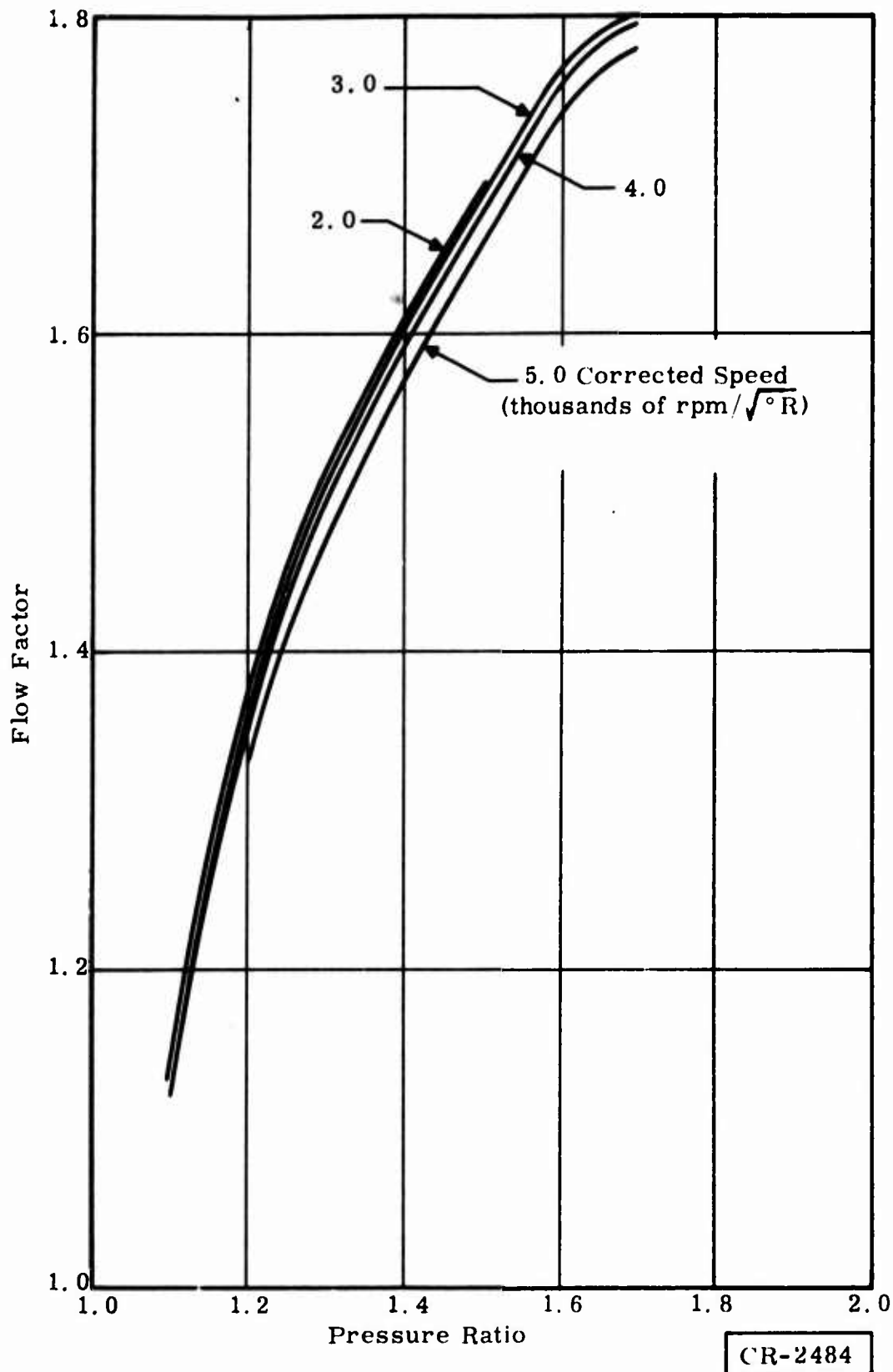


Figure 102. Turboalternator Performance -- Flow Factor Versus Pressure Ratio for Helium Gas at Room Temperature

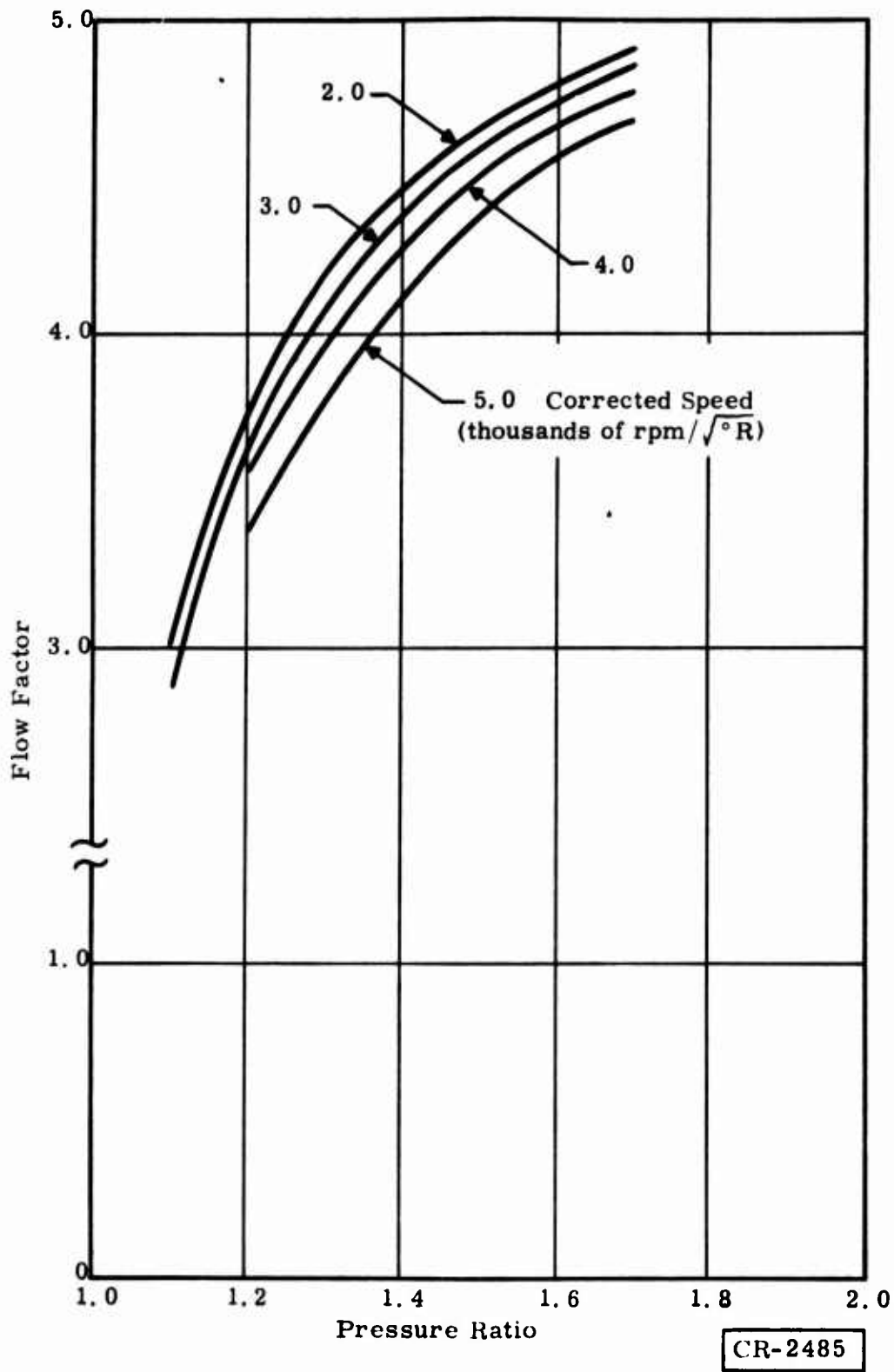


Figure 103. Turboalternator Performance -- Flow Factor Versus Pressure Ratio for Nitrogen Gas at Room Temperature

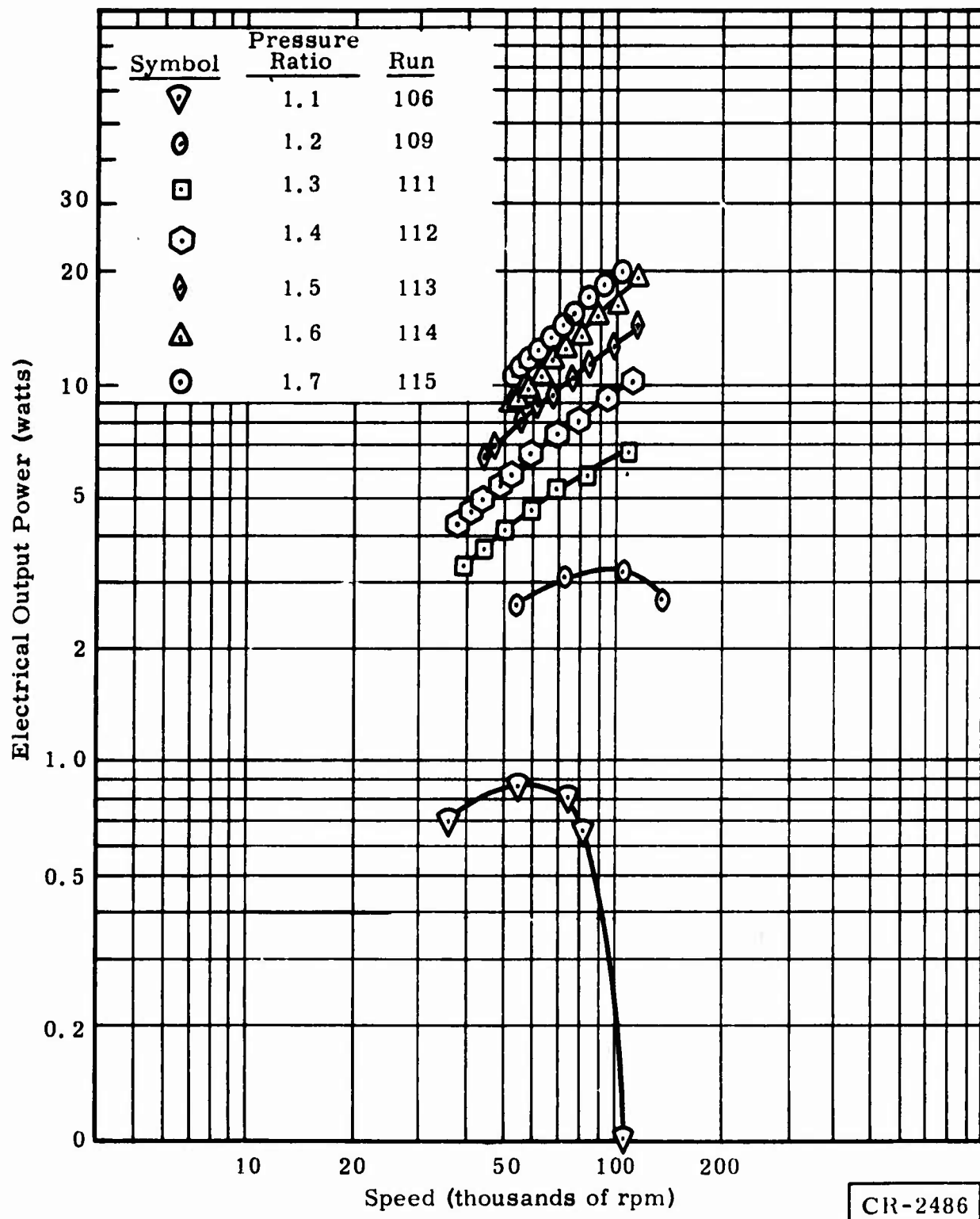


Figure 104. Turboalternator Performance -- Electrical Output Power Versus Speed for Helium Gas at Room Temperature

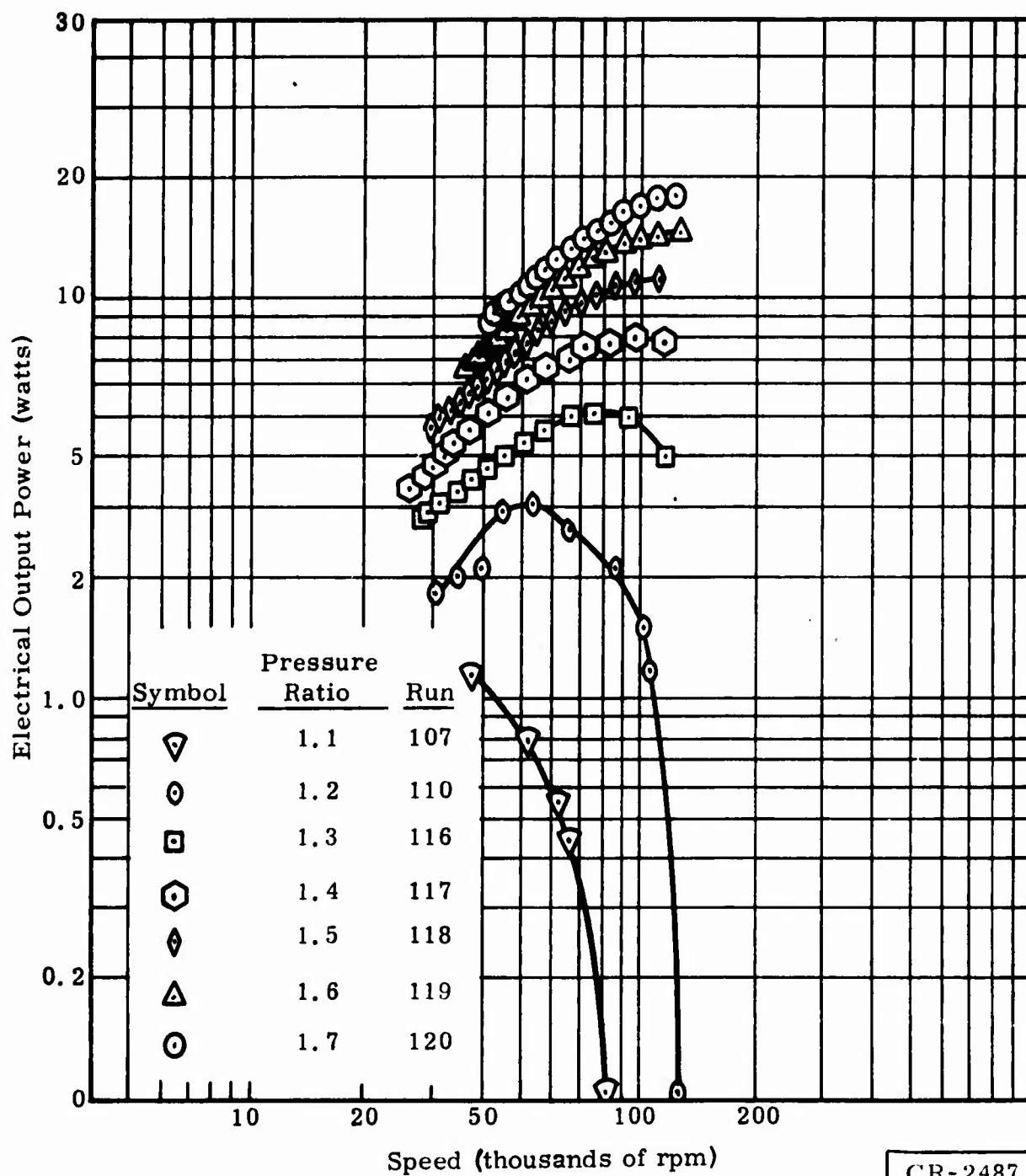


Figure 105. Turboalternator Performance -- Electrical Output Power Versus Speed for Nitrogen Gas at Room Temperature



## Section 4

### CRYOGENIC HEAT EXCHANGERS

This section describes the analysis, design, fabrication, and testing of a cryogenic heat exchanger system for Refrigerator B. Specifications for this heat exchanger system are given in Reference 2.

The design, fabrication, and testing of the exchanger were performed under a subcontract by Kinergetics, Inc. This section of the report was submitted by Kinergetics, Inc.

Because of a series of mechanical problems associated with the manifold connections, the heat exchanger system, as designed, could not be made to function without excess external leakage. As a result, a test exchanger cover and manifold assembly were fabricated and attached to the exchanger to allow thermal testing of one exchanger section. The design and fabrication descriptions of this report include the configuration of the exchanger, as tested, and the analysis and test portions include only the section tested and the tests actually performed.

### EXCHANGER SYSTEM CONFIGURATION

Figure 106 and Table 8 pertain to the tested configuration of the heat exchanger. The basic exchanger system is fabricated essentially as shown in

Table 8  
RPX-04 STACKING ORDER

Reference	Lamina (Section No.)	Length (inches)	Lamina Thickness (inches)	Screen Mesh	Screen Wire Diameter (inches)	Number of Required Screen Lamina	
7	3202(1)	0.100	0.020	20	0.010	5	.5
	3203(2)	2.045	0.015/0.020	26	0.010	148	148
	3204(3)	2.925	0.010/0.015	35	0.0075	195	195
	3203(4)	2.515	0.010/0.015	40	0.007	180	180
6	3205(5a & b)	1.042	0.020	20	0.010	52	52
	3203(6)	0.775	0.015	32	0.008	49	49
	3203(7)	0.970	0.010/0.015	35	0.0075	85	85
	3204(8)	1.080	0.015/0.020	26	0.010	54	54
5	3203(9a)	2.000	0.015/0.020	26	0.010	100	100
	3203(9b)	1.632	0.025/0.030	22	0.012	136	136
	3204(10)	2.475	0.015	32	0.008	155	155
	3203(11)	2.790	0.010/0.015	38	0.007	200	200
4	3205(12)	0.340	0.010/0.015	35	0.0075	23	23
	3207(13)	1.090	0.010/0.015	38	0.007	78	78
	3206(14)	0.660	0.010/0.015	35	0.0075	44	44
3	3207(15)	1.774	0.010/0.015	60/50	0.007	128	128
	3206(16)	1.774	0.010/0.015	60/50	0.007	128	128
	3207(17)	2.295	0.0075/0.010	60	0.005	230	230
2	3210(18)	0.803	0.010/0.015	38	0.0075	54	54
	3207(19)	0.842	0.010/0.015	60/50	0.007	61	61
	3211(20)	0.755	0.015	32	0.008	95	95
1	3212(21a)	0.281	0.010/0.015	60/50	0.007	20	20
	3212(21b)	1.097	0.010	60	0.006	92	92
	3213(22)	1.385	0.010	60	0.006	116	116
	3212(23)	1.385	0.0075/0.010	60	0.005	139	139
	3214(24)	0.630	0.010/0.015	35	0.0075	42	42

CR-1100

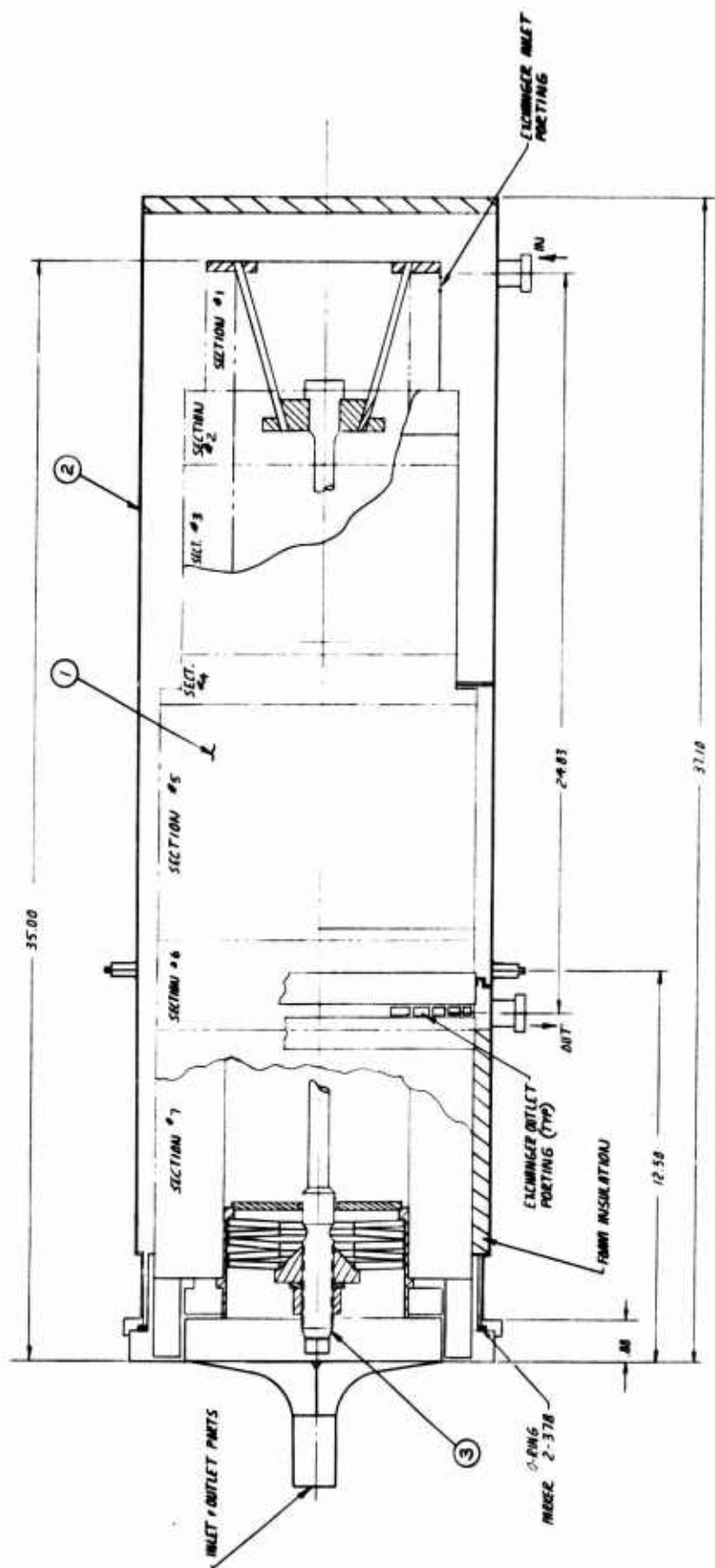


Figure 106. Reinforced Plastic Heat Exchanger Assembly -- As Tested

Figures 107 and 108, which is a design to satisfy the full system requirements. However, the manifolds depicted in Figures 107 and 108 have been removed, and the cover can shown in Figure 106 has been added. The clamping bolt assembly shown in Figure 106 was also added during the program and would remain as a part of the finished system.

### BASIC EXCHANGER

The basic exchanger is constructed of plastic and copper screen. It is fabricated by forming a sandwich layup of alternating screen disks and plastic lamina patterns (Figure 109) heating this mass and compressing it to force the plastic lamina through the voids in the screen mesh. When cooled, a solid cylindrical block is formed, with longitudinal openings through its length. The fused plastic forms solid walls that separate the gas flows from each other and from the outside atmosphere. The fine screen mesh that fills these gas flow passages creates a matrix with excellent heat transfer characteristics.

The separate gas flow passages are connected conductively by the screen wire, which passes through the separating walls. At the same time, the plastic forms an effective insulator to conduction in the longitudinal direction. The flow areas may be infinitely varied by changing the size of the pie-shaped segments that are stamped into the circular lamina patterns. Flow unbalance compensation is obtained by varying the size of these segments along the length of a given section (Ref. 3). Typical variation is  $\pm 10$  percent from nominal.

The screen material chosen for these exchanger modules is a woven wire mesh of ETP copper. The plastic material is polystyrene sheet. Figures 110 and 111 show typical lamina and screen parts.

In fabricating a complete exchanger, a number of modules of practical length (2 to 8 inches) are made. The exchanger system is then formed by bonding the required exchanger modules together. This bonding was accomplished using polyurethane glue (Crest Products 7343/7139).

Inlet and outlet openings were formed in the side of the exchanger by machining the circumference at selected points. These points contain selected manifolding laminae (Figure 112). When these laminae are machined to a given radius, the proper passages are exposed, while the alternate flow remains captive. Figure 113 shows the completed basic exchanger assembly.

The system is clamped together in the longitudinal direction by a through-bolt down the open center. This clamping greatly strengthens the exchanger and helps prevent leakage at the module joints. The bolt is a 1/2-inch-diameter Inconel 718 rod, threaded on the warm end. The flanged cold end is carried in a stainless steel cap structure, which transfers the loads to the exchanger body. The threaded end carries a nut and washer, which transfers loads to a set of Belleville springs. These springs are carried in the warm end manifold struc-





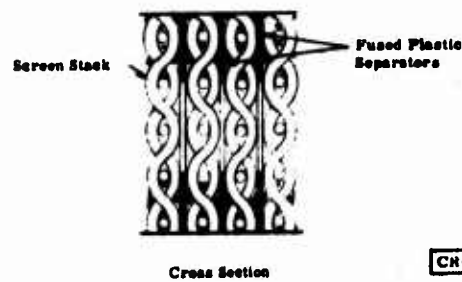
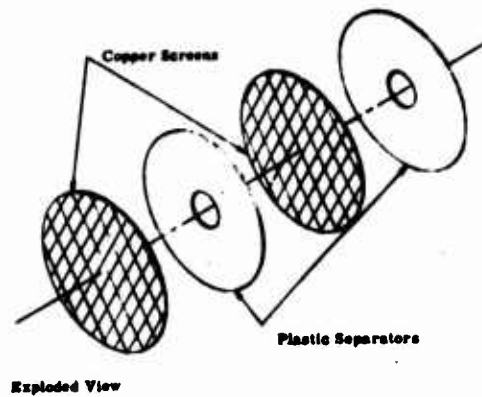


Figure 109. Basic Exchanger Construction

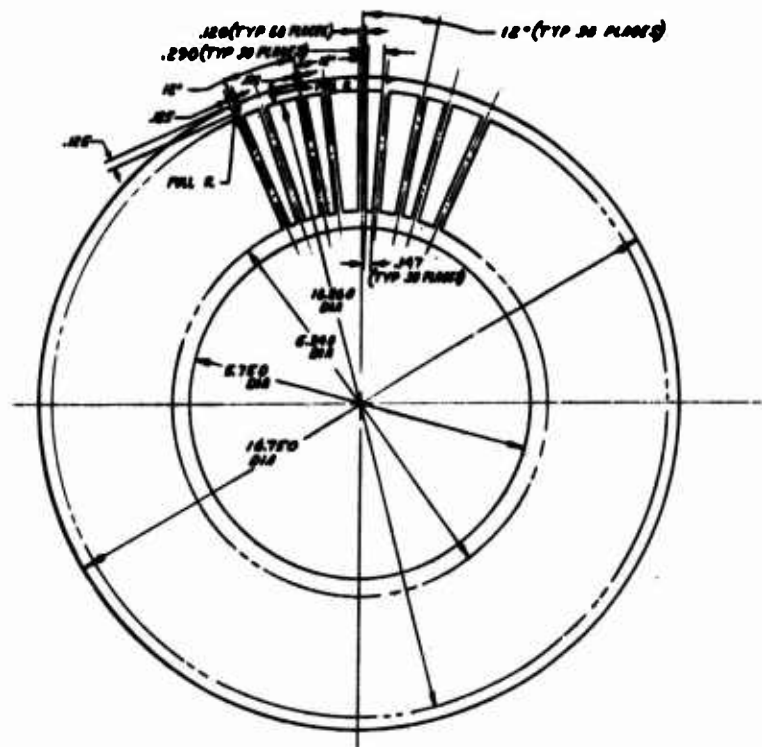


Figure 110. Typical Lamina





Figure 113. Basic Exchanger System

ture, and the loads are transferred to the exchanger body through this structure. An O-ring fits the shaft, where it passes through the warm manifold, sealing the exchanger interior cavity from the outside.

The Belleville springs are sized to provide a clamping load varying from 20,000 pounds warm to 15,000 pounds cold. The load variation occurs because of the approximately 0.335-inch differential in longitudinal contraction between the exchanger body and the bolt during cooldown.

#### COVER AND MANIFOLDING

To prevent external leakage and perform a substitute manifolding function, the cover can assembly shown as Item 2 in Figure 106 was fabricated and installed for testing. The can, made primarily from 0.060-inch wall thickness 304 stainless steel, forms a welded one-piece cover, with the only joints at the warm-end base and inlet and outlet ports. The warm end is sealed by an O-ring at the base flange. The port connections are sealed with copper crush washers, according to the original design.



The can was installed in two steps. The warm section, up to and including the Section 7 outlet port, was first slipped over the exchanger and bolted to the warm flange. A U-shaped Teflon ring was then bonded between the can and the exchanger, just above the outlet port. The annular space between the exchanger and the can forms an outlet manifold for exchanger Section 7. The area below the ports is filled with open-cell polyurethane foam, to prevent convection losses down this annulus to the warm end.

The top can section was then placed over the exchanger and welded at the intermediate flange. The upper cavity formed the inlet manifold. No insulation was used here, because this section is isothermal during testing. Figure 114 shows the exchanger system with the cover can installed.

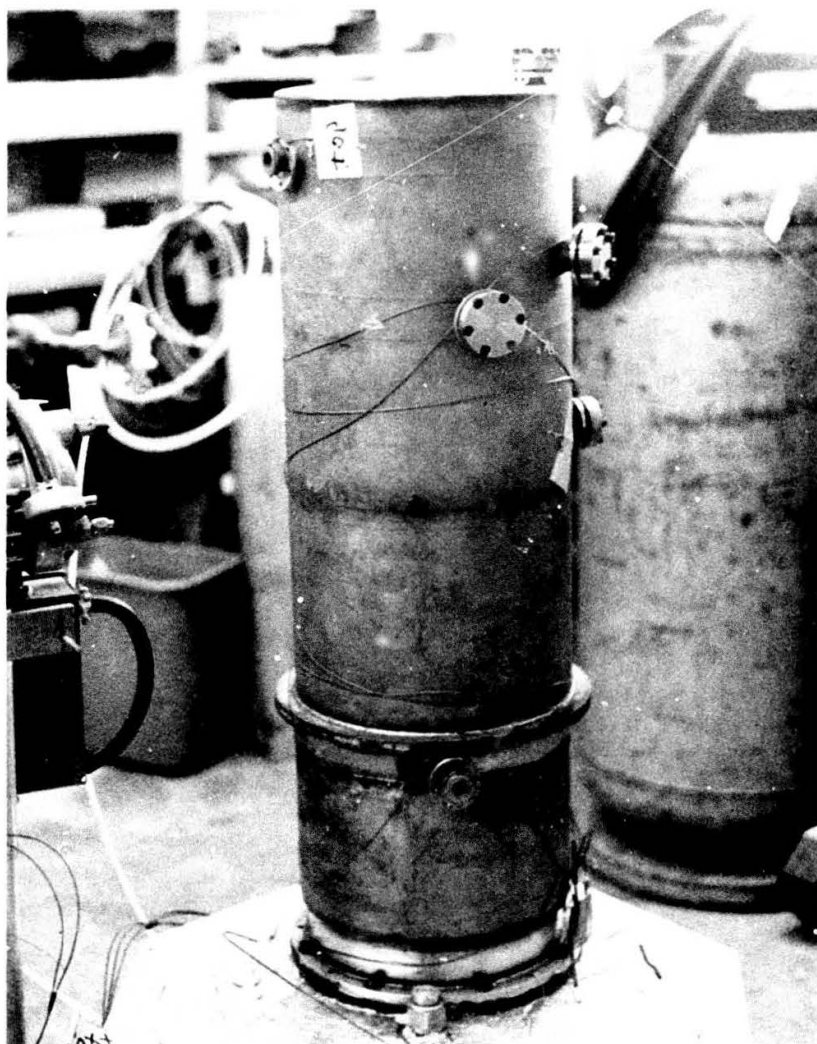


Figure 114. Exchanger and Cover

The warm-end manifold is fabricated from 302 stainless steel. It contains two annular rings that are connected to alternate passages by machined cutouts in the exchanger end, thereby separating the two flows. The system inlet and outlet connections are made to these annular rings. This manifold also carries the system mounting flange and the support structure for the clamping bolt.

## PERFORMANCE ANALYSIS

### BASIC APPROACH

The exchanger performance analysis utilizes the methods of the  $N_{tu}$  approach to heat exchanger design. (See Reference 4 for definitions and nomenclature.) Specifically, the following basic equations are used:

$$\lambda_o = \frac{\epsilon}{1 - \epsilon} \quad (1)$$

$$\frac{1}{\lambda_o} = \frac{1}{\lambda_h} + \frac{1}{\lambda_k} + \frac{1}{\lambda_c} \quad (2)$$

where  $\lambda_h$  and  $\lambda_c$  are the hot and cold gas  $N_{tu}$ 's, respectively and  $\lambda_k$  is the conduction  $N_{tu}$ .

$$\lambda_{gas} = \frac{j}{N_{pr}} \frac{L}{2/3 r_h} \quad (2a)$$

$$\lambda_k = \frac{k A_k}{L_k C_{sta}}$$

Finally, the pressure drop is found from the Fanning equation:

$$\Delta P = \frac{f}{2} \frac{G^2}{\rho} \frac{L}{r_h} \quad (3)$$

Values of  $j$  and  $f$  are found from the graphs of Appendix I, "Heat Exchanger Design Performance Calculations," using the familiar Reynolds No. equation:

$$N_R = \frac{4 r_h G}{\mu}$$

and the hydraulic radius equation for mesh screen:

$$r_h = \frac{d_v}{4} \frac{v}{1 - v}$$

where  $v$  is the screen void volume fraction.

The effect of longitudinal conduction is calculated using the method of Reference 4 (p.31). The conduction through the helium screen mesh is found

using Figure 124 and using the definitions and nomenclature of Reference 3. Gas properties data were taken from Reference 5.

## DESIGN PERFORMANCE CALCULATIONS

Using the basic exchanger relationships and the configuration data given above, the expected performance of the exchanger was determined. A number of parameters must be calculated for each of six distinct exchanger sections. Table 9 lists parameters for exchanger Section 7 at design flow condi-

Table 9  
PERFORMANCE CALCULATION PARAMETERS  
FOR HEAT EXCHANGER SECTION 7

Parameter	Subsection		
	2	3	4
Screen (diameter in inches)	26 mesh, 0.010 diameter	38 mesh, 0.0075 diameter	40 mesh, 0.007 diameter
Lamina	3203	3204	3203
Flow area (cm <sup>2</sup> )	65.2 high pressure 121.2 low pressure	53.2 high pressure 135.5 low pressure	64.5 high pressure 120.0 low pressure
Mass flow (gm/sec)	--	2.855	--
Hydraulic radius (centimeters)	$23.9 \times 10^{-3}$	$17.8 \times 10^{-3}$	$15.0 \times 10^{-3}$
G (gm/sec cm <sup>2</sup> )	4.36 high pressure 2.36 low pressure	5.37 high pressure 2.11 low pressure	4.43 high pressure 2.38 low pressure
Average temperature (°K)	309	257	206
$\mu$ (centipoise)	$2.04 \times 10^{-2}$	$1.81 \times 10^{-2}$	$1.60 \times 10^{-2}$
N <sub>R</sub>	20.6 high pressure 11.0 low pressure	21.1 high pressure 8.3 low pressure	16.6 high pressure 8.9 low pressure
$\dot{m}\mu$ (cm) <sup>-1</sup>	$1.40 \times 10^4$	$1.58 \times 10^4$	$1.78 \times 10^4$
j	0.345 high pressure 0.55 low pressure	0.34 high pressure 0.705 low pressure	0.395 high pressure 0.67 low pressure
f	3.3 high pressure 6.05 low pressure	3.2 high pressure 7.6 low pressure	4.0 high pressure 7.0 low pressure
L (cm)	7.48	7.43	6.39
N <sub>pr</sub>	0.703	0.688	0.695
$\lambda$	137 high pressure 217 low pressure	180 high pressure 372 low pressure	213 high pressure 361 low pressure
$\rho$ (gm/cm <sup>3</sup> ) $\times 10^3$	101 high pressure 53 low pressure	120 high pressure 62 low pressure	149 high pressure 77 low pressure
$\Delta P$ (atmospheres) $\times 10^2$	0.95 high pressure 0.95 low pressure	1.55 high pressure 1.08 low pressure	1.08 high pressure 1.09 low pressure
Screen conductivity ( $\frac{\text{watts}}{\text{cm}^2 \text{K}}$ )	--	4.24	--
Conduction area (cm <sup>2</sup> )	--	22.6	--
Conduction length (centimeters)	--	0.737	--
$\lambda_k = (kA/\dot{m}c_p)$	--	523	--
Helium conductivity ( $\frac{\text{watts}}{\text{cm}^2 \text{K}}$ )	--	$15.0 \times 10^{-4}$	--
$k_g/k_g$	--	283	--
$k_B/k_g$	--	1.7	--
$k_B$ ( $\frac{\text{watts}}{\text{cm}^2 \text{K}}$ )	--	$25.5 \times 10^{-4}$	--
Longitude conduction area (cm <sup>2</sup> )	--	227	--
$\epsilon/k$	--	0.00165	--

\*For calculated and test data comparisons only.

\*\*See curve A-4 in Appendix A:

$$\text{Net } \lambda: \lambda_H = 137 + 180 + 213 = 530$$

$$\lambda_L = 217 + 372 + 361 = 950$$

$$\lambda_T = \frac{1}{\frac{1}{530} + \frac{1}{950}} = 206$$

$$\epsilon_D = \frac{206}{207} = 0.9951$$

$$\epsilon_D = 0.9951 - 0.0017 = 0.9934$$

Total  $\Delta P$ :

$$\text{High Pressure} \rightarrow (0.95 + 1.55 + 1.08) \times 10^{-2} = 0.0359 \text{ atmospheres}$$

$$\text{Low Pressure} \rightarrow (0.95 + 1.08 + 1.09) \times 10^{-2} = 0.0312 \text{ atmospheres}$$

CR-1101

tions. Appendix III contains typical calculations for the parameters in the table, as well as exchanger matrix properties used in the analysis. The end data points are the effectiveness and pressure drop of the total section, presented with the corresponding specification values:

<u>Characteristic</u>	<u>Design</u>	<u>Specified</u>
Overall $N_{tu}$	206*	--
Overall effectiveness	0.9935	0.990
Pressure drop, high-pressure flow (atmospheres)	0.0359	0.0162
Pressure drop, low-pressure flow (atmospheres)	0.0312	0.0169

Calculated effectiveness and pressure drop, at design and off-design flow, are also presented on the test data curves in the following subsection.

## TESTING

Because of changes in the system contract and statement of work, exchanger testing was reduced from that called for in the original contract. The intent of the testing that was conducted was to demonstrate that the basic heat exchanger design could give the required thermal performance. Because of the physical limitations described above under "Exchanger System Configuration," only one section of the exchanger (Section 7, the warmest) was tested.

## TEST PROCEDURE

The test specifications called for four separate performance tests:

- External leakage
- Stream-to-stream leakage
- Thermal effectiveness
- Pressure drop

The following subsections describe the general test philosophy and methods utilized to perform these tests. Specific procedures are presented in Appendix II, "Heat Exchanger Test Procedure."

### External Leakage

During this test program, the exchanger was checked for external leakage using two methods. Before assembling the exchanger in the thermal test setup, it was pressurized with 10-psi helium, and the input flow rate was measured with a flowmeter having a maximum scale reading of 2000 scc/min

\*Does not include effect of longitudinal conduction.

air. If the flowmeter reading was zero, the unit was considered acceptable for testing. If leakage flow was indicated, repairs were made.

After the exchanger was installed in the test vacuum chamber, leak tightness was checked by a helium mass spectrometer with a sensitivity of  $1.5 \times 10^{-9}$  torr-liters/sec. Helium was introduced into the exchanger at 10 psi. Any reading on the leak tester was cause for disassembly and repair.

#### Stream-to-Stream Leakage

This test was conducted by pressurizing the high-pressure side of the exchanger and attaching a flowmeter to the only open low-pressure port. The flowmeter reading then indicated the leakage rate. This reading included any leakage past port coverings and seals as well as any internal leakage in the exchanger body.

#### Thermal Effectiveness Test

This test was the heart of the test program. A special test system (Figures 115 and 116) was constructed for this program. Measurement of heat exchanger effectiveness requires determination of the difference in temperature between the entering and leaving gas streams. Because this difference is very small (about 3°K in a high-efficiency exchanger), thermocouples or other direct measurement devices are not sufficiently accurate for efficiency determination.



Figure 115. Test System and Exchanger  
with Vacuum Chamber Removed

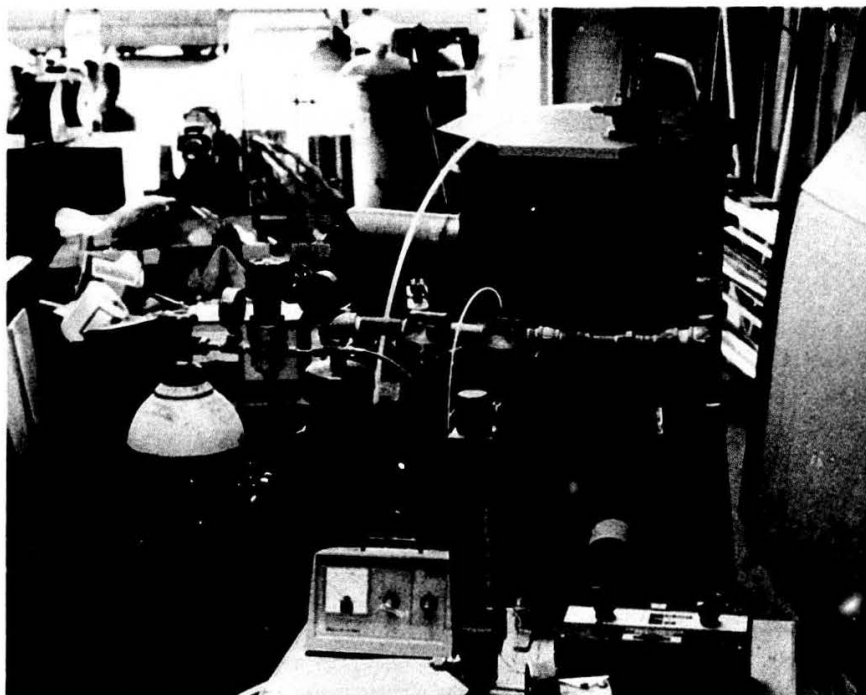


Figure 116. Test System with Vacuum Chamber Installed

The Kinergetics, Inc. test system used an indirect accurate scheme for the measurement of this temperature difference. The gas flow leaving the exchanger was circulated through a coil heat exchanger immersed in liquid nitrogen. This arrangement provided the cooling for the cryogenic test and also afforded the measured quantity, which determined the temperature difference. The cooling coil was contained in a dewar, which was effectively insulated from its surroundings. Thus the liquid nitrogen evaporated from the dewar was directly proportional to the cooling of the gas flow, and with knowledge of the gas mass flow, the corresponding temperature change could be easily calculated.

As shown in the schematic diagram (Figure 117), the exchanger and the liquid nitrogen dewar are contained in a common vacuum chamber. The exchanger warm-end inlet and outlet pipes are exposed, as is the top end of the liquid nitrogen dewar. Both the exchanger and the dewar are wrapped in 40 layers of 1/2-mil-thick aluminized Mylar, and the inner surfaces of the vacuum chamber are covered with aluminum foil. Flexible hoses, also wrapped in insulation, connect the appropriate exchanger supply and return ports with the cooling coil. Figure 117 indicates the hose connections used in the reported test.

The helium gas flow is supplied by a Roots-type blower driven by a 5-hp synchronous motor. The blower speed is 3000 rpm, and the maximum helium flow rate is 45 cfm at 10 psi, under test conditions.

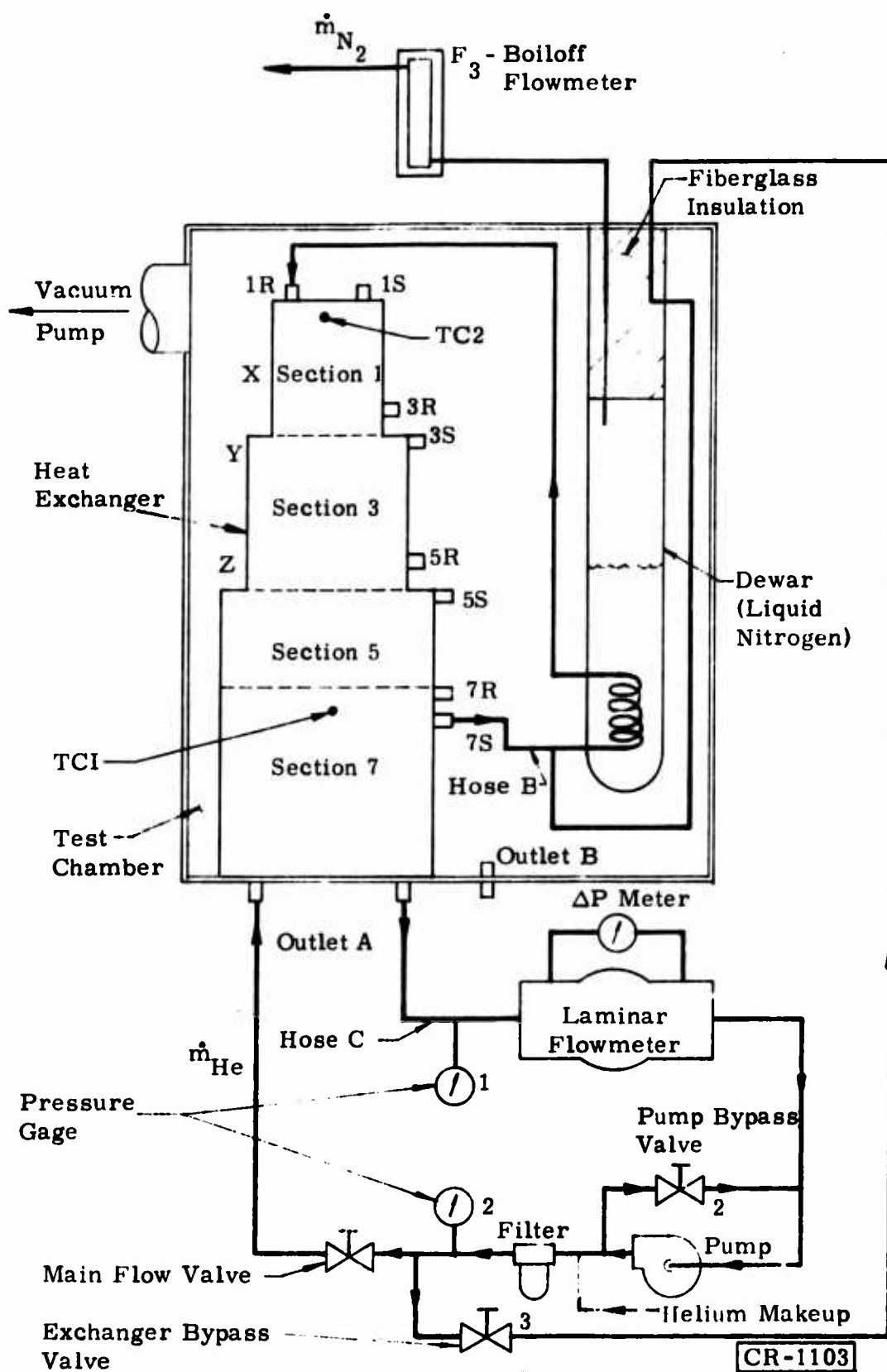


Figure 117. Schematic Diagram of Test System

The flow circuit is closed, and helium is supplied from a high-pressure bottle to make up the system leakage loss. The flow rate is measured by a Meriam Model 50 MC2-2S laminar flowmeter and a Barton differential pressure gage located in the return flow path. The flow rate is controlled by a bypass valve that allows the flow to circulate directly from the pump outlet to the inlet without entering the exchanger circuit. Closing this valve increases the flow. Pressure gages are located at the pump inlet and outlet points, as a check on the system pressure drop.

A branch circuit, which allows the flow to bypass the high-pressure side of the exchanger, is also included. This circuit is only used during cooldown and is closed during actual performance testing. By temporarily eliminating the warm gas flow in this manner, the exchanger cooldown rate is greatly increased.

Thermocouples were attached at several points on the exchanger cover. Their purpose was to indicate when the system had reached equilibrium, and they were not primary data sources.

A Fischer and Porter rotameter, with a maximum flow capability of 1.30 scfm air, was attached to the top of the liquid nitrogen dewar and was the only outlet for boiloff nitrogen during the test. A 12-foot-long, 1/2-inch-inside-diameter hose separated the flowmeter from the dewar, warming the nitrogen gas to nearly room temperature before it entered the flowmeter.

The basic test procedure was to cool the exchanger until equilibrium temperature was reached at the coldest point of the section to be tested. The helium flow was then varied from 10 percent of maximum to maximum, and the nitrogen boiloff flow rate was measured. The helium flow was maintained constant at each level for 5 minutes or until the nitrogen boiloff rate was stable.

### Pressure Drop

Exchanger pressure drop was measured at room temperature, using both nitrogen and helium gas. Because of the limitations of the exchanger porting configuration, only the high-pressure passages of Section 7 could be tested.

The procedure was to flow gas into the warm-end inlet port, through the exchanger, and out of the Section 7 supply port. Pressure gages were attached to the piping at the inlet and supply ports. In the helium test, flow was supplied by the Roots pump and read on the normal system flowmeter. With nitrogen, it was necessary to use a bottle and rotameter, in open circuit configuration, to obtain sufficiently small Reynolds numbers. Both Bourdon tube gages and manometers were used to check the inlet and outlet pressures.



## TEST RESULTS

### External Leakage

Leak testing with a CEC Type 24-120B helium mass spectrometer with a sensitivity of  $1.5 \times 10^{-9}$  torr-liters/sec showed no evidence of external leakage. During the thermal test, the minimum vacuum obtained in the chamber was  $25 \times 10^{-3}$  torr. This, however, included leakage into the chamber from the atmosphere, leakage through the test piping connections, and outgassing of the chamber interior and contents.

### Stream-to-Stream Leakage

Stream-to-stream leakage was tested at a 2-psi differential pressure. The total leakage flow was measured to be 3500 cm<sup>2</sup>/min of helium, which is 0.34 percent of the nominal system gas flow rate.

### Thermal Efficiency

The raw test data are presented in Appendix III, "Heat Exchanger Test Data and Data Reduction." Included is the test elapsed time, system flow rate and pressure, and the nitrogen boiloff flow rate. These data were taken under conditions of  $25 \times 10^{-3}$  torr chamber vacuum, 86°K temperature of the exchanger cover at the level of the Section 7 supply ports, and with the liquid nitrogen dewar approximately one-fourth full. The raw data of flowmeter differential pressure versus the liquid nitrogen boiloff rate are plotted in Figure 118.

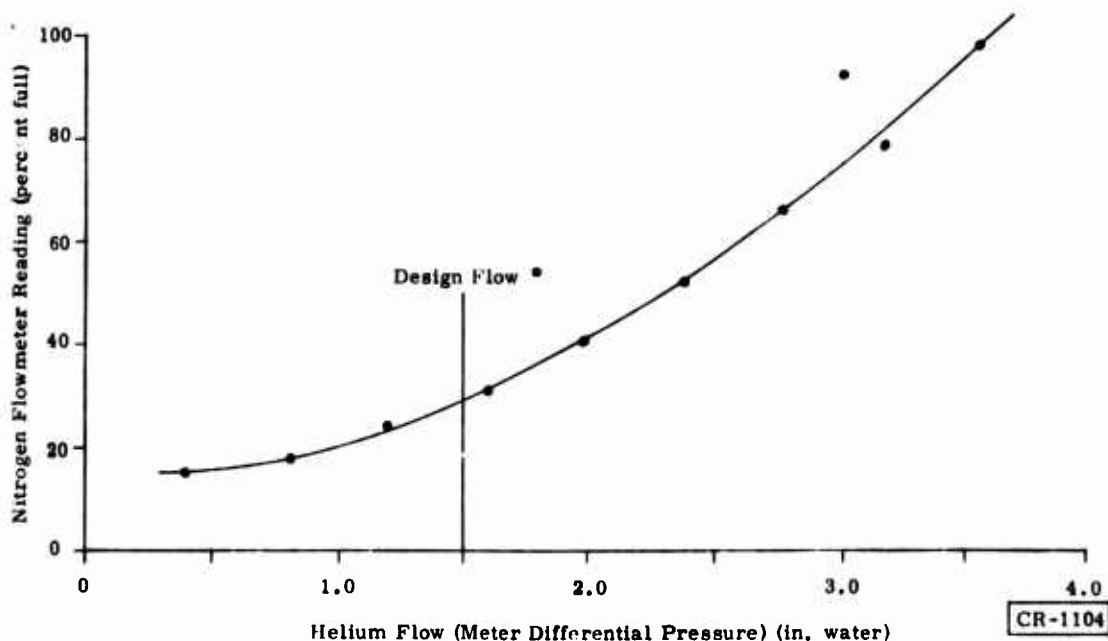


Figure 118. Helium Flow Versus Nitrogen Boiloff

To obtain exchanger thermal efficiency, the data are reduced by the following process:

1. The Meriam flowmeter curves are entered at the appropriate differential pressure to obtain the corresponding mass flow rate of air. This value is then corrected for helium viscosity ( $\times 0.912$ ) and multiplied by the density of helium, calculated at 70°F, and the system outlet pressure, to obtain the helium mass flow rate.
2. The nitrogen flowmeter readings are multiplied by 1.30 (the maximum flow rate) and the density of nitrogen at room conditions to obtain the nitrogen boiloff mass flow rate.
3. The temperature difference between the gas streams ( $\delta T$ ) is then found by comparing the heat capacity of the helium flow to the nitrogen mass flow times the latent heat of nitrogen ( $\lambda_{N_2}$ ). Again using the definitions and nomenclature of Ref. 4:

$$\dot{Q} = \dot{m}_{N_2} \lambda_{N_2} = \dot{m}_{He} C_{pHe} \delta T$$

or:

$$\delta T = \frac{\dot{m}_{N_2} \lambda_{N_2}}{\dot{m}_{He} C_{pHe}}$$

4. The effectiveness is calculated by:

$$\epsilon = \frac{\Delta T}{\Delta T + \delta T}$$

where  $\Delta T$  is the temperature difference between the gas entering the warm end and the gas leaving the cold end. In this case,  $\Delta T = 210.5^\circ\text{C}$ .

The measured effectiveness at the various helium mass flows is given in Appendix III. These effectiveness values are plotted against a modified Reynolds number in Figure 119. Because the flow areas and hydraulic radii vary through the exchanger section, there are actually six different Reynolds numbers for a given mass flow rate and viscosity. To avoid confusion, these parameters are eliminated from the Reynolds number, and the ratio  $\dot{m}/\mu$  is used instead. The viscosity,  $\mu$ , is taken at the average flow temperature (192°K). The value of  $\dot{m}/\mu$  for the actual design exchanger flow in this section is  $1.585 \times 10^4$  cm.

To obtain the effectiveness of the basic heat exchanger, the degradation in effectiveness due to longitudinal conduction in the cover was added to the measured effectiveness. This is calculated by the method given in Reference 4, p. 31. The upper broken curve in Figure 119 is this resultant effectiveness. The design effectiveness is also plotted as the solid curve. Measured exchanger effectiveness is slightly lower than the design value, but exceeds the system requirements at the design Reynolds number.

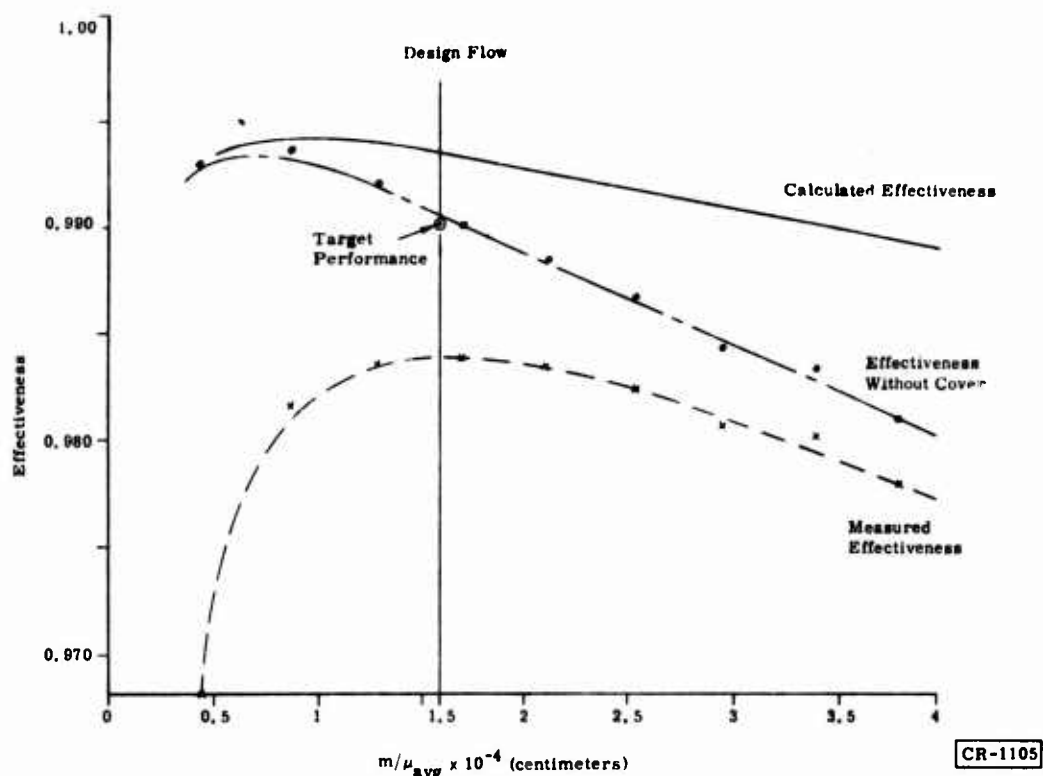


Figure 119. Effectiveness Versus Mass Flow for Section 7

### Pressure Drop

Pressure loss measurements were taken with room temperature gas flow. The pressure drop through the exchanger is simply the difference between the inlet and outlet pressure readings. The effective Reynolds numbers were computed by reading the flowmeter curves and applying the proper density and viscosity correction factors to obtain the mass flow, and then dividing by the room temperature viscosity (Appendix III).

For comparison with the design values, the pressure drops for the test gases and conditions were calculated. The configuration data and calculation methods utilized above under "Performance Analysis" were applied for this purpose. An additional factor of pressure drop through the outlet tube is also applied, because this is part of the measured  $\Delta P$ .

Pressure drop versus  $\dot{m}/\mu$  is plotted in Figures 120 and 121 for nitrogen and helium gas flows, respectively. As can be seen for the helium flow, the correlation between calculated and measured values is good at low  $\dot{m}/\mu$ , but the measured values curve inexplicably upward at a  $\dot{m}/\mu$  of about  $0.5 \times 10^4$ . The nitrogen flow showed a pressure drop excessive by a factor of two throughout the measured flow range.

### SUMMARY AND CONCLUSIONS

This heat exchanger system program has shown that the basic requirement of attaining high exchanger efficiencies in a small package size is definitely

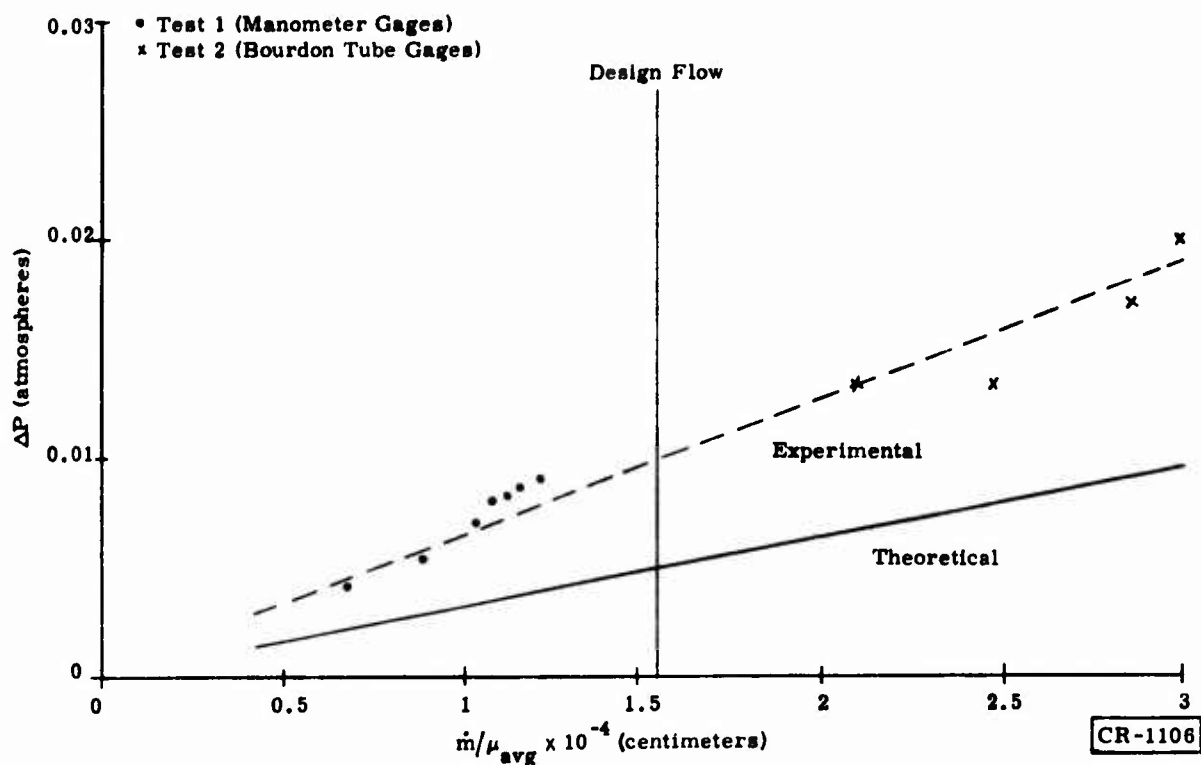


Figure 120. Pressure Drop Versus Mass Flow (Nitrogen at STP, High-Pressure Stream of Section 7)

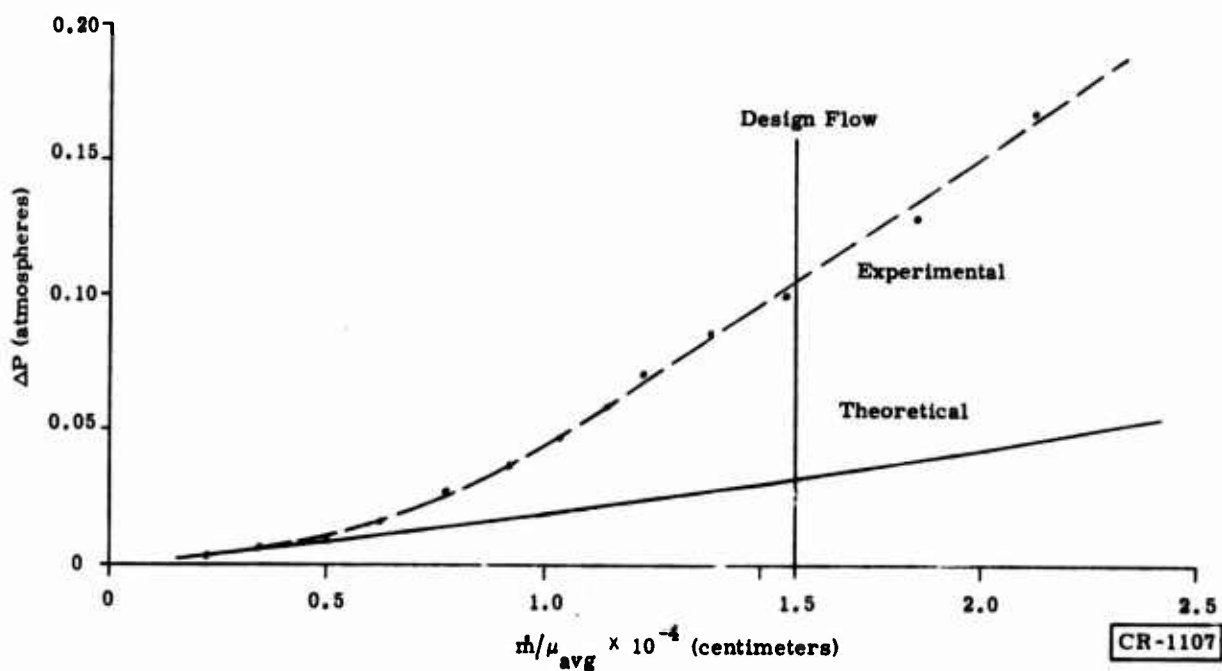


Figure 121. Pressure Drop Versus Mass Flow (Helium at 70°F and 20 Psig, High-Pressure Stream of Section 7)

realizable. Unfortunately, mechanical problems associated with flow manifolding at low temperatures rendered the exchanger that was fabricated to the original design unusable in the system. However, tests that were conducted demonstrated that an effectiveness of greater than 99 percent is attainable and that the thermal performance calculation methods utilized in the design of this type of exchanger produce realistic predictions. The measured pressure drops, while two to three times the calculated values, are still acceptable from a system standpoint. The discrepancies between calculated and measured  $\Delta P$ 's are probably explainable by changes in the screen mesh and passage size configuration, which may have occurred during the fabrication process.

The exchanger cover utilized in the final test program may have demonstrated a possible means of manifolding the exchanger without external leakage. While this cover created an unacceptable effectiveness degradation due to longitudinal conduction, a practical cover could be constructed with approximately one-fourth of the wall thickness, which would have given a net effectiveness of 98.9 percent at design flow.

Much was learned about the details of high-performance cryogenic heat exchanger construction and testing during this program; by itself, this new knowledge forms a significant output. The probability that future systems will perform as designed has been substantially increased.

## Section 5

### HEAT REJECTION SYSTEM

As described in the Phase B final report (Ref. 2), continuous operation of a refrigerator requires rejection of heat to the environment. The heat rejection system must be designed to operate in an ambient air temperature of 120° F and must be able to reject heat at a distance of 60 feet from the refrigerator.

The sources of heat are:

- Compressor stage aftercoolers
- Turboalternator dissipative loads
- Compressor motors
- Power conditioning and control electrical equipment

Although the compressor aftercoolers and compressor motor cooling coils are designed to pass the environmental tests, the coolant-to-air heat exchanger and the coolant pump would be designed to operate only in a static laboratory environment.

The heat rejection system would consist of a liquid coolant loop to which the heat loads are connected in parallel. The coolant would be pumped through the loads and through a remote coolant-to-air heat exchanger, which is provided with a fan. Coolanol 20 was selected as the coolant. The requirements for the heat rejection system and the four compressor aftercoolers were given in detail in Appendices XIV and XV, respectively, of the Phase B final report.

The two specifications, Specifications for Cryogenic Refrigeration Heat Rejection System and Specifications for Set of Four Refrigerator Compressor Aftercoolers, were sent to prospective vendors to solicit quotations. In response to these specifications, two proposals were received from the Standard-Thomson Corporation. The first proposal is for a set of four aftercoolers (dated 29 December 1972). A technical proposal (dated 10 January 1973) was also received from the Standard-Thomson Corporation for the heat rejection system. No immediate action was taken on either one of these proposals, because it was apparent that the immediate component testing needs did not require this equipment. Hence consideration for obligating contract funds to these two items was held in abeyance.

The proposals received for the aftercoolers and the heat rejection system are described in detail in Appendix IV, "Compressor Aftercooler Design," and Appendix V, "Heat Rejection System Design."

## Section 6

### REFERENCES

1. D. B. Colyer, et al. , Design and Development of Cryogenic Turbo Refrigerator Systems, Phase A Final Report, Report No. AFFDL-TR-71-117, Air Force Flight Dynamics Laboratory Contract No. F33615-71-C-1003, General Electric Company, Schenectady, N. Y. , 1971.
2. D. B. Colyer, et al. , Design and Development of Cryogenic Turbo Refrigerator Systems, Phase B Final Report, Report No. AFFDL-TR-72-154, Air Force Flight Dynamics Laboratory Contract No. F33615-71-C-1003, General Electric Company, Schenectady, N. Y. , 1972.
3. W. H. McAdams, Heat Transmission, McGraw-Hill Book Company, New York, N. Y. , 1954, p. 290.
4. W. M. Kays and A. L. London, Compact Heat Exchanger, McGraw-Hill Book Company, New York, N. Y. , 1964.
5. SAE Aerospace Applied Thermodynamics Manual, Society of Automotive Engineers, New York, N. Y. , 1969.

**Appendix I**

**HEAT EXCHANGER DESIGN PERFORMANCE CALCULATIONS**



## Appendix I

### HEAT EXCHANGER DESIGN PERFORMANCE CALCULATIONS

The definitions and nomenclature from Reference 4 are used in this appendix.

Given:

$$\dot{m}_{w_0} = 2.855 \text{ gm/sec}$$

26 mesh, 0.010-in. - wire-diameter screen, 79-percent void volume

Open area of lamina 3203 - 82.5 cm<sup>2</sup> (high-pressure passes)

Section length 7.48 inches; web width = 0.32 centimeter; passage width = 0.55 centimeter high pressure, 1.05 centimeters low pressure;

$$T_{avg} = 309^\circ \text{K}, P_{avg} = 0.656 \text{ atmosphere}$$

Find:

$$A_t = 82.5 \times 0.79 = 65.2 \text{ cm}^2$$

$$G = \dot{m}/A_t = 2.855/65.2 = 4.38 \times 10^{-2} \text{ gm/sec cm}^2$$

$$r_h = \frac{dw}{4} \frac{\epsilon}{1-\epsilon} = \frac{0.010 \times 2.54}{4} \times \frac{0.79}{0.21} = 0.0239 \text{ cm}$$

$$\mu = 2.04 \times 10^{-2} \text{ centipoise}$$

$$N_R = \frac{4r_h G}{\mu} = \frac{4 \times 0.0239 \times 4.38 \times 10^{-2}}{2.04 \times 10^{-2}} = 20.6$$

From Figures 122 and 123:

$$j = 0.345, f = 3.3$$

From Reference 5,  $N_{pr} = 0.703$

$$\lambda = \frac{j}{N_{pr}^{2/3}} \frac{L}{r_h} = \frac{0.345}{(0.703)^{2/3}} \times \frac{7.48}{0.0239} = 137$$

$$\rho = \frac{0.656}{21 \times 309} = 101 \times 10^{-6} \text{ gm/cm}^3$$

$$\Delta P = \frac{f}{2} \frac{G^2 L}{\rho r_h} = \frac{3.3}{2} \frac{(4.38 \times 10^{-2})^2}{101 \times 10^{-6}} \times \frac{7.48}{0.0239} = 9500 \frac{\text{dynes}}{\text{cm}^2} = 0.0095 \text{ atmosphere}$$

Conduction  $\lambda$  ( $\lambda_k$ ):

$$k_{\text{copper}} = 4.25 \text{ watts/cm}^\circ \text{K}$$

$$A_k = L \times h \times (1 - \epsilon) = 21.3 \times 4.98 \times 0.215 = 22.6 \text{ cm}^2/\text{web}$$

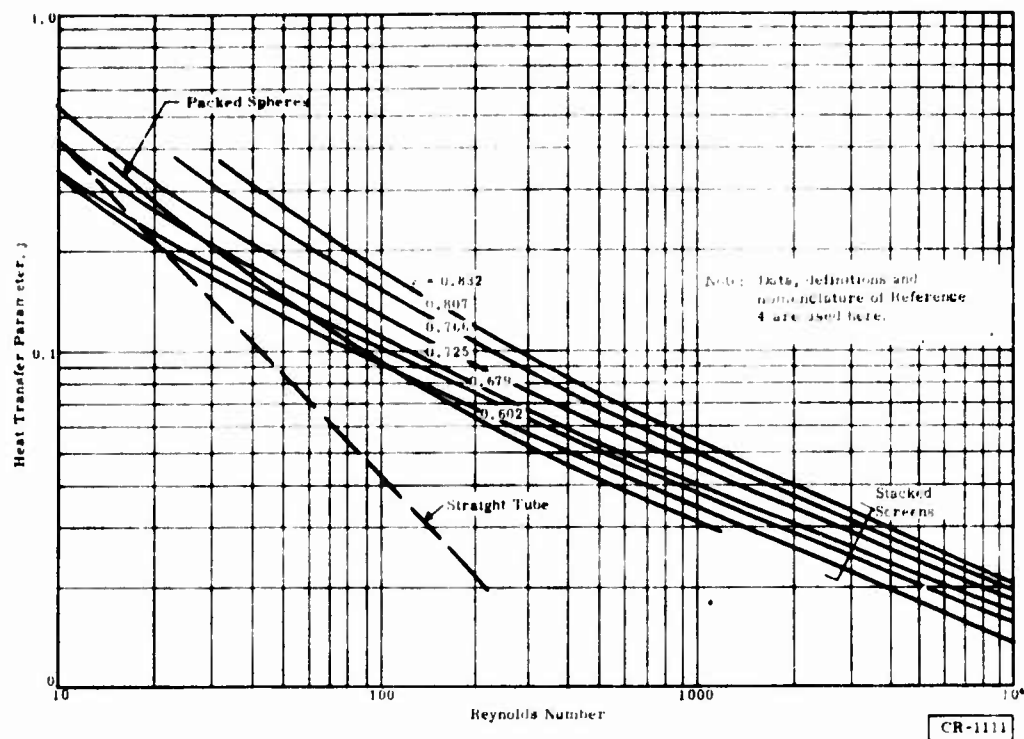


Figure 122. Heat Transfer Data for Mesh and Sphere Packing

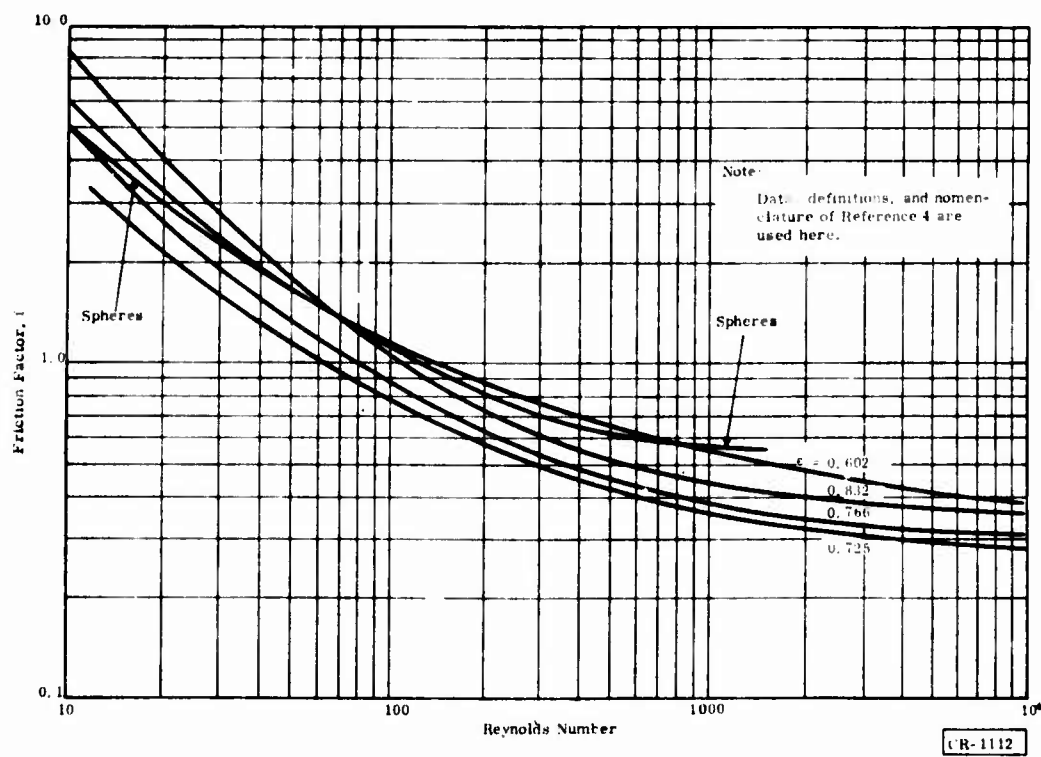


Figure 123. Friction Factors for Mesh and Sphere Packing

$$(h = \frac{OD-ID}{2} \text{ of passages})$$

$$l_k = \frac{[\text{web width} + \frac{1}{8} (\text{high-pressure pass. width} + \text{low pressure pass. width})]}{0.707}$$

$$= \frac{[0.32 + \frac{1}{8} (0.55 + 1.05)]}{0.707} = 0.737 \text{ cm}$$

$$\lambda_k = \frac{kA}{lmc_p} = \frac{4.25 \times 22.6 \times 60}{0.737 \times 2.855 \times 1.25 \times 4.18} = 523$$

Longitudinal conduction loss:

$$A_k = 30 \times 4.98 \times (0.55 + 1.05) = 227 \text{ cm}^2$$

$$k_{H_e} \text{ at } 261^\circ \text{K (from Ref. 5)} = 15 \times 10^{-4} \text{ watts/cm}^\circ \text{K}$$

$$\frac{k_{\text{screen}}}{k_{H_e}} = \frac{4.25}{15 \times 10^{-4}} = 2830$$

From Figure 124:

$$\frac{k_b}{k_{H_e}} = 1.7, \text{ and } k_b = 1.7 \times 15 \times 10^{-4} = 25.5 \times 10^{-4} \frac{\text{watts}}{\text{cm}^\circ \text{K}}$$

$$\frac{\delta \epsilon}{\epsilon} = \frac{kA}{Lmc_p} = \frac{25.5 \times 10^{-4} \times 227}{21.3 \times 2.855 \times 1.25 \times 4.18} = 0.00165$$

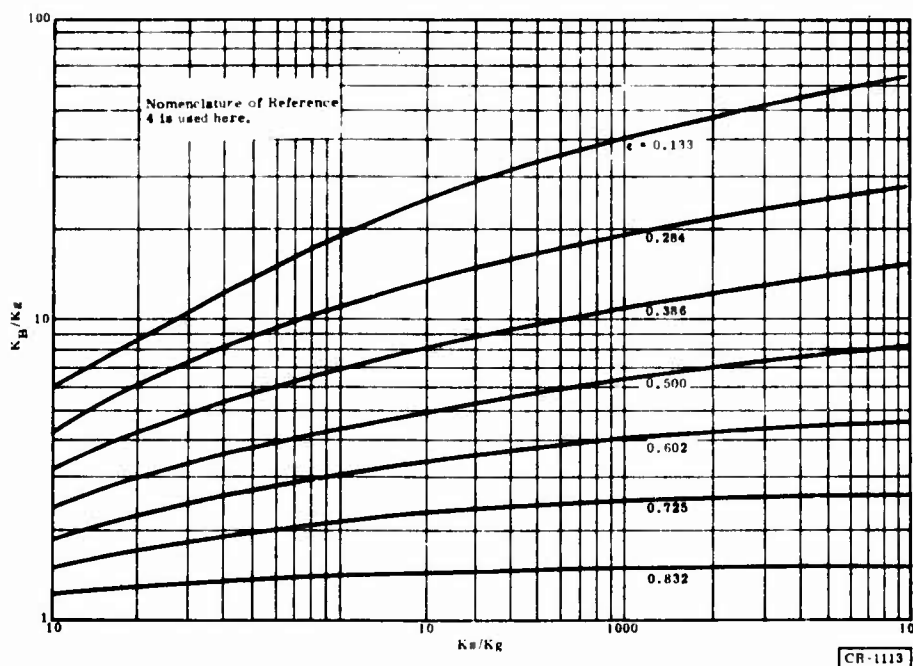


Figure 124. Effective Thermal Conductivity of Packed Bed

**Appendix II**

**HEAT EXCHANGER TEST PROCEDURE**

## Appendix II

### HEAT EXCHANGER TEST PROCEDURE

#### LEAKAGE TEST

##### EXTERNAL LEAK TEST

This test was performed in the test apparatus shown in Figure 125, prior to running the thermal effectiveness test. A helium leak detector that can detect a minimum leak rate of  $1.5 \times 10^{-9}$  torr-liter/sec was used.

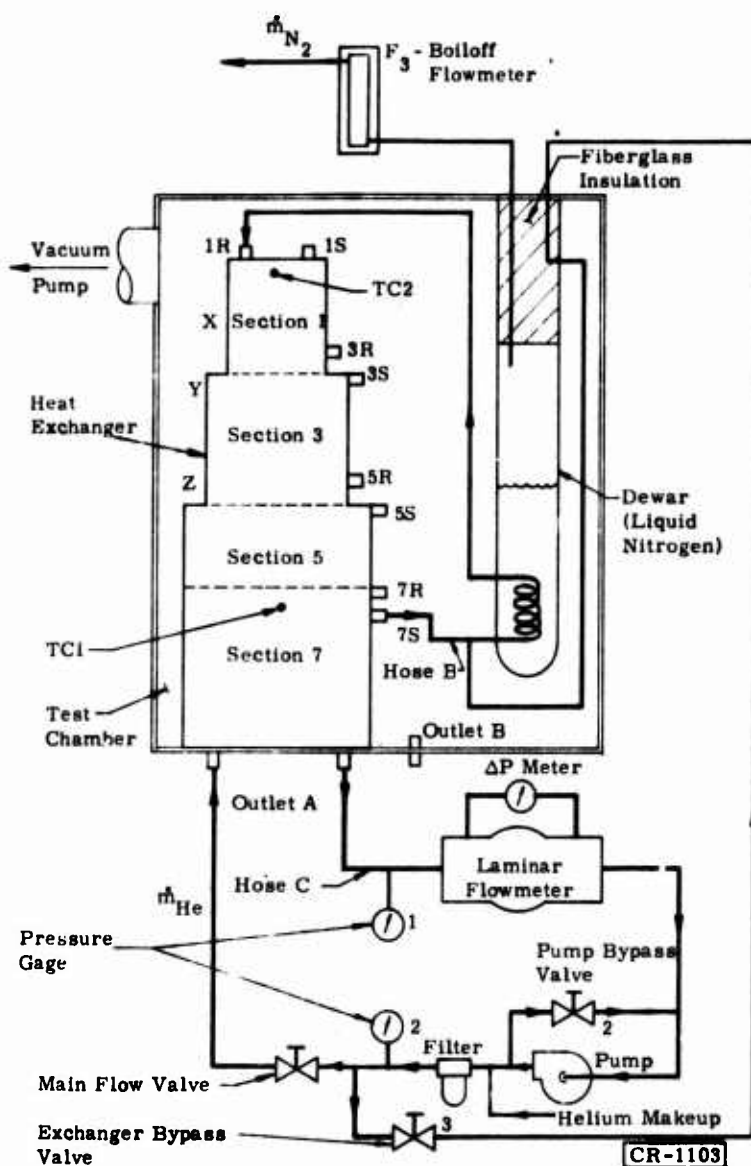


Figure 125. Schematic Diagram of Test System

After the test chamber was evacuated to  $10^{-3}$  torr or less, and the system was purged with dry helium, the leak detector was connected to the inside test chamber and the chamber was evacuated further by means of the leak detector. Any leakage indicated by the leak detector was located and repaired.

### STREAM-TO-STREAM LEAK TEST

This test was measured in all sections of the heat exchanger at once, according to the following procedure:

1. All ports and openings of the heat exchanger are blocked, except one return port and one supply port.
2. A helium supply is connected to the open supply port, and a flow-meter is connected to the open return port (Figure 126).

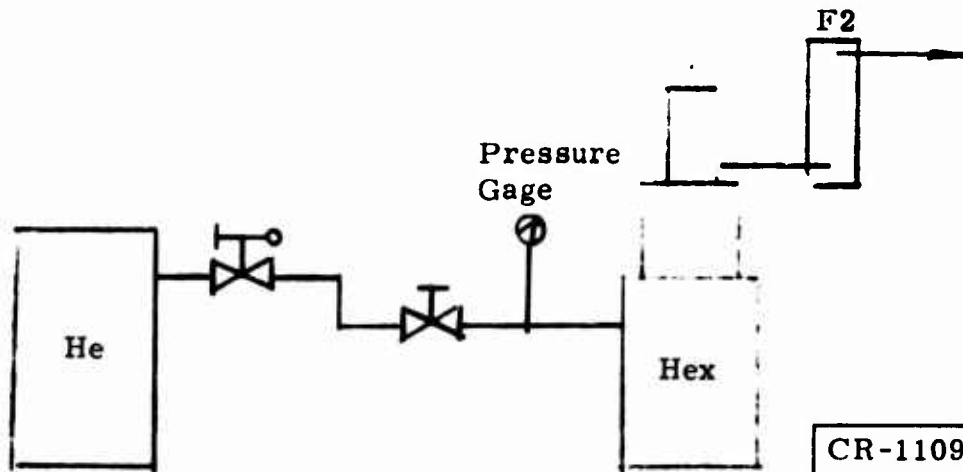


Figure 126. Test Setup for Stream-to-Stream Leakage

3. Helium gas at 2 psi is supplied to the heat exchanger, at room temperature, and the resulting flow rate from the return port, which is at atmospheric pressure, is monitored.
4. An acceptable leakage level will be a mass flow rate less than 0.1 percent of the system flow rate.

### THERMAL EFFECTIVENESS

#### PRELIMINARY LEAK TEST

This test is performed to check for leaks through the outer wall or through the cover of the heat exchanger (Figure 127):

1. Connect a helium supply to one supply port of the heat exchanger and to one return port. All other ports and openings are sealed. A flow-meter is placed in the helium supply line, as shown in Figure 127.

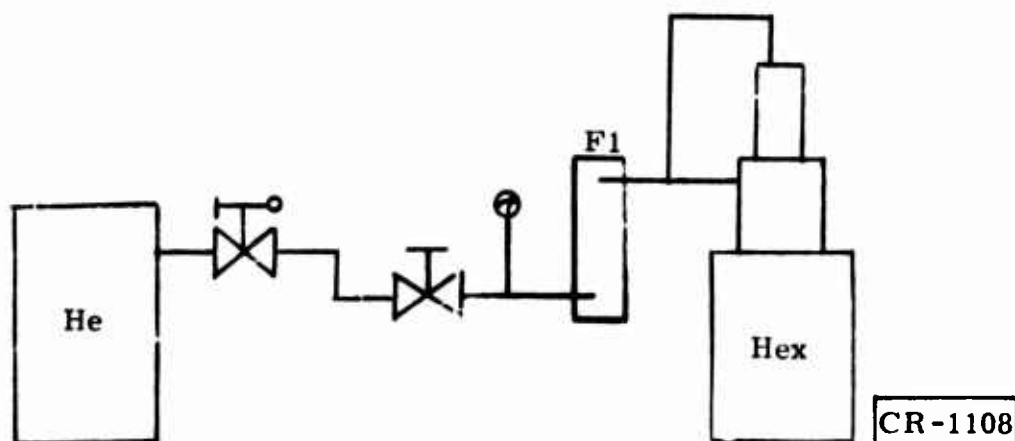


Figure 127. Test Setup for External Leakage Check

2. Supply helium to the heat exchanger until the flowmeter indicates a zero flow rate.
3. If a zero flow rate is reached, leakage is assumed minimal, and the test is satisfactory.
4. If leakage is indicated by a nonzero flow rate in the flowmeter, locate and repair the source(s). This test is then repeated until a zero flow rate is attained.

### THERMAL EFFECTIVENESS TEST

1. Connect flow hoses and thermocouples, for the section to be tested, according to Table 10 and Figure 125.

Table 10

#### HOSE AND THERMOCOUPLE CONNECTIONS

Section	$\dot{m}_T$ (gm/sec)	Hose B	Hose C	Thermocouple 1	Thermocouple 3
7	2.38	7S	OTLT. A	7S	Z
5	3.26	5S	7R, OTLT. B	5S	Y
3	4.53	3S	5R, OTLT. B	3S	X
1	2.50	1S	3R, OTLT. B	1S	X

CR-1094

2. Table 11 shows the test flow rates to be used. These flow rates are the flow rates prescribed by the specification, corrected to test conditions.
3. Evacuate the test chamber to  $10^{-3}$  torr or less, before beginning the test.
4. Be sure system is purged with dry helium, at 10 psi, before beginning the test. Do not vacuum-purge.

Table 11  
TEST MASS FLOWS

Section	Specified Flow Rate $\dot{m}_{\text{spec}}(\text{g./l./sec})$	$T_H(^{\circ}\text{K})$	$T_C(^{\circ}\text{K})$	$T_{\text{ave}}(^{\circ}\text{K})$	$\mu_{\text{ave}}\mu_{\text{spec}}$	Viscosity at Average Test Temperature (194° K)	Test Flow Rate $\dot{m}_T(\text{gm/sec})$
7	2.855	335.0	188.1	261.6	$3.85 \times 10^{-7}$	$3.2 \times 10^{-7}$	2.38
5	2.651	188.1	99.22	143.66	$2.6 \times 10^{-7}$	$3.2 \times 10^{-7}$	3.26
3	2.405	99.22	54.41	76.86	$1.7 \times 10^{-7}$	$3.2 \times 10^{-7}$	4.53
1	0.780	54.51	12.46	33.49	$1.0 \times 10^{-7}$	$3.2 \times 10^{-7}$	2.50

Note: viscosity,  $\mu$ , in lb-sec/ft<sup>2</sup>

$$N_R = \frac{\dot{m}_{\text{spec}}}{\mu_{\text{spec}}} = \frac{\dot{m}_T}{\mu_T}$$

$$\dot{m}_T = \frac{\mu_T}{\mu_{\text{spec}}} \dot{m}_{\text{spec}}$$

CR-1093

5. Begin the test with all flow valves open. Close the pump bypass valve slowly, until sufficient flow is obtained to begin cooldown (0.2 to 0.3 inch of water). Monitor cooldown, and vary the flow (by opening or closing the pump bypass valve) to maintain 6° to 8° F/min cooldown. When the cold end reaches about -250° F, switch to monitoring the middle thermocouple and finally the warm-end thermocouple.
6. If flow begins to drop significantly (more than 0.1 inch of water after stabilization at a particular flow) or if the pressure drop becomes too great (more than 2 psi for 0.4 inch of water flow), blockage is probably occurring and the test should be stopped.
7. When the warm-end (No. 1) thermocouple reaches about -200° F (or earlier, if the flowmeter begins to frost), close the exchanger bypass valve and run on full counterflow.
8. Stabilize the temperatures under full counterflow conditions at maximum flow (i. e., with the pump bypass valve closed). Attach the nitrogen boiloff flowmeter to the dewar and read the flow under stable conditions. (Use a 1/2 inch-inside-diameter tube about 10 feet long between the dewar and the flowmeter.)
9. Vary the flow to 80, 90, 110, and 120 percent of full flow. (No requirement exists to maintain the exact percentage, but obtain an accurate reading of the flow). At each level, allow temperatures to stabilize (probably 5 to 10 minutes of running), and then take nitrogen flow readings.
10. Shut down the system and warm up the exchanger. Do not allow air to contact any part of the exchanger. Maintain helium pressure ( $\approx$  5 psi) in the exchanger, and maintain vacuum in the chamber. Dry nitrogen should be substituted in the vacuum chamber if fast warmup is desired.



## PRESSURE DROP

The pressure drop over the high-pressure and low-pressure streams of each of four sections (Figure 128) of the heat exchanger will be measured with Reynolds numbers at two points below and two points above the design Reynolds number, as well as at the design Reynolds number.

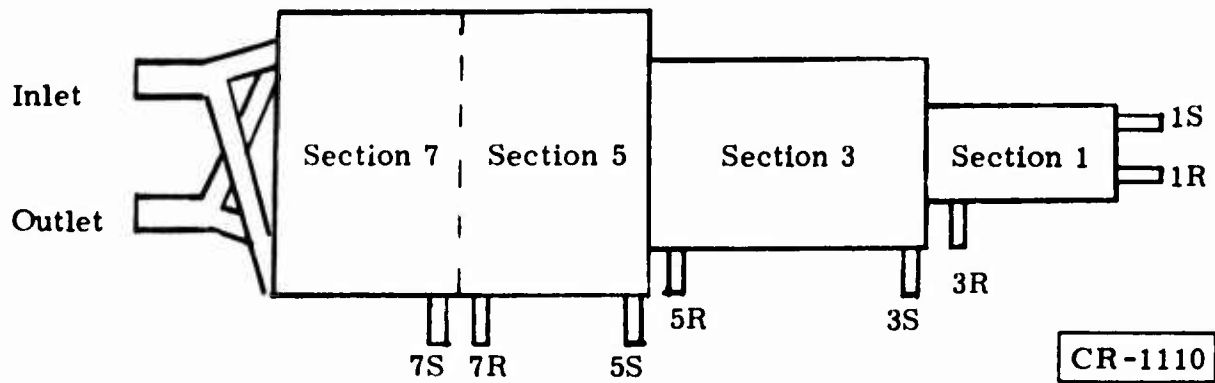


Figure 128. Port Locations (RPX 04)

These tests will be made using nitrogen gas flowing at room temperature and near atmospheric pressure. As an example of the procedure, to measure the pressure drop across the high-pressure stream of Section 7, connect the nitrogen gas source with a pressure gage to the inlet, connect the flowmeter and pressure gage to the port 7S (S = supply; R = return), and seal all other ports and openings. Adjust the nitrogen gas flow rate to the desired value, as read on the flowmeter, and read the pressure drop from the pressure gages. Table 12 lists the connections for each section.

Table 12  
PRESSURE DROP

Section	Stream	Nitrogen and Pressure Gage No. 1 Location	Flowmeter and Pressure Gage No. 2 Location
7	High pressure	Inlet	7S
7	Low pressure	Outlet	7R
5	High pressure	7S	5S
5	Low pressure	7R	5R
3	High pressure	5S	3S
3	Low pressure	5R	3R
1	High pressure	3S	1S
1	Low pressure	3R	1R

CR-1095

A similar test will be made with one stream of one section using helium gas at room temperature and near atmospheric pressure. The flow must be supplied by the effectiveness test pump in closed-circuit operation. Read the pressure drop from the inlet and outlet pressure gages and flow from the system flowmeter.

**Appendix III**

**HEAT EXCHANGER TEST DATA AND DATA REDUCTION**

### Appendix III

#### HEAT EXCHANGER TEST DATA AND DATA REDUCTION

##### EFFECTIVENESS DATA REDUCTION (TYPICAL)

Data point 4:

He flow reading 1.60 inches water,  $p = 9.75$  psi

$N_2$  flow reading = 0.325

Helium mass flow (Figure 129)

$\dot{V}$  scfm air = 21.0 cfm

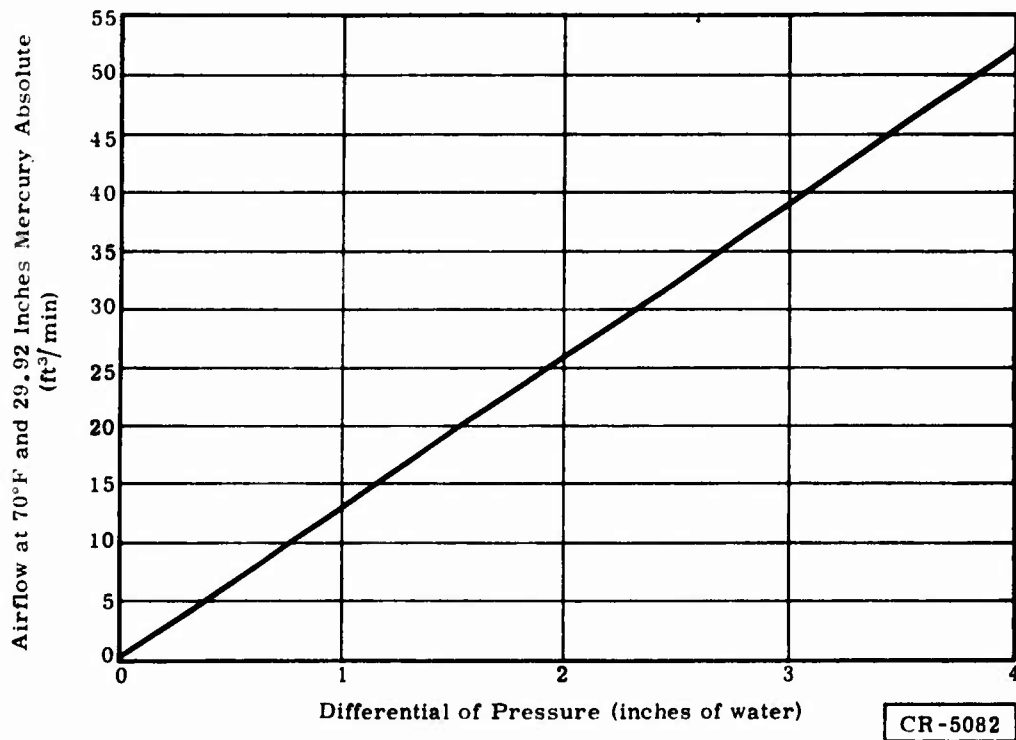


Figure 129. Meriam Flowmeter Curve

Viscosity correction factor is 0.912 for:

$$\mu_{He} = 1.98 \times 10^{-4} \text{ poise}$$

$$\mu_{air} = 1.80 \times 10^{-4} \text{ poise}$$

$$\dot{V} \text{ scfm He} = 0.912 \times 21.0 = 19.15$$

$$\rho_{He} = \frac{24.55 \times 144}{386 \times 530}$$

$$= 0.0173 \text{ lb/ft}^3$$

$$\dot{m}_{He} = \frac{19.15 \times 0.0173}{60}$$

$$= 0.0055 \text{ lb/sec}$$

$$= 2.50 \text{ gm/sec}$$

$$T_{avg} = 190^\circ\text{K}, \text{ and } \mu_{190} = 1.48 \times 10^{-2} \text{ poise}$$

$$\dot{m}/\mu = \frac{2.50}{1.52 \times 10^{-4}} = 1.69 \times 10^4$$

$N_2$  mass flow - (flowmeter maximum flow = 1.30 scfm)

$$\dot{V} \text{ scfm } N_2 = 0.325 \times 1.30 = 0.422 \text{ cfm}$$

$$\rho_{N_2} = 0.074 \text{ lb/ft}^3$$

$$\dot{m} = \frac{0.422 \times 0.074}{60}$$

$$= 5.21 \times 10^{-4} \text{ lb/sec}$$

$$= 0.236 \text{ gm/sec}$$

$\delta T$ :

$$\dot{Q} = \dot{m}_{He} c_p \delta T = \dot{m}_{N_2} \lambda_{N_2}$$

$$2.50 \times 1.25 \times \delta T = 0.236 \times 4.76$$

$$\delta T = 3.59^\circ\text{K}$$

$$\epsilon = \frac{\Delta T}{\Delta T + \delta T} = \frac{217}{217 + 3.6} = 0.9838$$

Effect of cover conduction:

$$k_{ss} = 0.12 \text{ watts/cm}^\circ\text{K}$$

$$A_k = \pi(29.2) \times 0.152 = 14.0 \text{ cm}^2$$

$$l_k = 21.3 \text{ cm}$$

$$\frac{\delta \epsilon}{\epsilon} = \frac{kA}{l \dot{m} c_p} \quad (\text{Ref. 4})$$

$$= \frac{0.12 \times 14.0}{21.3 \times 2.5 \times 1.25 \times 4.18}$$

$$= 0.0061$$

Therefore:

$$\epsilon_a = 0.9838 + 0.0061 = \underline{0.9899}$$

### PRESSURE DROP DATA REDUCTION

#### NITROGEN FLOW, TEST 2

Data Point 7:

Reading on flowmeter = 0.35,  $p \approx 1$ -atmosphere gage

Maximum flow = 11.0 scfm

Therefore:

$$\dot{V} = 0.35 \times 11.0 = 3.85 \text{ scfm}$$

(Assume no density correction required.)

$$\rho_{N_2} = 0.074 \text{ lb/ft}^3$$

$$\dot{m}_{N_2} = \frac{3.85 \times 0.074}{60}$$

$$= 0.00475 \text{ lb/sec}$$

$$= 2.16 \text{ gm/sec}$$

$$\dot{m}/\mu = \frac{2.16}{1.75 \times 10^{-4}} = 1.23 \times 10^4$$

$$\Delta P = 3.8 \text{ inches water} = 0.933 \times 10^{-2} \text{ atmosphere}$$

#### HELIUM FLOW, TEST 3

Data Point 11:

Laminar flowmeter  $\Delta P = 2.50$  inches water,  $P_{He} = 4.65$  psi

From Figure 129,  $\dot{V}_{air} = 32.7$  scfm. Correcting for viscosity:  $\dot{V}_{He} = 32.7 \times 0.912 = 29.8$  scfm

$$\rho_{He} = \frac{19.35 \times 144}{386 \times 530}$$

$$= 0.0136 \text{ lb/ft}^3$$

$$\dot{m}_{He} = \dot{V}\rho$$

$$= \frac{29.8 \times 0.0136}{60}$$

$$= 0.00675 \text{ lb/sec}$$

$$= 3.07 \text{ gm/sec}$$

and:

$$\dot{m}/\mu = \frac{3.07}{1.98 \times 10^{-4}} = 1.55 \times 10^4 \text{ cm}$$

$$\Delta P = 1.45 \text{ psi} = 0.099 \text{ atmosphere}$$

**PRESSURE DROP CALCULATION AT TEST CONDITIONS (TYPICAL) -  
NITROGEN AT DESIGN FLOW**

$$\dot{m}/\mu = 1.59 \times 10^4 \text{ centimeters (design flow)}$$

$$\mu_{N_2} = 1.75 \times 10^{-3} \text{ at STP}$$

$$\begin{aligned} \dot{m}_{N_2} &= 1.59 \times 10^4 \times 1.75 \times 10^{-4} \\ &= 2.78 \text{ gm/sec} \end{aligned}$$

Heat Exchanger:

	Section		
	<u>7-2</u>	<u>7-3</u>	<u>7-4</u>
$A_t$ (cm <sup>2</sup> )	65.2	53.2	64.5
$G$ (gm/sec cm <sup>2</sup> )	$4.28 \times 10^{-2}$	$5.24 \times 10^{-2}$	$4.31 \times 10^{-2}$
$r_h$ (centimeter)	0.0239	0.0178	0.0150
$N_R$	23.4	21.3	14.8
$f$	2.7	2.9	4.2
$l$	7.48	7.43	6.39

$$\rho_{N_2} = 1.186 \times 10^{-3} \text{ gm/cm}^3$$

$$\Delta P = \frac{2.7}{2} \times \frac{(4.28 \times 10^{-2})^2}{1.186 \times 10^{-3}} \times \frac{7.48}{0.0239}$$

$$= 654 \text{ dynes/cm}^2$$

$$= 0.654 \times 10^{-3} \text{ atmosphere}$$

$$\Delta P_3 = 1.41 \times 10^{-3} \text{ atmosphere}$$

$$\Delta P_4 = 1.42 \times 10^{-3} \text{ atmosphere}$$

$$\Delta P_T = (0.65 + 1.41 + 1.42) \times 10^{-3} = 3.48 \times 10^{-3} \text{ atmosphere}$$

Outlet Piping:

$$ID = 1.27 \text{ centimeters, } A_t = \frac{\pi(1.27)^2}{4} = 1.27 \text{ cm}^2$$

$$q = \frac{1}{2} \frac{G^2}{\rho}$$

$$= \frac{1}{2} \frac{(2.19)^2}{1.186 \times 10^3}$$

$$= 2.02 \times 10^3 \text{ dynes/cm}^2$$

$$G = \frac{2.78}{1.27} = 2.19 \text{ gm/sec cm}^2$$

K for abrupt contraction is about 0.46, and:

$$\Delta P_c = 0.46 \times 2.02 \times 10^3 \times 10^{-8} = 0.92 \times 10^{-3} \text{ atmosphere}$$

In the tube, ( $l \approx 8$  centimeters to pressure tap):

$$N_R = \frac{1.27 \times 2.19}{1.75 \times 10^{-4}} = 15900$$

and:

$$f = 0.0083$$

(Ref. 4)

$$\Delta P = \frac{0.0083}{2} \frac{(2.19)^2}{1.186 \times 10^3} \times \frac{8}{0.32}$$

$$= 421 \text{ dynes/cm}^2$$

$$= 0.42 \times 10^{-3} \text{ atmosphere}$$

$$\Delta P = (3.48 + 0.92 + 0.42) \times 10^{-3} = \underline{4.82 \times 10^{-3}} \text{ atmosphere}$$

Tables 13 through 15 list effectiveness test data, pressure drop test data, and effectiveness versus mass flow.

Table 13  
EFFECTIVENESS TEST DATA

Helium Flow Reading (inches water)	System Pressures (psi)*	Nitrogen Flow Reading (percent of F3)**	Time at Flow (minutes)
0.41	11/10.5	16	8
0.82	11/10.4	19	7
1.20	11/10.25	24.5	6
1.60	11/9.75	32.5	7
2.00	11.05/9.35	42	5
2.40	11/8.75	53	5
2.79	11/8.3	67.5	7
3.20	--	80	2
1.81†	10/8.5	55	42
3.05†	10/7.0	93	6
3.60†	10/6.2	100	12

Equipment:

Flowmeters

F3 Fisher and Porter Flowrator Model 10A27356, Tube FP-1/ 2-21-G-10/ 80

Pressure Gages

F7 Meriam 50MC2-2 and Barton DP Meter

Vacuum Gage

P29 U.S. Gage BU-2579-A

Thermocouple Bridge

P47 U.S. Gage AW 2926AB01  
VAC3, CVC Type GPH-100C  
T1, Leeds and Northrup, Model 8693

\*Pump Outlet/ Pump Inlet pressures.

\*\*Flowmeter F3, maximum flow 1.30 scfm air.

†These readings were taken at 95°K at the No. 7 supply port.



**Table 14**  
**PRESSURE DROP TEST DATA**

Test	Flow (percent of F4)	Pressure In (psi)	Pressure Out (psi)	$\Delta P$ (psi)
1 (nitrogen at 70° F, flowmeter F4, and gages P29 and P47)	0	0	0.5	0*
	50	0.2	0.65	0.05
	60	0.4	0.7	0.2
	70	0.45	0.75	0.2
	80	0.55	0.8	0.25
	85	0.6	0.8	0.3
	90	0.8	0.75	0.55
	95	0.8	0.8	0.5
	100	0.9	0.9	0.5
2 (nitrogen at 70° F, flowmeter F4, and gages M1 and M3)	Flow (percent of F4)	Pressure In (inches water)	Pressure Out (inches water)	$\Delta P$ (inches water)
	20	6.2	4.5	1.7
	25.5	7.3	5.0	2.3
	29.5	8.3	5.4	2.9
	31	7.6	4.2	3.4
	32	9.2	5.7	3.5
	33.5	9.5	5.9	3.6
	35	10.0	6.2	3.8
3 (helium at 70° F, flowmeter F7, and gages PG47 and PG29)	Flow Reading (inches water)	Pressure In (psi)	Pressure Out (psi)	$\Delta P$ (psi)
	0	6.60	6.70	0**
	0.3	6.60	6.65	0.05
	0.5	6.55	6.55	0.1
	0.7	6.55	6.50	0.15
	0.8	6.55	6.40	0.25
	1.1	6.55	6.25	0.4
	1.3	6.50	6.05	0.55
	1.5	6.50	5.80	0.7
	1.75	6.40	5.65	0.85
	2.0	6.30	5.35	1.05
	2.25	6.15	5.00	1.25
	2.5	6.00	4.65	1.45
	3.0	5.85	4.05	1.9
	3.5	5.60	3.25	2.45
Equipment: Flowmeters	F4 Fisher and Porter Flowrator Model 10A27352 FP-3/ 4-27-G-10/ 80 Tube F7 Meriam 50MC2-2 and Barton DP Meter			
Pressure Gages	P47 U.S. Gage BU-2579-A P29 U.S. Gage AW2926AB01 M1 Dwyer, Model No. 400 M3 Dwyer, +8 to -8 inches water			

\*0.5-psi correction.

\*\*0.1-psi correction.

CR-1097

Table 15  
EFFECTIVENESS VERSUS MASS FLOW

Helium Flow/ Average Viscosity (centimeter $\times 10^4$ )	Measured Effectiveness, $\epsilon'$	$\delta\epsilon$ , Cover	Corrected Effectiveness, $\epsilon_n$
0.43	0.9680	0.0249	0.9929
0.86	0.9815	0.0121	0.9936
1.27	0.9836	0.0084	0.9920
1.69	0.9838	0.0061	0.9899
2.11	0.9833	0.0051	0.9884
2.53	0.9823	0.0043	0.9866
2.95	0.9805	0.0037	0.9842
3.39	0.9801	0.0032	0.9833
3.80	0.9780	0.0029	0.9809

CR-1098

## **Appendix IV**

### **COMPRESSOR AFTERCOOLER DESIGN**

## Appendix IV

### COMPRESSOR AFTERCOOLER DESIGN

Four aftercooler heat exchangers, one following each of four helium compressed stages, are required to cool gaseous helium and transfer the heat to Coolanol 20, which is a liquid dielectric heat transfer fluid. Each aftercooler would be of flight-weight design and aircraft quality. The aftercoolers would be used in conjunction with the heat rejection system, as shown schematically in Figure 130.

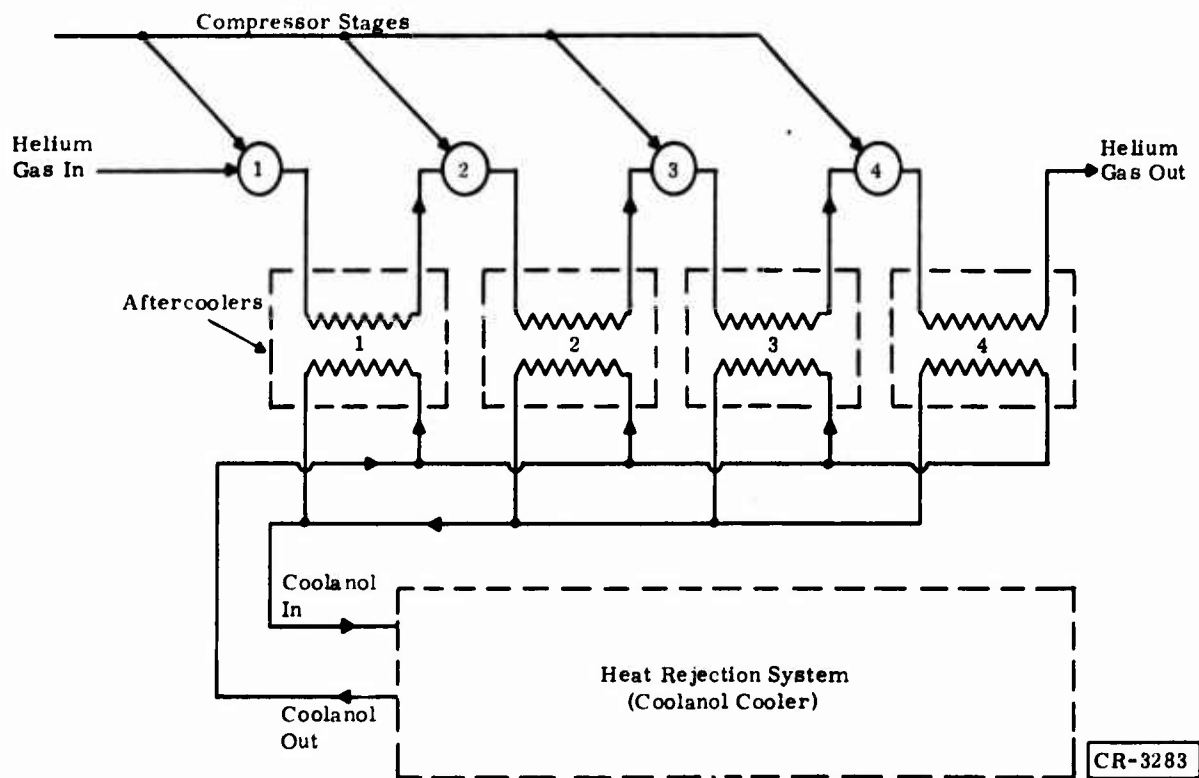


Figure 130. Schematic Diagram of Aftercoolers with Heat Rejection System

The aftercooler performance requirements are given in Table 16. The gas-side maximum pressure drop includes both the headers and the exchanger core. In addition, the design life of the heat exchangers was 30,000 hours.

The system must be designed to withstand an environment of ionizing radiation. The aftercooler must be cleaned so that no loose particles greater than 150 microinches are left on the inner surfaces and no vapors from organic materials are generated when operating below 300°F. All surfaces should also be cleaned for oxygen service.

**Table 16**  
**PERFORMANCE REQUIREMENTS**

Characteristic	Aftercooler			
	1	2	3	4
<b>Helium Side</b>				
Flow (lb <sub>m</sub> /hr)	22.6	22.6	22.6	22.6
Inlet temperature (°R)	672.0	679.0	679.0	679.0
Inlet temperature (°F)	212.0	219.0	219.0	219.0
Outlet temperature (°R)	603.0	603.0	603.0	603.0
Outlet temperature (°F)	143.0	143.0	143.0	143.0
Design inlet pressure (psia)	5.77	7.5	8.81	10.87
Maximum pressure drop (psi)	0.065	0.080	0.100	0.122
Maximum service pressure (psia)	30.0	30.0	30.0	30.0
<b>Coolanol 20 Side</b>				
Flow* (lb <sub>m</sub> /hr)	177	177	177	177
Maximum pressure* (psia)	30	30	30	30
Maximum temperature entering aftercoolers (°F)	130	130	130	130
Pressure drop* (psi)	4.8	4.8	4.8	4.8

\*Target values

### **PERFORMANCE**

The Standard-Thomson Corporation heat exchanger shown in Figure 131 was submitted in response to the request for proposals. These exchangers were designed to meet the performance requirements listed in Table 16.

The gas-side pressure drop values for each aftercooler at design conditions are:

<u>Aftercooler</u>	<u>Psi</u>
1	0.104
2	0.078
3	0.061
4	0.049

To accomplish the thermal performance required, it was necessary to increase the Coolanol 20 flow rate approximately 24 percent above the target value. The flow rate requirement is 220 lb/hr.

### **CLEANLINESS**

### **CONTAMINATION**

The Standard-Thomson Corporation has considerable experience with the contamination requirements of various heat exchangers. Standard-Thomson Corporation supplies units that have been cleaned to a predetermined level. They have a



cleaning facility that is adaptable to designs of any heat exchangers. All of the equipment used for actual analysis is supplied by the Millipore Corporation, the leader in the field of contamination detection and analysis. The actual procedures used are patterned after the procedures outlined in ARP598A.

Based on lengthy experience, the Standard-Thomson Corporation feels that a more realistic contamination level would be to allow particles up to 250 microinches and fibers up to 500 microinches. In addition, they would limit the number of fibers to a maximum of five in a fluid sample of 100-milliliters volume. The lower level of 150 microinches would be left open as a design goal. This requested level will keep costs in a practical range, whereas the level requested would require unrealistic control throughout the manufacturing cycle.

Based on experience, it is entirely possible to obtain a clean unit within specification limits, but remain unable to affirm the results. The Standard-Thomson Corporation would submit a cleaning procedure that would be mutually satisfactory.

#### OXYGEN SERVICE

The additional requirement that all surfaces be cleaned for oxygen service would add some complications to this unit. The Standard-Thomson Corporation has prior experience cleaning items for this class of service and is aware of the overall handling problems.

The Standard-Thomson Corporation is presently using oil conforming to MIL-H-6083 and VARSOL, an industrial-grade solvent, for flushing. The Standard-Thomson Corporation has found these fluids to be effective for most heat exchanger designs where control of particulate matter is of concern. For oxygen cleaning, the vapor of trichloroethylene followed by drying in an oven at 250° F has been used. If cleaning for this service is determined to be required, the Standard-Thomson Corporation is certain that a technique can be worked out to produce the desired results. A procedure for approval would be submitted.

#### STRUCTURAL CONSIDERATIONS

The Standard-Thomson plate-fin heat exchangers provide a relatively stiff structure that has proved quite reliable with respect to acceleration loadings and vibration. Ultimately, the structural integrity would depend on the type of mounting provided for the heat exchanger. A structural analysis would be performed when the mounting was determined. Based on size, weight, and geometry, no foreseeable areas of structural concern exist.

**Appendix V**

**HEAT REJECTION SYSTEM DESIGN**



## **Appendix V**

### **HEAT REJECTION SYSTEM DESIGN**

The detailed design requirements for the heat rejection system listed in Appendix XIV of the Phase B final report (Ref. 2) are summarized in the following paragraphs of this appendix.

A heat rejection system is required to transfer heat from Coolanol 20 to outside ambient air. The system must be completely self-contained, except electrical power will be available to the heat rejection system. The system will be designed for ground-based operation with an unattended life goal of 5000 hours of continuous operation.

The heat rejection system will be designed to cool the heat loads from a cryogenic refrigeration system. These heat loads consist of:

- Four compressor aftercoolers
- Power conditioner-controller
- Turboalternator loads
- Compressor motors

### **THERMAL PERFORMANCE AND PRESSURE DROP REQUIREMENTS**

The design performance requirements are:

- Ambient air side

Maximum temperature: 120° F

Minimum temperature: -30° F

Maximum altitude: 1000 feet

- Liquid Coolanol 20 side

Design point and maximum temperature: 130° F

Design point and maximum cooling load: 4000 watts

Flow rate, minimum: 3.4 gpm

Maximum heat loads pressure drop: 5.0 psi

Properties of Coolanol 20 are given in Table 17.

### **DESIGN AND CONSTRUCTION**

The heat rejection system should provide trouble-free, unattended, continuous operation without leaks over a period of at least 5000 hours. Hence, the components incorporated into the system should have had a reasonable history of satisfactory performance under similar operating conditions.

**Table 17**  
**COOLANOL 20 SPECIFICATIONS**  
**(From Monsanto Technical Bulletin O/FF-25)**

Property	Specification	
<b>Monsanto Specifications</b>		
Appearance	Clear, light-amber liquid	
Flash point	230°F min	
Fire point	240°F min	
Moisture	0.03% max	
Neutralization number	0.20 max (acid)	
Specific gravity at 25/25°C	0.884 to 0.890	
Viscosity		
at 210°F	0.88 to 0.96 cP	
at 100°F	1.90 to 2.10 cP	
Dielectric strength 0.1 in. gap at 25°C	35 kv min	
Refractive index at 25°C	1.406 to 1.410	
<b>Typical Physical Properties</b>		
Appearance	Clear, light-amber liquid	
Pour point	Below -100°F (-73°C)	
Boiling point (760 mm Hg)	Above 450°F (232°C) (with decomposition)	
Vapor pressure, mm Hg 300°F (149°C)	38	
Average coefficient of thermal expansion		
-60° to 300°F	0.00055/°F	
-51° to 149°C	(0.001/°C)	
Kinematic viscosity -85°F (-54°C)	43 centistokes	
100°F (38°C)	2.00	
210°F (99°C)	0.92	
Specific gravity (25°/25°C) (77°/77°F)	0.884	
Density 77°F (25°C)	7.35 lb/gal (U.S.) 0.884 grams/ml	
AIT	550°F (288°C)	
Flash point	240°F (116°C)	
Fire point	260°F (127°C)	
Refractive index, $n_D^{25}$	1.4075	
Specific heat 100°F (38°C)	0.47 Btu/lb/°F (or cal/g/°C)	
Thermal conductivity 100°F (38°C)	0.067 Btu-ft/hr ft <sup>2</sup> °F	
Acid number	0.08 mgKOH/gm	
Surface tension at 25°C	22.8 Dynes/cm	
Foaming (ASTM D892)	None	
<b>Typical Electrical Properties</b>		
Dielectric strength (60 Hz, 0.1 in., °T°F)	40 kv	
Dielectric constant at 77°F		
60 Hz	2.55	
1000 Hz	2.52	
10,000 Hz	2.51	
100,000 Hz	2.51	
Volume resistivity at 77°F	$1 \times 10^{14}$ ohm-cm	
<b>Typical Oxidation/Corrosion (250°F/168 Hr)</b>		
Metal weight change (mg/cm <sup>2</sup> )		
Al	+0.01	
Cu	-0.01	
Steel	0	
Cd	0	
Mg	-0.01	
Ti	-0.01	
Acidity, mgKOH/gm		
Initial	0.08	
Final	0.05	
Viscosity change at 210°F	-0.3%	
<b>Typical Hydrolytic Stability at 200°F</b>		
Property	75-Gm Fluid 25-Gm Water	75-Gm Fluid 1.5-Gm Water
Copper weight change (mg/cm <sup>2</sup> )	-0.42	-0.07
Acid number change (mgKOH/gm)		
Fluid layer	0	0
Water layer	+0.05	+0.02
Viscosity change at 210°F	+0.4%	0
Insolubles, %	0.03	0.02
<b>Typical Shell 4-Ball Test (167°F, 1 hr, 600 Rpm)</b>		
Load (kg)	Scar Diameter (mm)	
	Steel on Steel	Steel on Bronze
4	0.75	0.63
10	0.81	0.73
40	1.18	1.10

\*28 x 10<sup>-4</sup> cal-cm/sec cm<sup>2</sup> °C

Special consideration should be given to a motor driven pump, to have no dynamic seal that may leak outside the system. Redundant components are allowable, to meet the 5000-hour life goal.

The heat rejection system should consist of components, including the controls and instrumentation panel, mounted permanently on a skid. Provisions are necessary for the skid to be moved with an overhead crane.

The heat rejection system will be located outdoors, at a distance up to 60 feet from the refrigerator heat loads. The heat rejection system must be capable of providing the pressure necessary to operate at this distance from the refrigerator heat loads.

Any painting and/or covering for weather protection will be integral with the heat rejection system.

Fluid loop cleanliness requirements must be suitable to satisfy the individual heat rejection system component requirements. In addition, the largest particle size allowed to be transmitted to the heat loads shall be no larger than 0.001 inch in the greatest dimension.

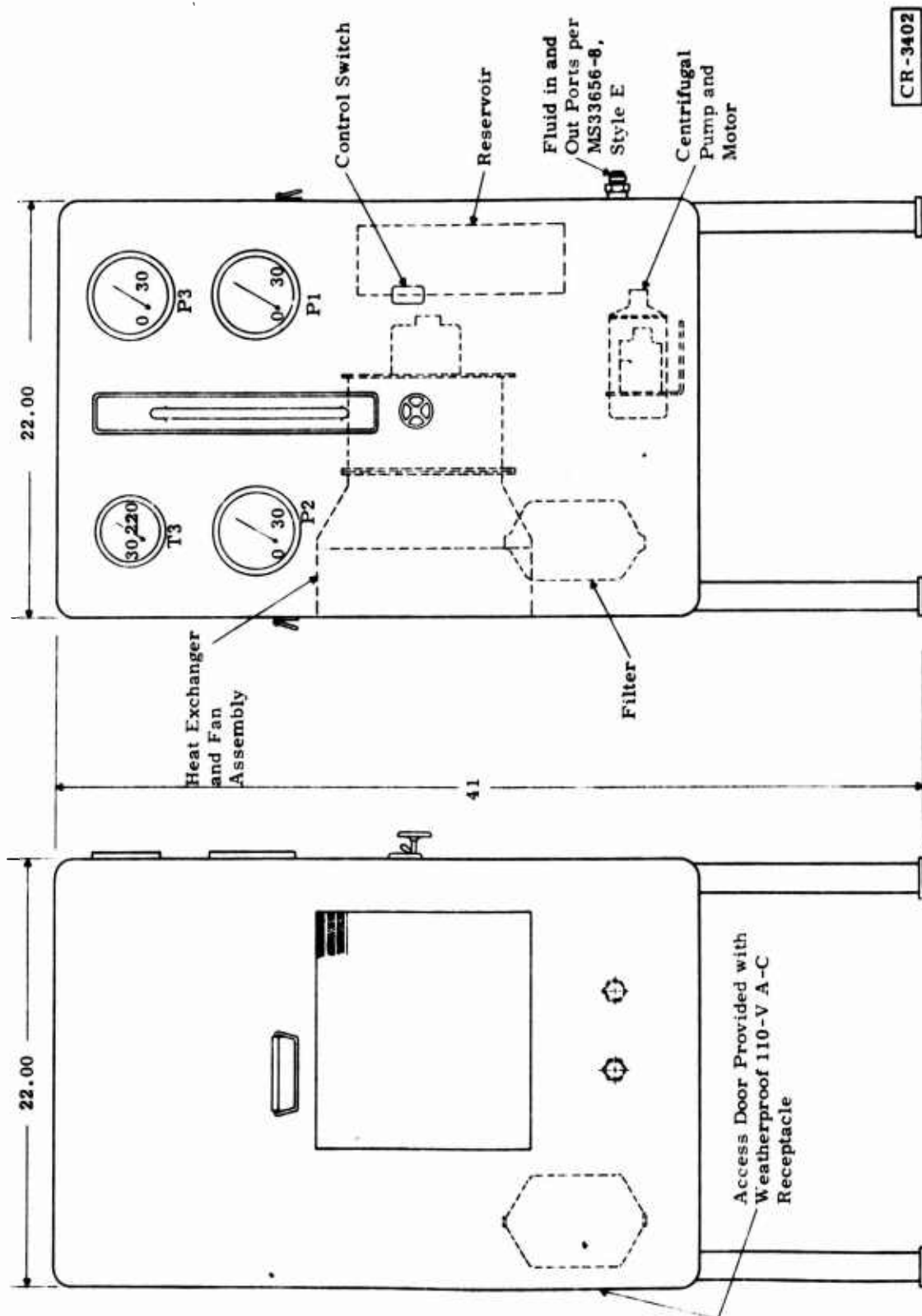
The Coolanol loop must be a closed system with a reservoir, fill valving, and provisions for thermal expansion of the Coolanol. Minimum pressure for the system must be above 1 atmosphere, so that any potential leaks will be outward. The power supply available will be 60-cycle, 460-volt, 3-phase power and/or 120/240 single-phase power.

The heat rejection system will consist of the following principal components:

- Motor driven pump to circulate the Coolanol 20
- Motor driven fan to circulate the ambient air
- Heat exchanger to transfer heat from the Coolanol to the ambient air
- Reservoir for the Coolanol 20
- Expansion chamber for the Coolanol 20
- Valving, ducting, tubing, and fittings, as required
- Automatic control valves with sensors
- Manual control valves
- Filter for Coolanol 20

## **CONTROLS AND INSTRUMENTATION**

Both adjustable automatic and manual controls will be incorporated into the heat rejection system. Automatic, adjustable controls for the cooled



CR-3402

Figure 132. Heat Rejection System

Coolanol 20 shall maintain the output temperature and heat load pressure drop to within  $\pm 5^{\circ}\text{F}$  and  $\pm 2$  psi.

Instrumentation will be used to monitor critical and functional stations in the heat rejection system. All controls and instrumentation will be mounted on a single panel, which in turn will be mounted on the skid.

In response to the request for quotations sent out (based on the requirements noted above), the Standard-Thomson Corporation responded by submitting the heat rejection system shown in Figure 132.

The Standard-Thomson Corporation 5D905 heat rejection system is designed to remove 13,640 Btu/hr (4000 watts) from Coolanol 20 at a minimum flow rate of 3.5 gal/min. The outlet fluid temperature would be automatically maintained at  $125 \pm 5^{\circ}\text{F}$ , once the system reached the  $125^{\circ}\text{F}$  operating temperature. All components for this system were selected on the basis of high-reliability and no-maintenance criteria. To minimize the number of connections and possible leaks, the temperature regulating valve would be fabricated as part of the heat exchanger manifold, and the reservoir and accumulator would be combined in one package.

### SYSTEM OPERATION

Coolanol 20 is pumped from the reservoir through the air-cooled heat exchanger by means of a magnetically coupled centrifugal pump. A Standard Thomson Corporation three-port mixing valve is incorporated into the heat exchanger manifold and serves to regulate the outlet temperature. The Coolanol 20 then passes through a 10-micron filter and out to the aftercoolers. The return flow from the heat loads passes through a flowmeter before returning to the reservoir. Figure 133 shows system operation. The electri-

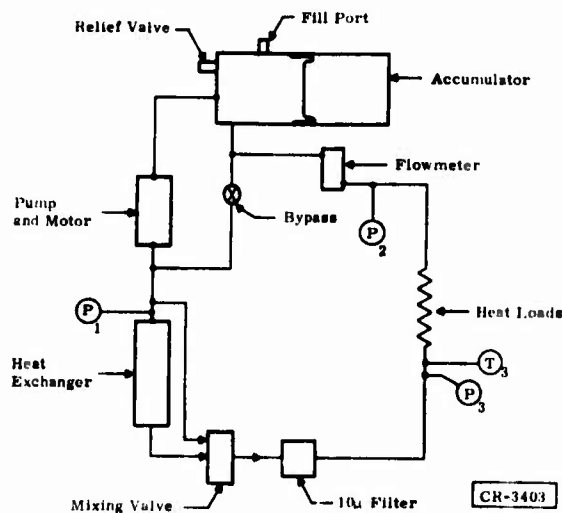


Figure 133. Schematic Diagram of System Operation

cal power requirements would be: 60 cycles, 115 volts, single phase. The pump and fan would be fused separately, and one off-on switch with an indicator light would be mounted on the instrument panel. A weatherproof, 115-volt receptacle would be provided at the rear of the cabinet.

### **SYSTEM COMPONENTS**

The reservoir used in this system is a Standard-Thomson Corporation designed accumulator; it has a capacity of 50 in.<sup>3</sup> and incorporates a rolling diaphragm to provide a nearly frictionless seal. The rolling diaphragm is compatible with the Coolanol 20 and temperature requirements. The Bellofram Corporation estimates the cycle life of a similar diaphragm to be  $20 \times 10^6$  cycles. The accumulator is equipped with a pressure relief valve and a Schraeder fill port.

The pump used in the heat rejection system is a magnetically coupled centrifugal pump. The pump body and impeller are made of 316 stainless steel and feature Teflon static seals. The pump is rated for continuous duty, with a guaranteed minimum life of 8000 hours. Micro-Pump, Inc. has been conducting life tests on this pump, as well as other model pumps, and feels that this 8000-hour continuous duty figure is conservative. The cooler used here is a plate-fin heat exchanger manufactured by the Standard-Thomson Corporation.

This type of construction has proved to be extremely reliable in vibration and high g-load environments. The fan coupled to the heat exchanger is a Joy series 66 axivane fan.

The fan features prelubricated sealed bearings and motor and is designed for no less than a 50,000-hour average life. The motor windings and lubrication are capable of operation within ambient temperatures of  $-30^{\circ}$  to  $+135^{\circ}\text{F}$ . The Standard-Thomson Corporation three-port mixing valve is a proportioning-type temperature regulating valve. In operation, this valve opens and closes the hot and cold inlets in proportion to the outlet temperature. Because of its simple design, it is very reliable and requires no adjustment. This basic mixing valve is used on other systems, including General Electric fuel cells, and has exhibited good results in providing the temperature regulation for which it was designed.

### **INSTRUMENTATION**

All instrumentation would be conveniently mounted on the front panel. Following are the specific gages and instruments selected:

- Three Marsh 4-1/2-inch-diameter pressure gages, 0 to 30 psi  $\pm 1.0$  percent
- One Marsh temperature indicator,  $30^{\circ}$  to  $220^{\circ}\text{F}$ , 3-1/2-inch-diameter
- One Dwyer flowmeter, 0 to 8 gpm

## **TESTING**

The Standard-Thomson Corporation has a test facility capable of performing the required testing directly. This direct approach is preferred over the method of extrapolating room temperature test results. This procedure would eliminate any errors in extrapolation and minimize variations in fluid properties versus temperature data.

# DISTRIBUTION LIST

	<u>Quantity</u>
2750th AEW/SSL Wright-Patterson Air Force Base Ohio 45433  (ATTN: Main Technical Library)	1
AFAL-POE-1 Wright-Patterson Air Force Base Ohio 45433 (ATTN: Mr. E. T. Mahefkey)	1
AFAL/TSR Wright-Patterson Air Force Base Ohio 45433	2
AFFDL/DOO (STINFO) Wright-Patterson Air Force Base Ohio 45433	1
AFFDL/DOE (LIBRARY) Wright-Patterson Air Force Base Ohio 45433	1
AFFDL/FEE Wright-Patterson Air Force Base Ohio 45433	52
Air University Maxwell Air Force Base Alabama 36112	1
Department of Defense Advanced Research Projects Agency 1400 Wilson Boulevard Arlington, Virginia 22209  (ATTN: STO/Major Robert Pulson)	1
Goddard Space Flight Center Auxiliary Propulsion Branch Greenbelt, Maryland 20771  (ATTN: Code 734/Mr. Max Gasser)	1



	<u>Quantity</u>
George C. Marshall Space Flight Center S&E-ASTN-D/Bldg 4666 Huntsville, Alabama 35812 (ATTN: Mr. Hans C. Paul)	1
National Aeronautics and Space Administration Scientific and Technical Information Facility P.O. Box 33 College Park, Maryland 20740	1
Office of Naval Research Power Program Arlington, Virginia 22217 (ATTN: Code 473/Mr. Keith Ellingsworth)	1
U.S. Army Electronics Command Night Vision Laboratory Far Infrared Technical Area Fort Belvoir, Virginia 22060 (ATTN: Mr. S. Rodak)	1
Commanding Officer U.S. Army Mobility Equipment Research and Development Center SMEFB-EA; AMSTUTZ Fort Belvoir, Virginia 22060	1
U.S. Army Safeguard Systems Command P.O. Box 1500 Huntsville, Alabama 35307 (ATTN: Mr. W. O. Davis, Chief, Optics Division)	1
U.S. Army Satellite Communications Engineering Directorate Fort Monmouth, New Jersey 07703 (ATTN: Mr. Robert Keller)	1
Aerospace Corporation 2350 East El Segundo Boulevard El Segundo, California 90245 (ATTN: Mr. M. Bello)	1

**Quantity**

Aerospace Corporation  
Applied Mechanics Division  
2350 East El Segundo Boulevard  
El Segundo, California 90245

(ATTN: Mr. Martin Donabedian) 1

Aerospace Corporation  
2350 East El Segundo Boulevard, P.O. Box 95085  
El Segundo, California 90245

(ATTN: Mr. R. A. Farran) 1

Aerospace Corporation  
Office for Technology  
2350 East El Segundo Boulevard  
P.O. Box 95085  
El Segundo, California 90245

(ATTN: Mr. Albert Straubinger) 1

Aerospace Corporation  
2350 East El Segundo Boulevard  
El Segundo, California 90245

(ATTN: Mr. R. W. Vance) 1

Air Products and Chemicals  
Advanced Products Department  
Allentown, Pennsylvania 18105

(ATTN: Dr. R. C. Longworth) 1

Airesearch Manufacturing Company  
A Division of the Garrett Corporation  
333 West First Street  
Dayton, Ohio 45402

1

Airesearch Manufacturing Company  
A Division of the Garrett Corporation  
2525 West 190th Street  
Torrance, California 98509

(ATTN: Mr. R. S. Hunt) 1

Atomics International  
8900 DeSoto Avenue  
Canoga Park, California 91304

(ATTN: Mr. J. K. Evert) 1

Quantity

The Cosmodyne Corporation  
2920 Columbia Street  
Torrance, California 90509

(ATTN: Mr. Paul A. Gira)

1

Cryogenic Technology, Inc.  
266 Second Avenue  
Waltham, Massachusetts 02154

(ATTN: Mr. Frank Maddocks)

1

Cryogenic Technology, Inc.  
Kelvin Park  
Waltham, Massachusetts 02154

(ATTN: Mr. Robert Stuart)

1

Donald W. Douglas Laboratories  
2955 George Washington Way  
Richland, Washington 99352

(ATTN: Dr. W. Martini)

1

Electro-Optical Research Company  
10845 Lindbrook Drive  
Los Angeles, California 90024

(ATTN: Mr. Khalil Seyfafi)

1

General Electric Company  
Research and Development Center  
P.O. Box 43, Bldg. 37  
Schenectady, New York 12301

(ATTN: Dr. P.A. Rios)

5

Hughes Aircraft Company  
Department 27-77  
Centinela and Teale Streets  
Culver City, California 90230

(ATTN: Mr. J. F. Skinner)

1

Kinergetics, Inc.  
60271/2 Reseda Road  
Tarzana, California 91356

(ATTN: Mr. K. W. Cowans)

1

**Quantity**

Arthur D. Little, Inc.  
20 Acorn Park  
Cambridge, Massachusetts 02140  
(ATTN: Mr. R. W. Breckenridge, Jr.)

1

Arthur D. Little, Inc.  
Room 20/448  
20 Acorn Park  
Cambridge, Massachusetts  
(ATTN: Mr. T. Heuchling)

1

Lockheed Missiles and Space Company  
Department 5221 Bldg. 205  
3251 Hanover Street  
Palo Alto, California 94304  
(ATTN: Dr. Glassford)

1

Lockheed Research Laboratories  
3251 Hanover Street  
Palo Alto, California 94304  
(ATTN: Dr. P. Caren)

1

McDonnell Douglas Corporation  
Bldg. 22, Mail Station 17  
5301 Bolsa Avenue  
Huntington Beach, California 92647  
(ATTN: Mr. Richard A. Madsen)

1

Mechanical Technology, Inc.  
968 Albany-Shaker Road  
Latham, New York 12110  
(ATTN: Mr. O. Decker)

1

Philips Laboratories  
345 Scarborough Road  
Briarcliff Manor, New York 10510  
(ATTN: Mr. Alexander Daniels)

1

Radio Corporation of America  
Defense Electronics Products  
Applied Research  
Camden, New Jersey 08102  
(ATTN: Mr. B. Shelpuk)

1

Texas Instruments, Inc.  
North Building, Box 6015  
Mail Station 220  
Dallas, Texas 75222

(ATTN: Mr. Terry Christensen)

Quantity

1

Texas Instruments, Inc.  
North Building  
P.O. Box 6015  
Dallas, Texas 75222

(ATTN: Mr. C. D. Taylor)

1